ISSN 2367-7570

Workshop
"Solar Influences on the Magnetosphere, Ionosphere and Atmosphere"

Book
of
Proceedings

Fifteenth Workshop

June, 2023

Organized by:
Space Research and Technologies Institute
Bulgarian Academy of Sciences

Editorial Board

Editors: **Katya Georgieva, Boian Kirov, Simeon Asenovski**

Acknowledgements

The Workshop's organizers acknowledge the support by the Bulgarian National Science Fund, Grant No KP-06-MNF/31, and the Bulgarian Academy of Sciences.

Scientific Organizing Committee

Preface

The Fifteenth Workshop "Solar Influences on the Magnetosphere, Ionosphere and Atmosphere" was held from June 5 to 9, 2023 in Primorsko, Bulgaria. 60 scientists from 17 countries participated in the workshop with 48 oral and 19 poster presentations. 23 papers are included in these Proceedings.

The Scientific Organizing Committee and the Editors of the Proceedings thank all the participants in the Workshop and the contributors to the Proceedings.

DOI: 10.31401/WS.2023.proc

CONTENT

Sun and Solar Activity

Solar Wind-Magnetosphere-Ionosphere Interactions

Instrumentation for Space Weather Monitoring

Solar Influences on the Lower Atmosphere and Climate

Data Processing and Modelling

Six EUV Solar Radiation Proxies: A Comparative Analysis

Elias A.G.[1,2], Medina F.D.[1,2], Duran T.[3,4], Zossi B.Z.[1,2], de Haro Barbas B.F.[1,2]

[1]Laboratorio de Ionosfera, Atmosfera Neutra y Magnetosfera (LIANM), Facultad de Ciencias Exactas y Tecnologia (FACET), Universidad Nacional de Tucuman (UNT), Argentina;
aelias@herrera.unt.edu.ar
[2]INFINOA (CONICET-UNT), Argentina
[3]Departamento de Física, Universidad Nacional del Sur (UNS), Bahía Blanca, Argentina
[4]Instituto de Física del Sur (CONICET-UNS), Bahía Blanca, Argentina

Abstract.

Six EUV solar radiation proxies (Mg II, Lyman alpha flux, F10.7, Rz, F30 and He II) are analyzed along the period 1979-2022, covering four solar activity cycles, to assess their differences and similarities along the different phases of the quasi-decadal cycle. Following a previous study based on four of these proxies, their variability is compared through: (1) a correlation analysis, (2) their sensitivity along the solar activity cycle through its variation in terms of percentage, and (3) their role in filtering the solar activity effect from ionospheric F2 region critical frequency, foF2. The differences detected through these approaches can be used to decide which solar proxy to use according to the research purpose.

Keywords: solar proxy; EUV solar indices; solar activity cycle; foF2 trends.

Introduction

In this study, we aim to explore two issues: how different solar EUV proxies behave, and how well do they represent solar EUV radiation for ionospheric studies. Based on two previous studies [Elias et al., 2021; Elias et al., 2023], and on the works by Bruevich et al. [2014] and Bruevich and Bruevich [2019], we make a comparative analysis of six EUV solar radiation proxies: Mg II, Lyman α, F10.7, Rz, F30, and He II along the period 1979-2022 which covers four solar activity cycles. Among the several statistical methods available for this purpose we choose a correlation analysis and a sensitivity evaluation along the different solar cycle phases. In addition, we compare these proxies' ability to filter out solar EUV variability effect on the critical frequency of the F2-layer of the ionosphere, foF2. This parameter is a measure of the peak electron density of the ionosphere and is highly sensitive to solar EUV variations.

Data

Six solar activity proxy were considered, that is we added two proxies to the four already analyzed in our previous works [Elias et al., 2021; Elias et al., 2023]:

(1) MgII core-to-wing ratio (MgII), which corresponds to the ratio of the h and k lines of the solar MgII emission at 280 nm to the background solar continuum near 280 nm. The composite MgII was used, which combines data from different satellites. It is available from the University of Bremen [Snow et al., 2014] (https://www.iup.uni-bremen.de/UVSAT/datasets/mgii).

(2) Lyman α flux (Fα) (in W/m^2), which corresponds to the full disk integrated solar irradiance over 121-122 nm, and is dominated by the solar HI 121.6 nm emission. The composite Fα was used, which combines multiple instruments and models, available from the Laboratory for Atmospheric and Space Physics (LASP, University of Colorado) Interactive Solar Irradiance Data Center (LISIRD) [Machol et al., 2019].

(3) F10.7 (in sfu=$10^{-22}Ws/m^2$), which corresponds to the radio emission from the Sun at 10.7 cm (2800 MHz), and is measured at the Earth's surface at the Penticton Radio Observatory in

British Columbia, Canada (https://www.spaceweather.gc.ca/forecast-prevision/solar-solaire/solarflux/sx-5-en.php).

(4) The sunspot number (Rz), from the revised Rz data base obtained from SILSO (Sunspot Index and Long-term Solar Observations), Royal Observatory of Belgium, Brussels (https://www.sidc.be/SILSO/datafiles).

(5) F30 (in sfu=10^{-22}Ws/m^2), which corresponds to the radio emission from the Sun at 30 cm (1GHz), and is available at the National Astronomical Observatory of Japan (http://solar.nro.nao.ac.jp/norp/html/daily_flux.html).

(6) HeII (in 10^{11} ph/cm^{2}s) which corresponds to solar flux at 30.4 nm, and is available at http://projects.pmodwrc.ch/solid-visualization/makeover/index.php until 2015 and updated to 2022 from https://lasp.colorado.edu/lisird/data/soho_sem_P1D.

MgII, Fα, F30 and HeII monthly means were estimated from their daily data base, while F10.7 and Rz monthly values were directly obtained from their data source. The period January 1979-December 2022 is considered. In terms of their solar origin, they are from: the photosphere for Rz, the higher chromosphere for MgII, the transition region to the corona for Fα, the higher chromosphere and the corona for F10.7 and F30, and the transition region for HeII.

foF2 data from 9 stations, listed in Table 1, at 12 LT were used. Monthly median foF2 data were obtained as follows. Japanese and Australian stations data are available from the National Institute of Information and Communications Technology, Japan (https://wdc.nict.go.jp/IONO/index_E.html) and the World Data Centre (WDC) for Space Weather, Australia (https://downloads.sws.bom.gov.au/wdc/iondata/au/), respectively. European stations monthly medians up to 2009 were obtained from Damboldt and Suessman database [Damboldt and Suessman, 2012] (https://downloads.sws.bom.gov.au/wdc/iondata/medians/). In the case of Juliusruh, the period was updated until 2022 from https://www.ionosonde.iap-kborn.de/mon_fof2.htm. In the case of Boulder and Rome the period was updated from Lowell GIRO Data Center (LGDC) [Reinisch and Galkin, 2011].

Table 1. Geographic coordinates and geomagnetic latitude of the 9 ionospheric stations analyzed

Station	Geographic Latitude [°]	Geographic Longitude [°]	Geomagnetic Latitude [°]
Okinawa	26.31	127.59	17.28
Wakkanai	45.25	141.40	37.06
Kokubunji	35.71	139.49	27.28
Canberra	-35.17	149.08	-41.74
Townsville	-19.16	146.48	-26.21
Hobart	-42.53	147.19	-49.22
Juliusruh	54.60	13.40	53.98
Boulder	40.13	-105.23	47.65
Rome	41.54	12.29	41.49

Correlation analysis

In Table 2 the squared correlation coefficients, r^2, which indicates the variance explained between each pair of EUV proxies considering annual mean series are listed. It can be noticed that all are greater than 0.94, which means that there is 94% of common variance between all of them, except the case between HeII and Fα. So we could say, at least statistically, that they have a common forcing, which we also assume is the same as for the EUV radiation.

When we correlate annual series of each month, without any averaging, the correlation decreases. In Fig. 1, as an example, we have r^2 between each EUV proxy and Mg II for each month along the period 1979-2022. The dashed line indicates the correlation for the annual mean series, which is clearly higher than almost every monthly correlation.

We also repeated the running correlation analysis, as in Elias et al. [2021], based on the work by Bruevich et al. [2014] in order to go through the different phases of the solar cycle, considering a 3-year window for each of the solar EUV proxy pairs. The results, with the addition of F30 and HeII in the present work, are the same to those shown in Fig. 1 of Elias et al. [2021]. The correlation decreases for maximum and minimum periods in all the cases.

Table 2. Squared correlation coefficient, r^2, between each pair of the 6 solar proxies considered, for the period 1979-2022, annual series.

	Mg II	Lyman α	F10.7	Rz	F30	He II
Mg II	1					
Lyman α	0.987	1				
F10.7	0.984	0.970	1			
Rz	0.974	0.959	0.987	1		
F30	0.987	0.982	0.987	0.974	1	
He II	0.940	0.935	0.962	0.974	0.941	1

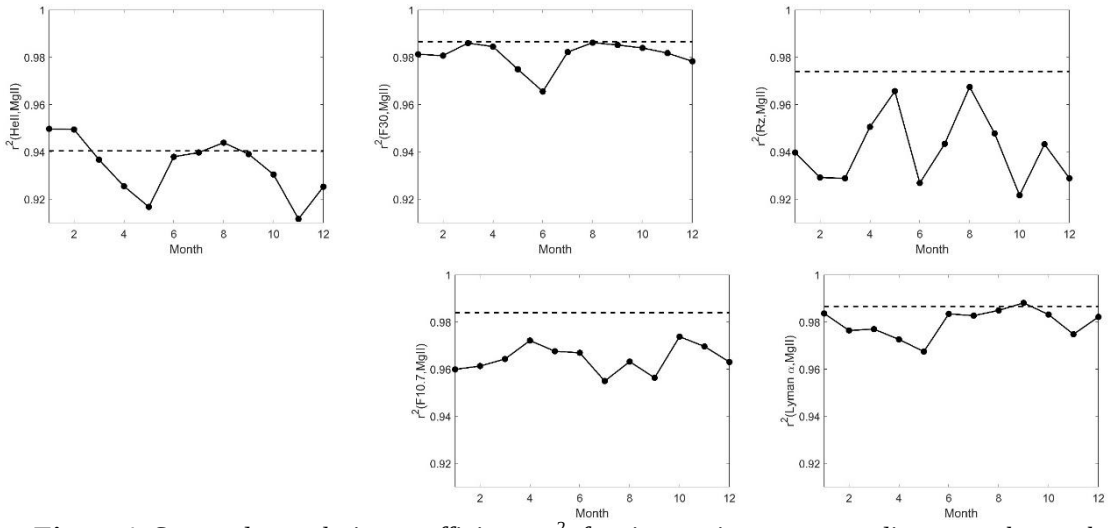

Figure 1. *Squared correlation coefficients, r^2, for time series corresponding to each month separately, for the period 1979-2022, between MgII and each of the other 5 solar EUV proxies. The dashed line indicates r^2 for the annual time series.*

Sensitivity analysis

Each proxy sensitivity along the solar activity cycle through its variation in terms of percentage was assessed as in Elias et al. [2023], adding F30 and HeII to the analysis. The amplitude of the decadal cycle relative to the mean value considering the corresponding cycle was estimated as $100 \times [X(\max) - X(\min)]/\text{mean}(X)$, where X represents each EUV proxy, and $X(\max)$ and $X(\min)$ correspond to the maximum and minimum value, respectively, for each cycle, as is shown schematically in Fig. 2 in the case of Rz. In this way, sensitivity is interpreted as the response of the proxy to the variation between the maximum and the minimum level of solar activity. From highest to lowest, the average percentage sensitivity was ~250% for Rz, ~140% for HeII, ~120% for F10.7, ~110% for F30, ~45% for Fα, and 10% for MgII. The two

extreme cases are Rz, for which the amplitude of variation in a cycle was two and a half times that of its average value, and MgII, for which this amplitude was of the order of one tenth of its average value.

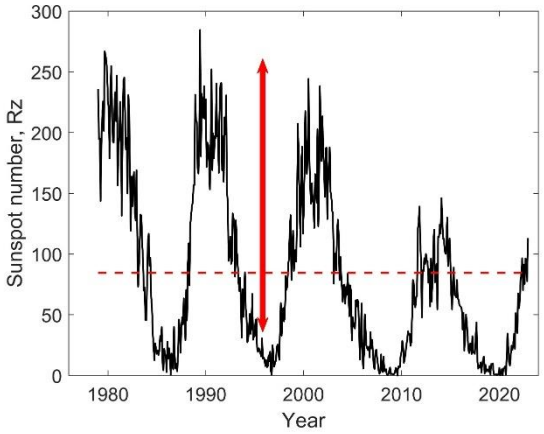

Figure 2. *Rz monthly mean series (black solid line), mean value along the period 1979-2022 (red dashed line) and amplitude from minimum to maximum of a complete cycle (red arrow).*

Trend analysis

Considering that foF2 long-term trends variability can be a “thermometer” of a solar index efficiency as an EUV proxy, we include an foF2 trend analysis as an additional characterization of the time behavior of each proxiy here analyzed. foF2 is a measure of the maximum ionospheric electron density and depends directly on solar EUV radiation, which is the main ionization source, especially at mid and low-latitudes. A key aspect of long-term trend assessments in ionospheric parameters is the solar activity filtering prior to the trend estimation. The foF2 filtering was done in the usual way by estimating the residuals from a linear regression between foF2 and each EUV proxy [Lastovicka, 2021] as follows:

$$\text{foF2 residual} = \text{foF2}_{exp} - (A\,X + B) \quad (1)$$

where $foF2_{exp}$ is the measured foF2 data, *X* stand for the solar proxy (Rz, F10.7, MgII, Fα, F30 or HeII), and A and B are the least squares parameters of the linear regression between $foF2_{exp}$ and X. Then, the linear trend is estimated from the linear regression between these residuals and time, that is

$$\text{foF2 residual} = \alpha\, t + \beta \quad (2)$$

where α is the desired trend in [MHz/year].

Long term trends in foF2, specifically decreasing trends, are expected due to increasing greenhouse gases concentration such as CO_2. This expected effect, however, is very small. Not more than 4%, or less, of foF2 variability, and that is why the filtering process is extremely important. Suspecting that not all EUV indices are equally efficient in representing solar EUV we estimate foF2 trends using each EUV proxy in the filtering process. It is assumed that trend values or variability patterns can show proxies' adequacy in representing EUV.

Fig. 3 shows the 9 stations' trends for each month and also for the annual means. It can be clearly seen that not all annual trends are equal. Furthermore, trends' monthly variation, even though quite similar in all the cases, are not exactly the same. Starting from the fact that all EUV proxies explain 95% or more of foF2 variance, there different possible interpretations to

distinguish each proxy efficiency. If the expected trend is an foF2 decrease due to the increase in greenhouse gases concentrations, then one could argue that the proxy that best reflects EUV behavior is the one that yields negative trends. Another possibility is to assume that the best proxy is the one that yields lower trends regardless of the sign. Based on the first reasoning, HeII appears to be the least suitable reflecting the true behavior of solar EUV, even though its corresponding wavelength falls within the EUV range that ionizes the F2 layer. According to the second reasoning, the best proxies would be Rz or F10.7, contrary to the results of recent publications that favor MgII and F30 [Lastovicka and Buresova, 2023; Zossi et al., 2023]. In fact, the differences are so small, that a deeper analysis should be made in order to clearly determine which index is the best EUV measure.

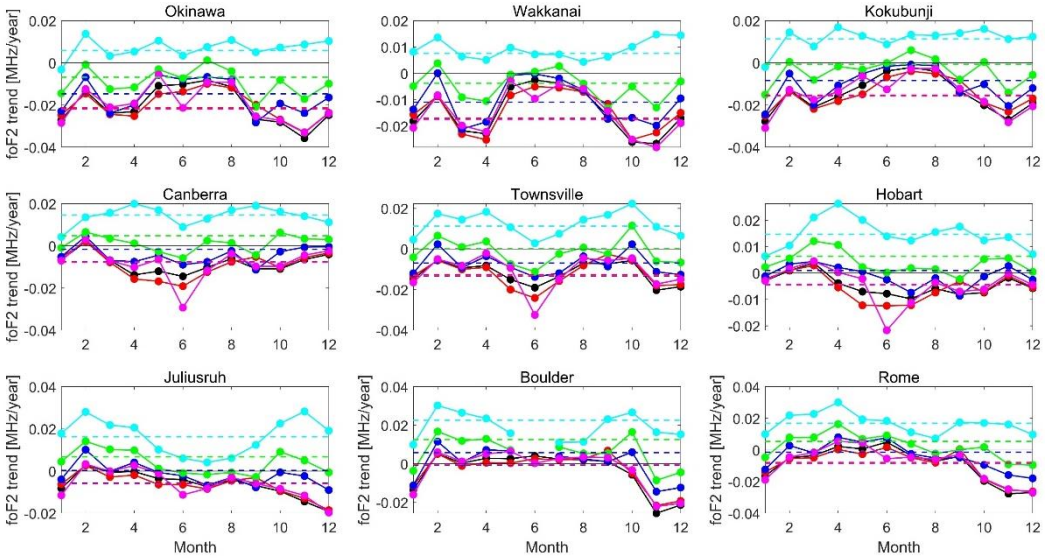

Figure 3. *foF2 trends along 1979-2022 for each month time series, filtering solar activity with MgII (black), Fα (red), F10.7 (blue), Rz (green), F30 (magenta) and HeII (cyan). Dashed lines correspond to foF2 trend assessed with annual mean values.*

Discussion and conclusions

Correlation coefficients between any pair of solar EUV proxies for the entire period 1979-2020 is greater than 0.94 but if we focus on monthly data or on shorter periods, it decreases. In monthly scales, each EUV proxy has a different source, and evidently in monthly timescales they do not have the same variation, as it is the case in annual timescale. In the case of correlation along periods shorter than the solar cycle, specifically during maximum and minimum periods when the correlation decreases, a reason could be purely statistical, as explained in Elias et al. [2021; 2023], being due to the EUV varies too little during minimum and maximum and the only variation left is the noise, which of course is not correlated with anything. Regarding each proxy sensitivity, they are all different, and probably this could explain the behavior along the last two solar minima periods which are not reflected equally by all the proxies: some are much lower than the previous minima and others present similar activity levels among all minima periods. we point this out as an important aspect that deserves a deeper research.

Going to the trend results, the difference observed in foF2 trend values, depending on which EUV proxy is used in the filtering process previous to trend calculation, may indicate their different ability to adequately represent solar EUV time variation. A possibility would be to assume that the proxy that gives smallest trends is the more adequate, or the proxy that gives the expected negative trends globally. Under both hypothesis, HeII seems to be the less

adequate. Another problem here is again, the last two minima levels. If they are really lower than the previous ones, and the proxy does not show this behavior, foF2 trend will be systematically negative. This is another aspect of EUV proxies, and also of ionospheric trends' study, that deserves a much deeper research (we would like to note that there are many papers in this last years dealing with this trend problem, being still controversial).

To conclude, we wish to emphasize the significance of this analysis. The solar irradiance in the EUV spectral range is a key parameter for aeronomy and for space weather [Dudok de Witt et al., 2008]. However, it is a long-standing issue the lack of continuous observations and their limited time span. This is due to EUV measurements must be carried out above the terrestrial atmosphere, along with significant sensitivity changes of space-borne EUV detectors during long-term periods due to instrument degradation. Therefore, it is of great importance to study how different solar EUV proxies behave and how well they represent solar EUV variability, not only for ionospheric studies but for other research purposes as well.

References

Bruevich, E., Bruevich, V. (2019). Long-term trends in solar activity. Variations of solar indices in the last 40 years. Res. Astron. Astrophys., 19, 090, DOI:10.1088/1674-4527/19/7/90

Bruevich, E.A., Bruevich, V.V., Yakunina, G.V. (2014). Changed relation between solar 10.7-cm radio flux and some activity indices which describe the radiation at different altitudes of atmosphere during cycles 21–23. J. Astrophys. Astron., 35, 1–15, DOI:10.1007/s12036-014-9258-0

Damboldt, T., Suessmann, P. (2012). Consolidated Database of Worldwide Measured Monthly Medians of Ionospheric Characteristics foF2 and M(3000)F2. INAG (Ionosonde Network Advisory Group) Bulletin 73 https://www.ursi.org/files/CommissionWebsites/INAG/web-73/2012/damboldt_consolidated_database.pdf.

Dudok de Wit, T., Kretzschmar, M., Aboudarham, J., et al. (2008), Which solar EUV indices are best for reconstructing the solar EUV irradiance? Adv. Space Res., 42, 903– 911, DOI:10.1016/j.asr.2007.04.019.

Elias, A. G., de Haro Barbas, B. F., Medina, F. D., Zossi, B. S. (2021). On the correlation between EUV solar radiation proxies and their long-term association. In Proceedings of the Thirteenth Workshop "Solar Influences on the Magnetosphere, Ionosphere and Atmosphere" (pp. 20–23). Sofia, Bulgaria.

Elias, A. G., Martinis, C. R., de Haro Barbas, B. F., Medina, F. D., Zossi, B. S., Fagre, M., Duran, T. (2023). Comparative analysis of extreme ultraviolet solar radiation proxies during minimum activity levels. Earth Planet. Phys., 7, 540–547, DOI:10.26464/epp2023050

Lastovicka, J. (2021). What is the optimum solar proxy for long-term ionospheric investigations? Adv. Space Res., 67, 2-8, DOI:10.1016/j.asr.2020.07.025.

Lastovicka, J. Buresova, D. (2023). Relationships between foF2 and various solar activity proxies, Space Weather, 21, e2022SW003359, DOI:10.1029/2022SW003359.

Machol, J., Snow, M., Woodraska, D., Woods, T., Viereck, R., Coddington, O. (2019). An improved Lyman-alpha composite. Earth Space Sci., 6, 2263–2272, DOI:10.1029/2019EA000648.

Reinisch, B.W. and Galkin, I.A. (2011). Global ionospheric radio observatory (GIRO), Earth Planets and Space 63, 377-381, DOI:10.5047/eps.2011.03.001.

Snow, M., Weber, M., Machol, J., Viereck, R., Richard, E. (2014). Comparison of Magnesium II core-to-wing ratio observations during solar minimum 23/24. J. Space Weather Space Clim., 4, A04, DOI:10.1051/swsc/2014001.

Zossi, B.S., Medina, F.D., Tan Jun, G., Lastovicka, J., Duran, T., Fagre, M., de Haro Barbas, B.F., Elias, A.G. (2023). Extending the analysis on the best solar activity proxy for long-term ionospheric investigations, Proc. R. Soc. A., 479, 202302252, DOI:10.1098/rspa.2023.0225.

Some Comments on the Matching of Photometric and Magnetic Properties of Structures at the Solar Surface

Obridko V.[1], *Sokoloff D.*[1,2], *Katsova M.*[3]

[1]IZMIRAN, 4, Kaluzhskoe Shosse, Troitsk, Moscow 108840, Russia; obridko@mail.ru
[2]Department of Physics, Moscow State University, 119991, Russia; sokoloff.dd@gmail.com
[3]Sternberg Astronomical Institute, Lomonosov Moscow State University, 13, Universitetsky Prospekt, Moscow 119234; mkatsova@mail.ru

Abstract

We investigate sharply outlined features recorded in solar magnetic field tracers. It is shown that the magnetic boundaries of a sunspot do not coincide with the photometric ones. Moreover, there is no clear magnetic boundary around sunspots. Thus, the widely accepted concept of a magnetic tube with clearly pronounced borders is not always correct and should be used with caution. It is also shown that even in the periods of complete absence of visible spots on the Sun, there are magnetic fields over 800 Gauss. The nature of these strong magnetic fields remains unclear; they may originate at relatively small depths under the photosphere.

Keywords: sunspot; solar cycle; magnetic field.

Introduction

Since it is known that the photometric and magnetic boundaries of sunspots do not coincide, Obridko et al. (2022) investigated sharply outlined features revealed in solar magnetic field tracers. Taking into account that the magnetic boundary is not determined accurately enough, they showed that photometric and magnetic properties of objects on the solar surface need further investigation. In this paper, we continue discussing the correspondence between the photometric and the magnetic boundaries. It should be noted right away that, generally speaking, the concept of a magnetic boundary is rather conventional. The magnetic field has no walls; so, it is impossible to imagine a physical object on the Sun, inside which the magnetic field exists and outside it is completely absent. This is a fundamental distinction between the magnetic and the photometric boundary, at least at the level of the photosphere, where the horizontal optical thickness is comparable to the resolution limits of up-to-date observational facilities. Therefore, the photometric boundary can be established more reliably than the magnetic one. A different matter is that we can specify the value of the magnetic field, which corresponds to the given photometric boundary.

There is no doubt that the magnetic field is the main factor determining the very existence of most objects in the Sun. However, the definition of their boundaries in terms of the magnetic field is not well developed in scientific literature. The fact is that we can only obtain information about the structure and dynamics of these objects from the analysis of their radiation. The magnetic field does not radiate directly. Radiation comes from plasma, whose characteristics (pressure, density, and temperature) are determined by processes that are affected by the magnetic field.

The magnetic field in the corona is often described as tubes and loops. Indeed, high-quality images of the corona display structures delineated by the field lines. Moreover, extrapolations of the potential field often agree well with the coronal structure (Aschwanden, 2001, 2004; Badalyan, 2013; Mac Cormack, 2022). However, one should remember that the radiation in this case depends on the differential emission measure calculated as a full integral of the squared electron density n_e^2 at the corresponding temperature; e.g., see (Priest, 1982; Aschwanden,

2004; Pevtsov, 2003). The density and temperature are determined by heating mechanisms (Parker, 1988; Aschwanden, 2004). The latter can be canalized along the field lines and, in any case, they strongly depend on the magnitude and structure of the magnetic field; see (Badalyan and Obridko, 2006, 2007) and references therein. In this case, weak variations in the magnetic field can significantly affect the radiation of the coronal plasma. The field structural features in the lower corona or in the photosphere can manifest themselves in the particular details of radiation of the coronal plasma. No wonder that in this case, the glow of the solar corona can outline the structure of field lines. The observed photometric feature can be associated with moderate variations in the magnetic field, while the large-scale field as a whole remains quasi-homogeneous. Therefore, identifying a luminous coronal feature with a magnetic tube or loop and assuming a correspondence between their spatial parameters can entail serious errors in modeling and calculation of mechanisms. To date, this question remains open due to the unclear mechanisms of heating and energy transfer in the corona, as well as due to a possible presence of strong currents.

Magnetic Field at the Photometric Boundary of a Sunspot

For a long time, the magnetic field outside sunspots was considered negligible. Equations were derived, according to which the magnetic field vanishes at the outer boundary of the penumbra (Broxon, 1942; Mattig, 1953), and the dependence of the field intensity on the distance from the center of a symmetric spot is fully determined by the maximum magnetic field at the center.

The magnetic and photometric boundaries were assumed to coincide. Although this assumption still needs verification, it, nevertheless, resulted in a theoretical concept of magnetic tubes and ropes. Nowadays, the concept of a floating magnetic tube is widely accepted. It is believed, that sunspots arise during the formation of active regions on the solar surface from a strong toroidal field generated by the solar dynamo. In fact, all arguments in favor of this concept are based on theoretical considerations (Caligari et al, 1995, 1998; Fan, 2008; Fan and Fang, 2014; Weber, 2011; Getling, 2016; Getling and Buchnev, 2019). The mechanism of formation of sunspots and (more broadly) bipolar active regions described above has been recently analyzed in detail in (Kosovichev, 2009, 2012; Smirnova et al, 2013; Solov'ev and Kirichek, 2014; Rempel and Cheung, 2014; Zagainova et al., 2022; Getling, 2016; Getling and Buchnev, 2019).

In (Obridko et al., 2022), we proposed a new method for determining the magnetic boundary of visible sunspots. The method was based on long-term data series, including SDO/HMI data on the daily longitudinal magnetic field for 2375 days (from 01.05.2010 to 31.10.2016) and the daily sunspot numbers from WDC–SILSO, Royal Observatory of Belgium, Brussels http://sidc.oma.be/ silso/datafiles (version 2). The cumulative daily sunspot areas were taken from the NASA Web site https://solarscience.msfc.nasa.gov/greenwch.shtml. At present, two databases of high–resolution observations carried out with single–type instruments are available. These are SOHO/MDI and SDO/HMI. The Michelson Doppler Imager (MDI) onboard the Solar and Heliospheric Observatory (SOHO) was continuously measuring the Doppler velocity, longitudinal magnetic field, and brightness of the Sun for 15 years up to 12 April 2011. The enhanced Helioseismic and Magnetic Imager HMI onboard the Solar Dynamics Observatory (SDO) started its routine observations on 30 April 2010. HMI observations provide the same data as MDI, but with much higher spatial and temporal resolution and of better quality.

We estimate the relative area of the solar surface occupied by the magnetic field exceeding a certain threshold value. This area is expressed in millionths of the visible hemisphere (m.v.h.) as is customary in studying the total sunspot areas. Then, we compare these calculations with

the daily sunspot data to find the field value, at which the area of the closed region bounded by this field according to magnetic measurements corresponds exactly to the sunspot photometric area on that day. As a result, we arrive at the conclusion that the magnetic field of a sunspot as defined by the field normal component is about 550 G.

However, the magnetic field at the visible boundary of a spot does not vanish. The field region does not have a sharp boundary and extends far beyond the photometric boundary. The relationship between the field intensity in a circular sunspot and its relative photometric radius is illustrated in Figure 1.

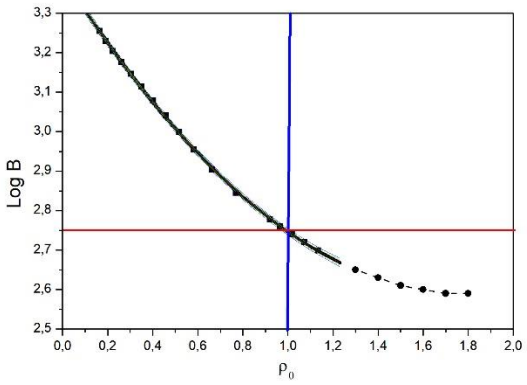

Figure 1. Empirical dependence of the magnetic field (dots, measured in G) in a symmetric sunspot on the relative sunspot radius (ρ_0 = 1 at the photometric boundary). The solid line is a polynomial approximation, the dashes extrapolate the approximation for weak magnetic fields. The thin blue lines near the approximation mark the 95% confidence interval. The thick blue line shows the photometric sunspot boundary, and the red line shows the magnetic sunspot radius, calculated presuming that the sunspot magnetic radius corresponds to the magnetic field strength of 550 G.

Thus, the sharpness of the boundary is not the result of the absence of magnetic field outside the "tube", but is rather due to a combined action of two interrelated phenomena. At a certain field value (i.e., at 500-550 G), the convective transfer from depth to the photosphere is suppressed, and the temperature (and, hence, the brightness of the region) drops. The energy of the 500 G magnetic field is comparable to that of the convective flow in the lower part of the photosphere at the optical depth τ =1 at a density of about 3 10^{-7} g/cm^{-3} and a speed of about 2 km/s. In this case, the sharpness of the boundary is determined by the fact that the horizontal optical thickness in the photosphere does not exceed 100 km and, therefore, the horizontal heating for the sunspot as a whole is ineffective.

Small Elements with a Strong Magnetic Field

The discussion above is aimed at determining the boundary of large spots. However, there is a local aspect of the problem. The fact is that the interaction between the magnetic field and the convective transfer depends on the size of the magnetic element. If the element is small enough (about 100 km in size), the horizontal optical thickness for the radiative transfer becomes comparable to the geometric size of the element. Then, the horizontal transfer can smooth out the temperature profile. This is why some elements with a strong magnetic field are present on the solar surface even if standard observations do not reveal any sunspots.

Stenflo (1973, 1982) claimed the existence of optically unobservable small elements of the magnetic field. Shiota et al. (2012) directly observed such elements in the solar polar region with extra-atmospheric high-resolution instruments.

In order to estimate the role of locally strong magnetic fields in the context of sunspot studies, we illustrate observations of elements with locally strong magnetic field obtained on spotless days (Figure 2). We have calculated the area covered with the field above the given threshold value.

The black dots stand for the magnetic field B>100 125 G. The area of these regions is of the order of several thousand m.v.h. The areas of the regions covered with magnetic fields B>400 G (squares) and B>600 G (circles) are slightly smaller.

However, it is most impressive that, even on spotless days, there are dozens of objects with B>800 G (crosses). Such objects should be considered as sunspots, although they are not observed by standard methods. The area of such regions is very small (several dozen m.v.h.), as well as their contribution to the total magnetic flux. Still the total magnetic field energy in these regions may reach 10^{30} erg and they may be responsible for moderate solar flares. We want to emphasize that dozens of such objects exist even in the epochs of very deep solar minimum. As they are not recorded by the sunspot patrol service, their size is apparently much smaller than 2-3 arcsec in cross section.

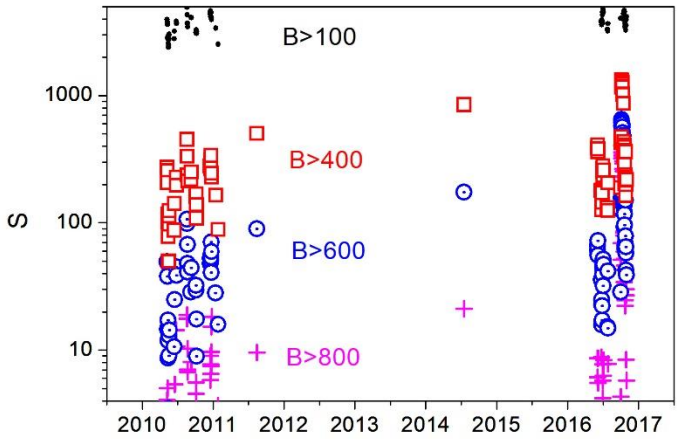

Figure 2. Statistics of the magnetic-field intensity on spotless days. The black dots stand for B>100 G, the red squares stand for B>400 G, the blue dotted circles correspond to B>600 G, and the purple crosses indicate the area covered by strong magnetic field B>800 G.

The role of small magnetic elements has to be somehow included in the scenario of the solar cycle. According to the conventional scenario, the large-scale toroidal magnetic field is produced from the poloidal field by differential rotation. The small magnetic elements are not inevitably formed as part of this scheme, but can be driven by turbulent processes. During the solar minima, i.e., in the periods, when the action of the large-scale dynamo is weak, turbulent mechanisms may produce small magnetic elements all over the solar surface and not just near the solar equator (see Sherrer et al,. 2012). Note that at the reversal of the large-scale polar magnetic field, the number of small magnetic elements with strong magnetic fields of both polarities is more or less equal.

Conclusion

Thus, we arrive at the conclusion that the sunspot is not an isolated magnetic tube. The photometric boundary of a sunspot is not its physical boundary, but is the region of a sharp change in the spot brightness as the magnetic field reaches the threshold value of 550 G. On the other hand, small elements with high magnetic fields permanently exist in the Sun, but their

contrast is too low due to the horizontal heat transfer, so that standard observations cannot identify them as spots. The brightness drops significantly only in large features that significantly exceed the horizontal optical thickness (≥100 km.)

The results obtained are of great importance for understanding the generation of magnetic field on the Sun and the formation of active regions. The generally accepted idea of the field tubes is not entirely correct. It is believed that sunspots appear as individual features on the solar surface in the course of the formation of AR from a strong toroidal field, which is generated by the solar dynamo mechanism at the base of the convection zone and is carried out into the photosphere. In fact, the arguments in favor of this concept are based rather on theoretical considerations than on reliable observational evidence. The emergence of a single magnetic tube as a source of sunspots contradicts the observed field structure of a single sunspot. During the generation process, the turbulent dynamo creates many elements with different field strengths. Their energy distribution changes with the phase of the cycle. However, these elements are not tubes with isolated boundaries. The field in them gradually decreases with distance from the center of the element to its periphery. The photometrically sharp boundaries of the spots are the result of influence of the magnetic field on the energy transfer process. Fields above 550 G greatly reduce the energy flux from below and a sharp boundary appears (Pikelner, 1960; Kaplan and Pikelner, 1974).

Moreover, sunspots emerge in the pre-existing magnetic environment and are included in active regions. The formation of sunspots is not at all a surface phenomenon. It rather develops in the leptocline and obviously requires further investigation and modeling (see, e.g., Kitiashvili, 2023).

Note that our analysis of objects on the solar surface, probably, entails a more general conclusion: the existence of objects with sharp photometric boundaries both on the Sun and in space by no means implies the existence of as sharply bounded magnetic structures.

Acknowledgements

VNO, MMK and DDS acknowledge the support of the Ministry of Science and Higher Education of the Russian Federation under the grant 075-15-2020- 780 (VNO and MMK) and 075-15-2022-284 (DDS). DDS thanks support by BASIS fund number 21-1-1-4-1.

References

Aschwanden, M.J., Schrijver, C.J., Alexander, D. (2001). Modeling of Coronal EUV Loops Observed with TRACE. I. Hydrostatic Solutions with Nonuniform Heating, Astrophys. J., Vol. 550, pp. 1036–1050. DOI:10.1086/ 319796.

Aschwanden, M.J. (2004). Physics of the Solar Corona: An Introduction, Springer, Berlin.

Badalyan, O.G. (2013). Relationship between the brightness in the coronal green line and magnetic fields on various scales, Astronomy Reports, Vol 57, Issue 3, pp. 222-232,

Badalyan, O.G., Obridko, V.N. (2006). Two Regularities in the Coronal Green-Line Brightness Magnetic Field Coupling and the Heating of the Corona, Solar Physics, Vol 238, Issue 2, pp.271-292.

Badalyan, O.G., Obridko, V.N. (2007). To the problem of solar coronal heating, Astronomy Letters, Vol 33, Issue 3, pp.182-191.

Broxon, J.W. (1942). Relation of the Cosmic Radiation to Geomagnetic and Heliophysical Activities, Physical Review, Vol. 62, No. 11-12, pp. 508–522, DOI:10.1103/PhysRev.62.508.

Caligari, P., Moreno-Insertis, F., Schussler, M. (1995). Emerging Flux Tubes in the Solar Convection Zone. I. Asymmetry, Tilt, and Emergence Latitude, ApJ, Vol 441, p. 886. DOI:10.1086/175410.

Caligari, P., Schuessler, M., Moreno-Insertis, F. (1998). Emerging Flux Tubes in the Solar Convection Zone. II. The Influence of Initial Conditions, ApJ, Vol. 502, No. 1, pp. 481–492, DOI:10.1086/305875.

Fan, Y., Fang, F. (2014). A Simulation of Convective Dynamo in the Solar Convective Envelope: Maintenance of the Solar-like Differential Rotation and Emerging Flux, ApJ, Vol. 789 (1), p. 35, arXiv:1405.3926, DOI:10.1088/0004-637X/789/1/35.

Fan, Y. (2008). The Three-dimensional Evolution of Buoyant Magnetic Flux Tubes in a Model Solar Convective Envelope, ApJ, Vol. 676 (1), pp. 680–697, doi: 10.1086/527317.

Getling, A.V., Ishikawa, R., Buchnev, A.A. (2016). Development of Active Regions: Flows, Magnetic-Field Patterns and Bordering Effect, Solar Phys., Vol. 291, No. 2, pp. 371–382. arXiv:1506.01848, DOI:10.1007/s11207-015-0844-3.

Getling, A.V., Buchnev, A.A. (2019). The Origin and Early Evolution of a Bipolar Magnetic Region in the Solar Photosphere, ApJ, Vol. 871, No. 2, p. 224, arXiv: 1805.06486, DOI:10.3847/1538-4357/aafad9.

Kaplan, S.A., Pikel’ner, S.B., Tsytovich, V.N. (1974). Plasma physics of the solar atmosphere, Phys. Rep., Vol. 15, No. 1, pp. 1–82, DOI:10.1016/0370-1573(74) 90041-6.

Kitiashvili, I N , Kosovichev, A.G., Wray, A.A., Sadykov, V.M., Guerrero, G. (2023). Leptocline as a shallow substructure of near-surface shear layer in 3D radiative hydrodynamic simulations, MNRAS, Vol. 518, No. 1, pp. 504–512, arXiv:2203.01484, DOI:10.1093/mnras/stac2946.

Kosovichev, A.G. (2009). Photospheric and Subphotospheric Dynamics of Emerging Magnetic Flux, Sp. Sci. Rev., Vol. 144 (1-4), pp. 175–195. arXiv: 0901.0035, DOI:10.1007/s11214-009-9487-8.

Kosovichev, A.G. (2012). Local Helioseismology of Sunspots: Current Status and Perspectives, Solar Phys., Vol. 279 (2), pp. 323–348. arXiv:1010.4927, DOI:10.1007/s11207-012-9996-6

Mac Cormack, C., Lopez Fuentes, M., Mandrini C.H., Lloveras, D., Vasquez, A.M. (2022). Enthalpy-based modeling of tomographically reconstructed quiet-Sun coronal loops, Advances in Space Research, Vol. 70, Issue 6, pp. 1570-1579.

Mattig, W. (1953). Die radiale Verteilung der magnetischen Feldst¨arke in normalen Sonnenflecken. Mit 2 Textabbildungen, Zeitschr. Astrophys., Vol. 31, p. 273.11

Obridko, V.N., Katsova, M.M., Sokoloff, D.D., Shelting, B.D., Livshits, I.M. (2022). Clarifying Physical Properties of Magnetic Fields in Sunspots, Solar Phys., Vol. 297, p. 131, DOI. ADS.

Parker, E.N. (1988). Nanoflares and the solar X-ray corona, Astrophys. J., Vol. 330, pp. 474–479, DOI:10.1086/166485.

Pevtsov, A.A., Fisher, G. H., Acton, L.W. et al. (2003). The Relationship between X-Ray Radiance and Magnetic Flux, Astrophys. J., Vol. 598, No. 2, pp. 1387– 1391. DOI:10.1086/378944.

Pikel’ner, S.B. (1960).The Mechanism of Formation of Active Regions in the 300 Presence of a Magnetic Field, Astron. Zh., Vol. 37, p. 616.

Priest, E.R. (1982). Solar Magnetohydrodynamics.

Rempel, M., Cheung, M.C.M. (2014). Numerical Simulations of Active Region Scale Flux Emergence: From Spot Formation to Decay, ApJ, Vol. 785 (2), arXiv:1402.4703, doi:10.1088/0004-637X/785/2/90.

Scherrer, P.H., Schou, J., Bush, R.I., Kosovichev, A. G., Bogart, R.S., Hoeksema, J.T., Liu, Y., Duvall, T.L., Zhao, J., Title, A.M., Schrijver, C.J. , Tarbell, T.D., Tomczyk, S. (2012). The Helioseismic and Magnetic Imager (HMI) Investigationfor the Solar Dynamics Observatory (SDO), Solar Phys., Vol. 275 (1-2), 295, pp. 207–227. DOI:10.1007/s11207-011-9834-2.

Smirnova, V., Efremov, V.I., Parfinenko, L.D., Riehokainen, A., Solov’ev, A.A. (2013). Artifacts of SDO/HMI data and long-period oscillations of 275 sunspots, A&A, Vol. 554, A121, DOI:10.1051/0004-6361/201220825.

Solov’ev, A., Kirichek, E. (2014). Basic properties of sunspots: equilibrium, stability and long-term eigen oscillations, Astroph. Sp. Sci., Vol. 352 (1), pp. 23–42, DOI:10.1007/s10509-014-1881-3.

Stenflo, J.O. (1973). Magnetic-Field Structure of the Photospheric Network, Solar Phys., Vol. 32 (1), pp. 41–63. DOI:10.1007/BF00152728.

Stenflo, J.O. (1982). The Hanle Effect and the Diagnostics of Turbulent Magnetic Fields in the Solar Atmosphere, Solar Phys., Vol. 80 (2), pp. 209–226. DOI:10.1007/BF00147969.

Shiota, D., Tsuneta, S., Shimojo, M., Sako, N., Orozco Su´arez, D., Ishikawa, R. (2012). Polar Field Reversal Observations with Hinode, ApJ, Vol. 753 (2), p. 157.,arXiv:1205.2154, DOI:10.1088/0004-637X/753/2/157.

Weber, M.A., Fan, Y., Miesch, M.S. (2011). The Rise of Active Region Flux Tubes in the Turbulent Solar Convective Envelope, ApJ, Vol. 741 (1), p. 11. arXiv:260 1109.0240, DOI:10.1088/0004-637X/741/1/11.

Zagainova, Y.S., Fainshtein, V.G., Obridko, V.N., Rudenko, G.V. (2022). Study of the Magnetic Properties of Sunspot Umbrae, Astronomy Reports, Vol. 66 (2), pp. 116–164, DOI:10.1134/S1063772922030064.

The Numerical Determining of the Magnetic Dynamo Growth Rate During a Parametric Resonance

Sokoloff D.D.[1,2], *Serenkova A.Yu.*[1,2], *Yushkov E.V.*[1,2,3]

[1]Physics Faculty, Lomonosov Moscow State University, Moscow, 119991 Russia
[2]Moscow Center of Fundamental and Applied Mathematics, Moscow, 119991 Russia
[3]Space Research Institute, Moscow, 117997 Russia; e-mail: serenkova.ai19@physics.msu.ru

Abstract.

Classical parametric resonance in oscillatory systems can be characterized by the appearance of exponential growth near the selected frequencies of parametric excitation. However, if the oscillatory system, even without parametric excitation, has exponential growth (which is typical, for example, for dynamo-systems describing stellar magnetic cycles), then the appearance of parametric excitation can lead not only to the change in exponential growth, but also to a splitting of oscillation frequencies, and, accordingly, to the appearance of unharmonic oscillations. The numerical analysis of such a structure with an exponentially growing amplitude is a complex problem for which we propose a special approach. Using the proposed approach, we analyze the dependence of generation rates and frequencies on the excitation frequency for a well-known Parker-type dynamo-system.

Keywords: MHD dynamo; parametric resonance; numerical methods.

Introduction.

Many astrophysical dynamo systems have their own oscillation frequencies, so for such systems the question of the periodic impact of their cosmic "neighbors" (satellites, planets and stars) becomes topical. The answer to this question can be sought both analytically and numerically [Serenkova et al., 2023], but it should be taken into account that the analysis must be highly accurate, since, for example, the effects of classical parametric resonance appear in the immediate vicinity of doubled and multiple frequencies. Here we use numerical analysis and develop a method to find dynamo growth rates and frequencies for a simple well-known dynamo model in a spherical thin convective shell. This model was proposed by Eugene Parker in 1955 to describe solar magnetic activity and is a direct consequence of averaging the magnetic induction equation over a random velocity field [Steenbeck et al., 1966], while the field itself, for convenience, is decomposed into a poloidal and toroidal component (A and B, respectively) with azimuthal spherical symmetry [Parker, 1955]:

$$\begin{aligned} \dot{A} &= R_\alpha B + A_{\theta\theta} - \mu^2 A, \\ \dot{B} &= R_\omega (A\sin(\theta))_\theta + B_{\theta\theta} - \mu^2 B, \end{aligned} \tag{1}$$

here the parameter R_α is responsible for hydrodynamic helicity, R_ω is responsible for differential rotation, the product $R_\alpha * R_\omega$ gives the dynamo number, and μ determines the radial part of the diffusion. The subscript represents the derivative of the zenith angle.

Hypothetically, some periodic influence on the system (for example, binary stars on each other or exoplanets on their star) can lead to periodic changes in R_α or R_ω, which, in turn, can cause the parametric resonance, since the magnetic field also oscillates with time. To analyze this situation, the following change is added to the system:

$$R_\omega \to R_\omega(1 + \sigma\sin(\omega t)), \tag{2}$$

where σ is the amplitude of the parametric effect.

The Parker system can be simplified by reducing it by a low-mode approximation to a system of ordinary differential equations, e.g., [Kalinin and Sokoloff, 2019], [Tarbeeva et al., 2011], [Kalinin and Sokoloff, 2018]. The analysis of the low-mode system is given in the work [Serenkova et al., 2023], where a special kind of resonant curve of the dependence of the exponential growth rate on the excitation frequency is shown. At the same time, for each frequency of parametric excitation, the velocity was determined as follows: the maxima of the oscillations were found, which were supposed to form a growing exponent, natural logarithms were taken from the obtained values and approximated by a straight line (Figure 1, left panel) using the least squares method [Stigler, 1986]. However, this method turned out to be inapplicable for the analysis of oscillations obtained by numerically solving a system of partial differential equations, due to the strong noise of the resonant pattern. The main problem is related to a more complex pattern of oscillations than with harmonic oscillations with exponentially increasing amplitude. In particular, there is a splitting of frequencies, so the local exponential growth of the maxima can be replaced by a decrease. Due to this reason, the histogram of the slope angles between the logarithms of neighboring maxima (Figure 1, right panel) has the form not of a single peak, but of some limited corridor of values, within which the true value of the growth rate is to be found.

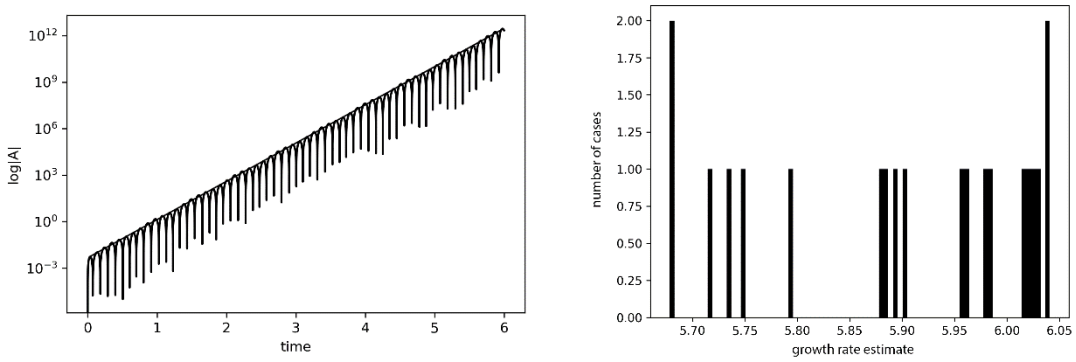

Figure 1. *Left panel: exponential growth of field A at zenith angle $\theta = \pi/4$. Right panel: histogram of slope angles between logarithms of neighboring maxima with exponential growth of the magnetic field in the Parker system.*

A new method for determining the speed.

In order to determine the actual rate of exponential growth, the following technique is used: for the already obtained solution of the system in the absence of diffusion for a given angle $\theta = \pi/4$, a histogram of the slope angles between the logarithms of the adjacent two maxima is constructed (Figure 1, right panel). The smaller slope is denoted by $\gamma_{\min}$, the larger one, respectively, $\gamma_{\max}$, and then the segment between them is divided into 1000 parts of length $d\gamma = (\gamma_{\max} - \gamma_{\min})/1000$. The diffusionless solution is multiplied by $e^{-\gamma t}$, iterating γ from $\gamma_{\min}$ to $\gamma_{\max}$ in increments of $d\gamma$ until the solution stops growing, this value is γ and is declared the exponential growth rate of the system by this frequency. For the numerical algorithm, the stopping criterion will be the location of the largest maximum of oscillations (not counting the first few pieces when the system has not yet entered its mode) in the left half of the graph, that is, if the time is counted in the program up to $T = 6$, then the greatest maximum is expected to

be seen up to $t = T/2 = 3$. An example of oscillations with such a γ is shown in (Figure 2, left panel).

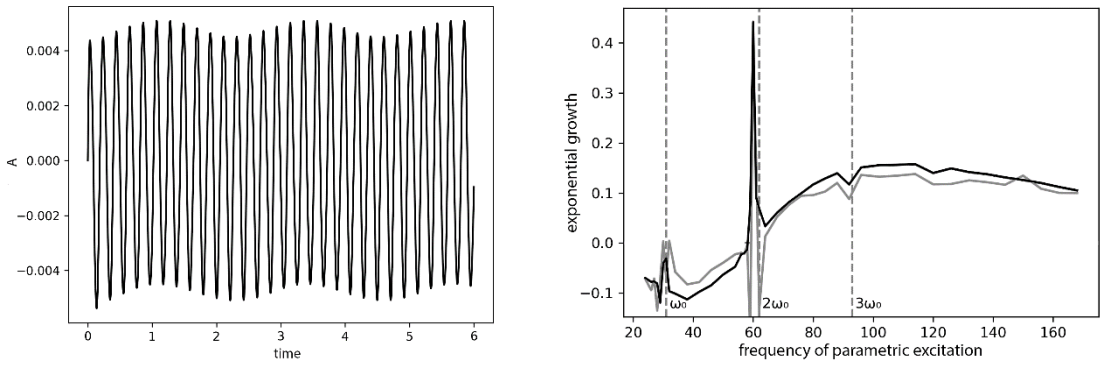

Figure 2. *Left panel: a type of oscillation for a solution with suppressed generation at a sufficiently accurately calculated exponential growth rate at zenith angle $\theta = \pi/4$. Right panel: the dependence of the exponential growth rate on the frequency of parametric excitation in the Parker system during calculations in the old way (gray) and new (black), vertical lines mark the natural, doubled and tripled frequencies of the system.*

The advantage of the new method for numerically determining the exponential growth rate of a system is that, in addition to a significant increase in accuracy and, as a result, a smoother dependence of this rate on the excitation frequency (Fig. 2, right panel), it becomes possible to do without any methods averaging values from the histogram. This averaging, which was included, in particular, in the least squares method used earlier, introduced the largest error due to the uniform distribution of growth rate estimates over individual maxima. In general, it would be possible to increase the number of maxima, but this requires more numerical power and results in less accuracy. Instead, the speeds calculated by the new method have a specific mathematical meaning - when multiplied by the corresponding exponent with a negative exponent, growth stops. The speed of calculation by the new method is also low, since for this the program only multiplies the ready-made solution by a number and looks for its local maximum.

Oscillation frequencies of the system.

Obtaining the correct exponential growth rate of a dynamo system with parametric action now allows us to more accurately determine the frequencies at which this system oscillates. By the type of vibrations (Figure 2, left panel), it can be understood that there should be several such frequencies, since there is some similarity of beats. The easiest way to determine the oscillation frequencies is using the Fourier transform [Fourier, 1822], but it is simply inhumane to force a computer to numerically reproduce such a transformation for an exponentially growing solution. With the advent of a sufficiently precisely found exponential growth rate, the solution can be made to stop growing by multiplying it by the corresponding exponent, and then calculate the spectrum and frequencies of oscillations. The Fourier spectra for different frequencies of parametric exposure are shown in Figure 3. On all graphs there are main peaks at the natural frequency of the system (its calculation is performed in the absence of parametric

effects), as well as at least one other low peak, the position of which varies depending on the frequency of exposure (Figure 4), the remaining peaks are even lower and lie to the right of both previous ones. Figure 3 clearly shows how when the frequency of exposure reaches values in the vicinity of the doubled natural frequency of the system, the second peak merges with the first, forming beats. It is worth noting that this side frequency increases with the frequency of the disturbance, but does not coincide with it.

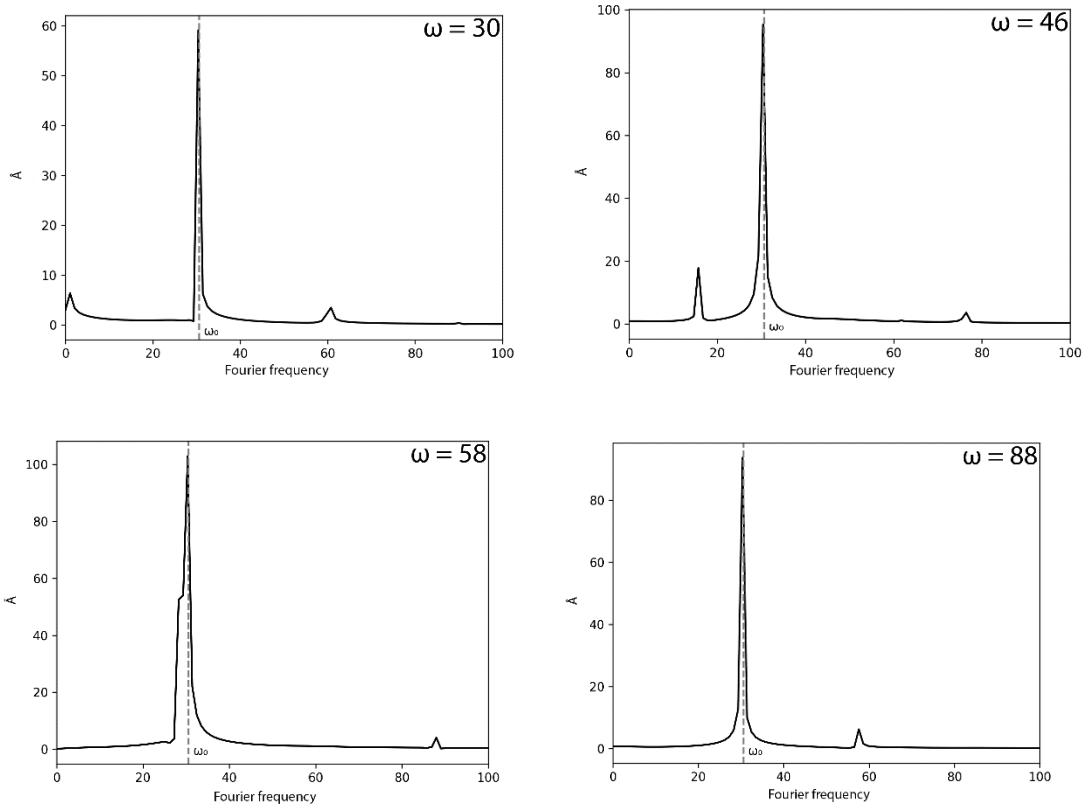

Figure 3. *The spectrum of the solution with suppressed generation for different frequencies of parametric excitation.*

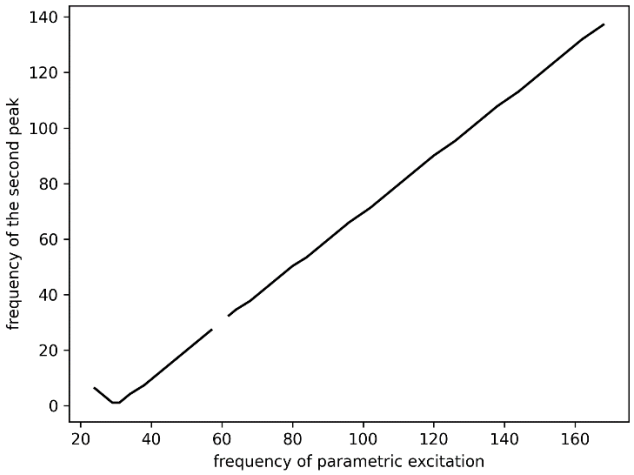

Figure 4. *The position of the second largest peak of the Fourier transform depending on the frequency of excitation. In the area of the doubled frequency of the system (about ω = 60), the peak merges with the main one.*

Conclusions.

The paper proposes a numerical algorithm that makes it possible to calculate the exponential growth rate of complexly oscillating solutions with any predetermined accuracy. The algorithm has demonstrated its advantage over previously used algorithms for harmonic oscillations with exponentially growing amplitude. Regarding the problem of parametric excitation in the Parker dynamo model, he made it possible to restore the dependence of the growth rate and the frequency Fourier spectrogram, which demonstrated fundamental differences from the classical parametric resonance. In particular, it was shown that, in addition to the generation rate peak at the doubled frequency, dynamo models can exhibit a resonant background (“non-selective resonance”), which corresponds to suppression of generation at low frequencies of the excitation force and enhancement of generation at high frequencies. In this case, the ratio of the amplitudes of the selective and non-selective resonance depends, as it turned out, on the parameters of the problem. Frequency Fourier spectrograms, which became possible to calculate after applying the developed algorithm to determine the generation rate, demonstrated the appearance of an additional peak along with the natural frequency of the system with a frequency that linearly depends on the frequency of the driving force. A distinctive feature in this case is that near the doubled (to the natural) frequency of the exciting force, a coincidence of frequencies is observed, and, accordingly, the behavior of the system takes the form of beats, which interferes with the operation of simpler mechanisms of numerical analysis.

Funding.

Theoretical statement about the parametric resonance problem in dynamo systems was carried out with the support of the Ministry of Education and Science of the Russian Federation within the framework of the program of the Moscow Center for Fundamental and Applied Mathematics (project no. 075-15-2019-1621). The numerical analysis of the periodic impact on the generation of large-scale structure was carried out with the support of the Basis Foundation (grant no. 21-1-1-4-1).

References

Steenbeck, M., Krause, F., and Rädler, K-H. (1966). Z. Naturforsch., A 21, p.369.

Parker, E.N. (1955). Hydromagnetic dynamo models, The Astrophys. J., Vol. 122, p. 293, doi: 10.1086/146087.

Serenkova, A.Yu., Sokoloff, D.D., Yushkov E.V. (2023). Nonlinear parametric resonance in the simplest model of a solar dynamo, JETP, Vol. 136, No. 4, pp. 456-464, doi: 10.1134/S1063776123030068.

Stigler, S.M. (1986). The history of statistics: The measurement of uncertainty before 1900, Harvard University Press.

Kalinin, A.O. and Sokoloff, D.D. (2019). Dynamo resonances in a simple dynamo model, Magnetohydrodynamics, Vol. 55, pp. 193—199, doi: 10.22364/mhd.55.1-2.23.

Tarbeeva, S.M., Semikoz, V.B., and Sokoloff, D.D. (2011). Magnetic fields in the radiative-transport zone and the solar cycle, Astr. Reps., Vol. 55, No. 5, pp. 456, doi: 10.1134/S106377291104007X.

Kalinin, A.O. and Sokoloff, D.D. (2018). Resonances in spherical dynamos and super-flares, Astr. Reps., Vol. 62, No. 10, pp. 689-695, doi: 10.1134/S1063772918100050.

Fourier, J.B.J. (1822). Théorie Analytique de la Chaleur, a Paris, Chez Firmin Fidot, P`ere et Fils.

Investigation of Solar Energetic Particles (SEPs) Associated with X-Ray Solar Flares

Melike Tirnakci[1], Simeon Asenovski[2], Ali Kilcik[1]

1.Department of Space Science and Technologies, Akdeniz University Faculty of Science, 07058, Antalya, Turkey, e-mail: meliketirnakci@gmail.com
2. Space Research and Technology Institute BAS, Sofia, Bulgaria

Abstract

In this study we focus on the relationship between Solar Energetic Particles (SEPs) and X-ray Solar Flares (SFs) during solar cycles 23 and 24. The data was obtained from relevant websites, and the SEP data was classified according to our predetermined criteria. SEP data was separately analyzed for each X-ray SF class. To investigate the relationship, the temporal variation analysis was performed initially, followed by cross-correlation analysis. The obtained findings are as follows: i) All data sets used in the study follow the average 11-year Solar Cycle, ii) as shown in Figure 1 there is an agreement between all SF groups and SEP groups. iii) It can be clearly stated that all three categorized SEPs are particularly influenced by X-class SFs. iv) The resulting time delays indicate that SEP events occur after the flares.

1. Introduction

The Sun is a highly active star that spends approximately 70% of its lifetime at moderate levels of magnetic activity, around 15-20% in periods of grand minima, and about 10-15% in grand maxima (Usoskin, 2017). These activity periods can be most clearly understood through variations in the Sunspot Number (SSN). Due to its long-term record and the well-defined nature of the sunspot cycle, it has proven to be quite useful. Advancements in technology over time have enabled the observation of relatively smaller structures on the Sun. These smaller features have contributed to the development of various parameters/structures to characterize solar activity. Examples of such parameters/structures include prominences, solar flares (SFS), and indirectly, solar energetic particles (SEPs).

Solar energetic particles are high-energy charged particles that occur during eruptive solar events, such as solar flares and coronal mass ejections (CMEs). In other words, during these events, there are temporarily increased electron, proton, and ion currents, which are referred to as solar energetic particle (SEP) events in the interplanetary (IP) space. The most energetic of these charged particles (500 MeV) can reach the Earth's magnetosphere (Miteva et al., 2017). However, whether an SEP event will be detected, for example near Earth, depends on the location of the main event on the Sun: eruptions on the western position of the solar disk are much more likely to result in an SEP event observed at Earth (Klein and Dalla, 2017).

During SEP events, there are two different particle accelerators originated from the sun. The first one is associated with the reconnection process during a solar flare, known as "Impulsive" events and the second one is related to shock acceleration directed by CMEs, known as "Gradual" events (Reames, 2013). Nearly all the shock- accelerated particles will ultimately propagate out beyond the orbit of Earth. These charged particles can impact the Earth's magnetosphere and cause changes in geomagnetic activity. They are important events from the point of space weather studies.

Solar flares are abrupt increases in brightness observed on the solar surface, caused by the rapid release of magnetic energy. The release of magnetic energy during solar flares can lead to various phenomena, such as the emission of radiation across the entire electromagnetic spectrum, from radio waves to gamma rays. These events can release amount of energy, often exceeding 10^{32} ergs, into space within a short time span of tens of minutes (Fletcher et al., 2011). Solar flares are classified based on their observed wavelength, and two common classifications are the Hα and X-ray classifications. The X-ray classification system ranges from 1 to 8 Å and is further divided into classes A, B, C, M, and X, with class X representing the most powerful flares and class A being the weakest. Each of these categories is subdivided into nine divisions and classifications are logarithmic in scale.

Solar flares occur in different layers of the Sun's atmosphere, including the corona, chromosphere, and transition layer. A flare’s temporal evolution exhibits distinctive dynamical patterns as well. The impulsive phase is the time of greatest energy release, which expels mass from the chromosphere and adds it to the corona (Hudson, 2011) The duration of these events can vary, lasting anywhere from a few minutes to several hours.

In this study, we investigated the relationship between Solar Energetic Particles (SEPs) and different X-ray Solar Flare classes. Data and Methods are presented in Section 2, The Results in Section 3, and the Discussion and Conclusion in Section 4.

2. Data and Methods

2.1. Data

The datasets used in this study cover the period between 1996 and 2020 which is almost equal two solar cycles (SC23 and SC24). The SEP data, specifically proton flux greater than 10 MeV, were obtained from the NASA webpage (https://omniweb.gSFsc.nasa.gov/). X-ray Solar Flare number data were acquired from the Space Weather Prediction Center (https://www.swpc.noaa.gov/), while sunspot number data were downloaded from the Sunspot Index and Long-term Solar Observations (SILSO) (https://www.sidc.be/SILSO/home). All datasets were processed into daily and monthly versions for the subsequent analyses.

2.2. Methods

In this study, our initial step involved calculating the monthly total values of all available data for analysis. We specifically excluded the calculation of data points with missing proton flux values to ensure the accuracy of our analysis. The SEP data were further categorized into three distinct groups: 0-10 pfu, 10-100 pfu, and >100 pfu.

To obtain a visual understanding of the distribution, histograms were plotted separately for each category. Additionally, the classes C, M, and X from the X-ray Solar Flare data were added on these histograms for comparison.

We then proceeded to cross-correlation analyses. To explore the relationship between the two sets the cross-correlation analysis was performed. This analysis enabled us to determine correlation coefficient any possible time delay between datasets.

3. Results

Figure 1 shows the temporal variations of used data sets. From these plots, we can clearly observe two solar cycles. Especially for the 10-100 and 100> pfu solar energetic particles, it is observed that the solar cycles exhibit a double/multiple-peaked structures.

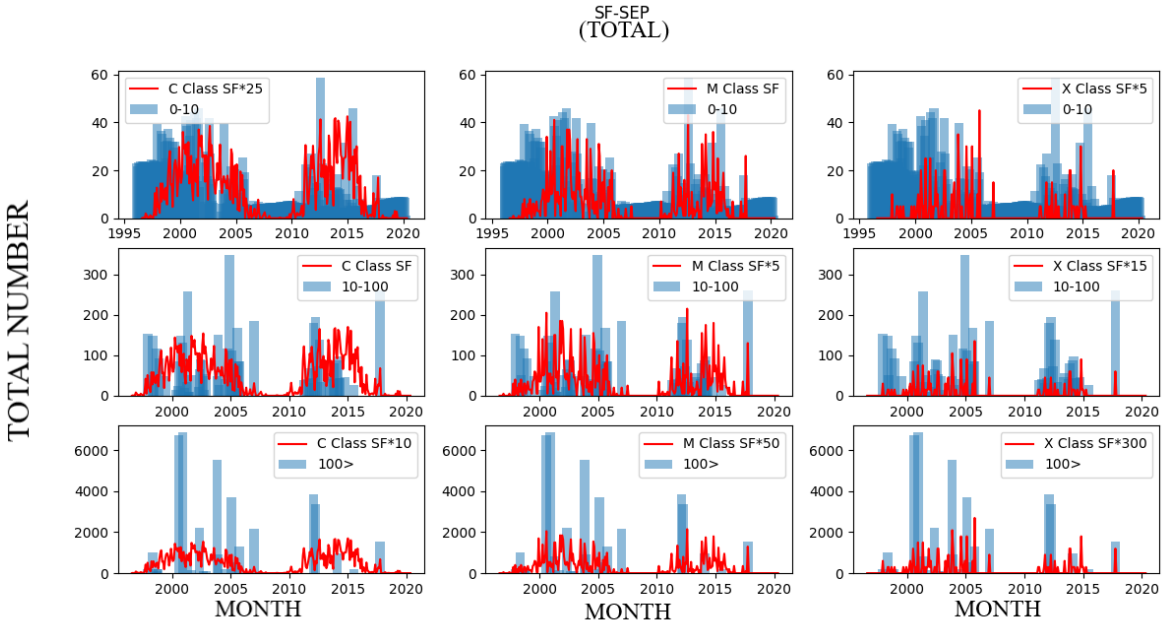

Figure1. Temporal variation plots of different class X-ray SFS and different categories of SEP events

Figure 2 plots the cross-correlation analysis results between different X-ray SFs and different SEP groups used in this study. The detailed results of the correlation analysis are given in Table 2.

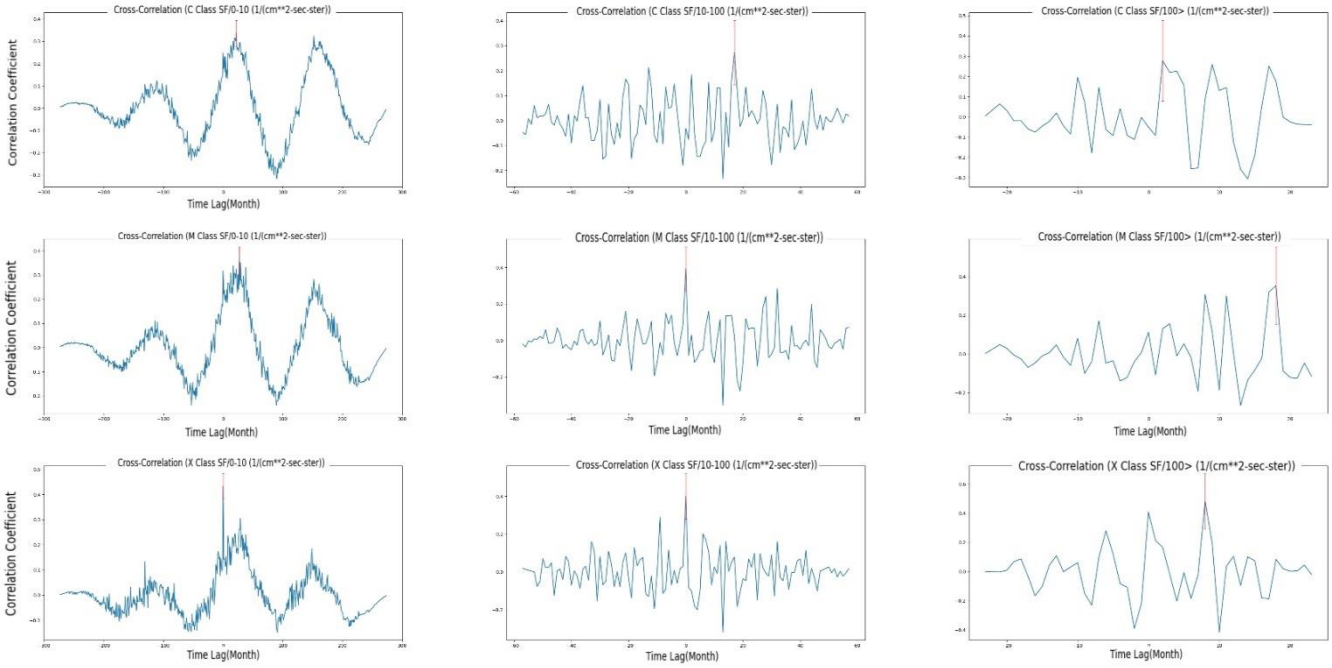

Figure2. Cross correlation analyses results between different X-ray SFS and SEP groups

The maximum peak in each graph represents the cross-correlation coefficient. The red line seen at the maximum correlation coefficient is the error bar. The error bars show the amount of standard errors.

Table1. Cross correlation coefficient and time delays

Cross correlation coefficient	**0-10 pfu**	**Time Delay (Month)**	**10-100 pfu**	**Time Delay (Month)**	**100> pfu**	**Time Delay (Month)**
C Class SFs	0.33±0.06	22	0.27±0.13	17	0.28±0.2	2
MClass SFs	0.37±0.06	27	0.39±0.12	0	0.35±0.2	18
X Class SFs	0.43±0.05	0	0.40±0.12	0	0.48±0.19	8

Based on Figure 2 and Table 1, we can conclude that X-class SFs are a source that influences all SEP groups.

In Figure 3, we compared the temporal variation of total SFs, SSN and SEPs. Here, it can be observed that both SFs and SSN are in good agreement with SEPs. The results of cross-correlation analysis can be found in Figure 4 and Table 2 for these data sets.

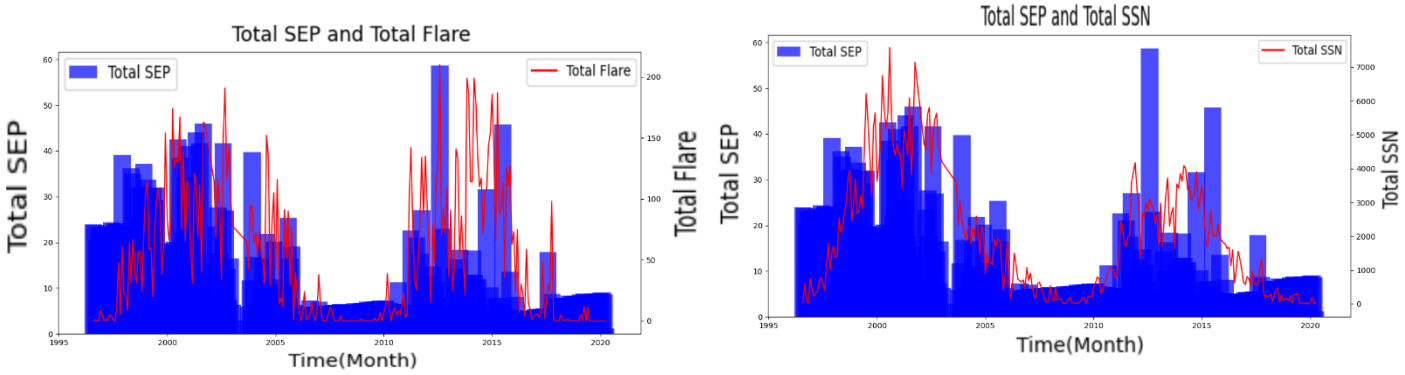

Figure3. Temporal variation plots (left: monthly total SEP and X-ray flare numbers, right: monthly total SEP and SSN)

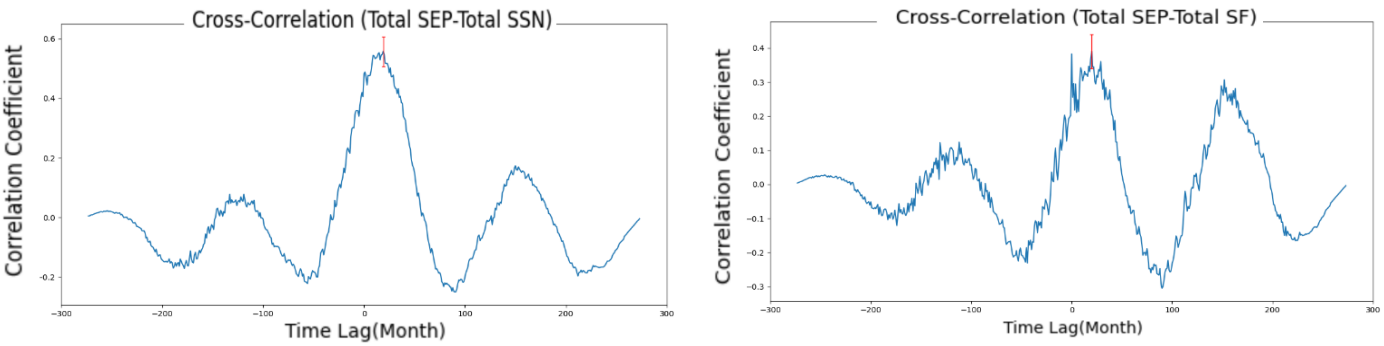

Figure4. Cross correlation analyses results (left: monthly total SEP and X-ray flare numbers, right: monthly total SEP and SSN)

Table2. Cross correlation coefficient and time delays

Cross correlation coefficient	SFs	Time Delay (Month)	SSN	Time Delay (Month)
SEP	0.39±0.06	20	0.56±0.05	19

When comparing Figure 4 and Table 2, there is a noticeable anomaly. However, this is not within the scope of this study. It will be explained in a follow-up study in the future.

4. Discussion and Conclusion

In this study, we have investigated SEP events and various X-ray Solar Flare classes. The findings of our study can be summarized as follows:

- All datasets used in the study follow the average 11-year Solar Cycle (Schwabe cycle).
- ii) iii) iv) as shown in Figure 1 there is an agreement between all SF groups and SEP groups. The correlation coefficient between SFS and SEP were also significant during the investigated time period (1996-2020).
- It can be clearly stated that all three categorized SEPs are particularly influenced by X-class SFs. The resulting time delays indicate that SEP events occur after the flares. While SSN data show a higher correlation than the X-ray SFs, this correlation mainly results from the 11-year cyclic trend. However, further examination of this relationship will be conducted in the forthcoming article.

As stated in Section 1, the primary sources of SEP events are CMEs and SFs. During times of high solar activity, there is a stronger correlation between the energies of CMEs and the X-ray flux of the flares they are associated (Youssef, 2012). Dierckxsens et al. (2015) found that events connected to large X-class flares, western solar longitudes, CMEs with high velocities, and halo CMEs typically have significantly higher possibilities of causing SEPs. In light of the influence of CMEs, we intend to expand this research in the future by introducing supplementary analyses, thus creating a follow-up to this paper. By doing so, we are planning to enhance the scope of our study considering the effects of CMEs.

References

Dierckxsens, M., Tziotziou, K., Dalla, S., Patsou, I., Marsh, M. S., Crosby, N. B., ... & Tsiropoula, G. (2015). Relationship between solar energetic particles and properties of flares and CMEs: statistical analysis of solar cycle 23 events. Solar Physics, 290, 841-874.

Fletcher, L., Dennis, B. R., Hudson, H. S., Krucker, S., Phillips, K., Veronig, A., ... & Temmer, M. (2011). An observational overview of solar flares. Space science reviews, 159, 19-106.

Hudson, H. S. (2011). Global properties of solar flares. Space Science Reviews, 158(1), 5-41.

Klein, K. L., & Dalla, S. (2017). Acceleration and propagation of solar energetic particles. Space Science Reviews, 212, 1107-1136.

Miteva, R., Samwel, S. W., & Krupar, V. (2017). Solar energetic particles and radio burst emission. Journal of Space Weather and Space Climate, 7, A37.

Usoskin, I. G. (2017). A history of solar activity over millennia. *Living Reviews in Solar Physics*, *14*(1), 1-97.

Reames, D. V. (2013). The two sources of solar energetic particles. Space Science Reviews, 175, 53-92.

Youssef, M. (2012). On the relation between the CMEs and the solar flares. NRIAG Journal of Astronomy and Geophysics, 1(2), 172-178.

The Analysis of Observations of Ionospheric and Geomagnetic Time Series for Detection of Precursors of Earthquakes

Adibekyan M.V.

Ministry of Emergency Situations of the Republic of Armenia Territorial Survey for Seismic Protection State Non-Commercial Organization
e-mail: adibekyan@yahoo.com

Abstract

The displays of earthquake preparation of Shorzha (Armenia, 29.05.2022, M=3.5) and Vardenis (Armenia, 29.04.2008г, M=3.6) in time-series have been studied using the geomagnetic and ionosphere tools and aiming at earthquake precursors apportionment.
There were received some results, which are allowing to make out the difference of seismogenic anomalies of ionosphere between the longer anomalies. They are connected to magnetic activity of ionosphere by the method of vertical reconnaissance of ionosphere. For a research of assessment of the current seismic hazard were studied observation geomagnetic fields and vertical sounding of ionospheric time series. Results of the analysis observation have confirmed communication between earthquakes magnitude $M \geq 3.5$ and absorption of a radio-emission of discrete radiation sources radio atmospheric observations and also dependence between and geomagnetic parameters. Lebed - A and Cassiopeia - A (ionospheric station of observation Saravand), geomagnetic station observation of Garni have been used.

Keywords: Earthquake, precursors, ionosphere, time-series, geomagnetic

Introduction

It is known, that the geophysical environment, including seismically active zones, are made up of solid, liquid and gaseous phases. In that zone of two phases separation is forming a Zone of Separated Changes (ZSC), or as they are called in physical chemistry, double ionic (electric) layers. Depending on their structure, each of the ZSC of geophysical environment is characterized by capacity, inductivity and resistance [Balassanian., 1990].

Seismic hazard assessment is carried out by continuous recording of various (electromagnetic, geomagnetic, ionospheric, etc.) symptoms in the hazard zone. Figure 1 shows observations of the daily variations of the geomagnetic field series (Garni station). For considering the geomagnetic field, the high accuracy proton magnetometers, which are measuring the T inductivity of geomagnetic field each 5 minutes, are used for measuring the geomagnetic field [Badalyan. et al., 2001]. There have been used the time – series for Saravand ionospheric and Garni geomagnetic stations.

The results obtained earlier allow to make out the difference between activity of ionosphere, by the method of vertical reconnaissance of ionosphere.
Radio astronomical monitoring method makes possible, along with immediate detection of electromagnetic emission from the Earth's depth in the selected frequency band, to observe other types of lithospheric impact on the atmosphere, such as aerosol, electrostatic, acoustical/gravitational, etc. Those sources ultimately create anomalies at different altitudes of the atmosphere, high affect the propagating radio astronomical signal [Martirosyan. R., 2006].

The method and technique of research

A new Methodology has been elaborated that provides possibility to estimate the current Seismic hazard (its intensity, location and time) with a sufficiently big probability. The elaborated methodology was used for analysis of data received in the process of perpendicular ionosphere from "Swan- A" and "Cassiopeia - A" point radio sources by radio astronomy methods. The time – series of geomagnetic field tension of T full vector.

Table 1

Year	*Month*	*Day*	*Lat*	*Lon*	*H*	*M*	*Region*
2022	*5*	*29*	*40.48*	*45.27*	*10*	*3.5*	*Armenia (Shorzha)*

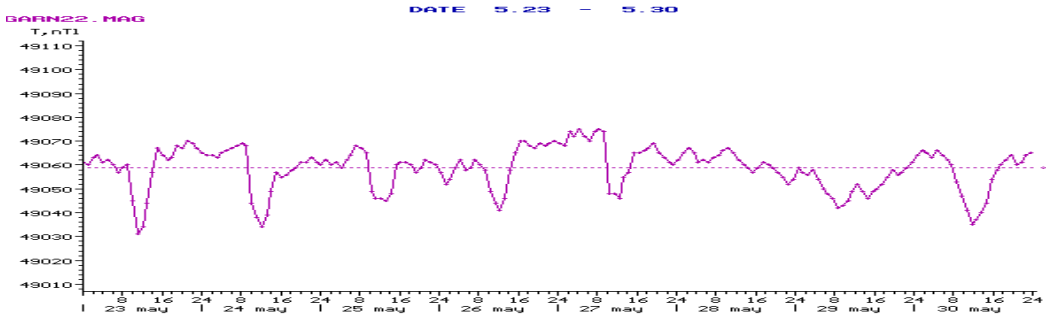

Fig 1. It can be seen that after the violation of the diurnal cycle, there were earthquakes with a magnitude m=3.5.

Swan –A Cassiopea-A

29.04.2008

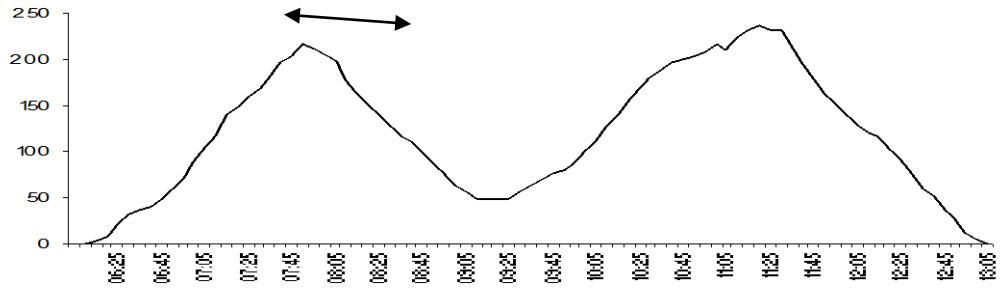

Fig 2. Radio astronomical observation of the radio emission of discrete radio sources Swan-A and Cassiopea-A before the Vardenis (Armenia, 29.04.2008, M=3.6) earthquake.

One can see a decrease in the power value of the discrete radio source Swan – a, which may be associated with seismic activity.

Conclusion

1. The above methods provide anomaly detection approximately 1-4 days before the earthquake.
2. The obtained anomalies are characterized by local dynamic changes, which are preceded by a significant and strong earthquake.

References

Badalyan M., Petrosyan. H., Adibekyan M.V. (2001) Peculiarities of Magnetic Precursors of Earthquakes on the Territory of Armenia.Journal of Georgian Geophysical Society.Physics of SolidEarth, vol.5, Tbilisi, p.37-43, 2001.

Balassanian S. (1990), Dynamic Geo-electricity. Novosibirsk, “NAUKA”, Siberian Department, pp.232.

Martirosyan R., Goulyan A., Sanamyan V., Piroumyan H., Adibekyan M., Mirsoyan. A. (2006). Remote sensing system of ionosphere for assessment of Seismic risks //Izv.NAN, RA Gyumri, Ser. TH. 2006. T.LIX, N 3.

Investigation of the Type of Radio Emissions from Sources of Radio Emissions Such as: Seismo-Ionospheric Communications, Galactic Background, "Swan-A" and "Cassiopeia-A" By Vertical Ionospheric Sounding at a Wavelength of 4.2 M

Adibekyan M.V.[1], Gulyan A.G.[2], Sargsyan S.A.[2], Arakelyan H.S.[2]

[1]Ministry of Emergency Situations of the Republic of Armenia -Territorial Survey for Seismic Protection (RSSP) State Non-Commercial Organization E-mail: adibekyan@yahoo.com
[2]Institute of Radiophysics and Electronics (IRPHE) of National Academy of Sciences of Republic of Armenia

Abstract

Vertical ionosphere sounding of seismic hazard assessment has carried out. The structure and system specifications of the vertical sounding of the ionosphere studied at a wavelength λ= 4,2 *m*. Opportunities were done to improve the sensitivity of the interference of the radio telescope with digital data observations for studing the seismic hazard assessment symptoms and the nature of change of flux density of the radio sources Swan-A and Cassiopeia-A. Earthquake in time-series have been studied using ionosphere tools which are aimed at earthquake precursors apportionment displays and preparation of Nakhichevan (Azerbaijan, 02.09.08, M = 5.1). There were received some results, allowing to make out the difference of seismogenic anomalies of ionosphere between the longer anomalies connected to magnetic activity of ionosphere by the method of vertical reconnaissance of ionosphere. Results of the analysis observation have confirmed communication between earthquakes magnitude M ≥ 3.5 and absorption of a radio-emission of discrete radiation sources radio atmospheric observations dependence between.

Keywords: Ionosphere, Radio Telescope, the Interference Harmonica, Digital Analysis

Introduction

Seismic hazard assessment is carried out by continuous recording of various (electromagnetic, geomagnetic, ionospheric, etc.) symptoms in the hazard zone. In a number of works [Barsukov,1991], models of the excited ionosphere are proposed in connection with the anomalous growth of the lithospheric-ionospheric interaction. The radio astronomical method of vertical sounding of the ionosphere unambiguously embraces the earthquake preparation zone is highly informative thanks to a sensitive radio telescope. Below are the structure and technical parameters of the radio telescope, as well as an analysis of the results of observations.

The ionosphere is called the upper ionized layers of the Earth's atmosphere D (60-90), E (100-120), F1 (160-180), F (300-450) *km*. Compared to oblique ionospheric sounding, its vertical sounding method has the following main advantages [Martirosyan1 et.al.,2006].

- The radio astronomical method of vertical sounding evenly covers the zone of preparation of a seismic event in contrast inclined sounding, where the receiving device is located - a radio telescope.
- Vertical sounding of the ionosphere mainly includes the image of complete changes in all its layers during the preparation of a seismic event, and oblique sounding - changes that are reflected only in its lower parts.
- In contrast to the methods of radio reception used in radar and communication technology, significantly different requirements are imposed on receiving systems for

radio astronomy observations, due to the nature of the received useful signal and its typical characteristics associated with its intensity.

- This radiation has a noise character: the spectral composition of the internal noise of such receivers does not differ from the noise of the receivers themselves, the radiation spectrum is constant in the receiver bandwidth.
- The power of the useful signal, due to the radio emission of a cosmic source, in the antenna output of the telescope is much less than the power of the intrinsic internal noise of the receiver, even in the case of antennas with a very large collecting surface.
- In addition to the low intensity and noise nature of the radiation of a radio source, it is often necessary to take into account its spatial distribution, the nature of polarization, etc. The choice of appropriate sources of cosmic radio emission is very important for conducting radio astronomy studies of vertical sounding of the ionosphere.

The main requirements for the selected radio sources are as follows:

- A radio source in a given geographical area of radio observation should be visible in the sky during the day, for as long as possible, and it should have an angular height close to the zenith of the given place (a mandatory condition for vertical sounding).
- The equatorial coordinates of the radio source (α, δ) must be known with sufficient accuracy for a given time.
- The radiation spectrum of the source must be well studied over a wide frequency range. It is desirable that its radiation flux density (S) be constant over time.
- The apparent angular dimensions of the radio source must be at least one order of magnitude smaller than the antenna system beamwidth for the radio source to be considered a point source

It is desirable that the radiation from the radio source be unpolarized.

Program and methodology of observations

Observations were made daily, nine hours long enough for both sources to pass through the radiation pattern of a fixed radio telescope in the interval $17h\ 30m \leq \alpha \leq 26h\ 30m$ of the right ascension of the source. Joint Registration radio emission from the Galactic background and discrete radio sources is carried out both in analog form - on a tape recorder and in the form of a digital series - in computer memory.

Filtering

The power digital filter amplifies the variable component of the cosmic radio source signal recorded after the detector, in this case, its spatial harmonic. Moreover, the greater its amplitude, the more it is amplified, and the selectivity of the system improves accordingly.

On Figure 1 shows the observations of the radio emission from discrete radio sources Swan-A and Cassiopea-A before the Nakhichevan (Azerbaijan, 02.09.08, M = 5.1) earthquake (Saravand station). On September 02, 2008, a decrease in the power value of Cassiopea-A discrete radio sources was registered, which may be associated with seismic activity.

Swan-A Cassiopea-A

02.09.08

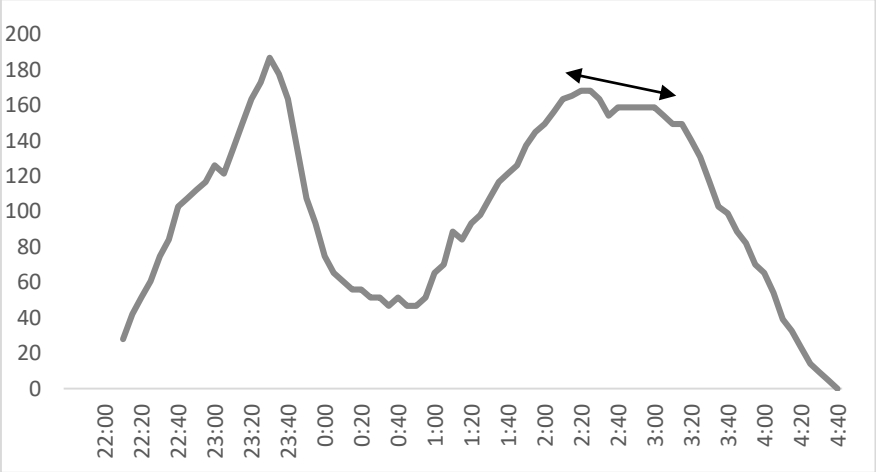

Fig 1. Radio astronomical observation of radio emission from discrete radio sources Swan-A and Cassiopea-A to Nakhichevan (Azerbaijan, 02.09.08, M = 5.1) earthquake (Saravand station).

Conclusion

The results of everyday, long - term observations presented in fig1. confirm the fact of the preparation of an earthquake with a magnitude $M \geq 5.1$ and the absorption of radio emission in the excited ionosphere, which can be explained by the deterioration of the radio transparency of the ionosphere due to the electromagnetic radiation of the deformed soil in the earthquake zone.

The encouraging results obtained substantiate the need for further studies of the seismo-ionospheric relationships of the vertical sounding method.

References

Barsukov O. (1991) Analisis Method for Seismoelectromagnetic Processes, M., Nayka, 1991, 56 p.

Martirosyan R., Goulyan A., Sanamyan V., Piroumyan H., Adibekyan M., Mirsoyan A., (2006) Remote sensing system of ionosphere for assessment of seismic risks //Izv.NAN, RA Gyumri, Ser. TH. 2006. T.LIX, N 3.

Verification of the Methodology for Forecasting the Ionosphere over Bulgaria in the Conditions of the Geomagnetic Storm on 27 February 2023

Bojilova R., Mukhtarov P.

National Institute of Geophysics, Geodesy and Geography, Bulgarian Academy of Sciences,
Acad. G. Bonchev St, Bl. 3, 1113 Sofia, Bulgaria
E-mail: rbojilova@geophys.bas.bg; engpjm@abv.bg

Abstract.

A study of the behavior of the ionosphere over Bulgaria on 27 February 2023 ionospheric storm caused by the G2 (Moderate) geomagnetic storm is presented. The examined geomagnetic indices describing the behavior of geomagnetic storm (Dst and Kp) indicate that this event had a sudden onset. The variability of the ionospheric critical frequency is represented by the data of 10 ionospheric stations for vertical sounding. The selected European stations are between 35° and 55° latitude and between 6°E and 33°W longitude. Based on interpolation of the data from all ionosondes, the values for foF2 (characterizing the maximum electron density) for the territory of Bulgaria were obtained. At the National Institute of Geophysics, Geodesy and Geography, there is a developed and integrated methodology for forecasting the critical frequencies over the territory of our country. In order to make verification in real conditions, the values of the combined empirical model for short-term forecasting were compared with the interpolated data from the ionospheric stations. The results show an extremely good match between the two types of data. All these results play an essential role and can be used for practical purposes and more precisely in preparing predictions for the propagation of radio waves at a given distance of radio path.

Keywords: ionosphere, geomagnetic storm; critical frequency

Introduction

It is well known that the ionospheric storms are the result of geomagnetic disturbances caused by streams of solar energetic particles that interact with the Earth`s magnetic field. Ionospheric storms can cause both an increase in electron density (so-called positive storms) and a decrease in electron density (so-called negative storms) [Chukwuma, 2007; Horvath and Lovell, 2015]. The investigation of variations in ionospheric characteristics is related to the main practical application of the ionosphere, namely the radio waves propagation. In some cases, ionospheric storms can causestrong disturbances to radio communications, where in middle and high altitudes, radio communications are considered "ineffective" [Hill, 1963]. The impacts of disturbances related to radio communications can include temporary blackouts of signal to radio-wave based technology such as radio paths and navigation systems [Rama Rao2009; Klimenko, 2011; Blagoveshchenskii, 2013].

Everything described above shows the importance of investigating the ionosphere and its variability in the conditions of geomagnetic storms. At present, there are various ionospheric data bases from individual points on planet Earth for vertical sounding of the ionosphere, as well as GNSS data for Total Electron Content (TEC). For the territory of the Republic of Bulgaria there is no working ionospheric vertical sounding station. To solve this problem, a team from the National Institute of Geophysics, Geodesy and Geography has created an empirical model for calculating of the critical frequencies of the ionosphere over Bulgaria based on TEC data in the absence of data from ionospheric station [Bojilova and Mukhtarov,2020a; Bojilova and Mukhtarov, 2021]. Based on a known model of the electron density profile and

the basic regularities of the reflection of radio waves from the ionosphere and through the obtained ionospheric parameters, it is possible to calculate specific radio paths (range of permissible radio communication frequencies) [Bojilova and Mukhtarov, 2020b].

In one of the latest studies related to the verification of the methodology for preparing daily forecasts for the propagation of radio waves on the territory of Bulgaria, a comparison was made between the measured values of the critical frequencies of the ionosphere (foF2 and MUF3000) for the San Vito station and the analogous ones obtained through the empirical model. The results show a very good coincidence between the model values and the measured ones in the conditions of the geomagnetic storm on 3-4November 2021 [Mukhtarov et al., 2021]. The obtained results confirm that the proposed dependency sufficiently accurately manages to solve the tasks set by the Ministry of Defense and the practical needs of environmental technologies [Ivanova et al., 2018].

The purpose of the present study is to reconstruct the state of the ionosphere over Sofia through a significant number of ionospheric stations. By interpolation between the values of foF2 in the ten points where the ionosondes are located, the value corresponding to the coordinates of the point of the city of Sofia is found.The data thus obtained should be compared with the data obtained by the created empirical model for short-term forecasting of the ionosphereat the National Institute of Geophysics, Geodesy and Geography - Bulgarian Academy of Sciences. A future task is a comparison of more extensive statistical material to improve the quality of the developed methodology for the purposes of radio paths forecasting, which is also the main practical application related to Space Weather prediction and the tasks serving the interested institutions.

Data and Methods

In order to study in detail the behavior of the geomagnetic disturbance, the indices disturbance storm time (Dst) and planetary Kp index were used, which were obtained from Goddard Space Flight Center (https://omniweb.gsfc.nasa.gov/). It is well known that the Kp index is used to illustrated the magnitude of geomagnetic storms. Kp is an excellent indicator of disturbances in the Earth's magnetic field. Dst index gives information about the strength of the ring current around Earth caused by solar energetic particles [Masters, 2012].

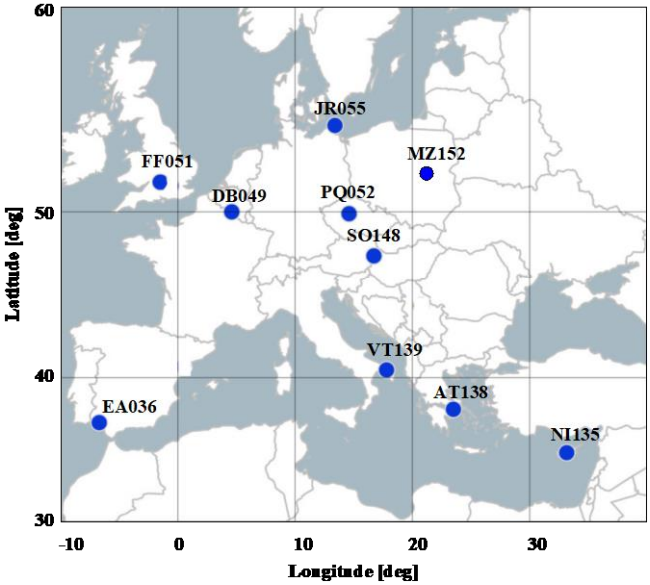

Figure 1. *Map of used European ionospheric stations*

Data on the F2-layer critical frequency obtained from ten ionospheric stations are available at the website of Global Ionosphere Radio Observatory (GIRO)

https://giro.uml.edu/didbase/scaled.php. The data used for comparison of foF2 for the territory of Bulgaria are calculated by an empirical model from TEC data [Bojilova and Mukhtarov, 2020a; Bojilova and Mukhtarov, 2021]. The model allows predicting the values of foF2 and MUF3000 based on real (measured on every hour) TEC data from the global database the Center for Orbit Determination of Europe (CODE) - http://ftp.aiub.unibe.ch/CODE/.

Figure 1 show all used GIRO data base stations. The selected European stations are between 35° and 55° latitude and between 6°E and 33°W longitude. After the stations are selected, the foF2 data is interpolated for each point. The ionospheric response over Sofia is investigated by taking data for the point with the coordinates of the city of Sofia from all the interpolated values. The obtained values are compared with the model values.

Results

The influence of geomagnetic activity on the ionosphere has been the subject of long-term and detailed research by scientists working in this field [Bojilova and Mukhtarov, 2020c; Bojilova and Mukhtarov, 2020d; Mukhtarov and Bojilova, 2017]. In order to analyze the behavior of the geomagnetic disturbance in the present study the Kp and Dst indices shown in Figure 2. On the two graphs, the values of the two indices corresponding to disturbed conditions are marked in red. In the example of Dst, values below -30nT are moments of disturbance, while Kp values above 5 are considered as disturbed geomagnetic conditions.

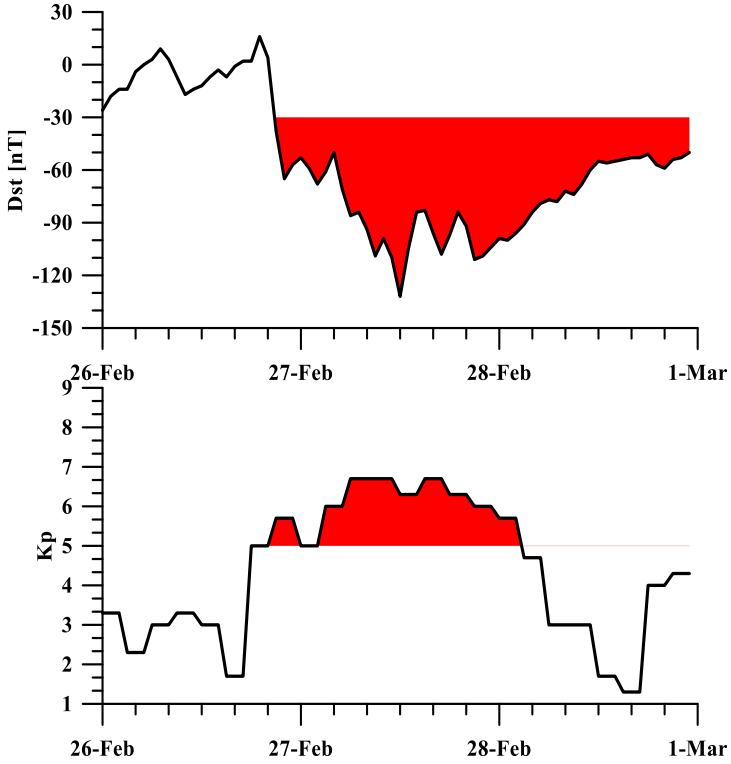

Figure 2. *Parameters describing geomagnetic storm- top panel Dst-index and bottom panel Kp-index*

From the graphs it is clear that the onset of the geomagnetic disturbance can be considered to be around 19:30UT on 26 February. The event under consideration has a sudden onset, which is clearly seen in the sharp rise of Kp to values around 5. The main phase of the storm occurs around noon (12UT) on 27 February when the Dst index reaches values -135nT. According to the accepted classifications for the magnitude of this index, the discussed geomagnetic storm is of the severe class (Dst ≤ -200 nT) [Loewe and Prölss, 1997]. The other considered index Kp

has a maximum value of 6.66 at the same time. According to this index, the geomagnetic disturbance is of class G2 (Moderate).

The recovery phase begins in the night hours (after midnight) on 28 February when the Kp index recovers values in quiet conditions. Unlike this index, Dst index does not go into a quiet conditions even until the beginning of March.

After the behavior of the geomagnetic activity has been examined in detail, the next task is to analyze the behavior of the ionosphere in the conditions of the geomagnetic disturbance on 27 February 2023. For this purpose, the values of foF2 for the interval from 26 to 28 February were used. Based on the values obtained from the ten European ionospheric stations, the data is interpolated by determining the values of the point with coordinates coinciding with those of the city of Sofia. This type of data is shown in Figure 3 with black color. The other type of data is obtained by the empirical model for the same point - marked in red color. The figure shows a good match of the two types of data.

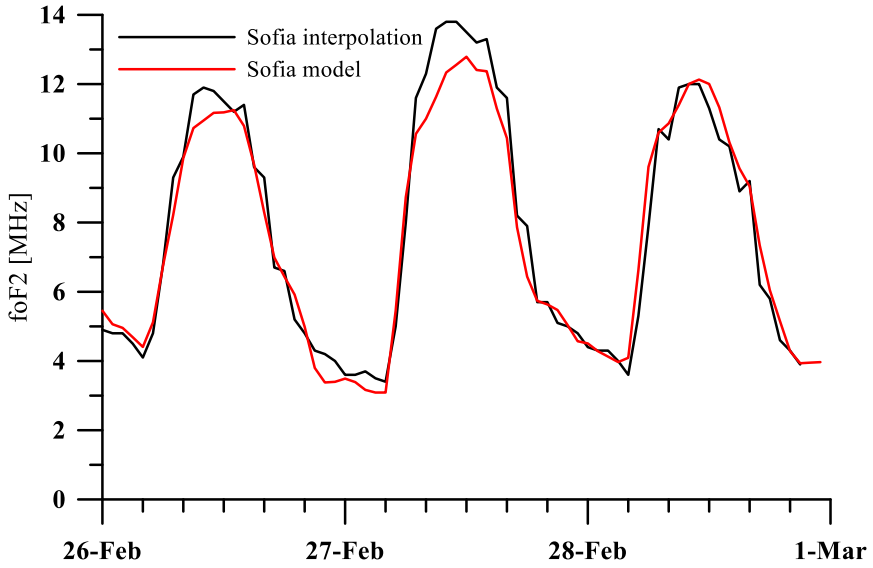

Figure 3.*Comparison between the data obtained from the interpolation of the stations and the data from the empirical model for Sofia*

The presented behavior of the critical frequency of the F2 layer in Figure 3 shows the reaction of the ionosphere for a mid-latitude region where Sofia is located according to coordinates. It can be seen from the graph that both types of data show an initial slightly negative reaction of the ionosphere at the onset of the storm in the hours after 20UT on 26 February 2023. The delay in response is due to the well-known fact of the inertness of the ionosphere. On 27 February around midday (which is also the main phase according to the geomagnetic activity indices, see Figure 2) an increase in foF2 of about 2MHz above the quiet condition values on 26 February is observed. The most probable explanation of the physical mechanism of the observed positive response of the ionosphere in the conditions of the geomagnetic storm under consideration is related to the changes of the ratio of atomic oxygen (O) to molecular nitrogen (N_2). It is well known that thermospheric composition (O/N_2) in winter is greater at high latitudes and decreases with distance from it, which is the reason for ionospheric winter anomaly and semiannual variation [Torr and Torr, 1973; Rishbeth, 1998;Millward, 1996]. Joule heating over the auroral region leads to longitudinal variations of thermospheric downwelling locations, which also causes changes in O/N_2 [Luan et al., 2017]. Effects such as Sudden Stratospheric Warming (SSW) have an additional influence in the period under consideration. SSW is a significant disruption of the stratospheric polar vortex

that begins with large-scale atmosphere Rossby waves getting pushed higher into the atmosphere. SSW effects extend into the upper atmosphere (i.e. the ionosphere), producing changes in the thermospheric circulation and ionospheric disturbances [Yiğit et al., 2016].

Conclusions

The present study presents a comparison of two types of data characterizing the ionospheric response during the 27 February 2023 geomagnetic storm. In order to trace the manifestation of the particular disturbance- the changes in the geomagnetic activity represented by Dst and Kp were studied. In the analysis of the response of the ionosphere over Sofia, two types of data were used: a) from the interpolation of ten ionosondes, using the values for the point matching with the coordinates of Sofia and b) ionospheric data for Sofia obtained from the empirical model created in the National Institute of Geophysics, Geodesy and Geography. The comparison results show a good coincidence between the two types of data. All this shows the good work of the created model. In addition, the physical impact mechanisms related to the observed ionospheric reaction are presented, namely: a) changes in the O/N_2 ratio, and b) the influence of SSW. A future task is a comparison of more extensive statistical material to improve the quality of the developed methodology for the purposes of radio paths forecasting, which is also the main practical application related to Space Weather prediction and the tasks serving the interested institutions.

Acknowledgment

This study was supported by the National Science Fund of Bulgaria (NSFB) (project number КП-06-Русия/15). This work was partially supported by the Bulgarian Ministry of Education and Science under the National Research Programme “Young scientists and postdoctoral students -2” approved by DCM 206/ 07.04.2022. This investigation was supported by the National Science Fund of Bulgaria (NSFB) project №КП-06-Н44/2 from 27.11.2020.

References

Blagoveshchenskii, D.V. (2013). Effect of magnetic storms (substorms) on HF propagation: A review, Geomagnetism and Aeronomy, Vol. 53, pp. 409-423, https://doi.org/10.1134/S0016792063761478.

Bojilova, R., Mukhtarov, P. (2020a). SHORT-TERM PREDICTION OF THE IONOSPHERIC CRITICAL FREQUENCIES OVER BULGARIA, Bulgarian Geophysical Journal, Vol. 43, pp. 81-88, DOI:10.34975/bgj-2020.43.7.

Bojilova, R., Mukhtarov, P. (2020b). Forecasting the propagation of HF radio waves over Bulgaria, Environmental Protection and Disaster Risks. EnviroRISK 2020. Studies in Systems, Decision and Control, Vol. 361, Springer, Cham, pp. 309–324, https://doi.org/10.1007/978-3-030-70190-1_21.

Bojilova, R., Mukhtarov, P. (2020c). Relationship between short-term variations of solar activity and critical frequencies of the ionosphere represented by FoF2 and MUF3000, Comptes rendus de l'Académie bulgare des Sciences, Vol. 73, No. 10, pp. 1416 – 1424, DOI: 10.7546/CRABS.2020.10.11.

Bojilova, R., Mukhtarov, P. (2020d). Relationship between the Critical Frequencies of the Ionosphere over Bulgaria and Geomagnetic Activity, Comptes rendus de l'Académie bulgare des Sciences, Vol. 73, No. 8, pp. 1113-1122, DOI: 10.7546/CRABS.2020.08.10.

Bojilova, R., Mukhtarov, P. (2021). RECONSTRUCTION OF IONOSPHERIC CRITICAL FREQUENCIES BASED ON THE TOTAL ELECTRON CONTENT OVER BULGARIA, Comptes rendus de l'Académie bulgare des Sciences, Vol. 74, No. 1, pp. 110-119, DOI:10.7546/CRABS.2021.01.14.

Chukwuma, V. (2007). On positive and negative ionospheric storms, Acta Geodaetica et Geophysica Hungarica, Vol. 42, No. 1, pp.1-21, https://doi.org/10.1556/ageod.42.2007.1.1.

Hill, Geoffrey E. (1963). HF communication during ionospheric storms, Journal of Research of the National Bureau of Standards, Vol. 67D, No. 1,pp. 23-30, http://dx.doi.org/10.6028/jres.067D.005.

Horvath, I., Lovell, B. C. (2015). Positive and negative ionospheric storms occurring during the 15 May 2005 geomagnetic superstorm, Journal of Geophysical Research: Space Physics, Vol. 120, No.9, pp. 7822-7837, https://doi.org/10.1002/2015JA021206.

Ivanova, Y., Partalin, T., Lakov, L., Jivov, B. (2018). Airborne sound insulation of new composite wall structures, MATEC Web of Conferences, Vol. 145, pp. 05013, https://doi.org/10.1051/matecconf/201814505013.

Klimenko, M. V., Klimenko, V. V., Bessarab, F. S., Ratovsky, K. G., Zakharenkova, I. E., Nosikov, I. A., Stepanov, A. E., Kotova, D. S., Vorobjev V. G., Yagodkina, O. I. (2015). Influence of geomagnetic storms of September 26–30, 2011, on the ionosphere and HF radiowave propagation. I. Ionospheric effects, Geomagnetism and Aeronomy, Vol. 55, No. 6, pp. 744-762, DOI: 10.1134/S0016792063761472.

Loewe, C. A., Prölss, G. W. (1997). Classification and mean behavior of magnetic storms, Journal of Geophysical Research: Space Physics, Vol. 102, No. A7, pp.14209-14213, https://doi.org/10.1029/96JA04020.

Luan, X., Wang, W., Burns, A., Dou, X. (2017). Solar cycle variations of thermospheric O/N2 longitudinal pattern from TIMED/GUVI, Journal of Geophysical Research: Space Physics, Vol. 122, No. 2, pp. 2605-2618, https://doi.org/10.1002/2016JA023696.

Masters, J. (2012). A future Space Weather catastrophe: a disturbing possibility, Weather Underground. Retrieved, 12.

Millward, G. H., Rishbeth, H., Fuller-Rowell, T. J., Aylward, A. D., Quegan, S., Moffett, R. J. (1996). Ionospheric F2 layer seasonal and semiannual variations, Journal of Geophysical Research: Space Physics, Vol. 101, No. A3, pp. 5149-5156, https://doi.org/10.1029/95JA03343.

Mukhtarov, P., Bojilova, R. (2017). Influence of solar and geomagnetic activity on the ionosphere over Bulgaria, Comptes rendus de l'Académie bulgare des Sciences, Vol. 70, No. 9, pp. 1289-1297.

Mukhtarov, P., Bojilova, R., Andonov, B. (2021). THE SECOND G3 (STRONG) GEOMAGNETIC STORM IN 25TH SOLAR CYCLE ON 3-4 NOVEMBER 2021, Bulgarian Geophysical Journal, Vol. 44, pp. 43-52, DOI: 10.34975/bgj-2021.44.4.

Rama Rao, P.V.S., Gopi Krishna, S., Vara Prasad, J., Prasad, S.N.V.S., Prasad, D.S.V.V.D. and Niranjan, K. (2009). Geomagnetic storm effects on GPS based navigation, Annales Geophysicae, Vol. 27, No. 5, pp. 2101-2110, https://doi.org/10.5194/angeo-27-2101-2009.

Rishbeth, H. (1998). How the thermospheric circulation affects the ionospheric F2-layer, Journal of Atmospheric and Solar-Terrestrial Physics, Vol. 60, No.14, pp. 1385-1402, https://doi.org/10.1016/S1364-6826(98)00062-5.

Torr, M. R., Torr, D. G.(1973). The seasonal behaviour of the F2-layer of the ionosphere, Journal of Atmospheric and Terrestrial Physics, Vol. 35, No. 12, pp. 2237-2251, https://doi.org/10.1016/0021-9169(73)90140-2.

Yiğit, E., Knížová, P. K., Georgieva, K., Ward, W. (2016). A review of vertical coupling in the Atmosphere–Ionosphere system: Effects of waves, sudden stratospheric warmings, space weather, and of solar activity, Journal of Atmospheric and Solar-Terrestrial Physics, Vol. 141, pp. 1-12, https://doi.org/10.1016/j.jastp.2016.02.011.

Space Weather Conditions and Non-Storm Supersubstorms Observations

Despirak I.V.[1], *Lubchich A.A.*[1], *Kleimenova N.G.*[2]

[1]Polar Geophysical Institute, Apatity, Russia, e-mail: despirak@gmail.com
[2]Schmidt Institute of Physics of the Earth, RAS, Moscow, Russia

Abstract

It is known that very intense substorms, so-called “supersubstorms” (SSSs: SML < −2500 nT) usually occur in the main phase of the magnetic storms. At the same time, it was found that such intense events are observed not only during very strong storms (superstorm with Dst<-250 nT), but also during intense or moderate magnetic storms (-100 nT >Dst>-250 nT; -50 nT >Dst>-100 nT). The aim of this work is to study the supersubstorms observed during non-storm conditions by the OMNI data base and global magnetometer networks SuperMAG, INTERMAGNET and IMAGE. For this purpose, we selected the SSS events observed by SYM/H>-50 nT. We found 18 such SSS events in the period 1998-2017. Among them, several typical events can be distinguished: (1) – the events near the magnetic storm commencements SC, (2) - the events observed in the distant recovery phase of the storm, (3) – the events observed outside of a magnetic storm. Besides, we discussed some special conditions in the solar wind and interplanetary magnetic field (IMF) under which such events have been observed.

Keywords: solar wind, magnetic cloud, high-speed streams, supersubstorm, magnetic storm

Introduction

For the first time the term “supersubstorms” was introduced by investigations of intense magnetic substorms based on the data of the SuperMag magnetometers network, the events with high negative values of SML index (< - 2500 nT) were called “supersubstorms” [Tsurutani et al. 2015]. Until now, there are several works where the statistical studies of the conditions for the occurrence of supersubstorms have been carried out, their dependence on solar activity, on conditions in the IMF and solar wind, and on the presence of magnetic storms [Haira et al., 2016; Despirak et al., 2019], the energy of supersubstorms [Tsurutani, Haira, 2023] and a detailed study of some individual events. Detailed studies of SSS development have been performed only for a few events: September 7-8, 2017; March 9, 2012; April 5, 2010 and May 28, 2011. On the Figure 1 shown the SML-index development during these four events as examples of supersubstorm determination.

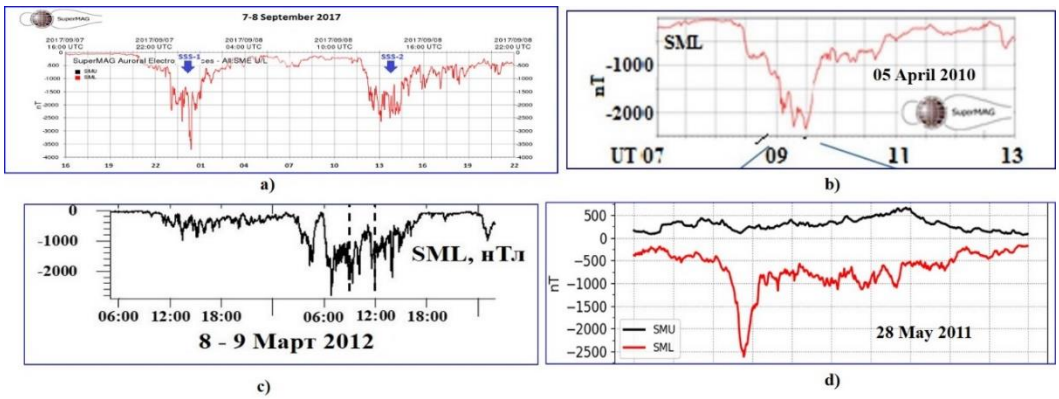

Figure 1. *Variations of the SML-index during SSS: a) on 7-8 September 2017; b)- on 05 April 2010; c) – 8-9 March 2012; d) – 28 May 2011*

Note that an analysis of these SSS events showed that the supersubstorm was characterized by some special features: an extremely intense magnetic reconnection, an unusually large dipolization, intense fast plasma streams directed towards the Earth, an unusual spatial pattern of the development of auroras and auroral electrojets: eastward and westward electrojets developed globally and surround the polar cap from different sides to reach the day side [Haira et al., 2018; Nishimura et al., 2020; Zong et al., 2021; Despirak et al., 2020, 2021, 2022a, 2022b]. It was shown also that SSS usually are connected with the development of large magnetic storms, but they can sometimes also be observed during moderate magnetic storms and under nonstorm conditions. The result presented on the Figure 2.

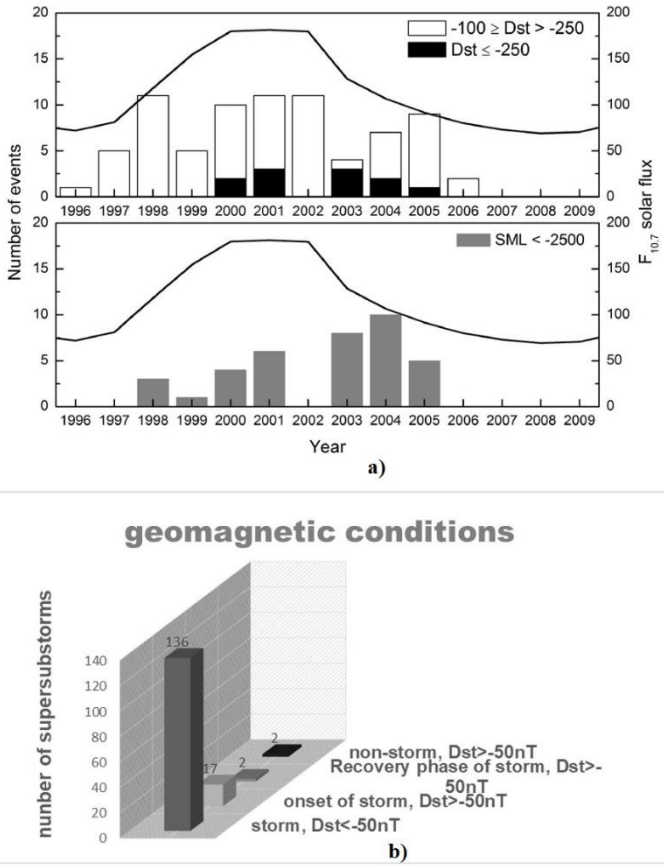

***Figure 2**. Distributions of SSS on the intensity of magnetic storms, the pictures were taken from work of Tsurutani et al., 2015 (a) and from work Despirak et al., 2019 (b)*

The purpose of our work is study of supersubstorm events observed during non-storm conditions. We selected all supersubstorm events for 2010-2020 period observed during non-storm conditions, i.e. by SYM/H- index > -50 nT. Three examples of typical supersubstorm development under nonstorm conditions are presented below.

Data

The solar wind and interplanetary magnetic field (IMF) parameters are taken from OMNI database https://cdaweb.gsfc.nasa.gov/ and the catalog of large-scale solar wind types ftp://ftp.iki.rssi.ru/pub/omni/catalog. Global magnetometer networks SuperMAG and IMAGE data were used for determination of the substorm development as at the midlatitudes well as at auroral latitudes. The IMAGE magnetometer data are taken from http://space.fmi.fi/image/. The global spatial distribution of electrojets was determined from the maps of magnetic field

vectors obtained on the SuperMAG network. SML- index is taken from http://supermag.jhuapl.edu/.

Results

1) SSS event registered out of the magnetic storm

We selected the event on April 22, 2017 as the example of SSS observation during non-storm condition. Solar wind and IMF conditions for period on April 21-26, 2017 shown in the Figure 3. It is seen that the features of recurrent high-speed stream from coronal holes are observed in this time period.

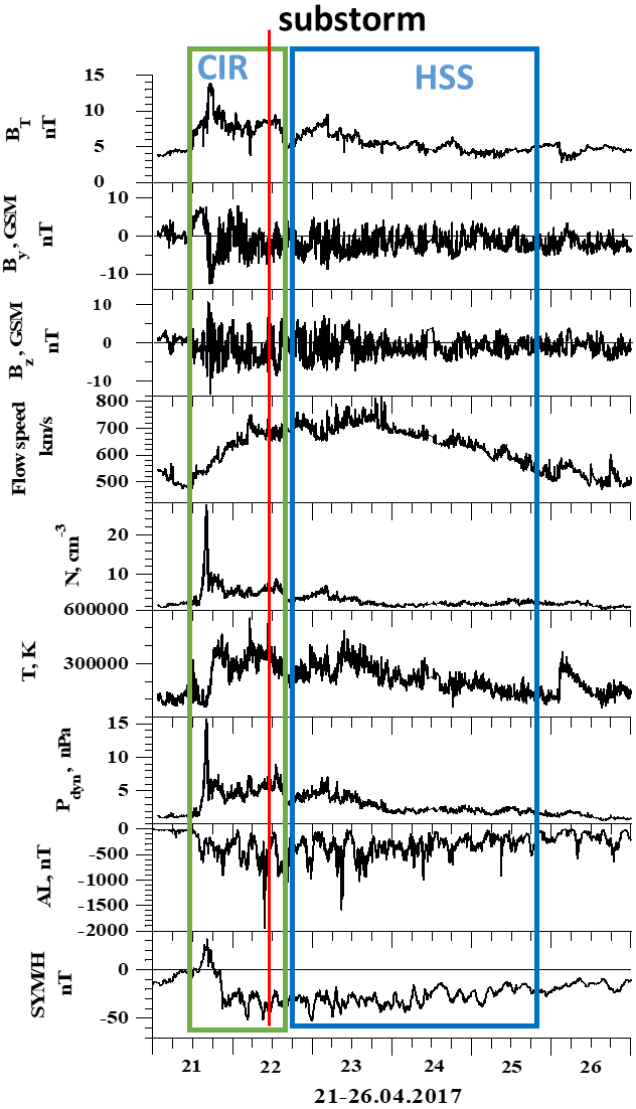

***Figure 3**. Solar wind and IMF parameters on April 21-26, 2017, from top to bottom: IMF magnitude (B_T), the IMF Y- and Z- components (B_Y, B_Z), the flow velocity (V), the dynamic pressure (P). and geomagnetic indexes SYM/H and AL.*

At the front of the HSS the region of compresed plasma – the CIR- was registered. CIR and HSS boundaries are marked by the green and blue rectangles, respectively. The CIR contains the intervals of negative values of the IMF Bz, but magnetic storm not developed (SYM/H~-40 nT). Against the background of CIR, at ~09:30 UT one intense substorm (SML ~-2100 nT)

began to develop. The moment of the substorm onset is shown by the vertical red line. Ground-based magnetic disturbances and Field Aligned Currents (FAC) distribution during this SSS are described in detail in our work Despirak et al., 2022c.

2) SSS registered during SC or at the onset of the magnetic storm

As the example of SSS observation during SC or onset of the magnetic storm was selected the event on April 11, 2001 Solar wind and IMF conditions for period on April 21-26, 2017 are shown in the Figure 4. Two consecutive structures in the solar wind were observed: SHEATH with EJECTA. As result, there was the magnetic storm on 11 April 2001 with SYM/H ~300 nT. Note, there were two events of SSS (SSS-1 and SSS-2, which were marked in the picture by the vertical dotted blue lines,) at this day observed during Sheath region of the solar wind. But we considered in our work only first SSS event (SSS-1) registered at the onset of storm (SYM/H ~-10 nT).

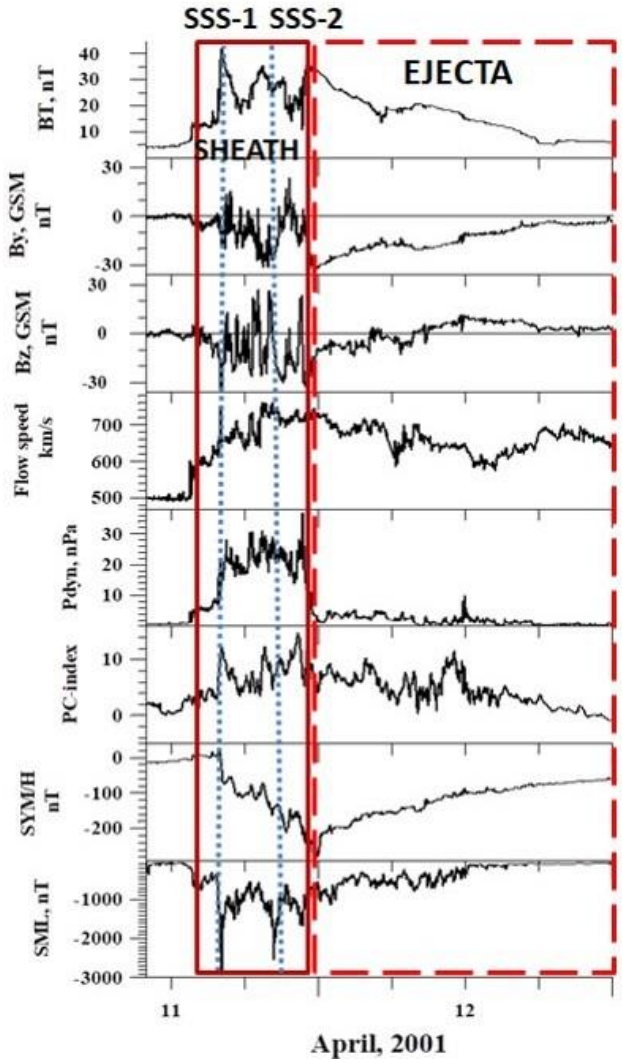

Figure 4. *Solar wind and IMF parameters on April 11-12, 2001, from top to bottom: IMF magnitude (B_T), the IMF Y- and Z- components (B_Y, B_Z), the flow velocity (V), the dynamic pressure (P). and geomagnetic indexes PC, SYM/H and SML.*

It is seen that before SSS-1 occurrence the solar wind dynamic pressure was ~ 20 nPa, the solar wind velocity shows very high values (~ 600-650 km/s), the magnitude of the IMF for SSSs was ~ 25-35 nT.

3) SSS in the distant recovery phase of the magnetic storm

As the example of SSS observation during the distant recovery phase of the magnetic storm was selected the event on September 12, 2011 Solar wind and IMF conditions for period at 16 UT on 10 September to 10 UT on 14 September are shown in the Figure 5. It is seen that the features of recurrent high-speed stream from coronal holes are observed in this time period.

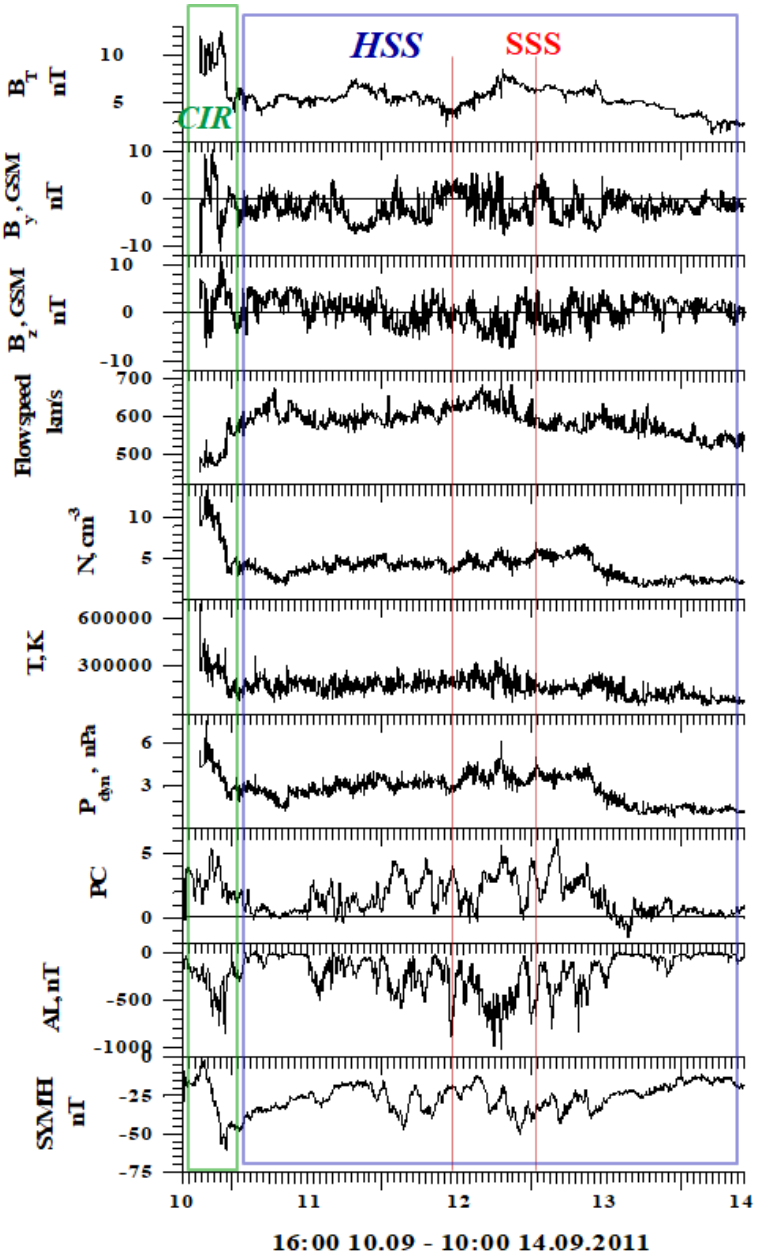

***Figure5**. Solar wind and IMF parameters on September 10-14, 2011, from top to bottom: IMF magnitude (B_T), the IMF Y- and Z- components (B_Y, B_Z), the flow velocity (V), the dynamic pressure (P). and geomagnetic indexes PC, AL and SYM/H.*

CIR and HSS boundaries are marked by the green and blue rectangles, respectively. It can be seen that the CIR region included a negative Bz component, which may have been the source

of a moderate magnetic storm with SYM/H~-60 nT. The storm lasted almost 3 days, from 11 to ~ 14 September 2011. Two supersubstorms were observed in the distant recovery phase of this magnetic storm. The moment of the SSS onset shown by the vertical red line.

It is seen that before SSSs, the Bz-component was small negative, but the solar wind velocity shows high values (~ 600 km/s), SSSs observed during the high-speed stream (HSS).

Summary

It is shown that non-storm SSS events (by SYM/H>-50 nT) were mainly registered:

1) during small CIR- storms development
2) during the late recovery phase of CIR-storms.
3) at the beginning of a magnetic storm caused by MC/ SHEATH;
4) moreover, the solar wind velocity for these events shows very high values (~ 600- 700 km/s)

Acknowledgments

This study was supported by the RFBR (project number 20-55-18003) and National Science Fund of Bulgaria (NSFB) (project number КП-06-Русия/15).

References

Despirak, I.V., Kleimenova, N.G. Gromova, L.I., Gromov, S.V., Malysheva, L.M. (2020). Supersubstorms during storms of September 7–8, 2017, Geomag. Aeron., Vol. 60, No. 3, pp. 292–300, https://doi.org/10.1134/S0016793220030044

Despirak, I.V., Kleimenova, N.G., Gromova, L.I., Lubchich, A.A., Guineva, V., Setsko, P.V., (2022a). Spatial features of a supersubstorm in the main phase of the magnetic storm of April 5, 2010. Bull. Russ. Acad. Sci.: Phys., Vol. 86, No. 3, pp. 249–255, https://doi.org/10.3103/S106287382203008X

Despirak, I.V., Kleimenova, N.G., Lyubchich, A.A., Setsko, P.V., Gromova, L.I., Werner, R. (2022b). Global development of the supersubstorm of May 28, 2011, Geomagn. Aeron., Vol. 62, No. 3, pp. 199-208. https://doi.org/10.1134/S0016793222030069

*Despirak Irina, Kleimenova Natalia, Gromova Lyudmila, Lubchich Andris. (*2022c*).* Spatial Features of Electojets Development during Non-Storm Supersubstorms: Case Study, Proceedings of Eighteenth international scientific conference “Space, Ecology, Safety”, ISSN 2603-3321, 19-21 October 2022, Sofia, Bulgaria, pp. 28-32.

Despirak, I.V., Lubchich, A.A., Kleimenova, N.G., Gromova, L.I., Gromov, S.V., Malysheva, L.M., (2021). Longitude geomagnetic effects of the supersubstorms during the magnetic storm of March 9, 2012. Bull. Russ. Acad. Sci.: Phys., Vol. 85, No. 3, pp. 246–251, https://doi.org/10.3103/S1062873821030096

Despirak, I.V., Lyubchich, A.A., Kleimenova, N.G., (2019). Supersubstorms and conditions in the solar wind, Geomag. Aeron., Vol. 59, No. 2, pp. 170-176, https://doi.org/10.1134/S0016793219020075

Hajra, R., Tsurutani, B.T. (2018). Interplanetary Shocks Inducing Magnetospheric Supersubstorms (SML < –2500 nT): Unusual Auroral Morphologies and Energy Flow, Astrophys. J., Vol. 858, No. 2, https://doi.org/10.3847/1538-4357/aabaed

Hajra, R., Tsurutani, B.T., Echer, E., Gonzalez, W.D., Gjerloev J.W. (2016). Supersubstorms (SML <-2500 nT): Magnetic storm and solar cycle dependences, J. Geophys. Res.: Space Physics, Vol. 121, pp. 7805–7816, DOI: 10.1002/ 2015JA021835.

Nishimura, Y., Lyons, L.R., Gabrielse, C., Sivadas, N., Donovan, E.F., Varney, R.H., Angelopoulos, V., Weygand, J.M., Conde, M.G., Zhang, S.R., (2020). Extreme Magnetosphere-Ionosphere-Thermosphere Responses to the 5 April 2010 Supersubstorm, J. Geophys. Res.: Space Phys., Vol. 125, No. 4, e2019JA027654, https://doi.org/10.1029/2019JA027654

Tsurutani, B.T., Hajra, R. (2023). Energetics of Shock-triggered Supersubstorms (SML<-2500 nT), Astrophysical Journal, Vol. 946, No. 1, https://doi.org/10.3847/1538-4357/acb143

Tsurutani, B.T., Hajra, R., Echer, E., Gjerloev, J.W. (2015). Extremely intense (SML≤ −2500 nT) substorms: isolated events that are externally triggered?, Ann. Geophys., Vol. 33, pp. 519–524, https://doi.org/10.5194/angeo-33-519-2015

Zong, Q.-G., Yue, C., Fu, S.-Y. (2021). Shock induced strong substorms and super substorms: Preconditions and associated oxygen ion dynamics, Space Science Review, Vol. 217, https://doi.org/10.1007/s11214-021-00806-x

Geomagnetically Induced Currents During Different Types of the Solar Wind

Despirak I.V.[1], Setsko P.V.[1], Sakharov Ya.A.[1], Bilin V.A.[1], Lubchich A.A.[1], Selivanov V.N.[2]

[1]Polar Geophysical Institute, Apatity, Russia; e-mail: setsko@pgia.ru

[2]Northern Energetics Research Centre KSC RAS, Apatity, Russia

Abstract

Relationship between geomagnetic activity and increasing of geomagnetically induced currents (GICs) during September 2017 have been studied. The September of 2017 was an extremely active space weather period. In this work were considered four time interval connected with various types of the solar wind (Magnetic Clouds, CIRs, Sheaths, High Speed Streams). The arrival of different types of solar wind to the Earth caused magnetic storms of different intensity (SYM/H~ -65- -150 nT). At the background these magnetic storms were registered several substorms from moderate to very intense (supersubstorms). The purpose of our work was to analyze which magnetic disturbances led to the enhancement of GICs. We analyzed the grow of westward electrojet using the latitudinal profiles of the IMAGE network and the equivalent currents of the MIRACLE system data. The increasing of GICs were controlled by EURISGIC data from Russian stations Vykhodnoy (VKH), Revda (RVD) and Kondopoga (KND) in the North-West of Russia (eurisgic.ru) and station Mäntsälä (MAN) in the South of Finland. The data from these stations are convenient for tracking the GIC increase from subauroral to high latitudes (~60° to ~69° geographical latitudes). Taking into account the fact that substorms are the main source of magnetic disturbances in the auroral zone, such an arrangement of GIC stations makes it possible to compare them with the motion of an electrojet to the pole during the expansion phase of a substorm. It was not possible to reveal the explicit dependence of the appearance of intense GIC on different solar wind streams. It is shown that, the main reasons for the growth of GICs during September 2017 were magnetic disturbances connected with an increasing and a moving of the westward electrojet during substorm expansion phase and sometimes with Pc5 pulsations observed at the recovery phase of substorms.

Keywords: different streams of the solar wind, substorms, magnetic pulsations, geomagnetically induced currents (GICs)

1. Introduction

It is known that sharp changes in magnetic field can produce Geomagnetically Induced Currents (GICs) in terrestrial technological networks [e.g. Pulkkinen et al., 2005; Viljanen et al., 2006]. Rapid changes in the geomagnetic field are usually associated with the arrival of solar wind shock waves, coronal mass ejections (CMEs) and high-speed streams from coronal holes to the Earth, which lead to the development of magnetic storms and substorms, as well as the appearance of magnetic pulsations [e.g. Lakhina et al., 2020]. Recently it has been confirmed that strong disturbances of the westward electrojet during expansion phase of substorm is one of the reason for the GICs growth in the auroral zone [Vorobjev et al., 2018; Kozyreva et al., 2020; Tsurutani and Hajra, 2021; Despirak et al., 2022].

The aim of this work is the study of intense GICs occurrence observed during magnetic disturbances at the background of different types of the solar wind. For this, an extremely active space-weather period, September 2017, was chosen. A large number of space-weather events took place during a period of only one month and resulted in several geomagnetic effects such as magnetic storms (of varying intensity), substorms and HILDCAAs [Haira et al., 2020].

2. Data

In the North-West of Russia, Polar Geophysical Institute together with Northern Energetic Research Centre built a system, called EURISGIC, to monitor such currents in the autotransformers neutral line in the existing Karelian-Kola power transmission line [Sakharov et al., 2007; 2016; 2019]. This power line is located at geographical (geomagnetic) latitudes from ~60° to ~69° (56.6º to 65.5º) directed from south to north. Note that this location corresponds to auroral latitudes where substorm disturbances are usually observed. Figure 1 shows the map of EURISGIC recording stations, as well as part of the PPN-NAL meridional chain of IMAGE magnetometers.

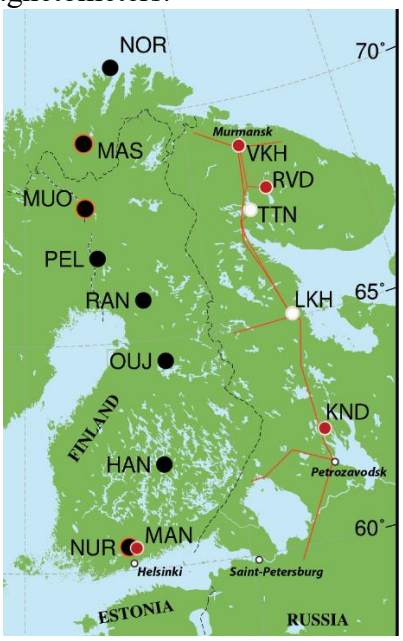

***Figure 1**. The geographic map of EURISGIC and nearby IMAGE observatories. Black dots – IMAGE magnetometer stations, red dots with a white border – used in work GIC registration stations, black dots with an orange border – the magnetometer stations closest to GIC registration stations, white dots – GIC registration stations with no data at selected time.*

The spatial distribution of the substorm electrojets was determined using the magnetometers of the IMAGE (http://space.fmi.fi/image/) and SuperMAG (http://supermag.jhuapl.edu/) networks. To study the spatial distribution of magnetic disturbances on the IMAGE profile, instant maps of the distribution of ionospheric equivalent electric currents MIRACLE (https://space.fmi.fi/MIRACLE/) have been analyzed. The IL- and SML- indexes are also taken from IMAGE and SuperMAG networks, correspondingly. Note, that the IL index shows the variation of the magnetic field at the selected IMAGE stations, that is, it is similar to the AL index, which is associated with the auroral electrojet. We used also the Wp (wave and planetary) index which related to the power of the Pi2 pulsation wave at low latitudes and associated with onset of substorm. The solar wind and IMF parameters are taken from OMNI database

https://cdaweb.gsfc.nasa.gov/ and the catalog of large-scale solar wind types ftp://ftp.iki.rssi.ru/pub/omni/catalog.

3. September 2017 - solar wind and IMF conditions

September 2017 was divided in four time intervals connected with various types of the solar wind. 7-8 September connected with magnetic storms caused by Sheath and magnetic cloud (MC). 12-13 September connected with magnetic storms caused by Sheath. 14-17 September connected with non-storm interval during High Speed Stream (HSS), when HILDCAA events were registered. And 27-28 September connected with magnetic storm caused by CIR, the region of compressed plasma before HSS. Solar wind and interplanetary magnetic field (IMF) parameters for four periods of September 2017 are shown in Figure 2.

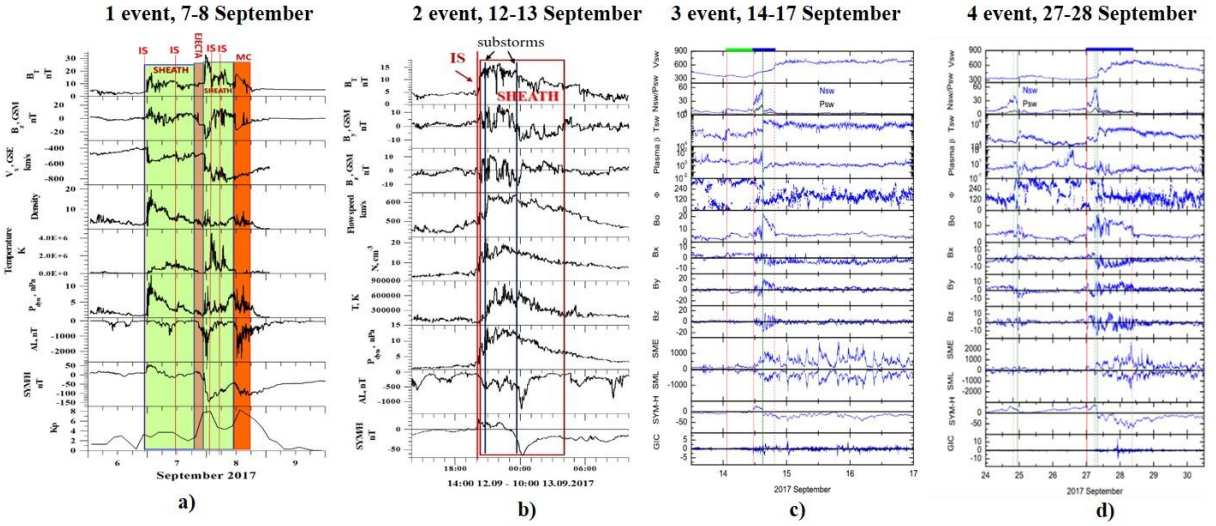

***Figure 2**. Solar wind and interplanetary magnetic field (IMF) parameters for 4 periods of September 2017: a) and b) -the magnitude (B_T) of the IMF; the Y- and Z-component of the IMF; the flow speed (V), the density (N), temperature (T), and dynamic pressure (P) of solar wind, and the geomagnetic indices AL and SYM/H; c) and d)- pictures taken from paper Haira et al., 2020.*

4. Magnetic disturbances and GIC observations

- **7-8 September 2017**

The increasing of GICs were considered during two periods corresponding to the development of supersubstorms: from 23 UT on September 7 to 04 UT on September 8 and from 12 UT to 20 UT on September 8 [see more Despirak et al., 2023]. These two periods are marked with ovals and arrows in the Figure 3. At the left panel shown the common picture of the geomagnetic variations and GIC: SML index; X- component of the magnetic field at IMAGE network; IL and Wp indices and GICs. At the right panel the first period presented in more detail*:* MIRACLE equivalent currents; the map of magnetic field vectors by the SuperMAG for 23:30 UT; IL and Wp geomagnetic indices and GICs at stations Mäntsälä, Kondopoga, Vykhodnoy and at stations TOR, HWB (GIC pictures for TOR and HWB are taken from [Clilverd et al., 2021]).

It was found that the increasing of the GICs was related to the poleward motion of the substorm westward electrojet and followed the development of its spatiotemporal structure (the occurrence and poleward propagation of each intensification of substorm). The highest GICs were observed when the recording station was in the night sector. The sudden commencement (SC) of the substorm was reflected in the GIC data regardless of the location of the recording station.

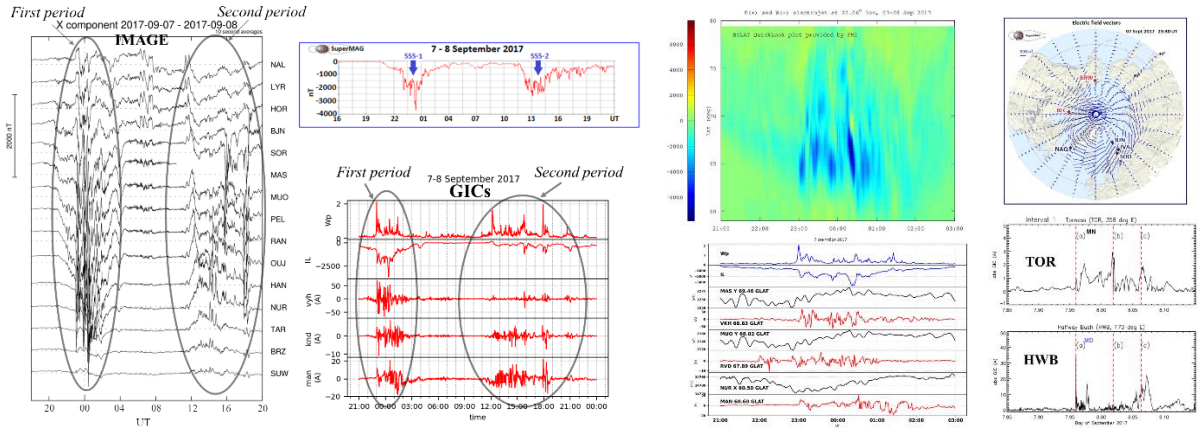

Figure 3 *The common (left) and detail (right) pictures of geomagnetic disturbances and GIC at 7-8 September 2017*

- **12-13 September 2017**

Geomagnetic activity and increasing of GICs during a moderate magnetic storm (SYM/H ~ −65 nT) on September, 12-13 2017 is shown on Figure 4. Note, that two intense substorms (AL ~600 nT and ~ 1200 nT) were observed within this period. Three periods of different magnetic disturbances and large values of GIC from 20 to 23 UT, from 23 to 01 UT and from 01 to 02:30 UT are marked by bars on the plots pf IMAGE magnetometers (PPN-NAL chain) and GICs data. The first two blue bars show the periods of two substorms. The orange bar shows the period of Pc5 pulsations, observed at the recovery phase of second substorm. SuperMAG polar maps correspond to maximum of magnetic disturbances for these three events in time. The map of latitudinal profile of the westward and eastward electrojet calculated by MIRACLE, and GICs (red lines) with corresponding magnetic component of nearest IMAGE station (black lines) and geomagnetic indexes Wp and IL (blue lines) are shown at the right side.

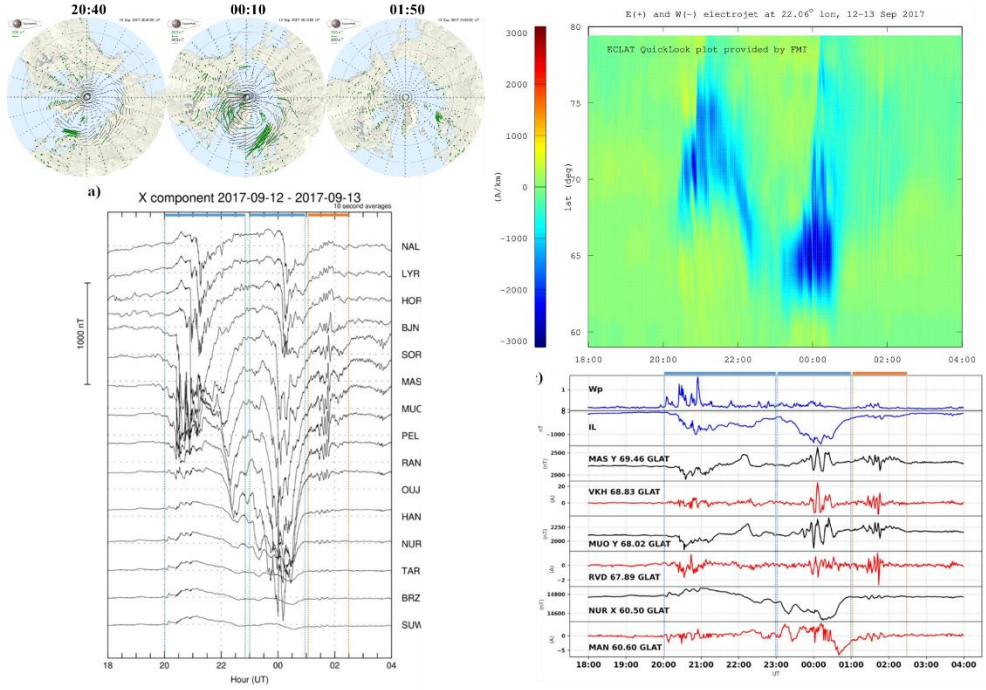

Figure 4 *The detail pictures of geomagnetic disturbances and GIC at 12-13 September 2017*

So, three events of GICs enhancement were connected with an increase and an expansion of the westward electrojet during two substorms and with short bursts of Pc5 pulsations. It was possible to track GICs enhancement along the meridian according to fine spatial temporal

structure of the substorm development for the given events. GICs increase at different latitudes corresponds to the poleward movement on the westward electrojet. The source of the GICs during the third period was short pulses of Pc5 pulsations at the recovery phase of an intense second substorm [see more Setsko et al., 2023].

- **14-17 and 27-28 September 2017**

Geomagnetic activity and increasing of GICs during HILDCAA period, on 14-17 September (left side) and during the moderate magnetic storm (SYM/H ~ −74 nT) with multistage development on September, 27-28 (right side) are shown on Figure 5.

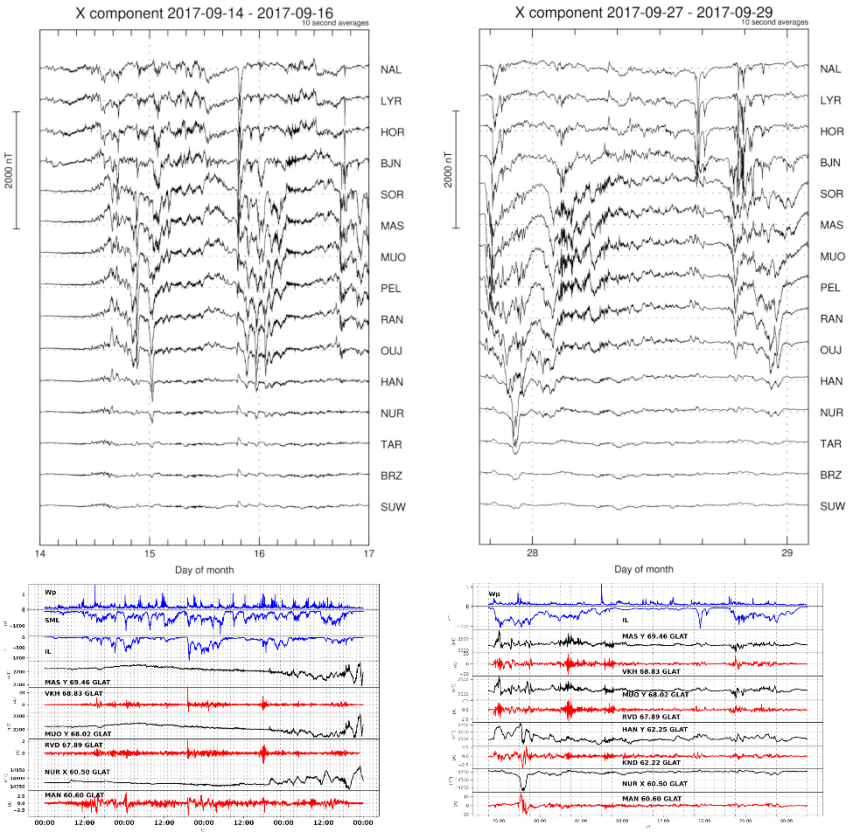

Figure 5. Geomagnetic disturbances and GIC at 14-17 (left) and 27-28 (right) September 2017

It is shown that despite on the HILDCAA event, GICs were associated only with the development of a substorms, when IMAGE network located close to the night sector. It was shown also that GICs corresponded to the fine spatiotemporal structure of the development of a substorm. For the period of September 27–28, GICs were associated with the increasing and expansion of the westward electrojet during three substorms and bursts of Pc5 pulsations during the recovery phase of the substorm.

5. Summary

Using the latitudinal profiles of the EURISGIC, IMAGE and MIRACLE data made it possible to trace the GIC amplification in accordance with the development of the fine structure of the substorm:

1) GIC amplification at different latitudes occurred simultaneously with the jump to pole of the westward electrojet during the substorm expansion phase

2) On September 12–13, the largest GICs were observed during the expansion phase of the second substorm. But on September 27-28, on the contrary, the largest GICs were

observed during Pc5 pulsations at the recovery phase of the substorm. Both of these events occurred during the main phase of the corresponding magnetic storm near the maximum.

3) On September 7–8 and 14–17, the largest GICs were also observed during intense substorms (or supersubstorms).

Thus, in September 2017, intense GICs observed by the EURISGIC system were associated with two sources - the movement and intensification of the substorm electrojet during the expansion phase of the substorm and Pc5 pulsations during the recovery phase of the substorm

Acknowledgments

The work of I.V. Despirak, P.V. Setsko, A.A. Lubchich and V.A. Bilin was supported by the RFBR (№ 20-55-18003 Bulg_a) and National Science Fund of Bulgaria (NSFB) (№ КП-06-Русия/15).

References

Clilverd M.A., Rodger C.J., Freeman M.P., Brundell J.B., Mac Manus D.H., Dalzell M., Clarke E., Thomson A.W.P., Richardson G.S., MacLeod F., Frame I., 2021. Geomagnetically induced currents during the 07–08 September 2017 disturbed period: a global perspective J. Space Weather Space Clim. 11. 33 https://doi.org/10.1051/swsc/2021014

Despirak I.V., Setsko P.V., Sakharov Ya.A., Lyubchich A.A., Selivanov V.N., Valev D., 2022. Observations of geomagnetic induced currents in Northwestern Russia: case studies. Geomagnetism and Aeronomy, Vol. 62, N. 6, pp. 711–723 https://doi.org/10.31857/S0016794022060037

Despirak I.V., Setsko P.V., Sakharov Ya.A., Lubchich A.A., Selivanov V.N. Geomagnetically Induced Currents during Supersubstorms on September 7–8, 2017, Bulletin of the Russian Academy of Sciences: Physics, 2023, Vol. 87, No. 7, pp. 999–1006. 10.3103/S1062873823702283

Hajra R., Tsurutani B.T., Lakhina G.S., 2020. The complex space weather events of 2017 September, The Astrophysical Journal, vol. 899:3 (15pp), https://doi.org/10.3847/1538-4357/aba2c5

Kozyreva O., Pilipenko V, Krasnoperov R, Baddeley L, Sakharov Y, Dobrovolsky M., 2020. Fine structure of substorm and geomagnetically induced currents. Ann. Geophys. 63(2), GM219. https://doi.org/10.4401/ag-8198

Lakhina G.S., Hajra R., Tsurutani B.T., 2020. Geomagnetically inducted current. Springer Nature Switzerland AG 2020 H. K. Gupta (ed.), Encyclopedia of Solid Earth Geophysics, Encyclopedia of Earth Sciences Series

Pulkkinen A., Lindahl S., Viljanen A., Pirjola R., 2005. Geomagnetic storm of 29-31 October 2003: Geomagnetically induced currents and their relation to problems in the Swedish high-voltage power transmission system. Space Weather, 3, S08C03, https://doi.org/10.1029/2004SW000123

Sakharov Ya. A., Danilin A.N., Ostafiichuk R.M., 2007 Recording of GICs in power systems of the Kola Peninsula, in Trudy 7-go Mezhdunar. simp. po elektromagnitnoi sovmestimosti i elektromagnitnoi ekologii (Proceedings of the 7th International Symposium on Electromagnetic Compatibility and Electromagnetic Ecology), St. Petersburg: IEEE, pp. 291–293

Sakharov Ya.A., Katkalov Yu.V., Selivanov V.N., Viljanen A., 2016. Recording of GICs in a regional power system, in Prakticheskie aspekty geliogeofiziki, Materialy spetsial'noi sektsii "Prakticheskie aspekty nauki kosmicheskoi pogody" 11-i ezhegodnoi konferentsii "Fizika plazmy v solnechnoi sisteme", Moscow. IKI, pp. 134–145.

Sakharov Ya.A., Selivanov V.N., Bilin V.A., Nikolaev V.G., 2019. Extremal values of geomagnetically inducted currents in the regional power system. “Physics of Auroral Phenomena”, Proc. XLII Annual Seminar, Apatity, pp. 53-56. https://doi.org/10.25702/KSC.2588-0039.2019.42.53-56 (in Russian)

Setsko P.V., Despirak I.V., Sakharov Ya.A., Lubchich A.A., Bilin V.A., Selivanov V.N. Geoinduced currents on Karelian-Kola power line and finnish gas pipeline on september, 12–13 2017, Journal of Atmospheric and Solar–Terrestrial Physics, 247, 2023. https://doi.org/10.1016/j.jastp.2023.106079

Tsurutani B.T. and Hajra R., 2021. The Interplanetary and Magnetospheric causes of Geomagnetically Induced Currents (GICs) > 10 A in the Mäntsälä Finland Pipeline: 1999 through 2019. J. Space Weather Space Clim., vol. 11, pp. 23. https://doi.org/10.1051/swsc/2021001

Viljanen A., Pulkkinen A., Pirjola R., Pajunpaa K., Posio P., Koistinen A. 2006. Recordings of geomagnetically induced currents and a nowcasting service of the Finnish natural gas pipeline system, Space Weather, 4, S10004, doi:10.1029/2006SW000234.

Vorobjev V.G., Sakharov Ya.A., Yagodkina O.I., Petrukovich A.A, Selivanov V.N., 2018. Geoinduced currents and their relationship with the western electrojet position and auroral precipitation boundaries, Tr. Kolsk. Nauchn. Tsentra Ross. Akad. Nauk, 2018, vol. 4, pp. 16–28. https://doi.org/10.25702/KSC.2307-5252.2018.9.5.16-28

Intense Geomagnetic Storms during Solar Cycles 23-25

Gopalswamy N.[1], *Akiyama S.*[1,2], *Yashiro S.*[1,2], *Makela P.*[1,2], *Xie H.*[1,2]

[1]Heliophysics, NASA GSFC, Greenbelt, MD, USA; nat.gopalswamy@nasa.gov
[2]The Catholic University of America, Washington DC

1. Abstract.

Intense geomagnetic storms are characterized by a minimum value of the Dst index at or below –100 nT. It is well known that these storms are caused by the southward magnetic fields in coronal mass ejections (CMEs) and corotating interaction regions (CIRs). While CIR storms are confined to Dst values at or above –150 nT, CME storms can reach Dst –500 nT or lower. In this report, we illustrate the need to understand the storm evolution based on solar source and solar wind parameters using a recent storm (2023 April 24) by way of providing the motivation to catalog such events for a better understanding of the main phase time structure of geomagnetic storms.

Keywords: Geomagnetic storms; Coronal mass ejections; co-rotating interaction regions

2. Introduction

Intense geomagnetic storms (Dst ≤ -100 nT) are known to have serious space weather consequences. They result in energization of particles in Van Allen belts, particle precipitation in the polar atmosphere, atmospheric heating, and geomagnetically induced currents (GICs; see Temmer 2021, and references therein). The time structure of geomagnetic storms represented by an index such as Dst can introduce large variability in the strength, duration, and consequences of geomagnetic storms. Rapid time structures can result in large GICs (Pulkkinen et al. 2005; Kappenman et al. 2005; Belakhovsky et al. 2019). One type of time structure of a geomagnetic storm is multiple steps in the main phase. The multistep storms constitute about two-thirds of all intense geomagnetic storms (Zhang et al. 2008). The classic case of two Bz<0 intervals in the sheath and MC separated by a Bz>0 interval results in the double-dip storm. Most multi-dip storms are due to coronal mass ejections (CMEs), but ~ 11% of dips are found in storms caused by corotating interaction regions (CIRs). Another source of two-dip storms is the passage of an interplanetary shock through the body of a preceding CME resulting in an abrupt enhancement of the Bz magnitude (Richardson and Zhang, 2008; Gopalswamy et al. 2015). Multiple dips can also occur in complex ejecta formed by two or more CMEs and their sheaths.

Another type of storm main phase time structure was reported in Gopalswamy et al. (2022). The time structure appears as a sudden change in the slope of the Dst profile in response to a change in the solar wind dynamic pressure (Gopalswamy et al. 2022). The slope change coincided with the density increase inside the second half of the 2018 August 25 MC. Simulation of the storm using the Comprehensive Inner Magnetosphere-Ionosphere (CIMI) model (Fok et al., 2014) confirmed that the Dst slope change coincided with an increase in the ring current energy. Murayama (1982) introduced the effect of the solar wind dynamic pressure (Pf) via the ring current injection (Q) in the form Q ~ VBz×Pf1/3). Following the work of several authors, Wang et al. (2003) refined Q and the ring-current decay rate (τ) as functions of solar wind electric field Ey = VBz and Pf. Xie et al. (2008) used Wang et al. formulas and showed that the Dst peak value of a storm increases when there is a large enhancement in Pf during the storm main phase. Le et al. (2020) and Zhao et al. (2021) found that the SYM-H index is highly correlated with the time-integral of the injection over the main phase. Thus, one

needs to derive Q and τ from solar wind parameters for a better understanding of the time structure of the main phase.

The origin of the main phase time structure is also related to the solar source properties such as the tilt angle and axial-field direction of the CME flux rope, and the flux rope kinematics as influenced by the coronal and interplanetary environment. These parameters can be derived from the Flux Rope from Eruption Data Technique (Gopalswamy et al. 2018). In this report, we examine the largest geomagnetic storm over the first three years of solar cycle 25 (2019 December 1 to 2023 April 30). We also compare the occurrence rate and intensity of geomagnetic storms over the corresponding phases in solar cycles 23 and 24.

3. Observations, Analysis, and Results

As of this writing the largest geomagnetic storm (Dst = –212 nT) in solar cycle (SC) 25 occurred on 2023 April 24 around 06:00 UT as obtained from the World Data Center in Kyoto (Nose et al. 2015). This is a double-dip storm with both dips being below –100 nT. The solar wind parameters showing the associated ICME were obtained from the OMNI database. The CME associated with the storm was observed by the Large Angle and Spectrometric Coronagraph (LASCO, Brueckner et al. 1995) on board the SOHO mission. The CME was also observed by the coronagraphs in the Sun Earth Connection Coronal and Heliospheric Investigation (SECCHI, Howard et al. 2008) instrument suite on board the STEREO mission. Information on the source active region was obtained from the Atmospheric Imaging Assembly (AIA, Lemen et al. 2012) on board the SDO mission. Plots and movies made available at the CDAW data center (https://cdaw.gsfc.nasa.gov) were also used for this investigation.

3.1. Solar Wind Parameters and the Geomagnetic Storm

The solar wind parameters associated with the storm are shown in Figure 1. We see that the interplanetary CME (ICME) in this event is a magnetic cloud (MC) according to the definition of Burlaga et al. (1981): enhanced magnetic field, smooth rotation of one of the magnetic field components and low proton temperature or plasma beta. The shock-driving MC was also expanding with the front and back speeds of 620 km/s and 490 km/s, respectively. The magnetic field in the MC was significantly enhanced, with a peak value of ~35 nT. The Bz component rotated from south to north while the By component remained east-west indicating that this is a low-inclination MC. The shock sheath had enhanced density and magnetic field while these two parameters were significantly depressed inside the MC. The shock seems to be propagating into a small preceding flux rope whose tail end was compressed by the shock resulting in a large negative Bz. The MC on April 24 is bipolar with south-north configuration, typical of an odd-numbered solar cycle. The ambient solar wind ahead of the MC has a speed of ~350 km/s as can be seen at the beginning of the plot (before 4:00 UT on April 23). At the shock arrival the IMF Bz suddenly decreased to -20 nT while the density increased to about 20 cm^{-3}. The density was high throughout the sheath region, dropping to below 5 cm^{-3} in the MC, remaining low throughout the MC interval.

The Dst index was already decreasing around 10:00 UT on 2023 April 23 from –13 nT to –49 nT at 16 UT ahead of the shock. When the shock arrived, the Dst slope changed suddenly and the Dst dropped to –56 nT. From then on the Dst index dropped rapidly reaching –165 nT (the first dip due to Bz reaching –10 nT in the sheath). The Dst slope changed from 6 nT/hr to ~22 nT/hr. Bz turned positive around 21 UT on April 23, so the storm started recovering for the next 3 hrs until the arrival of the MC. The Bz component turned negative in the beginning of the MC

reaching –30 nT right after the front boundary of the MC. Accordingly, Ey reached –20 mV/m, which is twice the value during the Bz <0 interval in the sheath (see Fig. 1).

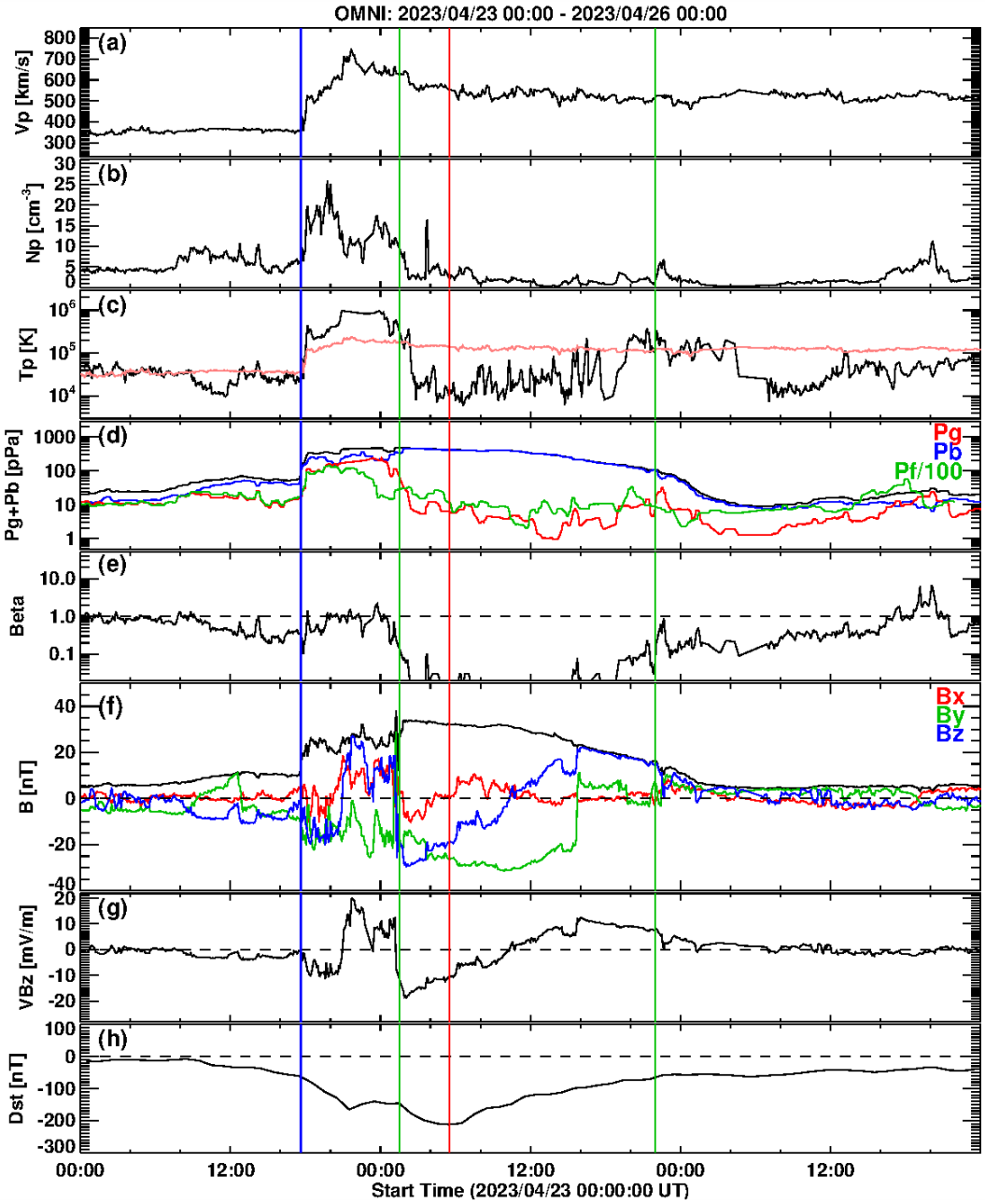

Figure 1. Solar wind observations from OMNI for the period 2023 April 23 – 26. (a) Solar wind speed (Vp), (b) proton density (Np), (c) proton temperature (Tp) along with the expected temperature (orange line), (d) gas (Pg – red curve), magnetic (Pb – blue curve), and flow (Pf – green curve) pressures and the total pressure (Pg+Pb – black curve), (e) plasma beta, (f) total magnetic field strength (B) along with the three components Bx (red curve), By (green curve), and Bz (blue curve) in GSE coordinates, (g) solar wind electric field (solar wind speed times the Bz component of the magnetic field), (h) the Dst index showing the intense double-dip geomagnetic storm. The vertical red line marks the time of minimum Dst (–212 nT at 06:00 UT on April 24). The first dip (–165 nT) in Dst occurred at 22:00 UT on April 23. The Dst data are from the World Data Center, Kyoto. The vertical blue line marks the shock (17:38 UT on April 23). The vertical green lines mark the boundaries of the magnetic cloud based on Tp and plasma beta (beginning and end of MC interval). B is also enhanced significantly during the MC interval (1:30 UT to 22:00 UT on April 24).

The larger difference in Ey is due to the higher solar wind speed during the Bz <0 interval in the MC. In spite of the large Ey, the Dst index displayed a shallower slope, taking ~5 hrs to decrease by 65 nT (13 nT/hr). The reason behind the shallow slope is the low density in the MC (<5 cm-3). The effect is opposite to that of the steep slope caused by high density (or high dynamic pressure) as shown in Gopalswamy et al. (2022) for the 2018 August 26 storm. After the minimum value, the Dst increases mainly due to the weakening of Ey until it changes sign when Bz turns positive. Further recovery is slow mainly because of the low density in the MC, consistent with the dependence of ring current decay under low dynamic pressure (Wang et al. 2003). Thus, for a full understanding of the Dst index (ring current evolution), one needs to consider the main-phase time structure caused by Ey and dynamic pressure.

3.2. Events at the Sun and the Source Active Region

The solar counterpart of the MC and the source region on the Sun can be determined by examining CMEs that occurred 1-4 days before the storm. This can be done using the composite plots involving the Dst index, CME height-time plot, and GOES soft-ray light curve available at https://cdaw.gsfc.nasa.gov/CME_list/daily_plots/dsthtx/2023_04/dsthtx_20230421.html (see Fig. 2). We see that was a series of 5 CMEs from the east limb On April 19. The CMEs on April 20 and the first one on April 21 are also limb CMEs, so none of these CMEs could have caused the intense geomagnetic storm. Therefore, it is easy to identify the CME that caused the geomagnetic storm as the CME on April 21 appearing in the SOHO/LASCO FOV at 18:12 UT. The CME was associated with a major flare (GOES intensity M1.7) originating from S22W11 on the solar disk.

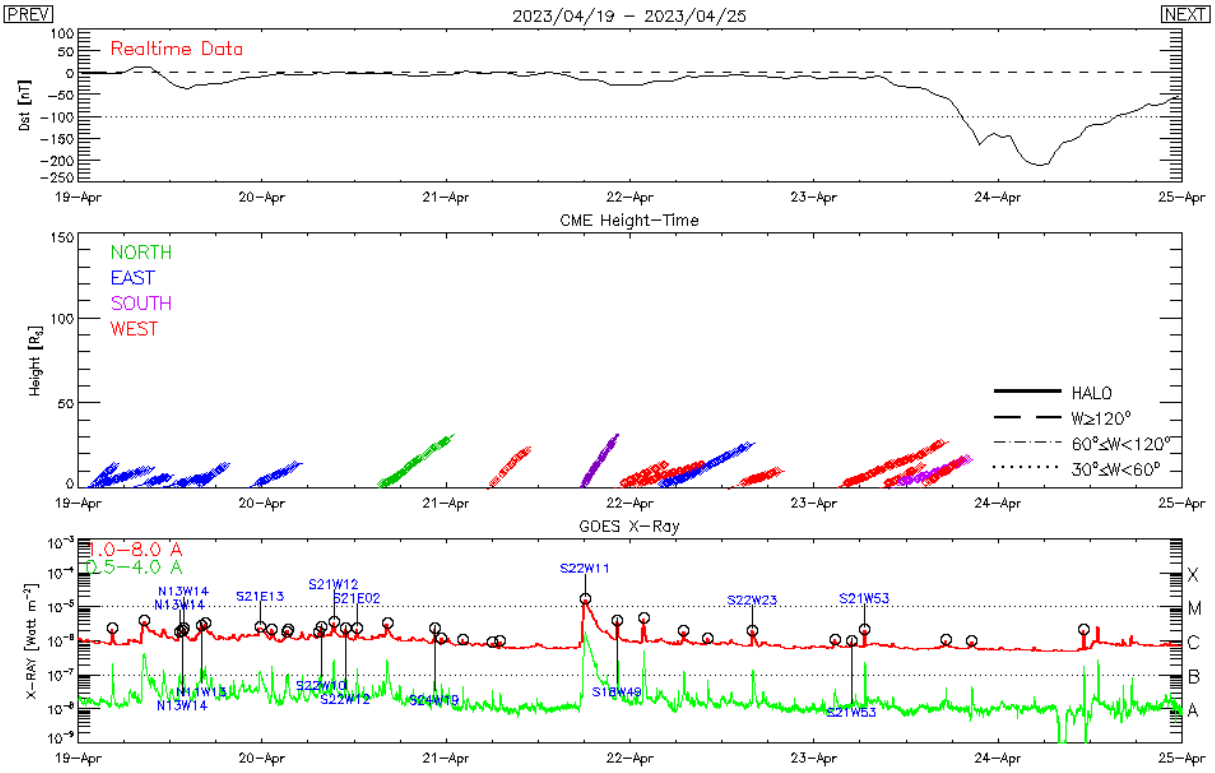

Figure 2. *Overview plot showing the Dst index over a six-day period starting from April 19, 2023. The CME that caused the geomagnetic storm originated from AR 13283 located at heliographic coordinates S22W11.*

Figure 3 shows the early manifestation of the CME using an EUV difference image at 17:56 UT obtained by SDO/AIA at 192 A. The EUV disturbance is from the southwest quadrant as expected from the flare location (S22W11). The figure also shows the fully formed halo CME with the ejecta part (bright feature) heading in the southwest direction. The diffuse features are thought to be manifestation of the shock sheath. The STEREO Ahead spacecraft located at E10 observed the CME with a similar morphology. The CME had a sky plane speed of ~1284 km/s, slightly higher than the average speed of CMEs causing intense geomagnetic storms. The CME produced an intense type II radio burst and a minor solar energetic particle (SEP) event indicating that the CME was driving a shock from near the Sun. The CME showed a deceleration of – 28 m s^{-2}, as expected for a fast CME. The MC speed measured at 1-au was ~600 km/s, consistent with the CME deceleration in the coronagraph FOV.

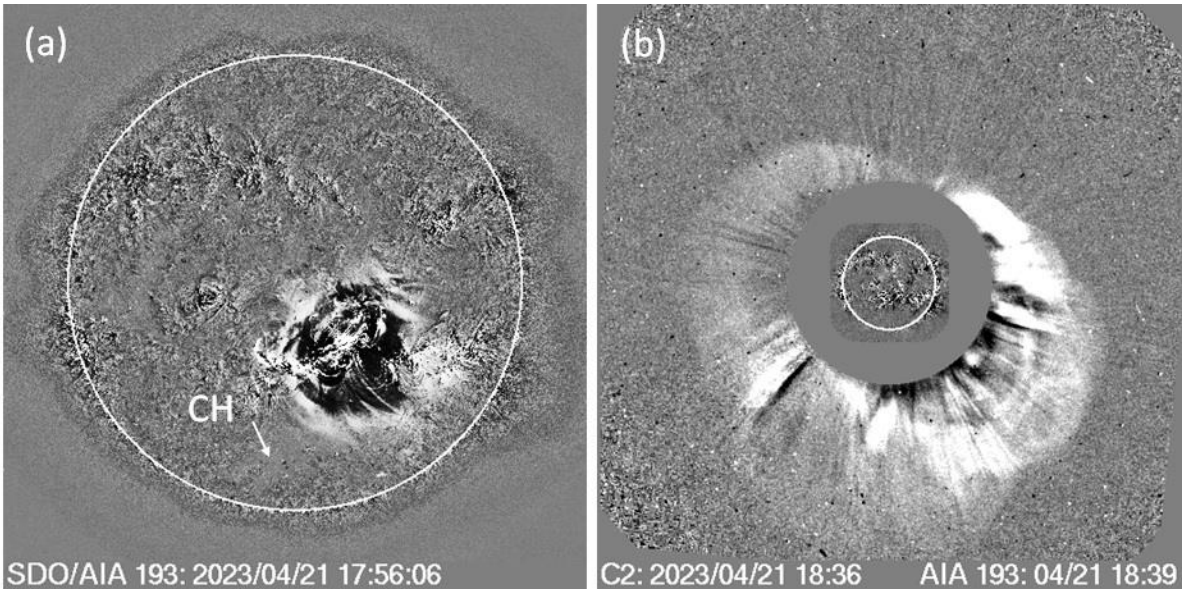

Figure 3. *Figure 3 (a) The solar source SDO/AIA at 193 Å difference image and (b) the CME as viewed in the SOHO/LASCO FOV. The active region 13283 was located at S22W11. The B0 angle was +6⁰. The larger latitudinal distance was likely reduced by deflection of the CME by the coronal hole located to the south of the eruption region. The deflection might have pushed the CME trajectory to the north and west of the Sun-Earth line.*

Figure 4 shows the CME source region (NOAA AR 13283) in the longitudinal magnetogram obtained by SDO's Helioseismic Imager (HMI) and the post eruption arcade (PEA) imaged by SDO's AIA at 193 Å. The coronal hole to the southeast of the active region has negative polarity. The main neutral line in the active region is in the east west direction. The PEA is also extended in the east west direction with a slight tilt. The neutral line orientation matches with the low inclination MC inferred from in-situ observations (see Fig. 1). The source location is close to the disk center, so the CME is likely hit Earth as confirmed by in-situ observations.

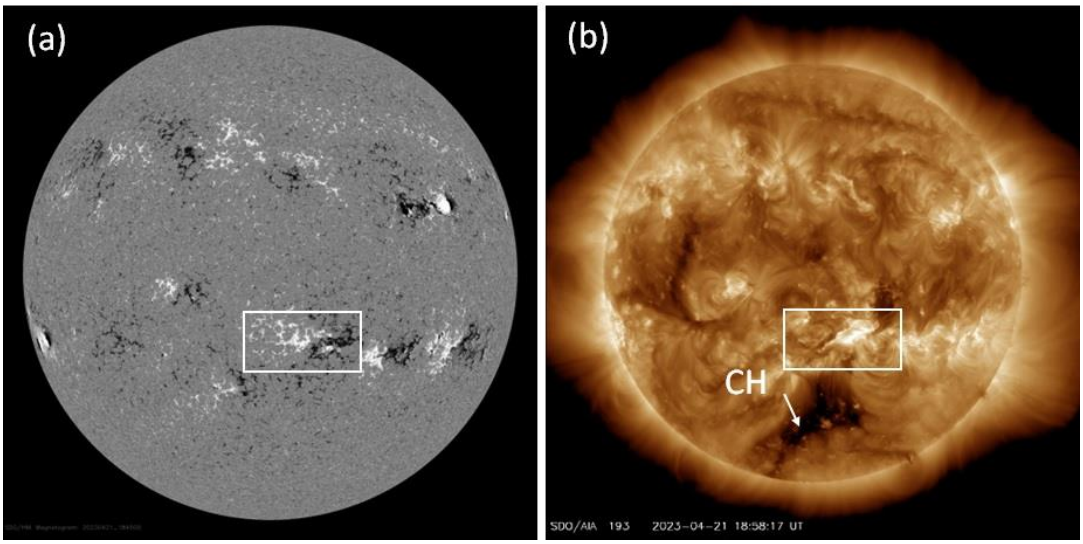

Figure 4*. (a) SDO/HMI magnetogram with the source active region marked by the white rectangle. (b) SDO/AIA image showing the post eruption arcade. The coronal hole (CH) to the southeast of the eruption region is marked by an arrow.*

3.3. Shock arrival time at 1 au

In order to compare the observed shock travel time with that expected from empirical models, we need to get the true speed of the CME in the earthward direction. STEREO was observing from very close to the Sun-Earth line, so we cannot use forward modeling with multiview observations. Instead, we use an empirical model obtained by Gopalswamy et al. (2015b) developed by comparing cone model results with direct measurements for CMEs in quadrature. According to this model, the space speed (V_{3D}) of the CME can be estimated from the sky-plane speed (V_{sky}) using the relation, $V_{3D} = 1.1\ V_{sky} + 156$ km/s as 1568 km/s. Based on the source location (S22W11) and the measured Vsky = 1284 km/s, we estimate the earthward speed (u) as 1428 km/s. Using u in the empirical shock arrival model for the travel time T as $T = AB^u + C$ (with A = 151.002, B = 0.998625, and C = 11.5981, see Gopalswamy et al. 2005). The result is T = 32.8 hrs. The actual travel time measured from the time of first appearance of the CME (08:12 UT on April 21) to the shock arrival at 1 au (17:38 UT on April 23) is ~47 hrs, indicating a major discrepancy. This discrepancy is likely due to a smaller earthward speed than computed above because of the CME deflection to the north and west by the coronal hole. Such deflections are very common on the Sun (Gopalswamy et al. 2009). If the CME is deflected by an angle of ~30º to the west, then the earthward speed becomes u = 1097 km/s, yielding a travel time of ~45 hrs, which is close to the observed travel time.

Table 1. *Number of intense storms during the first 41 months of solar cycles 23-25.*

Solar Cycle	#CME storms	#CIR Storms	Total
SC 23	18	3	21 (18)[1]
SC 24	5	0	5 (0)
SC25	4	0	4 (1)

[1]The numbers in the parentheses of this column correspond to the rise phase.

4. Discussion

We studied the solar and interplanetary causes of the 2023 April 24 geomagnetic storm, which is the largest in the first 41 months in solar cycle 25. It must be noted that the Sun is already in the maximum phase starting in late 2022. Only one intense storm occurred during the rise phase of SC 25 on 2021 November 4 with Dst = –105 nT. In contrast, SC 23 witnessed 18 intense storms in its rise phase including two storms with intensity <–200 nT. On the other hand, SC 24 had no intense storm in its rise phase. Table 1 compares the number of intense storms in the first 41 months in each. Note that this interval includes part of the maximum phase of the cycles. The numbers in the last column within parentheses correspond to the rise phase in each cycle. These numbers are consistent with the finding that the strength of SC 25 is likely to be similar or slightly greater than that of SC 24 (Gopalswamy et al. 2023).

How does the CME speed compare with the average speed of CMEs that result in major storms? Figure 5 shows the distribution of sky-plane speeds of 91 CMEs observed during SCs 23, 24, and part of SC 25 that caused intense storms. Also shown are the halo fraction and the average width of non-halo CMEs. We see that the intense storms are caused by fast and wide CMEs, most of them being halo CMEs. The average speed of the CMEs is 950 km/s, more than a factor 2 faster than the general population of CMEs. Note that these are sky-plane speeds. The true speeds are likely to be higher when the sky-plane speeds are deprojected. The speed of the 2023 April 24 storm is shown on the speed histogram, indicating that it has above-average speed. The CME in hand falls in the halo CME bin shown in Fig. 5(b). The location of the CME is also consistent with the distribution of source positions as indicated by the arrow mark in Fig. 5 (c).

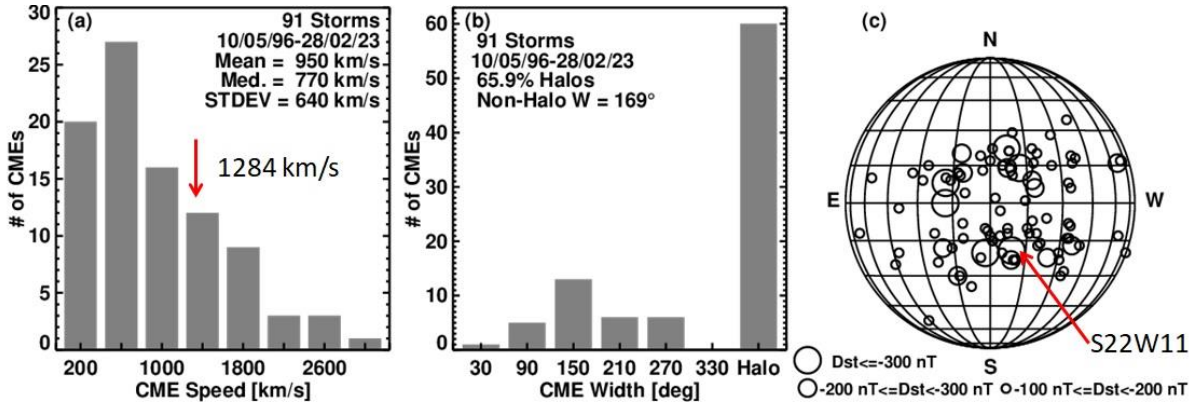

Figure 5*. Distributions of speed (a), width (b), and source locations (c) of CMEs responsible for intense geomagnetic storms. The mean and median speeds are along with standard deviations. The red arrows point to the parameters of the 2023 April 24 storm.*

5. Conclusions

The main finding of this work is that we need to consider both the solar wind electric field and the dynamic pressure. The slope changes in the main phase and the early decay phase are marked by the changes in proton density in the sheath and MC. When the dynamic pressure is low, say below 3 nPa, the Dst profile is controlled by the electric field. When the dynamic pressure is high, we need to consider the contributions from both electric field and the dynamic pressure. On the solar side we need to take into account of the presence of a coronal hole near the eruption region. The effect of the coronal hole is to deflect the CME in question away from the Sun-Earth line in the longitudinal direction. Note that depending on the relative location of the coronal hole and the eruption region, some CMEs can be deflected toward the Sun-Earth

line. Motivated by the results of this investigation, we are developing a catalog of intense storms linking them to the interplanetary event described in Fig. 1 and the solar sources and CMEs as illustrated in Figs. 3 and 4. Similar information on solar and solar wind links to CIR storms will also be included in the catalog (Gopalswamy et al. 2023, under preparation).

References

Belakhovsky, V., Pilipenko, V., Engebretson, M., Sakharov, Y., Selivanov, V. (2019). Impulsive disturbances of the geomagnetic field as a cause of induced currents of electric power lines. J. Space Weather Space Clim. A18, doi: 10.1051/swsc/2019015.

Fok, M. -C., Buzulukova, N. Y., Chen, S. -H., Glocer, A., Nagai, T., Valek, P., & Perez, J. D. (2014). The Comprehensive Inner Magnetosphere-Ionosphere Model. J. Geophys. Res, 119 (9), 7522–7540. doi: 10.1002/2014JA020239

Brueckner, G. E., Howard, R. A., Koomen, M. J., Korendyke, C. M., Michels, D. J., Moses, J. D., Socker, D. G., Dere, K. P., et al. (1995). The large angle spectroscopic coronagraph (LASCO), Solar Physics, 162, 357–402. doi: 10.1007/BF00733434

Burlaga, L., Sittler, E., Mariani, F., Schwenn, R. (1981). Magnetic loop behind an interplanetary shock: Voyager, Helios, and IMP 8 observations. J. Geophys. Res, 86, A8, 6673. doi: 10.1029/JA086iA08p06673

Gopalswamy, N., Yashiro, S., Liu, Y., Michalek, G., Vourlidas, A., Kaiser, M. L., Howard, R. A. (2012). Coronal mass ejections and other extreme characteristics of the 2003 October-November solar eruptions. JGR 110, A9, citeID A09S15. doi: 10.1029/2004JA010958

Gopalswamy, N., Mäkelä, Xie, H., Akiyama, S., Yashiro, S. (2009). CME interactions with coronal holes and their interplanetary consequences. Journal of Geophysical Research: Space Physics, 114 (A3), CiteID A00A22, doi: 10.1029/2008JA013686

Gopalswamy, N. , Makela, P. , Akiyama, S. , Yashiro, S. , Thakur, N.(2015a). CMEs during the Two Activity Peaks in Cycle 24 and their Space Weather Consequences. Sun and Geosphere 10, 111, doi: 10.48550/arXiv.1509.04216

Gopalswamy, N., Xie, H., Akiyama, S., Makela, P., Yashiro, S., Michalek, G. (2015b) The peculiar behavior of halo coronal mass ejections in solar cycle 24. Astrophys. J. Lett. 2015, 804, L23, doi: 10.1088/2041-8205/804/1/l23.

Gopalswamy, N. , Akiyama, S. , Yashiro, S., Xie, H. (2018). A New Technique to Provide Realistic Input to CME Forecasting Models. IAUS 335, 258, doi: 10.1017/S1743921317011048

Gopalswamy, N., Yashiro, S., Akiyama, S., Xie, H., Mäkelä, P., Fok, M.-C., Ferradas, C.P. (2022). What Is Unusual About the Third Largest Geomagnetic Storm of Solar Cycle 24? J. Geophys. Res. 2022, 127, e30404.

Gopalswamy, N., Michalek, G., Yashiro, S., Mäkelä, P., Akiyama, S., Xie, H. (2023). What Do Halo CMEs Tell Us about Solar Cycle 25? ApJ 952, L13, doi: 10.3847/2041-8213/acdde2

Howard, R. A., Moses, J. D., Vourlidas, A., Newmark, J. S., Socker, D. G., Plunkett, S. P., Korendyke, C. M., Cook, J. W. et al. (2008). Sun Earth Connection Coronal and Heliospheric Investigation (SECCHI). Space Science Reviews, 136(1–4), 67–115. doi: 10.1007/s11214-008-9341-4

Kappenman, J.G. (2003) Storm sudden commencement events and the associated geomagnetically induced current risks to groundbased systems at low-latitude and midlatitude locations. Space Weather, 1, 1016. doi: 10.1029/2003sw000009.

Le, G.-M., Liu, G.-X., & Zhou, M.-M. (2020). Dependence of Major Geomagnetic Storm Intensity (Dst≤−100 nT) on Associated Solar Wind Parameters. Solar Physics, 295, 108. doi: 10.1007/s11207-020-01675-3

Murayama, T. (1982). Coupling Function Between Solar Wind Parameters and Geomagnetic Indices (Paper 2R0436). Rev. Geophys. Space Phys. 20, 623.

Lemen, J. Title, A., Akin, D., Boerner, P. F., Chou, C., Drake, J. F., Duncan, D. W., Edwards, C. G., et al. (2012). The Atmospheric Imaging Assembly (AIA) on the Solar Dynamics Observatory (SDO). Solar Physics, 275(1–2), 17–40. doi: 10.1007/s11207-011-9776-8

Nose, M., Iyemori, T., Sugiura, M., & Kamei, T. (2005). World Data Center for Geomagnetism, Kyoto Geomagnetic Dst index, doi: 10.17593/14515-74000

Pulkkinen, A., Lindahl, S., Viljanen, A., Pirjola, R. (2005). Geomagnetic storm of 29-31 October 2003: Geomagnetically induced currents and their relation to problems in the Swedish high-voltage power transmission system. Space Weather, 13, S08C03, doi: 10.1029/2004sw000123.

Richardson, I. G. , Zhang, J. (2008). Multiple-step geomagnetic storms and their interplanetary drivers. Geophys. Res. Lett. 35, 6, citeID: L06S07. doi: 10.1029/2007GL032025

Temmer, M. (2021)Space weather: The solar perspective. Living Rev. Sol. Phys. 18, 4.

Wang, C. B., Chao, J. K., & Lin, C. H. (2003). Influence of the solar wind dynamic pressure on the decay and injection of the ring current. Journal of Geophysical Research, 108(A9), 1341. doi: 10.1029/2003JA009851

Xie, H., Gopalswamy, N., Cyr, O. C. S., & Yashiro, S. (2008). Effects of solar wind dynamic pressure and preconditioning on large geomagnetic storms. Geophysical Research Letters, 35(6), L06S08. doi: 10.1029/2007GL032298

Zhang, J., and Richardson, I. G., Webb, D. F. (2008). Multiple-step geomagnetic storms and their interplanetary drivers. JGR 113, citeID: A00A12. doi: 10.1029/2008JA013228

Zhao, M. X., Le, G. M., Li, Q., Liu, G. A., & Mao, T. (2021). Dependence of Great Geomagnetic Storm (ΔSYM-H≤−200 nT) on Associated Solar Wind Parameters. Solar Physics, 296(4), 66. doi: 10.1007/s11207-021-01816-2

Determination of the Parameters of Midlatitude Positive Bays Caused by Magnetospheric Substorms

Guineva V.H.[1], Werner R.[1], Atanassov A.M.[1], Bojilova R.Ts.[2], Raykova L.N.[1], Valev D.T.[1]

[1]Space Research and Technology Institute (SRTI) – Bulgarian Academy of Sciences, Stara Zagora Department, Bulgaria; v_guineva@yahoo.com
[2]National Institute of Geophysics, Geodesy and Geography (NIGGG) - Bulgarian Academy of Sciences, Sofia, Bulgaria

6. Abstract.

Magnetospheric substorms are an important feature of the space weather. Apart of the variety of phenomena that they provoke, they influence the magnetic field at the Earth surface. Negative X-bays at auroral latitudes and positive bays in the X magnetic component at midlatitudes known as midlatitude positive bays (MPB) are observed. The study of the MPB development serves in the investigation of the solar-magnetosphere coupling during the substorm progress. At the Space Research and Technology Institute of the Bulgarian Academy of Sciences, the magnetic variations at Panagjurishte were calculated, based on data by the Bulgarian magnetic station Panagjurishte (PAG) with the main goal to determine the variations related to the substorm activity (MPB) and estimate the MPB main parameters. In this work we described the development of a processing tool to determine the beginning and end of the MPB registered at PAG. The tool is based on smoothing by moving average and by inspection of the consecutive minima of the X-component before and after the MPB maximum, calculated by the first derivative of the X variations. The MPB amplitude was obtained by the difference between the MPB maximum and the X value at the MPB beginning. Criteria to choose the minima of the beginning and end of the MPB have been specified. A minima find algorithm has been worked out and applied to specific cases. All results were made available to the scientific community by a created catalog, described also in this paper.

Keywords: *midlatitude positive bays (MPB), catalog of magnetic variations, MPB parameters*

7. Introduction

Substorms are a typical phenomenon, associated with many processes in the magnetosphere and ionosphere, summarized by Akasofu (2004). During magnetospheric substorms, a big amount of energy is released from the magnetospheric tail into the ionosphere and inner magnetosphere [Akasofu, 1968]. Magnetospheric substorms are the cause for the major disturbances in the Earths magnetic field. As it is well known, at auroral latitudes negative bays in the X (North) magnetic component at ground are observed [Akasofu, 1964]. It is also known, that during large magnetospheric substorms the negative bays at auroral latitudes are accompanied by positive bays in the X component at midlatitudes. [Akasofu, 1968; McPherron et al., 1973]. Moreover, a systematic variation of the Y (East) component is observed in the same time. First, the presence of MPB was explained with low latitude return currents of the westward electrojet [Akasofu et al., 1965]. Later, the positive bays were associated to the upward field-aligned currents [Meng and Akasofu, 1969]. The accepted theory at present is, that the midlatitude positive bays are the result of a current system, namely the Substorm Current Wedge (SCW) [McPherron, 1972; McPherron et al., 1973]. SCW is formed, when the tail current is deviated along the magnetic field lines through the ionosphere. The magnetic variations at midlatitudes during substorms have been used as tools for the study of magnetospheric substorms by a lot of authors. MPB's appear a good indicator of substorm onset [e.g. Hones et al., 1971; Mende et al., 1972; McPherron, 1972; McPherron and Chu, 2017]. The

sign of the Y component can be used to deduce whether the direction of the field aligned currents is down or up in the ionosphere at the longitude of a given station [Meng and Akasofu, 1969]. A method to determine the geomagnetic longitude of the auroral substorm onset was worked out [Rostoker et al., 1980, Sergeev and Tsyganenko, 1980]. Thus, the study of the midlatitude positive bays and the estimation of their parameters can be very useful in the magnetospheric substorms research.

At the Space Research and Technology Institute of the Bulgarian Academy of Sciences, an original catalog of the magnetic variations at Panagjurishte is developed, based on data by the Bulgarian magnetic station Panagjurishte (PAG) (~37° GMLat, ~97° GMLon), as one of the tasks of a bilateral project Bulgaria – Russia. The catalog is available at: http://space.bas.bg/Catalog_MPB/. The objectives of this work are to create a processing tool to determine automatically the basic parameters of the midlatitude positive bays registered at PAG and to use it to complete the Panagjurishte station catalog of the magnetic variations.

8. Content of the catalog of the magnetic variations at Panagjurishte and envisaged additions

In Fig.1, the structure of the catalog, which went through several modifications (e.g. Guineva et al., 2021a, Guineva et al., 2021b) is presented.

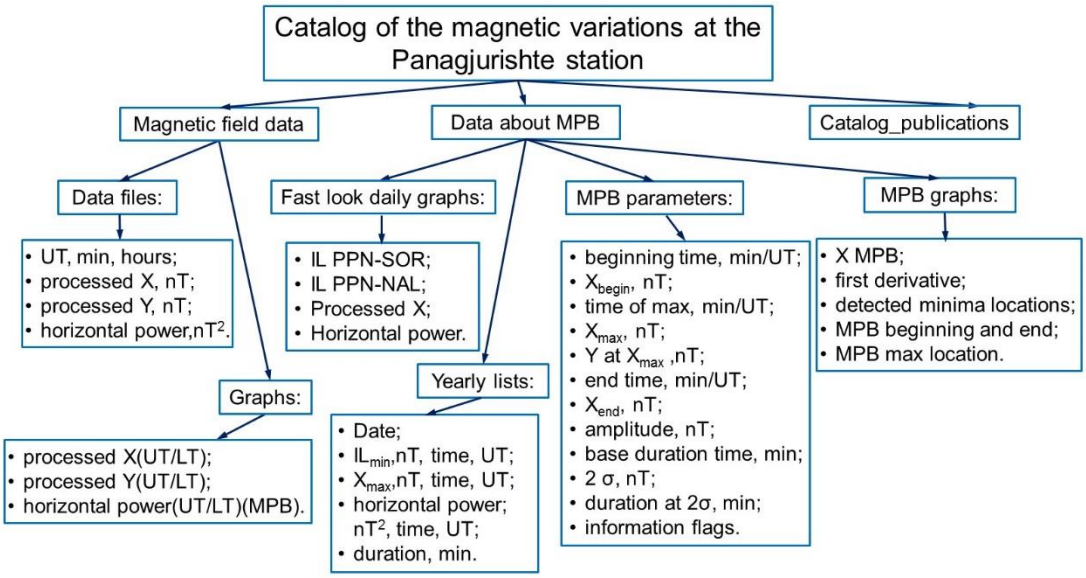

Fig.1. Scheme of the structure of the Catalog of the magnetic variations at the Panagjurishte station.

In the present variant, the catalog comprises three main sections: Magnetic field data, Data about MPB, and Catalog publications. In the section Magnetic field data, the processed X and Y magnetic components and the computed horizontal power of the magnetic field at PAG (subsection Data files), as well as their graphics (subsection Graphs), from 2007 to 2022, are stored. The processing procedure, based on the algorithm by McPherron and Chu [2017] with some new developments is described in Werner et al. (2021a), and Werner et al. (2021b). The second section, Data about MPB, consists of four subsections: Fast look daily graphs, Yearly lists, MPB parameters and MPB graphs. Fast look daily graphs comprises combined graphics, including the IL index, computed for the IMAGE PPN-SOR and PPN-NAL magnetometer station chains, the X-component variations and the horizontal power of the magnetic field. The Yearly lists include data about the cases in which noticeable variations (midlatitude positive

bays - MPB) are observed at the time of the substorms, verified by the IL index. In the sections Fast look daily graphs and Yearly lists are uploaded data and graphs from 2007 to 2022. The present work is intended to develop a processing tool to determine automatically the parameters of the MPB's and to create graphs of the MPB's presenting the minima and maxima illustrating the beginning and the end of the MPB's. The data in the sections MPB parameters and MPB graphs were determined based on the procedure described in section 5 of the paper. They are preliminary in the sense of later procedure improves. Section Catalog publications grants access to the papers, describing the catalog or using data from it for some study.

4. Data used

To determine the basic MPB parameters, data from sections Yearly lists and Magnetic field data of the Catalog have been used. Yearly lists are created for the evening sector (18-24 UT) which corresponds roughly to the night sector in LT at Panagjurishte (21-03 LT). They cover cases, meeting the following conditions: the minimal value of the IL index for the PPN-NAL chain in the negative bay exceeds -200 nT (IL_{min}< -200 nT), the negative bay duration at 2σ is greater than 10 minutes and at PAG station a maximum of the X component near the time of the IL minimum, which is g reater than 5 nT, is obtained. From the Yearly lists, the date of the respective case, the maximum of the X component and the time of this maximum are used. From Magnetic field data section, data about the X variations during the day of the respective case are used.

5. Processing procedure to determine the beginning and end of the MPB

The processing procedure consists of several parts: determination of the extrema locations of the X variations, elaboration of criteria to locate the beginning and end of the MPB, application of these criteria to determine the beginning and end of the MPB, determination of other parameters of MPB and creation of files with numerical data about the parameters of every MPB and graphics with MPB.

5.1. Determination of the minima of the X variations development

The minima determination passes through two steps:

Step 1: Smoothing of the data series of the processed X component by 5 points moving average which enables the elimination of some false extrema originating by noise, and facilitates the further computations.

Step 2: Computing the first derivative to obtain the extrema locations (the crossings of the zero line). The crossing from negative to positive values indicates a minimum, and from positive to negative values – a maximum. The beginning and end of the MPB's coincide with a X minimum before and after the MPB maximum, respectively, which are not always the first ones before or after the maximum. We have implemented a search procedure for a minimum in the time interval from 90 minutes before the moment of the X maximum to 90 minutes after it. This interval ensures the evaluation of the correct locations of the beginning and end of MPB. It was estimated based on tests with several years data from PAG.

5.2. Criteria to locate the beginning and end of MPB

To the beginning and end of a MPB, a minimum before and after the MPB maximum, respectively, is assigned. As this may not be the first minimum before or after the MPB maximum, criteria to choose the minima locating the beginning and end of the MPB have been worked out and applied. The following two criteria were taken.

Criterion (1) concerns two consecutive minima: n^{th} and $(n+1)^{th}$. To assume that the n^{th} minimum is not the beginning or end of MPB, the following condition has to be met: the ratio of the X drop from the maximum to the current, $(n+1)^{th}$ minimum to the X drop to the previous minimum is greater or equal to a constant c:

$$ratio_n = (X_{max}-X_{min,n+1})/(X_{max}-X_{min,n}) \geq c, \quad (1)$$

where X_{max} is the value of the MPB maximum, $X_{min,n}$ is the n^{th} minimum earlier or later from X_{max} time, $X_{min,n+1}$ is the $(n+1)^{th}$ minimum and *c* is a constant. This criterion was introduced by McPherron and Chu (2017). They used c = 1.25. Based on tests of the MPB's registered at PAG, we have chosen 1.20 for the ratio boundary. If condition (1) is met, the n^{th} minimum is not taken as the beginning or end of the MPB, and the check-up continues.

Criterion (2): if criterion (1) is not met, but $X_{min,n} > 0$, then the following check is made: the ratio of the n^{th} minimal value to the maximal one is greater or equal to 0.4:

$$X_{min,n}/X_{max} \geq 0.4 \quad (2)$$

This criterion was accepted based on empirical studies of the PAG data.

If this condition is met, the n^{th} minimum is not taken as the beginning or end of the MPB, and the search continues.

5.3. Determination of the MPB parameters

The following parameters were determined and included in the data file for each detected midlatitude positive bay:

- Beginning time (the time of the MPB beginning, in min., and in hh:mm, UT);
- Xbegin (the value of X at the time of the beginning in nT);
- Time of max (the time of the maximal X value, in min., and in hh:mm, UT);
- Xmax (the maximal value of X in nT);
- Y at Xmax (the value of Y at the time of Xmax in nT);
- Endtime (the time of the MPB end, in min., and in hh:mm, UT);
- Xend (the value of X at the time of the MPB end in nT);
- Amplitude (the amplitude of the MPB, equal to the difference Xmax-Xbegin in nT);
- Base duration time (the MPB duration at the base, equal to endtime-beginning time in min.);
- 2sigma (the 2σ value in nT, computed for the whole day data);
- Duration at 2 sigma (the MPB duration at 2σ level in min.).

5.4. Creation of MPB graphics

For every MPB, a graphic was created. The graphic is designed to give as much as possible visual information about the event. In Fig.2, an example of such graphic is given, for the case of the MPB at 23:05 UT (beginning) on 22.03.2013. In Fig.2, the variations of the X component of the magnetic field are drawn in blue colour. The first derivative of X is drawn by red

continuous line. The 2σ level is given by a dotted black line with inscription "2σ" over it. The MPB maximum location is shown by dark red vertical line. The locations of all detected minima are also shown, by green dotted vertical lines. The locations of the minima of the beginning and end of MPB are given by green continuous vertical lines. The maximum, beginning and end of the MPB are indicated by inscriptions, as well. The time interval, in which the graphic is constructed, covers all detected minima in the time range ±90 min. from the MPB maximum. If this range continue in the next day, data from it are used, too, in the computations and drawings. For example, in the presented case MPB is found 7 min. after midnight, and two more minima are detected after it.

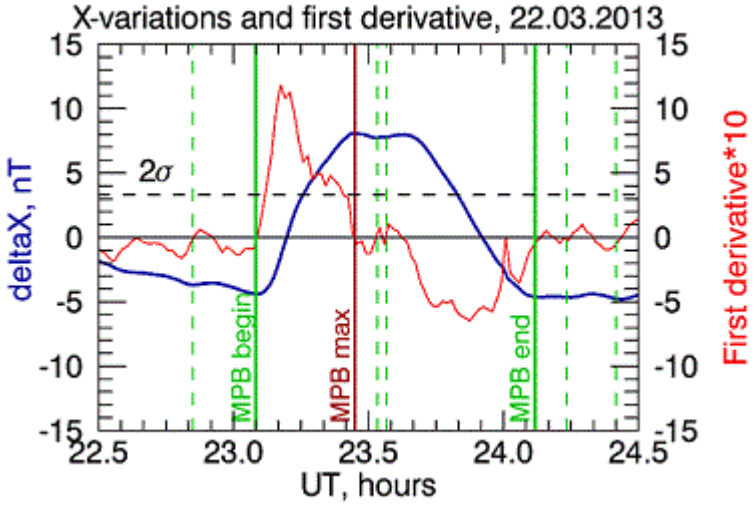

Fig.2. Example of a MPB graphic for a substorm: substorm at 23:05 UT on22.03.2013.

6. Comparison with other authors results

Some of the obtained MPB beginnings were compared with the substorm onsets by Newell and Gjerloev (2011), Forsyth et al. (2015), and Ohtani and Gjerloev (2020), determined from SML index. The results are presented in Table 1. In the consecutive columns the number of the event, the date, the substorm onset times by Newell and Gjerloev (2011), Forsyth et al. (2015), and Ohtani and Gjerloev (2020), the MPB beginning time determined by us, the difference between our result and the results of the other authors in min., and the geomagnetic longitude of the substorm meridian, determined in the cited papers. For more clarity, the results by different authors are given in different colours. The results by Newell and Gjerloev (2011) are written in blue colour, the ones by Forsyth et al. (2015) – in green colour, and the ones by Ohtani and Gjerloev (2020) – in red colour.

From the column next to the last it is seen, that the MPB beginnings at PAG, determined in this work, are close to the substorm onsets. Taking into account, that the substorm meridians are also close to the longitude of Panagjurishte (at maximum distance of about 15°), the results appear reasonable. It is well known, that the beginning of MPB's can be used as indicator of the substorm onset [e.g. Hones et al., 1971; Mende et al., 1972; McPherron, 1972; McPherron and Chu, 2017]. As substorm onset, the time of the earliest beginning of MPB is taken, and the longitude of the station of this MPB is accepted as the substorm meridian. The negative bays in the auroral zone may sometimes precede this onset, and if this is the case, Clauer and McPherron (1974) suppose that the disturbances in the auroral zone, before the onset at

midlatitudes are the appearance of small localized disturbances in the magnetosphere, which have no effect at midlatitudes. In our cases, the reason for later MPB beginning may be also the fact, that the station PAG, although near the substorm meridian, howsoever is located at some degrees apart.

Table 1. Some substorm onset times estimated by SML index, and the MPB beginnigs, obtained in this work.

№	date	Substorm onset time (Newell and Gjerloev, 2011)	Substorm onset time (Forsyth et al., 2015)	Substorm onset time (Ohtani and Gjerloev, 2020)	MPB beginning time (this work)	Δt, min.	GMlon (PAG: ~97° GMlon)
1	02.01.2015	22:11	22:11		22:05	-6	107.29, 114.46
2	04.01.2015	22:36	22:26		22:35	-1, 9	106.15, 106.15
3	05.01.2015	-	21:32		21:21	-11	104.95
4	08.01.2015	-	21:49	21:54	21:54	-5, 0	108.61, 106.46
5	25.01.2015	23:11	23:09	23:05	23:09	-2, 0, 4	100.42, 114.46, 106.46
6	31.01.2015	22:52	22:36		22:41	-11, 5	107.29, 114.46
7	21.02.2015	23:09	-	23:04	23:09	0, 5	109.43, 114.46, 106.21
8	17.03.2015	22:56	-		23:05	9	115.13
9	26.03.2015	23:22	23:16	23:11	23:26	4, 10, 15	95.33, 114.46, 100.42
10	03.04.2015	23:32	23:26		23:19	-13,-7	106.21, 101.82
11	26.12.2015	21:23	20:58		21:03	-20, 5	109.62

More interesting are the cases, when the determined MPB beginning at PAG is some earlier than the sumbtorm onsets, estimated by auroral zone data. We tried to find an explanation of such cases. In most of the cases, the substorms are not isolated. If several consecutive substorms develop, the conditions in the time between them cannot quieten down, and there are magnetic disturbances between the substorm disturbances. In that sort of cases, it is difficult to estimate whether the smaller disturbances between the substorms are the result of localized or global events in the magnetosphere. We assume that the onsets, determined by MPB beginnings, can help to resolve this problem. In Fig.3, an example is given for the event on 03.04.2015, for which the MPB beginning at PAG is earlier than the substorm onsets, determined by Newell and Gjerloev (2011) and Forsyth et al. (2015) (see Table 1). In the left panel of Fig.3, the IL index, computed for the IMAGE PPN-NAL chain, is presented. It is seen, that after 20 UT, two consecutive substorms develop. The examined event is the second one, preceded by a substorm at about 21:12 UT. The blue vertical line shows the sharp decrease of the IL index at 23:32 UT. This time coincides with the substorm onset, determined by Newell and Gjerloev (2011). The red vertical line indicates the obtained MPB beginning time at PAG. It would be difficult to set a boundary at that time, especially by a processing procedure.

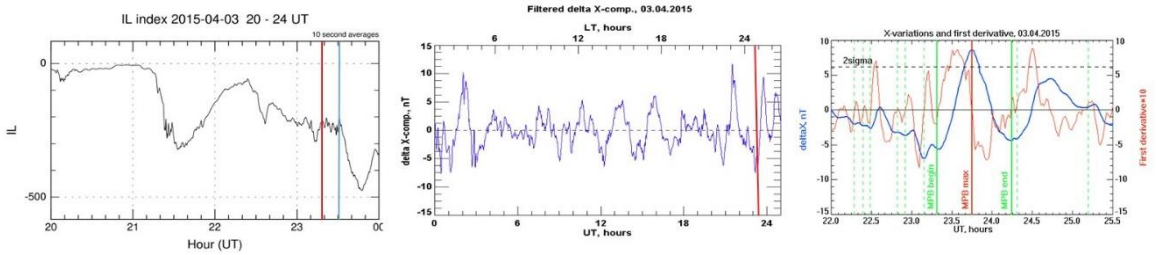

Fig.3. Example of a case when the determined MPB beginning at PAG is earlier than the substorm onsets estimated by auroral zone data. In the left panel, the IL index by the IMAGE PPN-NAL chain is given, the central panel presents the obtained X variations for the day, and the right panel is the MPB graphic for the event.

In the central panel, the variations of the X component on 03.04.2015 are given. The red vertical line points at the MPB beginning for the event under examination. The right panel is the MPB graphic for this case (its appearance is described in section 5.3). The MPB beginning is clearly seen, it coincides with the first minimum before the MPB maximum. Maybe the disturbances after 23:19 UT are provoked by the beginning of the global magnetospheric disturbances.

After McPherron (1972) MPB is a good indicator of the substorm onset, it is coincident with the auroral expansion and less sensitive to interference from small details in the electrojet.

We suppose that the beginning of global magnetospheric disturbances as the substorm current wedge (SCW) is, and respectively the substorm onset, is easily determined by the midlatitude positive bays beginnings.

7. Results and conclusions

- A program tool to compute automatically the parameters of the midlatitude positive bays, registered at Panagjurishte station was developed, including application of criteria to locate the beginning and end minima of the midlatitude X positive bays (MPB);
- The program was tested on different cases of MPB from 2015 and 2013;
- The content and design of the MPB graphs and the MPB parameters files were specified;
- The obtained MPB beginning times are close to the substorm onsets determined from the SML index by Newell and Gjerloev (2011), Forsyth et al. (2015) and Ohtani and Gjerloev (2020). Some of them are later than the substorm onsets, and the others are earlier than the substorm onsets, determined based on the SML index. We suppose that this is due to small scale magnetospheric perturbations, superimposed on or border the global disturbances. We came to the conclusion, that the substorm onsets are more easily and accurately determined by the midlatitude positive bays data from a global or regional set of midlatitude magnetic stations.

The processing of all yearly lists and the addition of the MPB images and MPB data files in the MPB Catalog are forthcoming.

Acknowledgements. The authors are grateful to the creators of the databases IMAGE (http://space.fmi.fi/image/), INTERMAGNET (http://intermagnet.org/), SuperMAG (http://supermag.jhuapl.edu/), and the solar wind large-scale phenomena catalog (http://www.iki.rssi.ru/omni/) for the opportunity to use them in this work.
This study was supported by the National Science Fund of Bulgaria (NSFB) (project number КП-06-Русия/15) and by the RFBR (project number 20-55-18003Болг_а).

References

Akasofu, S.-I. (1964). The development of the auroral substorm, Planet. Space Sci., Vol. 12, No. 4, pp. 273–282, DOI: 10.16/0032-0633(64)90151-5.

Akasofu, S.-I. (1968). Polar and magnetospheric substorms, D,Reidel, Norwell, Mass., DOI: 10.1007/978-94-010-3461-6.

Akasofu, S.-I. (2004). Several `Controversial' Issues on Substorms. Space Sci. Rev., Vol. 113, pp. 1–40, DOI: 10.1023/B:SPAC.0000042938.57710.fb.

Akasofu, S.-I., Chapman, S., Meng, C.-I. (1965). The polar electrojet, J. Atmos. Terr. Phys., Vol. 27, No. 11-12, pp. 1275–1305, DOI: 10.1016/0021-9169(65)90087-5.

Clauer, C.R., McPherron, R.L. (1974). Mapping the local time – universal time development of magnetospheric substorms using midlatitude magnetic observations, J. Geophys. Res., Vol.79, No. 19, pp. 2811-2820, DOI: 10.1029/JA079i019p02811.

Forsyth, C., Rae, I. J., Coxon, J. C., Freeman, M. P., Jackman, C. M., Gjerloev, J., Fazakerley A. N.,, (2015). A New Technique for Determining Substorm Onsets and Phases from Indices of the Electrojet (SOPHIE), J. Geophys. Res. Space Physics, Vol. 120, DOI:10.1002/2015JA021343.

Guineva, V., Werner, R., Lubchich, A., Atanassov, A., Bojilova, R., Raykova, L., Valev, D., Despirak, I., (2021a). Development of a substorms catalog including the MPB observed at Panagjurishte station, Bulgaria, EPJ Web of Conferences, Vol. 254, 01002, DOI: 10.1051/epjconf/202125401002.

Guineva V., Werner, R., Atanassov, A., Bojilova, R., Raykova, L., Valev, D., Despirak, I., Kleimenova, N., (2021). Construction of a catalog of the magnetic variations by data of the Bulgarian station Panagjurishte, Proceedings of the Seventeenth International Scientific conference SES2021, 20-22.10.2021, Sofia, Bulgaria, pp.39-44.

Hones, E.W., Singer, S., Lanzerotti, L.J., Pierson, J.D., Rosenberg, T.J. (1971). Magnetospheric substorm of August 25-26, 1967, J. Geophys. Res., Vokl. 76, No. 13, pp. 2977-3009, DOI: 10.1029/JA076i013p02977

McPherron, R.L., (1972). Substor related changes in the geomagnetic tail: The growth phase, Planet. Space Sci., Vol. 20, No. 9, pp. 1521-1539, DOI: 10.1016/0032-0633(72)90054-2.

McPherron, R. L., Russell, C. T., Aubry, M. (1973). Satellite studies of magnetospheric substorms on August 15, 1968, 9: phenomenological model for substorms, J. Geophys. Res., Vol. 78, No. 16, pp. 3131–3149, DOI: 10.1029/JA078i016p03131.

McPherron, R.L., Chu, X., (2017). The midlatitude positive bay and the MPB index of substorm activity, Space Sci. Rev., Vol. 206, pp. 91-122, DOI: 10.1007/s11214-016-0316-6.

Mende, S.B., Sharp, R.D., Shelley, E.G., Haerendel, G., Hones, E.W., (1972). Coordinated observations of the magnetosphere: The development of a substorm, J. Geophys. Res., Vol. 77, No. 25, pp. 4682-4699, DOI: 10.1029/JA077i025p04682.

Meng, C.-I., Akasofu, S.-I., (1969). A study of polar magnetic substorms. 2. 3-dimensional current system, J. Geophys. Res., Vol. 74, pp. 4035–4053, DOI: 10.1029/JA074i016p04035.

Newell, P. T., Gjerloev, J. W., (2011). Substorm and magnetosphere characteristic scales inferred from the SuperMAG auroral electrojet indices, J. Geophys. Res., Vol. 116, A12232, DOI:10.1029/2011JA016936.

Ohtani, S., Gjerloev, J.W., (2020). Is the substorm current wedge an ensemble of wedgelets?: Revisit to midlatitude positive bays, Journal of Geophysical Research: Space Physics, Vol. 125, No. 9, p. e2020JA027902, DOI:10.1029/2020JA027902.

Rostoker, G., Akasofu, S.-I., Foster, J., Greenwald, R.A., Camide, Y., Kawasaki, K., Lui, A.T.Y., McPherron, R.L., Russell, C.T., (1980). Magnetospheric substorms – definition and signatures, J. Geophys. Res., Vol. 85, No. A4, 1663-1668, DOI: 10.1029/JA085iA04p01663.

Sergeev, V. A., Tsyganenko, N. A., (1980). Magnitosfera Zemli. Nauka, p.174, (in Russian).

Werner, R., Guineva, V., Atanassov, A., Bojilova, R., Raykova, L., Valev, D., Lubchich, A., Despirak, I., (2021a). Calculation of the horizontal power perturbations of the Earth surface magnetic field, Proc. of the Thirteenth Workshop "Solar Influences on the Magnetosphere, Ionosphere and Atmosphere", pp. 159-164, DOI: 10.31401/ws.2021.proc.

Werner, R., Guineva, V., Lubchich, A., Despirak, I., Bojilova, R., Valev, D., Atanassov, A., Raykova, L., (2021b). Determination of power perturbations of the horizontal magnetic field on the Earth surface, Proc. Of the Seventeenth International Scientific Conference Space, Ecology, Safety, pp. 34-38.

Harang Discontinuity, "Polar" Substorms and Subauroral Positive Magnetic Bays

Kleimenova N.G.[1], Despirak I.V.[2], Malysheva L.M.[1], Gromova L.I.[3], Lubchich A.A.[2], Gromov S.V.[3]

[1]Schmidt Institute of Physics of the Earth, RAS, Moscow, Russia; e-mail: kleimen@ifz.ru
[2]Polar Geophysical Institute, Apatity, Russia
[3]Pushkov Institute of Terrestrial Magnetism, Ionosphere, and Radio Wave Propagation, Moscow, Troitsk, Russia

Abstract

The Harang discontinuity (HD) is a longitudinally extended ionospheric signature before the local magnetic midnight of a latitude flow reversal (from westward to eastward). The "polar" substorms are those substorms that recorded at the geomagnetic latitudes above 70° MLAT under the absence of negative magnetic bays at the lower latitudes. Like the "classical" substorms, the "polar" substorms are accompanied by aurora brightening, poleward expansion, substorm current wedge formation. Onsets of "polar" substorms are typically located near 70° MLAT at ~19-23 MLT. This MLT sector is common area of the HD development. The aim of our work is to study a possible relationship between the "polar" substorm onsets and the HD location. Our study of about 250 "polar" substorms, recorded at IMAGE magnetometer profile in 2010-2020, revealed the tendency of these substorms to occur near the HD location, detected by the AMPERE measurements at the 66 ionospheric satellites. It was found that in the case of the "polar substorm", the Harang reversal was observed at higher latitude then during the "classical" substorm. That explained why the strongest amplitudes of lower-latitude positive magnetic bays, accompanied "polar" substorms, are recorded not at middle, but at subauroral latitudes. Near the eastward edge of the HD, we found a magnetic vortex associated with FACs enhancement separated the evening "polar" substorms and after-midnight westward electrojet. Some individual events of the "polar" substorms are discussed.

Keywords: magnetic substorm, interplanetary magnetic field, mid-latitude positive bay

Introduction

The "polar" substorms are the high-latitude magnetic substorms observed at geomagnetic latitudes higher 70° MLAT under the absence of negative magnetic bays at the lower latitudes [Kleimenova et al., 2012, 2023; Despirak et al., 2014, 2022; Safargaleev et al., 2018; 2020]. It is well known that during the low magnetic activity, the magnetic substorms and visible auroras are observed at the geomagnetic latitudes higher than the normal auroral oval location so that the auroral oval becomes contracted and poleward shifted. In earlier publications, these high-latitude substorms have been termed as "substorms on contracted oval" [e.g., Akasofu et al., 1973; Lui et al., 1976], because according to (Lui et al., 1973), the equatorward boundary of the contracted auroral oval is located higher 66◦MLAT.

We found [Kleimenova et al., 2023] that the onset of a "polar" substorm is typically located near 70° MLAT at ~19-23 MLT. Another important phenomenon, namely, the Harang discontinuity [Harang. 1946, Heppner,1972; Kamide and Vickrey, 1983] is often observed at this area.

The Harang discontinuity (HD) represents a narrow latitude-zone between the closely spaced simultaneous westward and eastward electrojets [e.g., Kissinger et al., 2013 and the

references there]. The schematic picture of the Harang discontinuity is given in Figure 1, adopted from [Koskinen and Pulkkinen, 1995].

The Harang discontinuity (HD) is a region of sharp reversal of the evening sector (around 2200-2400 MLT) ionospheric convection. In the terms of auroral electrojets, the Harang discontinuity corresponds to the shear zone where the eastward electrojet (EEJ), equtorward of the shear, and the westward electrojet (WEJ), poleward of the shear, meet. That is, HD is the area latitude separating the positive and negative bay regions. The HD is dynamic in nature. As magnetic activity decreases, it shifts poleward and spreads out in latitudinal width.

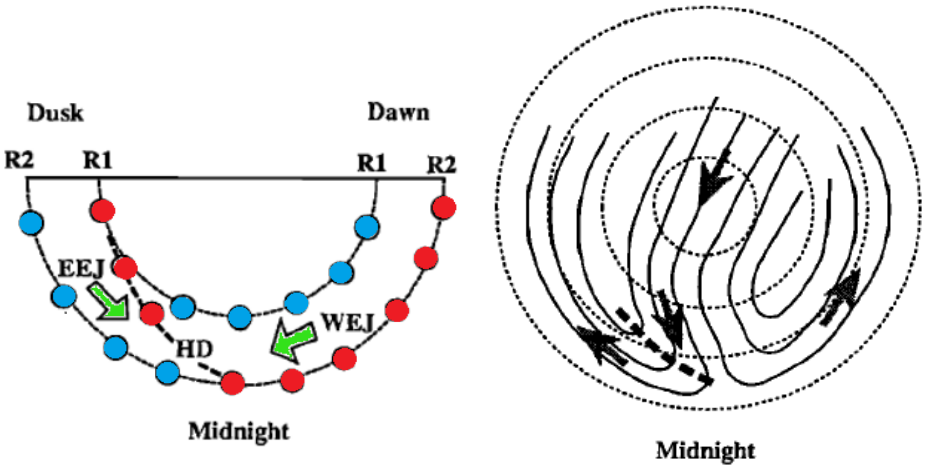

Figure 1. *Schematic picture of the Harang discontinuity (HD) in the nightside northern hemisphere. The HD is indicated by the dashed line. In the left panel the directions of the dominating electrojets are given and in the right panel the green arrows indicate the plasma flow in the velocity shear zone. The R1 and R2 indicate the region 1 and 2 of the Field-aligned currents (FACs); EEJ - eastward electrojet; WEJ, westward electrojet. Adopted from, 1995.*

The aim of our work is to study a possible relationship between the "polar" substorm observed at the Scandinavian IMAGE magnetometer chain (http://space.fmi.fi/image/) and the HD location obtained from AMPERE (*Active Magnetosphere and Planetary Electrodynamics Response Experiment)* magnetic measurements by the simultaneous 66 ionospheric Iridium communication satellites planetary distributed at the altitude of ~780 km (https://ampere.jhuapl.edu) as 10-min averages with the 2 min cadence [e.g., Anderson et al., 2014].

Observations

We selected the 254 "polar" substorm events, recorded at the IMAGE chain during the winter seasons of 2010-2020 and compared their occurrence with the global distribution of the ionospheric electrojets and field-aligned currents (FACs) obtained from the AMPERE project.

It is well known [e.g., McPherron al., 1973, McPherron and Chu, 2018] that at the meridian of a substorm onset, a mid-latitude positive magnetic bay in the *X* magnetic component is observed under near a zero variations in the *Y* component. The positive deviations in the *Y* component occur if the substorm onset meridian is located far eastward, the negative *Y* values occur if the substorm onset is located westward.

As the mid-latitude stations, we used Borok station (BOX, 54.5° MLAT) located in near the IMAGE meridian and Irkutsk station (IRT, 47.8° MAT) located 65° eastward (https://intermagnet.org/#services).

Here we show the results of the analysis of the three selected events observations: 28 January 2020 (Figure 2), 5 December 2020 (Figure 3), and 28 December 2020 (Figure 4).

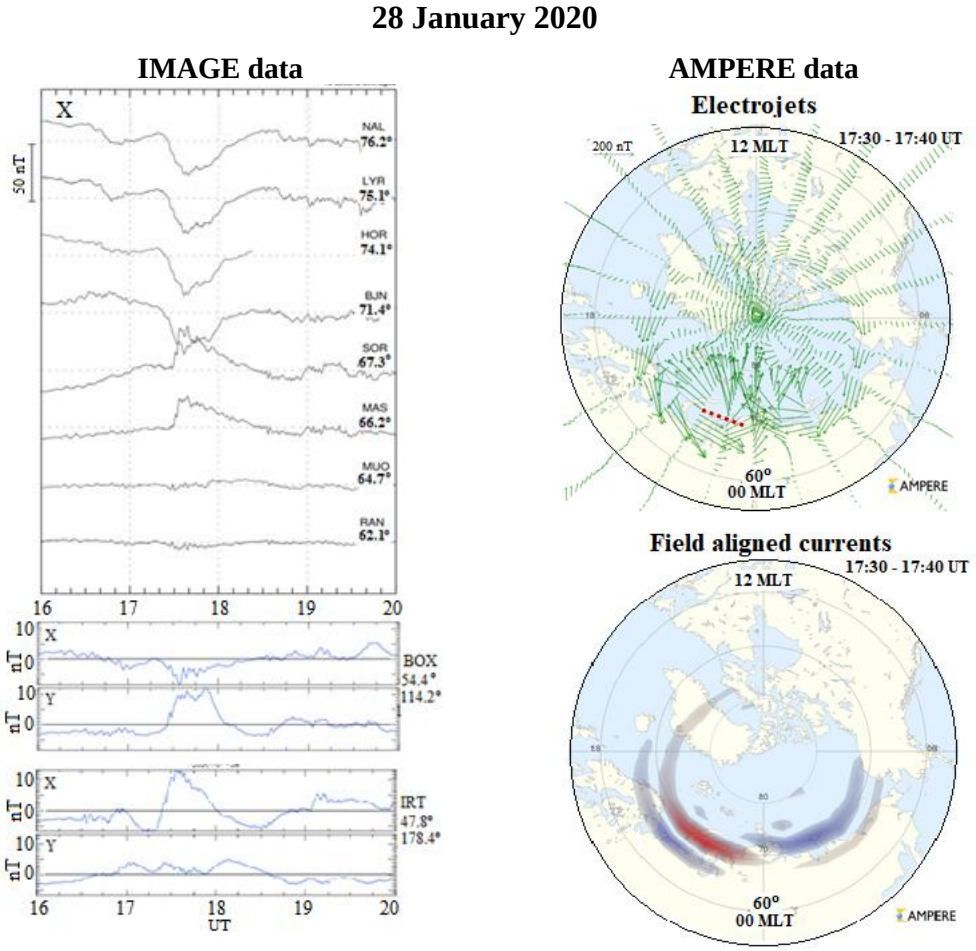

***Figure 2**. Magnetograms from polar- and mid-latitude stations and AMPERE electrojets and FAC data on 28 January 2020*

As one can see in Figure 2, the AMPERE maps of 28 January 2020 demonstrate two vortices in the magnetic field near the ends of the enhanced downward (blue) and upward (red) field aligned currents (FACs).

At the mid-latitude BOX station, the amplitude of the magnetic *X* component was significantly less than the amplitude of the *Y* component. It indicates that this station was located far westward of the meridian of the onset of the "polar" substorm. The AMPERE maps confirm this.

At the mid-latitude IRT station, the amplitude of the magnetic *X* component was much stronger than the amplitude of the *Y* component. It indicates that this station was located near the meridian of the onset of the "polar" substorm. It is seen on the AMPERE maps as well.

The AMPERE maps on 5 December 2020, shown in Figure 3, demonstrate two vortices in the magnetic field near the ends of the enhanced downward (blue) and upward (red) field aligned currents (FACs).

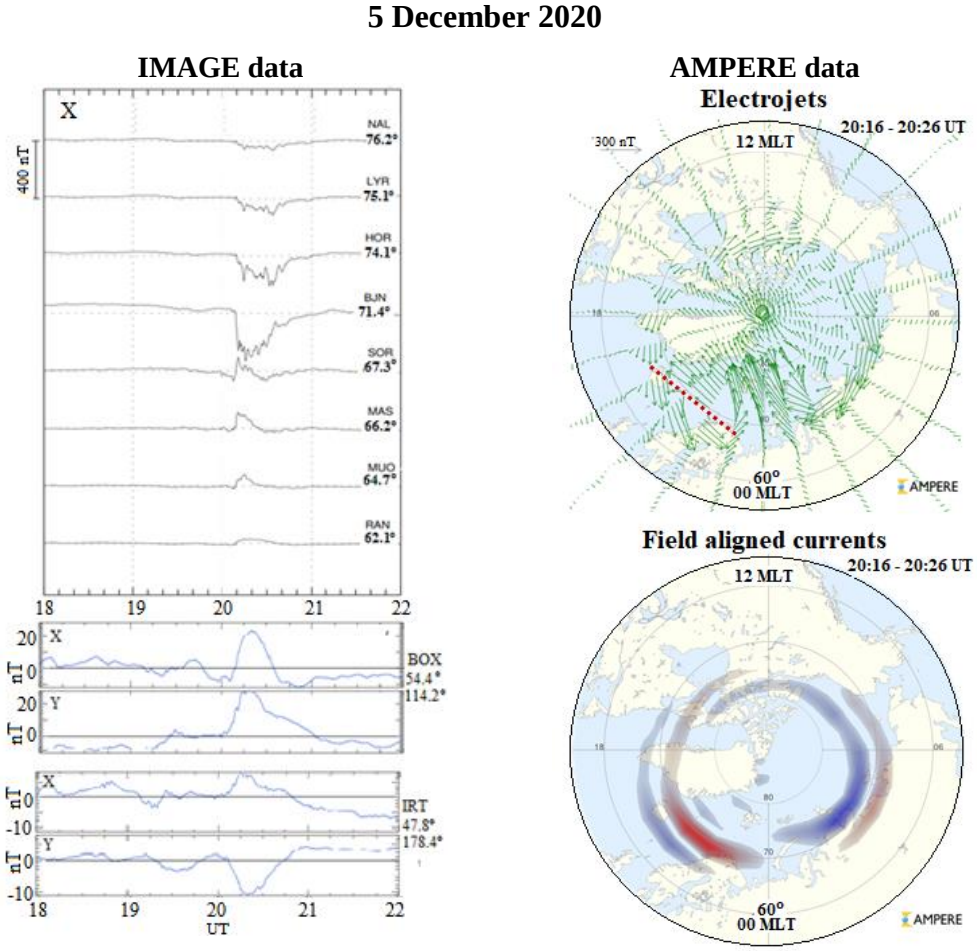

Figure 3. *Magnetograms from polar- and mid-latitude stations and AMPERE electrojets and FAC data on 5 December 2020*

At the mid-latitude BOX station, the amplitude of the magnetic *X* component was similar than the amplitude of the *Y* component, which was positive. It indicates that this station was located away from the meridian of the onset of the "polar" substorm, namely westward. It is seen at the AMPERE maps too.

At the mid-latitude IRT station, the amplitude of the magnetic *X* component was less than the amplitude of the Y component, which was negative. It indicates that this station was located far eastward the meridian of the onset of the "polar" substorm. The AMPERE maps confirm this. The meridian of the polar substorm onset was located between the BOX and IRT stations**.**

Figure 4 shows the AMPERE maps of 28 December 2020. They demonstrate two vortices in the magnetic field near the ends of the enhanced downward (blue) and upward (red) field aligned currents (FACs).

At the mid-latitude BOX station, the amplitude of the magnetic *X* component was much stronger than the amplitude of the *Y* component. It indicates that this station was located near the meridian of the onset of the "polar" substorm. It is seen on the AMPERE maps too. At the mid-latitude IRT station, the amplitude of the magnetic *X* component was significantly less than the amplitude of the *Y* component, which was negative. It indicates that this station was located far eastward of the meridian of the onset of the "polar" substorm. The AMPERE maps confirm this.

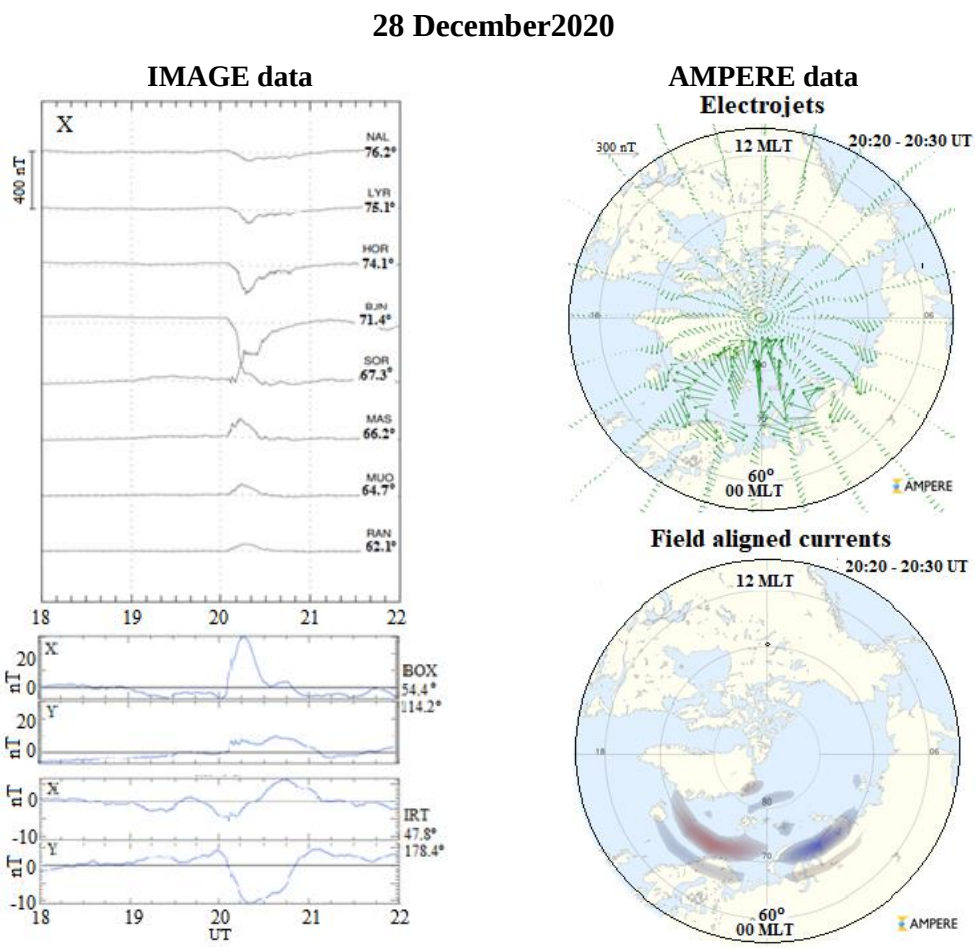

Figure 4*. Magnetograms from polar- and mid-latitude stations and AMPERE electrojets and FAC data on 28 December 2020*

Results

- We found that all studied “polar” substorm events were associated with the Harang discontinuity observed by the ionospheric AMPERE satellites.
- The “polar” substorms were recorded at the ground-based IMAGE magnetometer chain poleward the Harang discontinuity location.
- The onset of the “polar” substorms was located in the vicinity the latitude of the poleward boundary of the Harang discontinuity.
- In most cases, “polar” substorms were accompanied by the development of magnetic vortices indicating the appearance of enhanced field-aligned currents at the edges of the eastward and westward electrojets.
- - The Harang discontinuity started usually between the center location of these vortexes.

Acknowledgments

This study was partly supported by the RFBR (project number 20-55-18003) and National Science Fund of Bulgaria (NSFB) (project number КП-06-Русия/15).

References

Akasofu, S.-l., Perreault, P.D., Yasuhara, F., Meng, C.-I. (1973). Auroral substorms and the interplanetary magnetic field. J. Geophys. Res., Vol 78 (31), pp. 7490-7508. https://doi.org/10.1029/JA078i031p07490

Anderson, B.J., Korth, H., Waters, C.L., Green, D.L. et al. (2014). Development of large-scale Birkeland currents determined from the Active Magnetosphere and Planetary Electrodynamics Response Experiment, Geophys. Res. Lett., Vol 41, No 9, pp. 3017-3015, https://doi.org/10.1002/2014GL059941

Despirak, I.V., Lyubchich, A.A., Kleimenova, N.G. (2014). Polar and high latitude substorms and solar wind conditions, Geomagn. Aeron., Vol 54, No 5, pp. 575-582. https://doi.org/10.1134/S0016793214050041

Despirak, I.V., Kleimenova, N.G., Lubchich, A.A., Malysheva, L.M., Gromova L.I., Roldugin A.V, Kozelov, B.V. (2022). Magnetic Substorms and Auroras at the Polar Latitudes of Spitsbergen: Events of December 17, 2012, Bulletin of the Russian Academy of Sciences: Physics, Vol 86, No 3, pp. 266–274. https://doi.org/0.3103/S1062873822030091

Harang, L. (1946). The mean field of disturbance of polar geomagnetic storms, Terr. Magn. Atmos. Electr., Vol 51. https://doi.org/10.1029/TE051i003p00353

Heppner, J. P. (1972). The Harang discontinuity in auroral belt ionospheric currents, Geophys. Publ., Vol 29, pp. 105–119.

Kamide, Y., Vickrey, J.F. (1983). Variability of the Harang discontinuity as observed by the Chatanika radar and the IMS Alaska magnetometer chain, Geophys. Res. Lett., Vol 10, pp. 159-1962.

Kissinger, J., Wilder, F.D., McPherron, R.L., Hsu, T.-S., Baker, J.B.H., Kepko, L. (2013). Statistical occurrence and dynamics of the Harang discontinuity during steady magnetospheric convection, J. Geophys. Res. Space Physics, Vol 118, pp. 5127–5135. https://doi.org/10.1002/jgra.50503.

Kleimenova, N.G., Antonova, E.E., Kozyreva, O.V., Malysheva L.M., Kornilova T.A., Kornilov I.A. (2012). Wave structure of magnetic substorms at high latitudes, Geomagn. Aeron., Vol 52, No 6, pp. 746-754. https://doi.org/10.1134/S0016793212060059

Kleimenova, N.G., Despirak, I.V., Malysheva, L.M., Gromova, L.I., Lubchich, A.A., Roldugin, A.V., Gromov, S.V. Substorms on a contracted auroral oval, J. Atmos. Solar-Terr. Phys 2023, Vol 245, pp. 106049-106062. https://doi.org/10.1016/j.jastp.2023.106049

Koskinen, H.E.J., Pulkkinen, T. (1995) Midnight velocity shear zone and the concept of Harang discontinuity, J. Geophys. Res., Vol 100, pp. 9539-9547.

Lui, A.T.Y., Perreault, P.D., Akasofu, S.-I., Anger, C.D. (1973). The diffuse aurora. Planet. Space Sci. Vol 21. No 5, pp. 857–861. https://doi.org/10.1016/0032-0633(73)90102-5.

Lui, A.T.Y., Akasofu, S.-I., Hones, E.W. Jr., Bame, S.J., McIlwain, C.E. Observation of the plasma sheet during a contracted oval substorm in the prolonged quiet period (1976). J. Geophys. Res. Vol 81, No 7, pp. 1415–1419. https://doi.org/10.1029/JA081i007p01415

McPherron, R.L., Russell, C.T., Aubry, M.P. (1973), Satellite studies of magnetospheric substorms on August 15, 1968: 9. Phenomenological model for substorms, J. Geophys. Res., Vol 78, No 16, pp. 3131-3149, https://doi.org/10.1029/JA078i016p03131

McPherron, R. L., & Chu, X. (2018). The midlatitude positive bay index and the statistics of substorm occurrence. Journal of Geophysical Research: Space Physics, Vol 123, No 4, pp. 2831–2850. https://doi.org/10.1002/2017JA024766

Safargaleev, V.V., Mitrofanov, V.M., Kozlovsky, A.E. (2018). Complex analysis of the polar substorm based on magnetic, optical and radar observations near Spitsbergen. Geomagn. Aeron., Vol 58, No 4, pp. 793–808. https://doi.org/10.1134/S0016793218040151.

Safargaleev, V.V, Kozlovsky, A.E., Mitrofanov, V.M. (2020). Polar substorm on 7 December 2015: pre onset phenomena and features of auroral breakup, Ann. Geophys., Vol 38, No 4, pp. 901-917. https://doi.org/10.5194/angeo-38-901-2020

Intense Mid-Latitude Magnetic Disturbances and Solar Wind Conditions

Lubchich A.A.[1], Despirak I.V.[1], Werner R.[2]

[1]Polar Geophysical Institute, Apatity, Russia, e-mail: lubchich@pgia.ru
[2]Space Research and Technology Institute, Bulgarian Academy of Sciences, Stara Zagora Department, Bulgaria

Abstract

The purpose of this work is to find out the solar wind conditions under which high values of magnetic disturbances at the middle latitudes are observed. The intensity of magnetic disturbances was determined according Midlatitude Positive Bay (MPB) index proposed by McPherron and Chu, 2017. The list of the MPB index dating back to 1991 and can be found in the supplementary information for the online version of McPherron and Chu, 2018. Calculations of MPB index is based on data from 41 stations in the northern and southern hemispheres (from 20° to 52° magnetic latitude). In additional, for several selected events, we analyzed the variations of horizontal component of magnetic field at the mid-latitudes stations (including the Panagjurishte station in Bulgaria). The study of the magnetic disturbances was based on the data from the magnetometer networks SuperMAG, INTERMAGNET and IMAGE. The solar wind conditions before the substorms were determined using the CDAWeb OMNI database (http://cdaweb.gsfc.nasa.gov/), the solar wind structures were determined according to the catalog of large-scale solar wind phenomena (ftp://ftp.iki.rssi.ru/omni/). It was found the dependences of occurrence of high values of MPB index on solar wind parameters (components of the interplanetary magnetic field, solar wind velocity, density, dynamic pressure etc.). Several examples of very intensive events are discussed.

Keywords: solar wind, magnetic substorm, Mid-latitude Positive Bay (MPB-index)

Introduction

Our work is devoted to the study of intense mid-latitude magnetic bays appearance in dependence of solar wind and IMF conditions as well as on the magnetic storms and substorms development. It is known that the substorm development associated with substorm current wedge (SCW) formation [e.g., McPherron al., 1973; Sergeev et al., 2011]. The SWC produces a distinctive pattern of changes in the ground-based magnetic field components at the mid-latitudes: X- component of the magnetic field is positive and symmetric about the central meridian of the SCW, while the Y component is antisymmetric [Kepko et al., 2015]. The positive deviations in the Y- component occur if the substorm onset meridian is located far eastward, the negative Y values occur if the substorm onset is located westward [e.g., McPherron al., 1973; McPherron and Chu, 2018]. Recently, McPherron and Chu have introduced a new index - the Mid-latitude Positive Bay index (MPB), which characterized the intensity of SCW [McPherron and Chu, 2017].The list of the MPB index dating back to 1982 and can be found in the supplementary information for the online version of McPherron and Chu, 2018. In our work we use the list of the MPB index kindly provided by Chu [Chu et al., 2015]. Calculations of MPB index is based on data from 41 stations in the northern and southern hemispheres (from 20° to 52° magnetic latitude). Werner et al. (2021) proposed a modification of the calculation procedure, adding the data from the Bulgarian station Panagjurishte (PAG) (42.5°N, 24.2°E, ~37° GMLat; ~97º GMLon). Figure 1 shown the example of the daily MPB-index on 28 August 2018, the horizontal line marks the values of MPB-X= 10 000 nT^2 (i.e., intense variations in the X-component, ΔX = 100 nT).

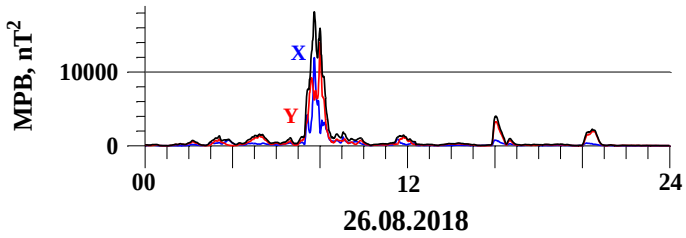

***Figure 1**. MPB-index for August 28, 2018: MPB calculated only on X component (MPB-X) marked by blue line, only on Y- component (MPB-Y) – by red line, on X and Y components - by black line.*

Data

The solar wind and IMF parameters are taken from OMNI database https://cdaweb.gsfc.nasa.gov/. Global magnetometer networks SuperMAG and IMAGE data were used for determination of the substorm development as at the midlatitudes well as at auroral latitudes. SML- index is taken from http://supermag.jhuapl.edu/. The IMAGE magnetometer data are taken from http://space.fmi.fi/image/. MPB index is taken from the Chu list [Chu et al., 2015]. It includes minute values of squared X and Y horizontal field variations and their sum, equal to total power in horizontal field variations, from 1991-01-01/00:00 to 2019-12-31/23:59.

Results

1) The relationship between extreme values of the MPB index and magnetic storms

For this purpose, we selected all events in the period from 1991 to 2019, when MPB-X > 10 000 nT^2 (i.e., ΔX > 100 nT). MPB-X values were taken so that events developed at close longitudes. For comparison, the Table of superstorms was used (superstorm criterion: Dst_{min} < -250 nT) [Meng et al., 2019]. We added the last column to this table, which indicates the maximum value of the MPB index, the date (month, day) and the time of the event.

1	2	3	4	5	6	7	8
Solar cycle	Dst_{min} time (yyyy-mm-dd UT)	Dst_{min} (nT)	SYM-Hmin/time (nT)/(mm-dd UT)	SI+/time (nT)/(mm-dd UT)	Type	Interplanetary Case	MPB (nT^2)/(mm-dd UT)
SC23	2003-11-20 20:30	-422	-490/11-20 18:17	49/11-20 08:06	III	Sheath+MC Bxz-	~69 000/11-20 17:03
SC23	2001-03-31 08:30	-387	-437/03-31 08:06	129/03-31 01:00	I	Sheath+MC Bxzc-	~26 000/03:31 06:09 ~21 000/03:31 15:53
SC23	2003-10-30 22:30	-383	-432/10-30 22:55	76/10-30 20:08	III	Sheath	~46 000/10-30 21:35
SC23	2004-11-08 06:30	-374	-394/11-08 05:55	92/11-07 19:20	I	Sheath+MC Bxz-	~27 000/11-08 01:19 [MPB X~9 300]
SC22	1991-11-09 01:30	-354	-402/11-09 01:32	49/11-08 13:15	I	Unknown	~575000/11-08 22:20
SC23	2003-10-30 00:30	-353	-391/10-30 01:48	81/10-29 06:14	III	Sheath+MC Bxz-	~69000/10-29 19:56
SC23	2000-07-16 00:30	-301	-347/07-15 21:54	93/07-15 15:04	II	MC Bxz-	~23000/07-15 21:48
SC22	1991-03-25 00:30	-298	-337/03-25 03:41	118/03-24 03:55	II	Unknown	~105000/03-24 21:33 ~24000/03-24 04:06
SC23	2001-11-06 00:30	-292	-320/11-06 04:06	88/11-06 01:54	II	PICME+sheath	~11000/11-06 02:05 [MPB X~6 300]
SC22	1992-05-10 14:30	-288	-363/05-10 14:15	81/05-09 20:02	II	Likely sheath+MC	~28000/05-10 18:29
SC23	2000-04-07 00:30	-288	-320/04-07 00:09	46/04-06 16:45	III	Sheath	~60000/04-06 23:27
SC23	2001-04-11 23:30	-271	-280/04-11 23:57	26/04-11 15:53	III	Sheath	~24000/04-11 21:37 ~23000/04-12 00:16
SC23	2004-11-10 10:30	-263	-282/11-10 09:31	46/11-09 18:51	III	Sheath+MC Bxz+	~31000/11-09 20:32
SC22	1991-10-29 07:30	-254	-284/10-29 08:02	51/10-28 11:03	III	Sheath+MC Bxz+	~223000/10-28 16:06

***Table 1**. Table of superstorms (was taken from Meng et al.,2019) and added MPB >10 000 nT^2.*

It is seen that most of extreme MPB events took place during superstorms. In addition, it turned out that the remaining events of extreme MPB were also observed during magnetic storms (Dst < -100 nT). This result shown in the Table 2, the format of Table 2 is the same of Table 1. The first storm (Dst_{min} = -247 nT) is disputable, someone also relates it to superstorms.

Solar cycle	**Dst_{min} time (yyyy-mm-dd UT)**	**Dst_{min} (nT)**	**SYM-Hmin/time (nT)/(mm-dd UT)**	**SI+/time (nT)/(mm-dd UT)**	**Type**	**Interplanetary Case**	MPB (nT^2)/(mm-dd UT)
SC23	*2005-05-15 08:30	-247	-305/05-15 08:20	62/05-15 02:41	I	Sheath+MC	~38 000/05-15 08:50
SC22	1991-06-05 19:30	-223	-238/06-05 16:56	30/06-04 15:39	II		~50 000/06-05 17:14
SC23	2001-11-24 16:30	-221	-234/11-24 12:37	86/11-24 06:04	III	Sheath(M)+ICME	~49 000/10-30 07:15
SC22	1991-11-01 23:30	-196	-200/11-01 19:37 20:22	21/11-01 12:00	II		~36 000/11-01 20:30
SC22	1991-07-13 15:30	-183	-238/07-13 15:42	47/07-13 08:26	I		~42 000/07-13 16:20
SC23	2002-10-01 16:30	-176	-154/10-01 12:53	26/09-30 8:26 (?)	III	Sheath+MC+CIR	~18 000/10-01 16:28
SC24	2018-08-26 06:30	-175	-206/08-26 07:11	11/08-25 12:31 (?)	I	MC+CIR	~18 000/08-26 07:44
SC22	1992-02-26 22:00	-174	-167/02-26 22:31	35/02-26 17:02	I		~61 000/02-26 19:44
SC22	1992-02-08 16:30	-114	-126/02-08 15:18	33/02-08 14:32	I		~41 000/02-08 15:35

***Table 2**. Table of magnetic storms with Dst < -100 nT and extreme MPB events.*

2) MPB index distribution and their correlations with geomagnetic indexes

To conduct a statistical analysis of the MPB index, we took the entire data series for the MPB from 1991 to 2019, regardless of its value. During the same time, one-minute values of geomagnetic indices for different latitudes were taken: low-latitudes index SYM-H, mid-latitudes index ASY-H; auroral index AL, universal index SML and high-latitudes index PC(N). We carried out a statistical analysis of these data series and obtained the distributions of the MPB, SML, AL, SYM-H, ASY-H, and their possible correlations, some results are presented in Figure 2.

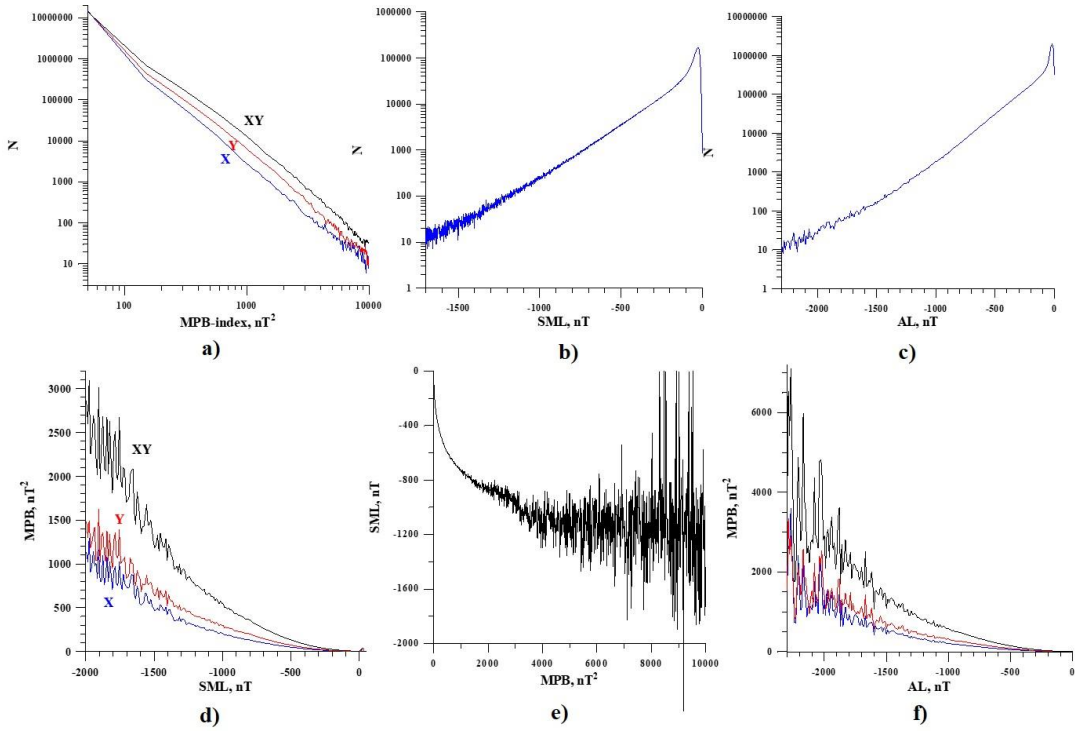

***Figure 2.** Distributions of the MPB (a), SML (b), AL (c); dependence of MPB on SML (d) and vice versa (e), on AL (f).*

It is seen that the distributions of geomagnetic indices, as well as most SW and IMF parameters (Figure 3 and 4) are far from normal (Gaussian) distributions. Therefore, if for two quantities A and B we construct the dependences A(B) and B(A), then they, in the general case, will not coincide and may even differ greatly. For example, this can be seen in Figure 2d and 2e, the dependences of the MPB(SML) and SML(MPB). Recently, Werner et al. (2023), having analyzed the distributions of the geomagnetic IL index for the interval 2007–2020, also found that this distribution is not Gaussian, but is well described by exponential functions, in particular, by the Weibull distribution.

From Figure 2 it is seen that the more disturbed the geomagnetic conditions, the higher the MPB index. So, the MPB index strongly depends on the value of SML. As SML decreases from 0 to -2000 nT, the MPB increases from 0 to about 2500 nT^2. There is observed also an inverse relationship: with an increase of MPB-index from 0 to 3000 nT^2, the SML-index decreases from the maximum value to approximately -900 nT, with a further increase in MPB, SML decreases slightly (but in this region there are few events).

It should be noted that the dependence of the MPB on all geomagnetic indices, which is similar in form, can be explained as follows: in the analyzed time interval, all indices are approximately related by a linear dependence:

AL ≈ 0.81 * SML -26.5;

ASY-H ≈ -0.086 * SML + 3.14;

SYM-H ≈ 0.073 * SML + 1.31;

PC(N) ≈ -0.0051 * SML + 0.66.

3) MPB index correlations with the solar wind and IMF parameters

To conduct the analysis of the correlations between the MPB index and different solar wind parameters, the entire data series for the MPB-index and one-minute values of solar wind and IMF parameters were taken: the magnitude of the IMF and its components, solar wind velocity and its components, density, temperature, dynamic pressure etc.

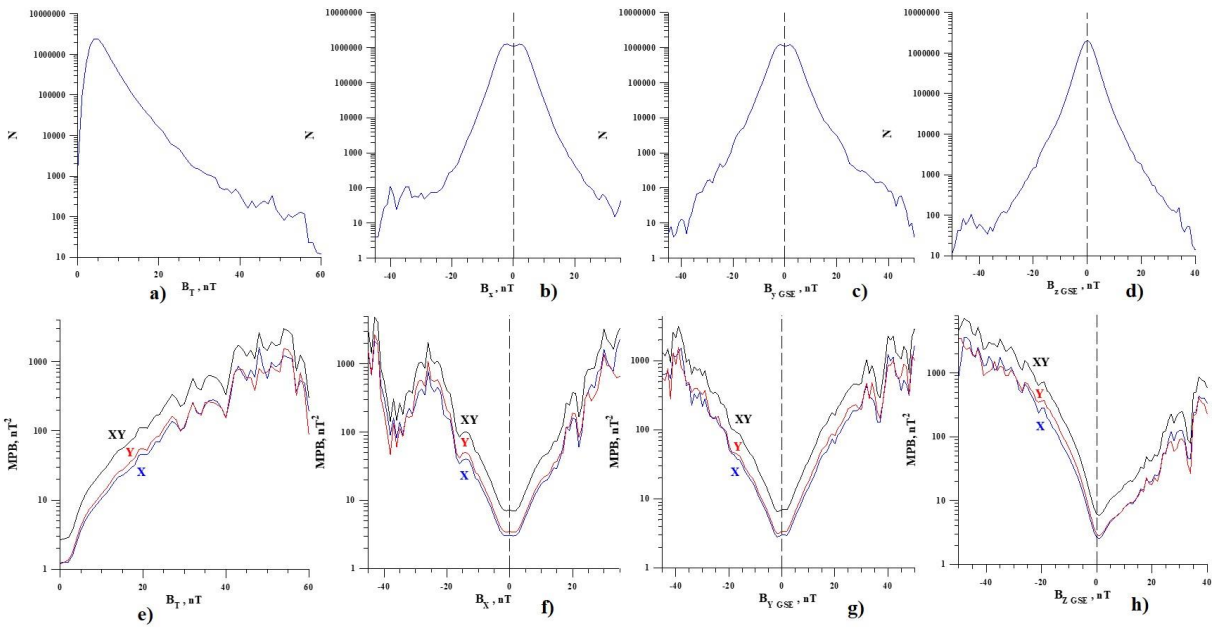

Figure 3*. Distributions of the magnitude of the IMF and its components- B_T (a), B_X (b), B_Y (c), B_Z (d); dependence of MPB on B_T (e), B_X (f), B_Y (g) and B_Z (h).*

We carried out a statistical analysis of these data series and obtained the distributions of the parameters of the solar wind and IMF and all possible correlations, some results are presented in Figures 3 and 4.

At the top panels of Figure 3 (a, b, c, d) shown the distributions of modulus of the IMF (B_T) and all IMF components (B_X, B_Y, B_Z). It is seen that the distributions of all IMF components are more or less symmetrical with respect to zero values. The distribution of the IMF modulus (B_T) reaches a maximum at 4–5 nT, then gradually decreases. At the bottom panels of Figure 3 (e, f, g, h) shown the dependences of the MPB index on the interplanetary magnetic field (IMF). The MPB index grows with the growth of the IMF modulus. The MPB index also grows with an increase in the modulus of the IMF components. For the B_X and B_Y components of the IMF, the dependence is more or less symmetrical. For the B_Z-component, as expected, the dependence is asymmetric, because the MPB index is more dependent on the negative values of the B_Z.

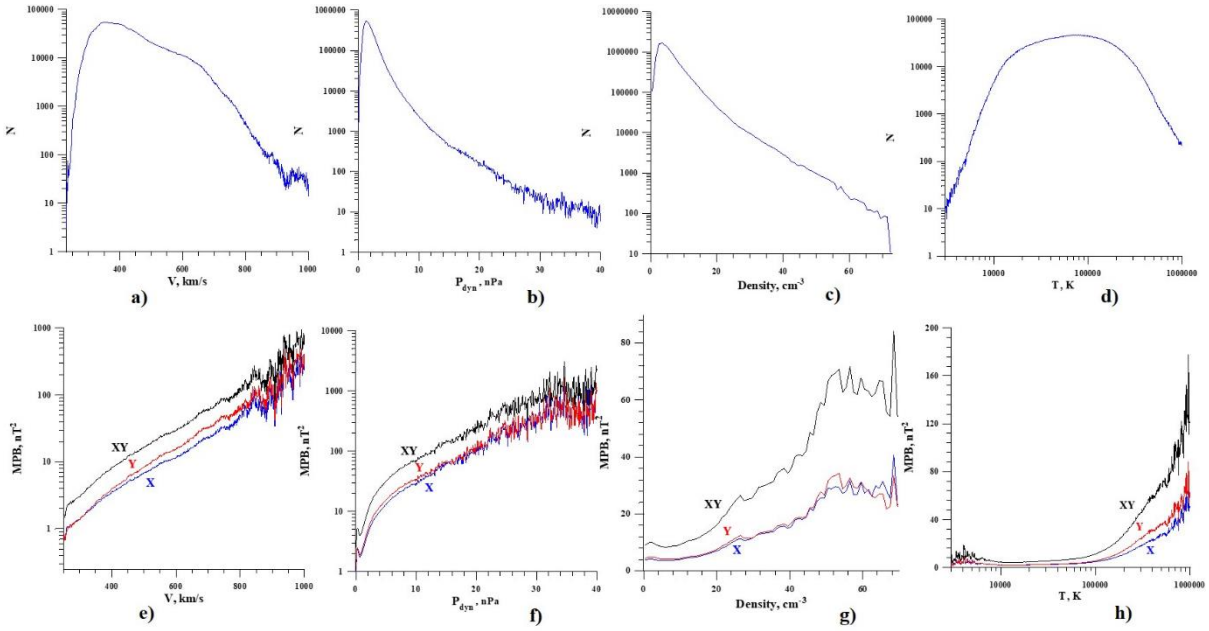

Figure 4*. Distributions of the V (a), P_{dyn} (b), density (c), T (d); dependence of MPB on V (e), P_{dyn}(f), density (g) and T (h)*

On the Figure 4 shown the distributions of solar wind parameters and their dependences of the MPB index, the format of Figure 4 is the same as Figure 3. It is seen that the distribution of the solar wind velocity increases sharply with increasing V, reaches the maximum at ~ 350 km/s, then gradually decreases. The distribution of temperature (in the picture was presented ln(T)) is more or less symmetrical with respect to value T = 70000 K. The distributions of the density and the dynamic pressure initially increase sharply, reach maximums at N~ 3.5 cm^{-3} and P_{dyn} ~1.3 nPa, and then gradually decrease.

At the bottom panels of Figure 4 (e, f, g, h) shown the dependences of the MPB index on the solar wind velocity V, dynamic pressure P_{dyn}, density N and temperature T. It is seen that the MPB index grows almost exponentially with the grow of the solar wind velocity V. That is, the dependence of the ln(MPB) on module of the velocity V is close to linear. An almost similar dependence on the solar wind dynamic pressure (the dependence of the ln(MPB) on the P_{dyn}) is close to linear by P_{dyn} > 6 nPa. The MPB index also strongly depends on the electric field of the solar wind (not shown at the Figure 4).

Although the MPB increases with an increase of the solar wind density and solar wind temperature T, these dependences are very weak (i.e. when these values change, the MPB index changes in a small interval).

Summary

The one-minute values of the Midlatitude Positive Bay index for 19 years, from 1991 to 2019, were analyzed. It was found that:

- All extremely high values of the MPB index (MPB > 10 000 nT^2) were observed during magnetic storms with Dst_{min} < -100 nT.
- All superstorms (Dst_{min} < -250 nT) were accompanied by extremely high values of the MPB index.
- The MPB index increases with increasing in the level of geomagnetic activity. The higher the -SML, -SYM-H, -ASY-H, -AL, AE index or the absolute value of PC(N)-index, the on average higher the MPB index.
- The MPB index increases with increasing the IMF magnitude and the absolute values of interplanetary magnetic field components.
- The MPB index rapidly increases with increasing the solar wind speed and dynamic pressure. The MPB index is less dependent on the density and temperature of the solar wind.

Acknowledgments

This study was supported by the RFBR (project number 20-55-18003) and National Science Fund of Bulgaria (NSFB) (project number КП-06-Русия/15).

References

Chu, X., McPherron, R.L., Hsu, T.S., Angelopoulos, V. (2015). Solar cycle dependence of substorm occurrence and duration: Implications for onset, J. Geophys. Res.: Space Physics, Vol. 120, pp. 2808 - 2818, DOI: 10.1002/2015JA021104.

Kepko, L, McPherron, R.L., Amm, O., Apatenkov, S., Baumjohann, W., Birn, J., Lester, M., Nakamura, R., Pulkkinen, T.I., Sergeev, V.A. (2015). Substorm Current Wedge Revisited, Space Sci. Rev., Vol. 190, pp. 1–46, https://doi.org/10.1007/s11214-014-0124-9

McPherron, R.L., Chu, X. (2018). The midlatitude positive bay index and the statistics of substorm occurrence, J. Geophys. Res.: Space Physics, Vol. 123, No. 4, pp. 2831–2850, https://doi.org/10.1002/2017JA024766

McPherron, R.L., Chu, X., (2017). The midlatitude positive bay and the MPB index of substorm activity, Space Sci. Rev., Vol. 206(1–4), pp. 91–122.

McPherron, R.L., Russell, C.T., Aubry, M.P. (1973). Satellite studies of magnetospheric substorms on August 15, 1968: 9. Phenomenological model for substorms, J. Geophys. Res., Vol. 78, No. 16, pp. 3131-3149, https://doi.org/10.1029/JA078i016p03131

Meng, X., Tsurutani, B.T., Mannucci, A.J. (2019). The Solar and Interplanetary Causes of Superstorms (Minimum Dst ≤ −250 nT) During the Space Age. J. Geophys. Res.: Space Physics, Vol. 124, No. 6, pp. 3926-3948, https://doi.org/10.1029/2018JA026425

Sergeev, V.A., Angelopoulos, V., Kubyshkina, M., Donovan, E., Zhou, X.-Z., Runov, A., Singer, H., McFadden, J., Nakamura, R. (2011). Substorm growth and expansion onset as observed with ideal ground-spacecraft THEMIS coverage, J. Geophys. Res., Vol. 116, A00I2, https://doi.org/10.1029/2010JA015689

Werner, R., Guineva, V., Atanassov, A., Bojilova, R., Raykova, L., Valev, D., Lubchich, A., Despirak, I. (2021). Calculation of the horizontal power perturbations of the Earth surface magnetic field, Proceedings of the Thirteenth Workshop “Solar Influences on the Magnetosphere, Ionosphere and Atmosphere”, September, 2021, Book of Proceedings, pp. 159-165, DOI: 10.31401/WS.2021.proc.

Werner, R., Guineva, V., Despirak, I.V., Lubchich, A.A., Setsko, P.V., Atanassov, A., Bojilova, R., Raykova, L. Valev, D. (2023). Statistical Studies of Auroral Activity and Perturbations of the Geomagnetic Field at MiddleLatitudes, Geomagnetism and Aeronomy, Vol. 63, No. 4, pp. 473–485, DOI: 10.1134/S0016793223600303.

Temporal Offsets between Solar Flare Index and Cosmic, Geomagnetic, and Interplanetary Indicators during Solar Cycle 24

Özgüç A.[1], Kilcik A.[2]

[1]Kandilli Observatory and Earthquake Research Institute, Bogazici University, 34684 Istanbul, Turkey; ozguc@boun.edu.tr

[2]Department of Space Science and Technologies, Akdeniz University Faculty of Science, 07058, Antalya, Turkey; alikilcik@akdeniz.edu.tr

Abstract

We analyzed modulation of cosmic-ray intensities (CRIs) during Solar Cycles 24 by using the solar flare index (FI), interplanetary magnetic field strength, and the geomagnetic Ap and Dst indices. Temporal variations, cross-correlations, and hysteresis patterns of CRI, FI, scalar B, Ap and Dst data were investigated. As a result, we concluded that the FI better describes solar modulation of the CRI as compared to the other solar indicators. We also analyzed the temporal offsets between the flare index and the above-mentioned cosmic, geomagnetic, and interplanetary indices. It is found that this solar activity index, analyzed jointly with cosmic, interplanetary parameters, and geomagnetic activity indices, shows a hysteresis phenomenon. It is observed that these parameters follow different paths for the ascending and descending phases of Cycle 24. The hysteresis phenomenon represents a clue in the search for physical processes responsible for linking the solar activity to near-Earth and geomagnetic responses.

Keywords: solar flare index; geomagnetic activity; temporal variation

Introduction

The sun is not a-quiet star, and the amount of its energy emits variously over time. Changes observed in the sun can be revealed using many indices called solar activity indicators. The majority of these indices are based on the observation of active events such as sunspots, solar flares, coronal mass ejections, etc. All solar activity indices show cyclic variation from days to hundreds of years and they are strongly related to each other (Hathaway, et al. 2002; Özgüç et al. 2022; and reference therein). Active events in the sun such as solar flares, coronal mass ejections, and solar winds are closely related to changes in the geomagnetic field. Observed changes in geomagnetic activity can also be measured using various indices of geomagnetic activity such as Ap, Dst, aa, AE, etc. and all these indices are also closely related to each other (Verbanac et al. 2011; Sarp and Kilcik, 2018; and reference therein).

Statistical properties of solar activity and their relations with the geomagnetic indices has been investigating for a long time (e.g., Obridko and Shelting, 2009; Kirov et al., 2013; and reference therein). Trends in geomagnetic indices were reported by many authors in the literature (Demetrescu and Dobrica, 2008; and reference threein).

The hysteresis behavior can be described as a manifestation of unclear relationships between two different parameters. Since hysteresis plots provide useful information about the phase switches of non-stationary variables, hysteresis analysis has a wide range of applications in many disciplines like Astronomy, Physics, Engineering, etc.

Here we analyzed modulation of cosmic-ray intensities (CRIs), solar flare index (FI), interplanetary magnetic field strength, and the geomagnetic Ap and Dst indices for solar cycle 24. Temporal variations, cross-correlations, and hysteresis patterns of CRI, FI, scalar B, Ap and Dst data were investigated. Data and Methods are presented in Section 2, the Results in Section 3, and the Conclusion and Discussion in Section 4.

Data and Methods

In this study we focused on the temporal and periodic variation of solar and geomagnetic activity indices during Solar Cycle 24 and the data covers January 2009 - December 2020 (complete solar cycle 24) time interval. We used hemispheric and total flare index (FI), which is a rough measure of the total energy emitted by a flare as solar data which is taken from Boğaziçi University Kandilli Observatory web page (https://astronomi.boun.edu.tr/flare-index). Cosmic-ray Intensities (CRI), Ap index, Dst index and the interplanetary magnetic field (IMF)/Scalar B as geomagnetic activity indices used in this study are taken from Oulu/Finland neutron monitor station (https://cosmicrays.oulu.fi/#solar), while Ap, Dst and IMF data sets are downloaded from https://omniweb.gsfc.nasa.gov.

To investigate the possible relationship between above mentioned data sets first we plotted the time variation of them. To remove the short term fluctuations all monthly mean data sets were smoothed with 11 step running average smoothing method. Then to show the hysteresis effects occurred between the CRI, solar FI, Dst index, IMF/Scalar B, and Ap index during solar cycle 24 the hysteresis analysis were performed. To measure the degree of relationship between investigated parameters the cross correlation analysis were performed. This method gives the maximum correlation between two data sets together with possible time delay between the data sets. If the delay is negative that means the first parameter leads the second one and vice versa. The error levels of obtained correlation coefficients were calculated by using Fisher's test that gives the upper and lower boundary of the correlation coefficient with 95 % confidence level.

Results

The temporal variation profiles of the 11 step smoothed data sets are presented in Figure 1.

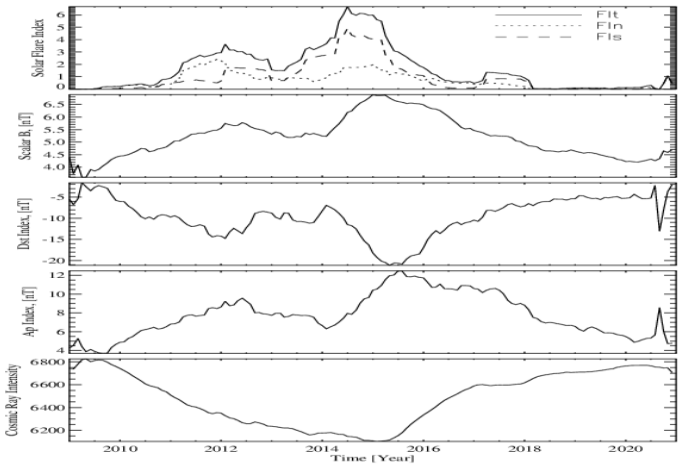

Figure 1. The temporal variations of investigated time series. In the upper panel of the figure, Fit is total FI, Fin is FI in the north hemisphere, and Fis is the FI in the south hemisphere of the sun.

Upper panel of this figure shows hemispheric and total FI temporal variation. In this plot, North and South hemisphere FI show different behavior; the highest peak of North hemisphere FI is around 2012, while South hemisphere FI peaked around the middle of the year 2014. In general the South hemisphere FI was dominant during the investigated cycle (Cycle 24). The temporal variations of all data sets show clear double/multiple peak structures except CRI data set. In general, both peaks of the solar FI data set occur slightly earlier than the other data sets.

To describe the hysteresis pattern of used data sets we first calculated the yearly mean values. As a first step cosmic ray intensity was chosen to be the abscissa of the plots with the equal scale in this figure to display the effects of hysteresis most clearly (see Figure 2).

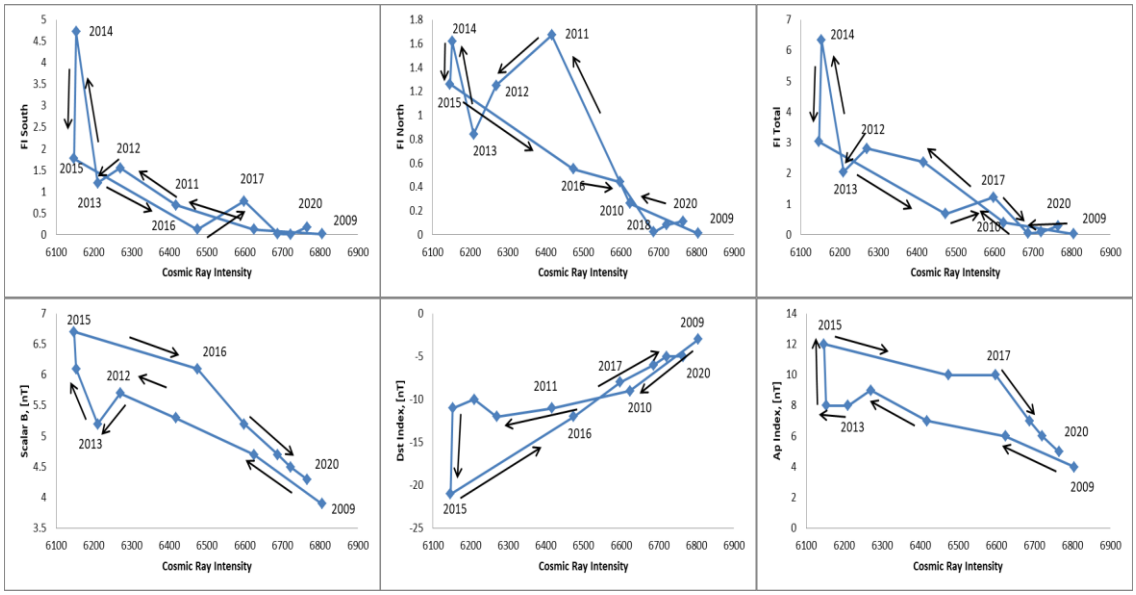

Figure 2. Hysteresis plot of CRI versus other data sets.

From these plots we obtained following results; i) FI data shows hysteresis behavior in all phases of the cycle, while geomagnetic activity indices show hysteresis only around the maximum phase of the cycle 24, ii) all FI and Dst data show counter clockwise circulation, while the Ap Index and Scalar B show clockwise circulation which is not a normal characteristic of hysteresis in magnetic materials.

As a second step of hysteresis analysis total FI was chosen to be the abscissa of the plots with the equal scale (see Figure 3).

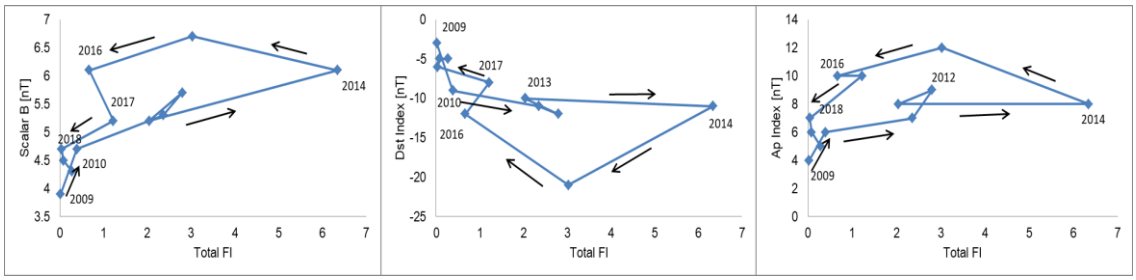

Figure 3. Hysteresis analysis of total FI and other data sets used in this study except CRI.

From these plots we obtained following two results; 1) FI data and Dst data show clockwise circulation while the Ap Index and Scalar B show counter clockwise circulation. 2) The hysteresis behavior generally exists in the maximum and the descending phases of the cycle for all data sets.

The cross correlation analysis results between CR intensity and other parameters are shown in Figure 4 and the list of correlation coefficients are given in Table 1

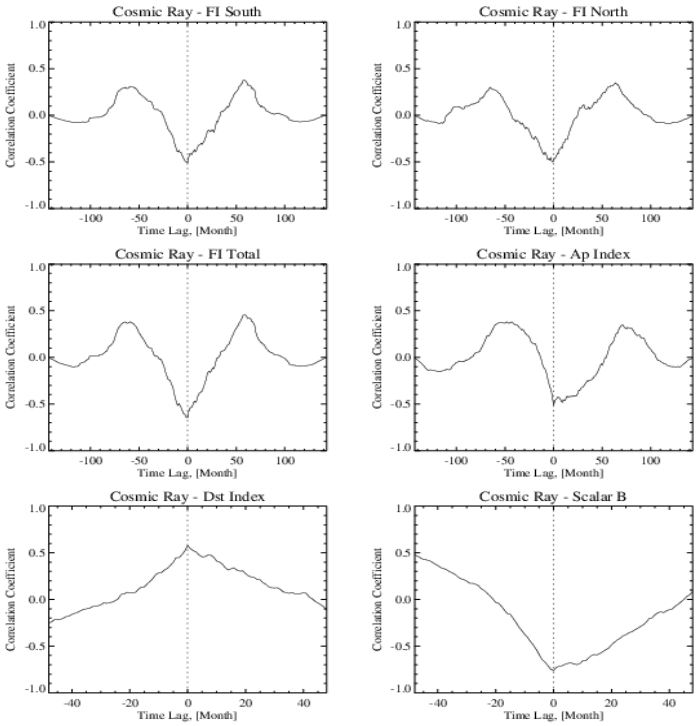

Figure 4. Cross correlation analysis between CR intensity and other parameters

Table 1. list of cross correlation analysis results between CR intensity and other parameters

Data	Correlation Coefficient	Time Lag
CIR-FI South	-0.51 ± 0.11	0.00
CIR-FI North	-0.50 ± 0.12	-1.00
CIR-FI Total	-0.65 ± 0.10	0.00
CIR-Ap Index	-0.51 ± 0.11	0.00
CIR-Dst Index	0.58 ± 0.11	0.00
CIR-Scalar B	-0.76 ± 0.08	0.00

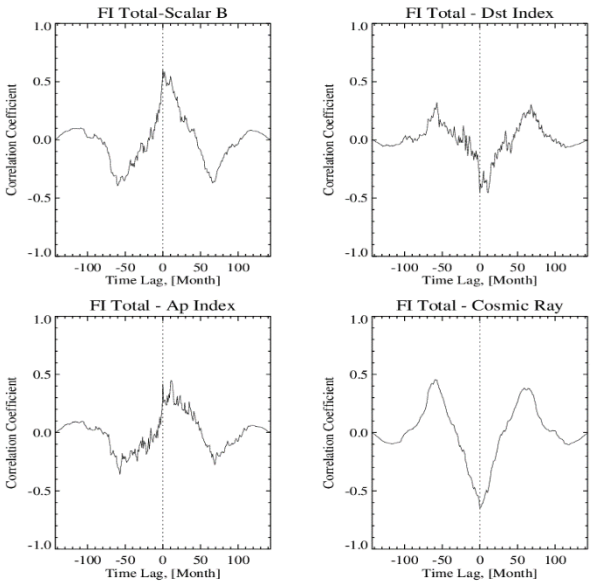

Figure 5. Cross correlation analysis between total FI and other parameters

Table 2. List of cross correlation analysis results between total FI and other parameters

Data	Correlation Coefficient	Time Lag
FI Total-Scalar B	0.60 ± 0.1	0.00
FI Total- Dst Index	-0.46 ± 0.13	0.00
FI Total- Ap Index	0.45 ± 0.13	11.00
FI Total- Cosmic Ray	-0.65 ± 0.10	0.00

Conclusions and Discussions

The hysteresis phenomenon between a pair of indices, which is due to a temporal offset between their variations, can be used as a diagnostic tool to better understand the chain of phenomena linking various manifestations of solar activity, interplanetary medium, the Earth's magnetic field and CRI. In the present study we have compared CRI, with solar activity parameter FI and some geomagnetic activity parameters (IMF/Scalar B, Ap and Dst indices). We found following results;

- Except North hemisphere FI data, all smoothed monthly data sets reach to their maxima at around of the second peak of solar cycle 24.
- South hemisphere FI was dominant during the Solar Cycle 24
- The temporal variations of all data sets show clear double/multiple peak structures except CRI data set.
- In general, both peaks of the solar FI data set occur slightly earlier than the other data sets.
- In the comparison of CRI, FI data shows hysteresis behavior in all phases of the cycle, while geomagnetic activity indices show hysteresis only around the maximum phase of the Solar Cycle 24. Also, all FI and Dst data sets show counter clockwise circulation while the Ap Index and Scalar B show clockwise circulation which is not a normal characteristic of hysteresis in magnetic materials.
- In the comparison of FI, the Dst data shows clockwise circulation while the Ap Index and Scalar B show counter clockwise circulation. Also, the hysteresis behavior generally exists in the maximum and in the descending phases of the cycle for all data sets.
- All data sets used here show meaningful correlation with both CIR and total FI data sets.
- The only Ap index data shows remarkable time lag (11 month) that the Ap index follows the total FI.

Verbanac et al. (2011) analyzed some yearly solar (sunspot number and 10.7 cm solar radio flux) and geomagnetic activity indices (IMF, Ap and Dst) for the period 1960 – 2001. They found that during the analyzed time span, all geomagnetic activity indices show a double peak maximum with a variation from cycle to cycle and meaningful correlations between solar and geomagnetic activity indices. Here we did similar comparison and further confirm their results for Cycle 24(th.SİL) They reported time lag between Ap index and solar indices that we also confirm this result for the Cycle 24.

As shown in Table 1 and 2 the scalar B shows the highest correlation with both solar FI and CIR data sets during the solar cycle 24. Verbanac et al. (2011) reported the higher correlation between geomagnetic activity indices and IMF compared to solar indices and IMF. From their results, we may argue that scalar B/IMF can be used as a geomagnetic activity index as we did in this study.

The hysteresis phenomenon has long been known in solar and solar-terrestrial physics (Bachmann and White, 1994; Bruevich et al. 2016). Bruevich et al. (2016) reported that solar, ionospheric and geomagnetic activity parameters have hysteresis behavior. They concluded that the hysteresis behavior of the Ap index is due to the hysteresis of solar dynamo. Later Sarp et al. (2019) analyzed hysteresis behavior between CIR and sunspot number for solar cycle 23 and 24. Contrary to cycle 23 they conclude weaker link between two parameters during cycle 24. Here we found hysteresis behavior for all data

sets especially during the maximum and descending phases of solar cycle 24 and thus confirm their results for cycle 24.

References

Bachmann, K. T., White, O. R. (1996). Observations of Hysteresis in Solar Cycle Variations among Seven Solar Activity Indicators, SolPhys, Vol 150, Issue 1-2, pp. 347-357, DOI:10.1007/BF00712896

Bruevich, E. A., Kazachevskaya, T. V., Katyushina, V. V., Nusinov, A. A., Yakunina, G. V. (2016). Hysteresis of indices of solar and ionospheric activity during 11-year cycles, Geomagnetism and Aeronomy, Vol 56, Issue 8, pp.1075-1081, DOI:10.1134/S001679321608003X

Demetrescu, C., Dobrica, V. (2008), Signature of Hale and Gleissberg solar cycles in the geomagnetic activity. JGRA, Vol 113, Issue A2, CiteID A02103, DOI:10.1029/2007JA012570

Hathaway, D. H., Wilson, R. M., Reichmann, E. J. (2002). Group Sunspot Numbers: Sunspot Cycle Characteristics, SolPhys, Vol. 211, Issue 1, pp. 357-370, DOI:10.1023/A:1022425402664.

Kirov, B., Obridko, V. N., Georgieva, K., Nepomnyashtaya, E. V., Shelting, B. D. (2013). Long-term variations of geomagnetic activity and their solar sources, Geomagnetism and Aeronomy, Vol 53, Issue 7, pp.813-817, DOI:10.1134/S0016793213070128

Obridko, V. N., Shelting, B. D. (2009). Anomalies in the evolution of global and large-scale solar magnetic fields as the precursors of several upcoming low solar cycles, Astronomy Letters, Vol 35, Issue 4, pp.247-252, DOI:10.1134/S1063773709040045.

Ozguc, A., Kilcik, A., Yurchyshyn, V. (2022). Temporal and Periodic Variations of the Solar Flare Index During the Last Four Solar Cycles and Their Association with Selected Geomagnetic-Activity Parameters, SolPhys, Vol 297, Issue 9, article id.112, DOI:10.1007/s11207-022-02049-7.

Sarp, V., Kilcik, A. (2018). Solar flare and geomagnetic activity relations, Turkish Journal of Physics, Vol 42, Issue 3, pp. 283-292, DOI:10.3906/fiz-1712-18.

Sarp, V., Kilcik, A., Yurchyshyn, V., Ozguc, A. Rozelot, J.P. (2019). Cosmic Ray Modulation with the Maximum CME Speed Index During Solar Cycles 23 and 24, SolPhys, Vol. 294, Issue 7, article id. 86, 11 pp. DOI:10.1007/s11207-019-1481-z.

Verbanac, G., Mandea, M., Vrsnak, B., Sentic, S. (2011), Evolution of solar and geomagnetic activity indices, and their relationship: 1960 – 2001. SolPhys. Issue 1-2, pp. 183-195, DOI:10.1007/s11207-011-9801-y.

Short Period Variations of the Parameters of Ionospheric Scintillations on the Long-Time Observations of the Cosmic Radio Sources at the Decameter Radio Waves

Panishko S.K., Lytvynenko O.A.

Observatory URAN-4 of the IR of the NASU, Odesa; spanishko@ukr.net

1. Abstract

On the observations of the power cosmic sources at the radio telescope URAN-4 (working frequencies 20 and 25 MHz) long-time rows of ionospheric scintillation parameters such as index, characteristic time and spectral index of the intensity fluctuations were obtained. As shown earlier the yearly mean values correlate with the indices of solar and geomagnetic activity, monthly mean estimations have well expressed seasonal-daily dependence. In this work the behavior of daily mean values of index and spectral index of the ionospheric scintillations during multiply solar cycles were analyzed. These values were compared with geomagnetic Ap-index. Daily mean estimations of the ionospheric parameters show significant variability but also they are regulated by processes in the ionosphere which caused the geomagnetic activity. Investigation of the relationship between several of the cosmic weather indicators allow to clarify the mechanisms of the formation of ionosphere irregularity structure that including caused the ionospheric scintillations.

Keywords: cosmic radio sources; ionospheric scintillations; time variations

2. Introduce

Passing through the Earth's ionosphere a radio wave from the cosmic radio source crosses a layer with electron density irregularities which cause the random phase fluctuations of the radio wave that leads to intensity fluctuations. Due to the movement of irregularities on the line of sight intensity fluctuations in the reception point observed as the time amplitude fluctuations of the radio signal which vary widely depending on the frequency, magnetic and solar activity, time of day, season and latitude. Together this makes *the effect of the ionospheric scintillations* [Aarons, 1982]. On the one side scintillations affect the quality of the radio communication, radar, satellite navigation systems, making radio astronomical observations. On the other side the scintillations are one of the manifestations of the cosmic weather. Comparison of different indicators of the cosmic weather can contribute to further investigations of the nature of heterogeneous structure of the ionosphere and their dynamics.

The purpose of this work is to study the relationship between the daily mean values of the ionospheric scintillation parameters obtained from long-term observations of the cosmic sources at the radio telescope URAN-4 with the geomagnetic Ap-index.

Basic ratios for description of the scintillation effect were obtained by the theory of the *thin phase screen* for the case of the single scattering of the radio waves [Rino, 1982]. In this model, it is that irregularities which revolt the phase of incoming wave are in the thin layer. Main characteristics of the scintillations are as follows [Yeh and Liu, 1982]:

scintillation index

$$s_4 = \sqrt{(I(t) - \langle I \rangle)^2 / \langle I \rangle^2}; \quad (1)$$

autocorrelation function

$$B(\tau) = \langle \Delta I(t) \Delta I(t + \tau) \rangle; \quad (2)$$

time spectrum of the intensity fluctuations

$$\Phi(f) = \int_{-\infty}^{\infty} B(\tau) e^{-j2\pi f\tau} d\tau, \quad (3)$$

that caused by

space spectrum of the ionospheric irregularities

$$\Phi_{\Delta N_e}(k) \propto k^{-p}. \quad (4)$$

Here: τ – time shift; f – frequency; p – spectrum slope index of the ionospheric irregularities (p = 4); k – wave number.

3. Observations and processing at the radio telescope URAN-4

Radio telescope (RT) URAN-4 (Figure 1) is a component of the interferometric system of the radio telescopes at the decameter wave range. It is located near city Odessa. From 1987 to present time the monitoring observations of the power cosmic sources (3C 144, 3C 274, 3C 405, 3C 461) have been made on the RT URAN-4 as single instruments at the frequencies 20 and 25 MHz [Derevyagin et al., 2005]. Since 1998, the digital form of radio sources records has been used.

Figure 1. *Radio telescope URAN-4*

An example of observations of one radio source is shown in the Figure 2. Several radio source records were registered during the day. Each record was processed separately by fitting of the calculating function of the direction pattern (DP) which is shown in the Figure 3.

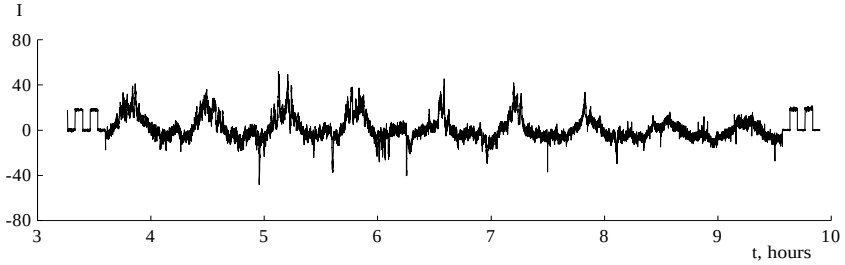

Figure 2. *Example of the observation record of radio source 3C 274 during day (05.01.2004) at the frequency 20 MHz*

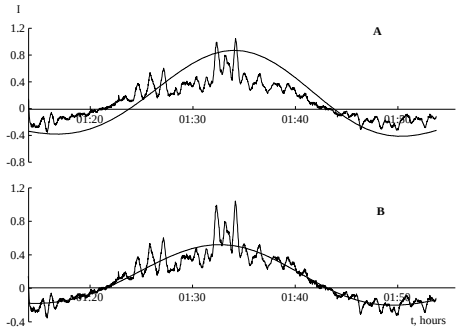

Figure 3. *Example of the fitting of the calculating DP function to the observation record:* ***A*** *– observing record and calculating DP function;* ***B*** *– observing record and fitting DP function*

All observing radio sources scintillate on the irregularities of the ionospheric electron concentration. The parameters of the ionospheric scintillations were obtained for each record, for this the high-frequency series of the intensity fluctuations was extracted from record in its central part. This series was used to calculate scintillation index SI; period ST (measured in seconds) was obtained as a shift of auto-correlation function of series when it reaches zero; spectral index SP was estimated from inclined part of the power spectrum of fluctuation series. An example of processing of the ionospheric scintillations is shown in the Figure 4. Processing results were placed in text files where they are available for analysis.

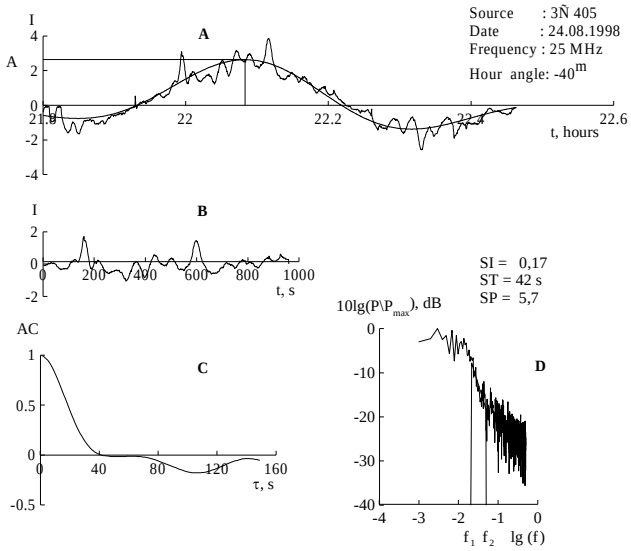

Figure 4. *Example of the proceeding of the radio source record:* ***A*** *– row obtained from observations with fitting direction pattern;* ***B*** *– high frequency part in the center of record (observation row without fitting DP) that associated with ionospheric scintillations;* ***C*** *– autocorrelation function;* ***D*** *– power spectrum of the signal scintillations*

4. Time variations of the ionospheric scintillation parameters and comparison with Ap-index

From 1987 to present the long series of the estimations of ionospheric scintillation parameters were obtained from the observations of the cosmic sources on the RT URAN-4 that

allow to analyze a behavior of these values during different time intervals. Graphics of the yearly mean variations of the index SI, period ST and spectral index SP are shown in the Figure 5 for four observing radio sources. Here and further data at the frequency 20 MHz marked by crests and at the frequency 25 MHz – by circles. For comparison the graphics of yearly mean values of geomagnetic Ap-index and solar radio flux at wavelength 10.7 cm F10 are shown in the Figure 6 for considered time interval which covers three cycle of the solar activity – from 22 to 24 and also the beginning of 25. From the graphs you can see that yearly mean values of all parameters in general are changed accordingly to the solar cycles that show the influence of the solar activity on the heterogeneous structure of ionosphere.

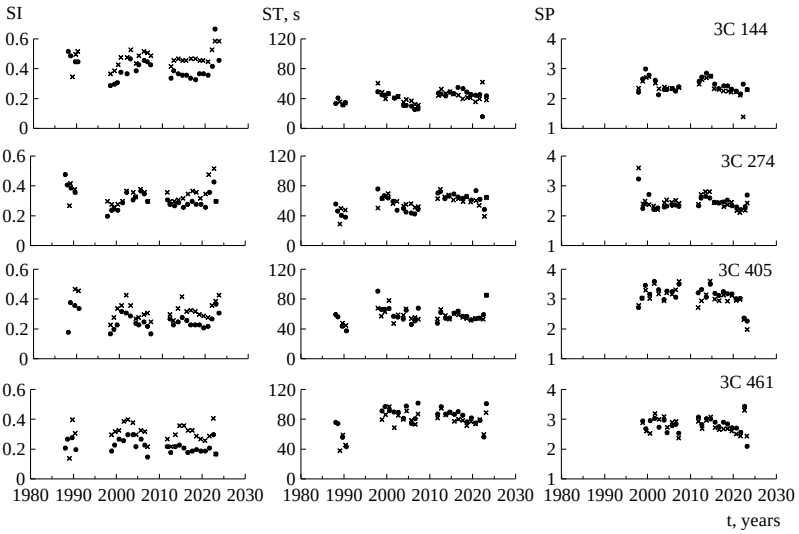

Figure 5. *Yearly variations of ionospheric scintillation parameters*

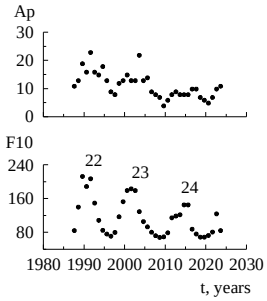

Figure 6. *Plot of the yearly mean values of the geomagnetic Ap-index and solar flux at the wavelength 10.7 cm F10. Numbers of solar cycles are given*

For monthly mean values the marked seasonal-daily dependence is characteristic for all ionospheric scintillation parameters of each observing radio sources [Lytvynenko and Panishko, 2015] that is shown in the Figure 7.

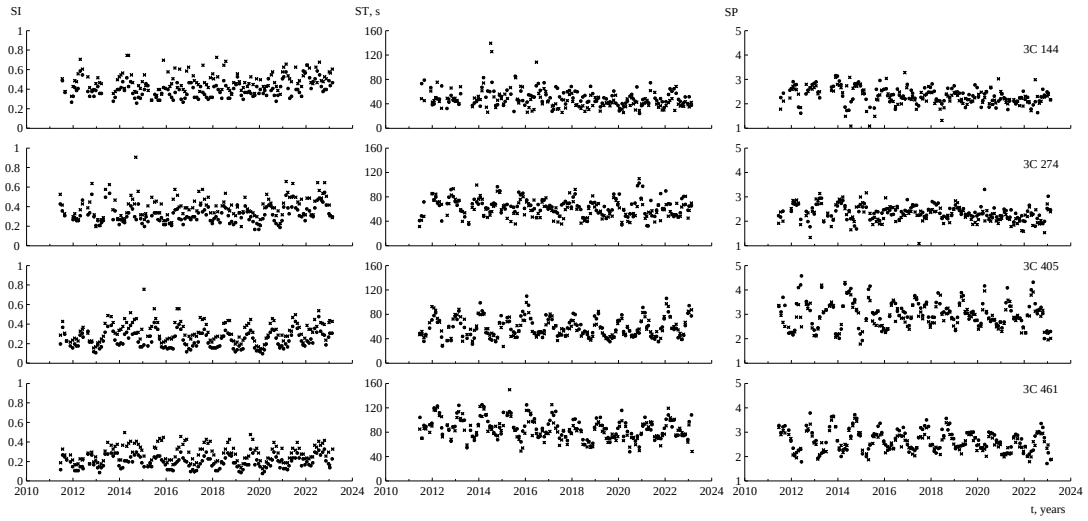

Figure 6. *Seasonal-daily dependence of the ionospheric scintillation parameters*

Because the data is not homogeneous the continuous intervals of 30 days or more have been selected to study the behavior of the daily mean values of the ionospheric scintillation parameters. There were 56 such intervals. The mean values of scintillation parameters and Ap-index were calculated for each of them. Geomagnetic index changed within 4..37 and solar flux within 67.3..183.7 (s.f.u.) during these intervals. Also correlation coefficients of the scintillation parameters with Ap-index were calculated. The examples of the daily mean values graphics of the index, period, spectral index and Ap-index are shown in the Figure 8. The graphs demonstrate significant variability of the scintillation parameters daily mean values. This reflects the nature of the ionospheric heterogeneous structure for which is characteristics high variability that caused by a large number of different factors.

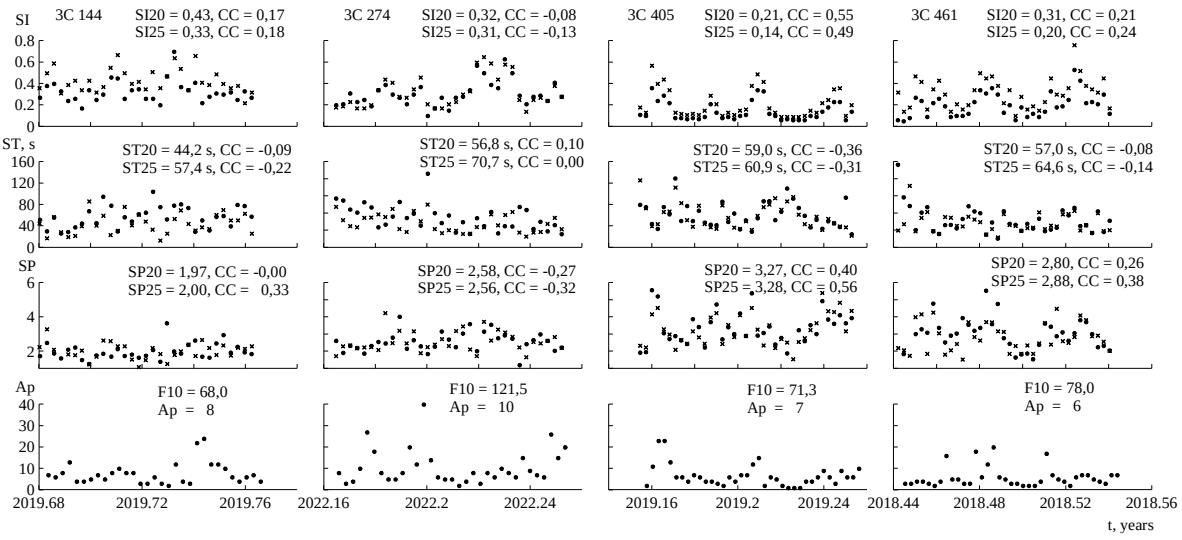

Figure 8. *Examples of daily variations of the ionospheric scintillation parameters for selected observing intervals. Mean values of the scintillation parameters, Ap-index solar flux F10 and correlation coefficients with Ap-index are given*

The Table 1 shows the minimum and maximum mean values of the scintillation parameters which observed for considered data intervals.

Table 1. *Limits of changing of the daily mean values of ionospheric scintillation parameters during considered time intervals*

Radio source	20 MHz			25 MHz		
	SI	ST	SP	SI	ST	SP
3C 144	0.41..0.43	39.7..50.4	1.96..2.73	0.29..0.33	46.8..57.4	2.00..2.81
3C 274	0.27..0.43	53.7..68.9	2.03..2.88	0.25..0.32	57.1..70.1	2.15..2.67
3C 405	0.19..0.52	40.5..83.1	2.41..3.86	0.13..0.38	35.3..79.8	2.67..4.06
3C 461	0.16..0.45	57.0..103.2	2.18..3.18	0.10..0.34	64.6..113.0	2.05..3.24

The minimum and maximum correlation coefficients of the scintillation parameters with Ap-index that calculated for selected data intervals are contained in the Table 2.

Table 2. *Minimum and maximum values of the correlation coefficients of the ionospheric scintillation parameters with the geomagnetic Ap-index*

Radio source	20 MHz			25 MHz		
	SI-Ap	ST-Ap	SP-Ap	SI-Ap	ST-Ap	SP-Ap
3C 144	-0.17..0.24	-0.20..0.18	-0.24..0.08	-0.40..0.25	-0.26..0.00	-0.29..0.33
3C 274	-0.10..0.28	-0.27..0.20	-0.10..0.33	-0.19..0.02	-0.27..0.06	-0.32..0.17
3C 405	-0.27..0.55	-0.27..0.51	-0.36..0.47	-0.31..0.50	-0.49..0.40	-0.29..0.56
3C 461	-0.34..0.36	-0.35..0.24	-0.52..0.22	-0.52..0.35	-0.30..0.46	-0.45..0.40

Data from Table 2 show no significant correlation of the scintillation parameters with Ap-index. The larger correlation coefficients are characteristics for radio source 3C 405 and 3C 461. You can note these sources observe near zenith whereas two others – at lower heights, that is, conditions for the occurrence of the scintillations may differ. The analysis of the daily mean values of scintillation index for four intervals of 13–28 days during 1998–2007 was carried out in the work [Lytvynenko and Panishko, 2017]. In some cases significant values of correlation coefficients with Ap-index were observed (0.60..0.80). Further research is required for the interpretation of the obtained results.

5. Conclusions

- According to the long-term observations at the decameter range of radio waves the ionospheric scintillation parameters such as index, period and spectral index of the fluctuations were obtained.
- In general yearly mean values of the parameters that obtained follow to the cycles of the solar activity.
- For monthly mean values seasonal-daily dependence is characteristic.

- Daily mean estimations of ionospheric scintillation parameters demonstrate significant variability. The comparison with geomagnetic Ap-index do not shows direct relationship between these values.

References

Aarons, J. (1982). Global Morphology of Ionospheric Scintillations, Proc. IEEE, Vol. 70, No 4, pp. 360-378.

Derevyagin, V.G., Isaeva, E.A., Kravetz, R.O., Litvinenko O.A., Panishko, S.K. (2005). Observations of power cosmic radio sources on the radio telescope URAN-4 during 1998-2004, Astronom. and Astrophys. Trans., Vol. 24, No 5, pp. 421-424, http://dx.doi.org/10.1080/10556790600631652.

Yeh, K.C., Liu, C.-H. (1982). Radio wave scintillations in the ionosphere, Proc. IEEE, Vol. 70, No 4, pp. 324-360.

Lytvynenko, O.A., Panishko, S.K. (2015). Seasonal variations of the ionosphere scintillations parameters obtained from the long observations of the power cosmic radio sources at the decameter wave range, Odessa Astronom. Publ., Vol. 28, No 2, pp. 235-237.

Lytvynenko, O.A., Panishko, S.K. (2017). Variations of ionospheric scintillation index for the short-time intervals observed on the power cosmic radio sources at the decameter wavelengths, RadioPhys. and RadioAstron., Vol. 22, No 4, pp. 304–309, DOI: https://doi.org/10.15407/rpra22.04.304.

Rino, C. L. (1982). On the application of phase screen models to interpretation of ionospheric scintillation data, Radio Science, Vol. 17, No 4, pp. 855-867.

Summer tropospheric mesoscale situations with impact on the ionospheric plasma

Potužníková K.[1], *Koucká Knížová P.*[1], *Chum J.*[1], *Podolská K.*[1], *Kouba D.*[1], *Mošna Z.*[1], *Georgieva K.*[2], *Bojilova R.*[3], *Kirov B.*[2], *Asenovski A.*[2]

[1]Institute of Atmospheric Physics CAS, Prague, Czech Republic; kaca@ufa.cas.cz

[2]Space Research and Technology Institute, BAS, Sofia, Bulgaria; katyageorgieva@msn.com

[3]National Institute of Geophysics, Geodesy and Geography, Bulgarian Academy of Sciences, Sofia, Bulgaria; rbojilova@geophys.bas.bg

1. Abstract.

Coupling between distant regions of the atmosphere has been widely confirmed by theoretical and experimental studies. The tropospheric influence on the upper atmospheric ionosperic plasma is the primary focus of this report. As the troposphere warms, the absolute humidity and wind shear increase over the whole of Europe. This increase suggests that convective environments contributing to formation of summer thunderstorms will become more frequent.

Here we analyze and discuss the possible effects of cold fronts and thunderstorms and their influence on the upper atmosphere up to the ionospheric plasma. The state of the ionosphere is monitored by means of digisonde DPS 4D and continuous monitoring by Doppler sounder CDS. In coincidence with severe meteorological situations we have identified a variety of spread F echo on the ionograms and particular types of CDS spectrograms.

Keywords: Tropospheric weather systems; atmospheric gravity waves; ionospheric plasma irregularity

2. Introduction

The troposphere-ionosphere coupling is a hot topic. The atmosphere supports the propagation of a wide range of waves. Within the troposphere there are permanent sources of waves mostly tied to the orography [Hoffmann et al., 2013]. Other wave sources are more spread around the globe, locally less intense than orographic, however the integrated contribution of non-orographic waves can be comparable to that of orographic waves [Fritts and Alexander, 2003; Hertzog et al., 2008]. Their dissipation may act as a source of secondary waves with impacts in the thermosphere [Oyama and Watkins, 2012; Vadas and Azeem, 2021]. A large scientific community is convinced that the meteorologically induced effects should be taken into account in the energy balance of the ionosphere.

In our several previous case studies we have analyzed particular cases of synoptic-scale atmospheric fronts with significant pronounced effects on the ionosphere as detected by the ionosond [Boška and Šauli, 2001; Šauli and Boška, 2001]. As we have shown in some studies [Koucká Knížová et al., 2020; Koucká Knížová et al., 2023], significant disturbances in the ionosphere can also be related to tropospheric distortions of sub-synoptic scales and enhanced by local orographic features. Recently, we have been focusing on the summer tropospheric situations as manifested by tropospheric thunderstorms. Preliminary results (presented at international workshops and conferences) show more frequent occurrence of severe weather systems and consequent effects on ionospheric plasma. These results are in agreement with climatological studies [Rädler et al., 2019; Kolendowitz et al., 2017; Taszarek et al., 2019]

highlighting high occurrence of severe tropospheric events. Temperature and moisture of mid-tropospheric summer days have increased in the last decade. Furthermore, according to the EURO-CORDEX climate model projections at 0.44° resolution, the probability of severe weather events will increase significantly across Europe. For example, under the most aggressive RCP8.5 climatic scenario, the occurrence of large hail (greater than or equal to 2 cm in diameter) is projected to become 40-80% more likely across central and eastern Europe by the end of the century [Rädler et al., 2019]. This is due to anthropogenic climate change, which is associated with a variety of changes in the troposphere. As the planet warms, absolute humidity and vertical wind shear increase in the troposphere over all Europe [Brooks, 2013]. In addition, there is increasing evidence that the polar jet stream has become more meandering as a result of Arctic amplification [Rädler et al., 2019]. Faster warming of the Arctic region compared to the mid-latitudes leads to a smaller temperature difference between northern and southern Europe, and thus to both a decrease in the speed of the zonal flow in the upper troposphere and a more pronounced meandering of the polar front.

This paper describes two typical tropospheric situations of the summer season. One of them is a late summer rapid transition of an extratropical frontal cyclone over Europe in the mid-latitudes. The other is the case of a summer storm within a tropical air mass extending over central Europe. In both cases, we analyze the pressure pattern structures and the associated flow at different heights in the troposphere. We also discuss the ionospheric disturbances associated with both events as they are seen on ionograms and Doppler spectrograms.

3. **Troposphere**

3.1. Frontal thunderstorms associated with a fast-moving extratropical cyclone Fabienne

The synoptic conditions, ground-level observations of the transition of a significant cold front associated with extratropical cyclone Fabienne, are described in detail in the paper [Koucká Knížová et al., 2020], so we report them briefly. The Fabienne case is used to compare the two different situations and to complete the view. In general, frontal extratropical cyclones typically occur in autumn and winter, and their movement from west to east is driven by a polar front that separates the colder polar air in the north from the tropical air in the south. (At the same time, there is a jet stream at the upper boundary of the troposphere.) The greater the horizontal temperature gradient, the more severe the extratropical cyclone is, which initially originates as a wave disturbance on the polar front. Moreover, the Central European region is characterized by a transition between the maritime Atlantic air and the continental Asian climate. The difference in temperature and moisture from the Atlantic gives energy and speed of motion to extratropical cyclones and associated fronts in the low and mid-troposphere. Cold fronts are often associated with thunderstorms (even in the cold season of the year, but not discussed here). Figure 1A plots the pseudoequivalent temperature (θ_{ep}) in the lower troposphere, at 850 hPa, which corresponds to a height of about 1.5 km above the surface. The θ_{ep} field is used by meteorologists to identify atmospheric fronts. It contains information about both the temperature and the humidity of the atmosphere. It is the theoretical temperature of the air mass, which we calculate by extracting both the water and water vapor in that air mass by condensation and precipitation and then increasing its temperature by the latent heat of condensation released. In Figure 1A, there are clearly visible narrow transformation zones with a strong gradient in θ_{ep} that separate the polar air mass from the tropical air mass. Physically, these are regions of a narrow boundary where the troposphere tries to quickly return to the equilibrium temperature homogeneous state and consequently the generation of waves that potentially propagate up to ionospheric heights.

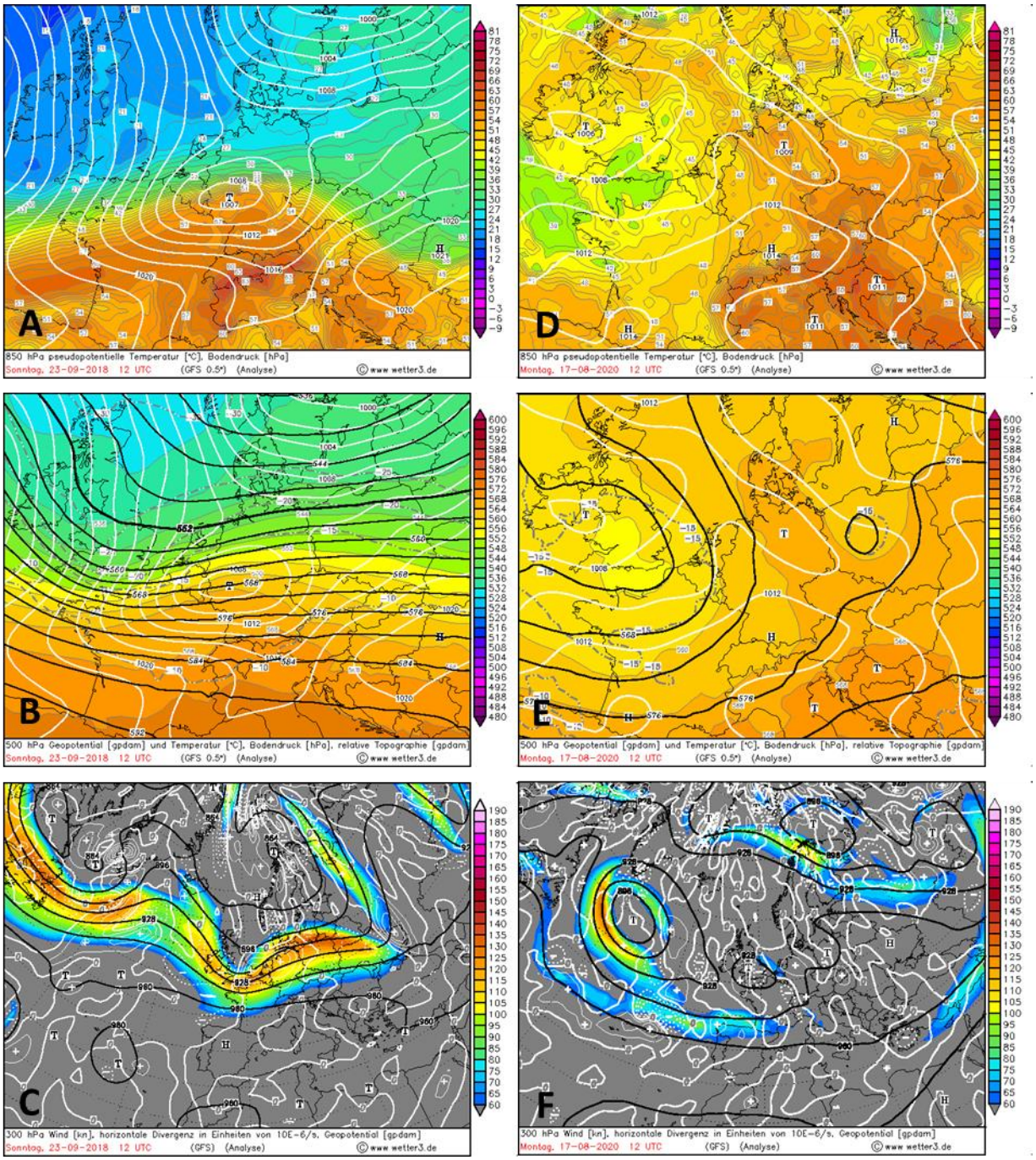

Figure 1. *The panels in the left column refer to the fast moving frontal cyclone Fabienne, passing the IAP observatory on 23 September 2018, and the panels in the right column refer to the air-mass thunderstorm on 17 August 2020. The analyses are valid for 12 UTC. Panels (A, D) show the pseudo-equivalent potential temperature at the 850 hPa pressure level (color scale) and the sea level pressure (white contours). Panels (B, E) show the geopotential height of the 500 hPa level (black contours, decameter), the sea level pressure (white contours), and the relative topography between 500 and 1,000 hPa (color scale)—this represents the vertical distance between the 1,000 hPa (surface) and 500 hPa (middle troposphere, about 5.5 km) levels and varies with temperature and moisture (it is a function of the mean virtual temperature). Thus, the color scale regions are directly related to the mean temperature and*

moisture of the middle troposphere (orange/red values indicate tropical air mass, and yellow/green indicate polar air mass). Panels (C, F) show geopotential height at the 300 hPa (black contours, decameter), wind speed (color scale) and horizontal divergence/convergence (white contours with "+"/"-").

All images are displayed from the GFS analysis. Archived from: https://www.wetter3.de/archiv_gfs_dt.html.

Figure 1B shows both the surface pressure field (white lines, T marks the center of cyclone Fabienne) and the pressure and temperature field in the mid-troposphere at about 5.5 km altitude (black lines and colored field). Figure 1B shows that low-level pressure pattern, including the Fabienne cyclone, moves very fast, as the 500 hPa height isolines are very close together. The atmosphere at 5.5 km is no longer under frictional influence from the surface, which is why the 500 hPa field is called the steering flow field in synoptic meteorology and is used to predict the speed and direction of movement of surface pressure patterns. The color field of the relative topography, indicating the thickness of the layer between the 1000 hPa and 500 hPa pressure levels, shows a strong gradient between the relatively thin and therefore cooler troposphere in the north and the vertically thicker and therefore warmer troposphere in the south.

Figure 1C shows the pressure field near the top of the troposphere at 300 hPa. The jet stream axis (maximum flow velocity indicated by the color scale) follows the polar front between the polar air mass and the tropical air masses. In the areas marked with a "+" sign, there is an horizontal divergence of the flow, which favors the formation of convective clouds and thunderstorms.

3.2. Air-mass thunderstorm 17 August. 2020

The second type of the meteorological situation associated with extreme weather events that we focus on is a thunderstorm within a homogeneous air mass. These events are accompanied by large hail, torrential rain, strong wind gusts, etc. They often occur in summer in very unstable warm and humid air masses of tropical origin, usually on the weak horizontal pressure gradient in the lower troposphere.

Figure 1D shows a pressure field near the ground at 2 m height (white lines) with a weak pressure trough extending from the Atlantic to central Europe (1010 hPa isobar) and a weak ridge from the Black Sea towards southern Scandinavia (1012 hPa isobar). Hot and humid tropical air was blown into the area between the trough and the ridge from the south. This is reflected in θ_{ep} values in the lower troposphere at about 1.5 km altitude, which reach up to 60°C. In the Czech Republic, values above 60°C at 850 hPa are very rare, occurring at most a few days per year.

Figure 1E shows that, in the mid-troposphere, central Europe is under the influence of a moderate flow from the southwest along a trough of low pressure, associated with the small upper-level cyclone that has formed over the Czech Republic and is slowly advancing towards northern Poland. The center of the upper-level cyclone, enclosing an area of local cold air minimum temperatures of -15°C, is over southern Poland at 12 UTC. The air below an upper-level cyclone is potentially unstable due to the rapid decrease in temperature with height, which supports convective motion and provides suitable conditions for the formation of cumulus clouds. It usually forms and breaks up within a few hours but can bring more persistent

precipitation if it remains over an area for a longer period. However, unlike precipitation associated with atmospheric fronts, the intensity and duration of precipitation caused by an upper-level cyclone is generally difficult to predict.

The pressure field map near the upper tropospheric boundary also shows that Central Europe is under the influence of both the low pressure trough and the horizontal flow divergence, as is shown inFigure 1F. This means that convection occurs throughout the entire depth of the troposphere.

4. Ionosphere

4.1. Fabienne case

The case of Fabienne was in detail analyzed and discussed in paper Koucká Knížová et al. (2020). Here we only briefly summarize the observed effects.

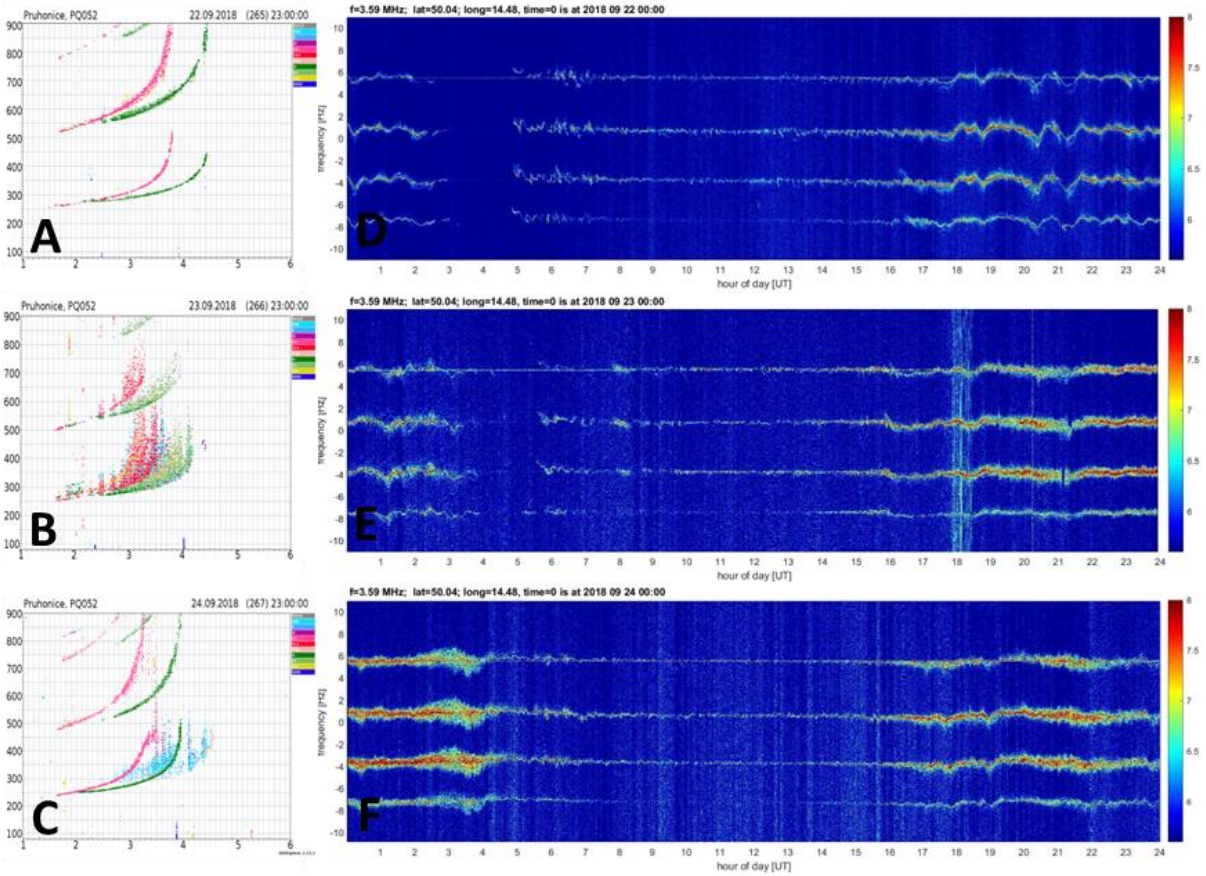

Figure 2. *Panels in the left column show the ionograms recorded by DPS 4D in Průhonice. Red color and green color denote ordinary and extraordinary reflection traces. Other colors denote off-vertical echoes registered by the antenna field. In particular, blue represents the north north-east direction of signal arrival.*

Panels in the right column show Continuous Doppler Sounder spectra measured during three consequent days. The quality of the spectra (width, oscillation of the central frequency) is changing.

Figures 2A,B,C show the sequence of ionograms recorded during three consecutive days around 23:00 UT at the Průhonice Ionospheric Observatory. Figure 2A shows a typical night

time ionogram, recorded on 22 September, with a clear reflection trace of the ordinary and extraordinary electromagnetic waves. On the ionogram, one can observe typical quiet time reflection from the F2 region. No irregularities are apparent on the electron density profile. An important feature to point out is the presence of strong Spread F echo on ionograms on 23 September (Figure 2B) and slightly the following day of 24 September (Figure 2C). On both (middle and bottom) ionograms there are strong off-vertical echoes present. The ionogram on panel 2B is recorded on 23 September shortly after the passage of a cold front with strong storm activity. Spread F echo on ionograms is observed when the sounding frequency does not reflect on a horizontal plane, but it meets an undulated plane that causes reflected waves to scatter. Such a situation, departure from horizontal stratification, may be caused by presence of wave-like activity (propagating TIDs excited by geomagnetic activity, atmospheric waves from lower lying regions). In this particular case, the geomagnetic activity is rather low to moderate, hence we assume to attribute the effects to the propagating frontal system that effectively launches the atmospheric gravity waves (see details in the paper Koucká Knížová et al, 2020).

Figure 2D,E,F shows Continuous Doppler Sounder spectra for the consecutive days 22-24 September recorded for sounding frequency 3.59 MHz. Here on the plots, there are important features to comment on. The clear narrow echo is observed during the day with oscillations in the gravity wave band on Figure 2D. On the day of the Fabienne event on Figure 2E, there is a wide frequency noise, likely caused by the lightning in the vicinity of the receiver. With a delay of about two hours, we observe a spread spectrum that lasts till the following day on Figure 2F.

4.2. Air-mass thunderstorm case

Figures 3A, B, C show the sequence of ionograms recorded during three consecutive days around 23:00 UT recorded at the Průhonice Ionospheric Observatory by DPS 4D.

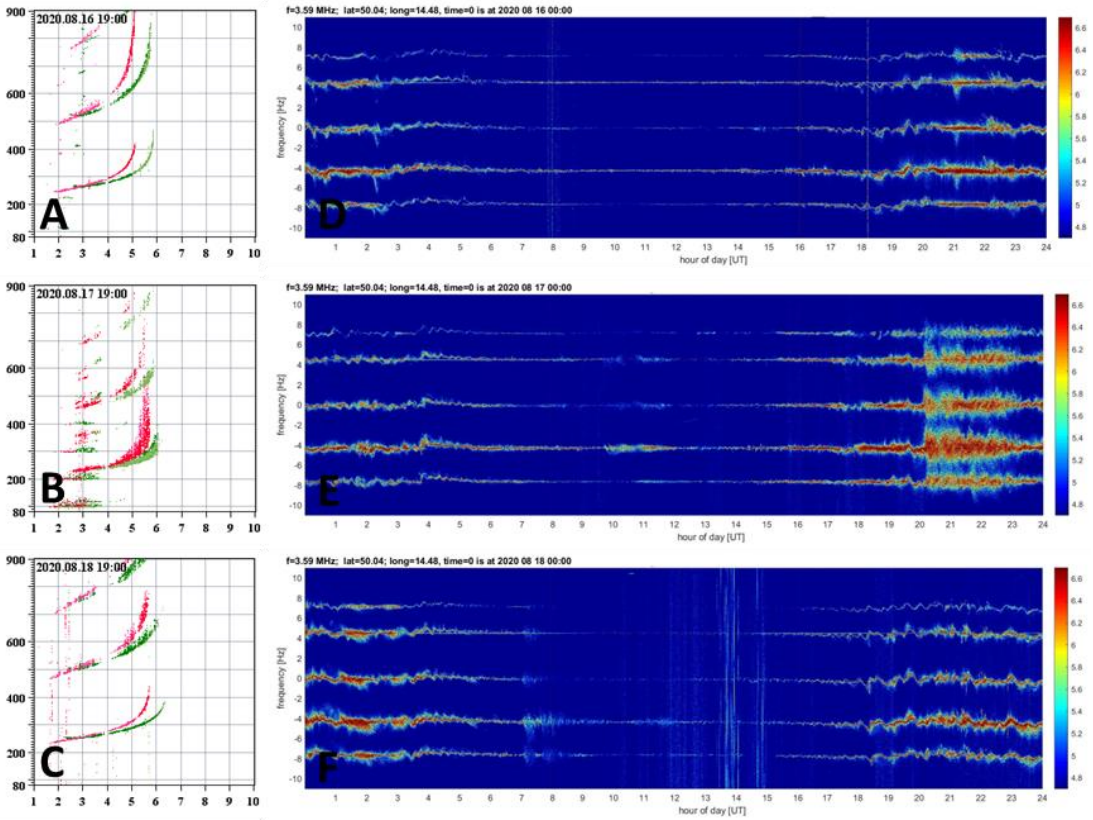

Figure 3. *Same as Figure 2., for days 16-18 August, 2020.*

Figure 3A shows the typical ionogram monitored before the event. The clear echoes of ordinary and extraordinary traces indicate a quiet regular ionosphere that is normally stratified. Hence the reflection happens on the horizontal planes. Figure 3B shows a rather strong spread F echo. Besides that, a strong Sporadic E layer is present. Also the Es echo shows the spread of the reflected signal. Figure 3C shows that the ionosphere at the F layer returns to a regular stratification and the traces are no longer spreaded. Figure 3C,D,E show CDS spectra for the three consecutive days. On 16 August (Figure 3A) clear or slightly spread spectra can be observed during night hours till the morning of the following day on Figure 3D. During the night hours, first a slight spread spectrum is observed till about 20 UT, after that exceptional strong spread appears on the signal. Following day, slight spread of the signal can be observed during the entire day (Figure 3E). As in the previous case, we suppose that spread F echo during the Air-mass thunderstorm event can be attributed to the atmospheric gravity waves of a tropospheric origin.

It is well known that geomagnetic disturbances strongly influence the ionosphere. The geomagnetic disturbances are due to two major solar activity drivers: coronal mass ejections (CMEs – clouds of solar coronal plasma with embedded magnetic fields ejected from the corona when enough energy has been stored there), and high speed solar wind streams (HSSs – emanating from unipolar solar magnetic regions, propagating and accelerating along the open magnetic field lines from the Sun far into the heliosphere). Both affect the ionosphere through electric fields, enhanced particle precipitation, Joule heating, ion drag, and composition changes (see e.g. Ren et al., 2020; Fagundes et al., 2023 among others). Two indices are mostly used to evaluate the level of geomagnetic disturbances: Dst which is more sensitive to CMEs, and Kp in which the effects of HSSs are more obvious. Figure 4 presents them for the two studied events. Fabien cyclone, September 23, 2018 (left panel) occurred after a minor disturbance characterized as "quiet to mild" according to Dst index which did not exceed -40 nT (geomagnetic disturbances are related to negative values of Dst) and "minor" according to Kp which did not exceed 5. During the passage of Fabien and the observed ionospheric effects on 23 and 24 September, the geomagnetic activity according to both indices had returned to "quiet". The air mass thunderstorm event on August 17, 2020 occurred during a prolonged period of very low geomagnetic activity. Before and during the thunderstorm Dst index was positive and Kp index was below 2, and after the event Dst did not reach -20 nT while Kp remained about 3, which, according to both indices, is defined as "quiet". Therefore, we can expect that the effects observed in the ionosphere in these particular cases are not related to geomagnetic activity but are mainly due to tropospheric processes.

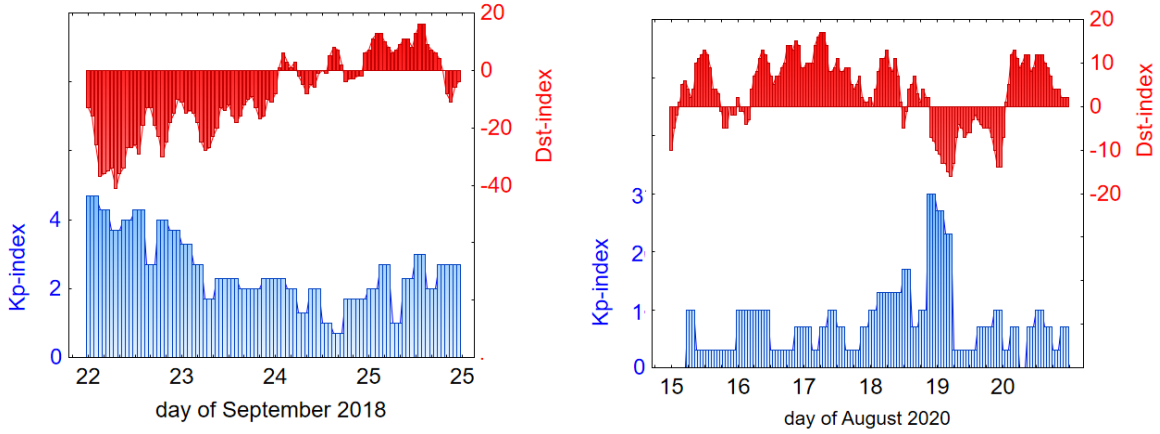

Figure 4. *Behavior of Kp-index (blue, left-sided scale) and Dst-index (red, right-sided scale) for the period 22-25 September 2018 (left panel) and 15-20 August 2020 (right panel).*

5. Conclusion

Our results highlight the importance of studying the meteorological influence on the upper atmosphere, in particular the ionosphere. Under favorable conditions (when the waves reach ionospheric heights in the form of primary and/or secondary waves), both described tropospheric situations can induce significant detectable changes up to ionospheric heights. At the same time, the response is not the same for both situations, but suggests some differences.

We observe long duration spread F echoes on ionograms during both discussed cases. As has been pointed out many times, the spread F echo indicates undulations of the reflection planes. These are very likely caused by the atmospheric waves propagating up to the ionosphere. This spread F on the ionograms measured in association with the frontal cyclone passage appears to be stronger, showing both range and frequency spread.

On the Continuous Doppler Sounding spectra we observe the increase of the spread of the Doppler shift in both analyzed cases. The observed frequency shift spread of the CDS spectra is larger in case of Air-mass thunderstorms. In case of the Fabienne storm we observe the echo from the F layer while in the air-mass thunderstorms event the echo of Doppler shift may come from the Sporadic E layer. However, in both cases we observe wave-like activity in the ionosphere.

Rather low geomagnetic activity allows us, as we suppose, to attribute the observed disturbance to the atmospheric gravity waves launched by the fast moving cyclone border Fabienne across Europe and to the air-mass thunderstorms.

Work has been supported by H2020-INFRAIA-2018-2020 **PITHIA-NRF** (number: 101007599) and Project HORIZON-CL4-2022-SPACE-01101081835 **T-FORS,** grant GA21-03295S by the Czech Science Foundation, Mobility project Academy of Sciences BAS-23-07 and Mobility project of Academy of Sciences CONICET-22-02.

References

Boška, J., Šauli, P. (2001). Observations of gravity waves of meteorological origin in the F-Region ionosphere. Phys. Chem. Earth Part C, Vol. 26, pp. 425–428. DOI: 10.1016/S1464-1917(01)00024-1.

Brooks, H. E. (2013). Severe thunderstorms and climate change. Atmos. Res., Vol. 123, pp. 129–138, DOI: 10.1016/j.atmosres.2012.04.002.

Fagundes, P. R. et al. (2023) Ionospheric storm due to solar Coronal mass ejection in September 2017 over the Brazilian and African longitudes, Adv. Space Res., Vol. 71, Iss. 1, pp. 46-66, DOI: 10.1016/j.asr.2022.07.040.

Fritts, D. C., Alexander, M. J. (2003). Gravity wave dynamics and effects in the middle atmosphere. Rev. Geophys., Vol. 41, No. 1003. DOI: 10.1029/2001RG000106.

Hertzog A., Boccara, G,. Vincent, R. A., Vial, F., Coquerez P. (2008). Estimation of gravity-wave momentum fluxes and phase speeds from long-duration stratospheric balloon flights. Part II: Results from the Vorcore campaign in Antarctica. J. Atmos. Sci., Vol. 65, pp. 3056–3070. DOI: 10.1175/2008JAS2710.1.

Hoffmann, L., Xue, X., Alexander, M. J. (2013), A global view of stratospheric gravity wave hotspots located with Atmospheric Infrared Sounder observations, J. Geophys. Res. Atmos., Vol. 118, pp. 416–434. DOI: 10.1029/2012JD018658.

Koucká Knížová, P., Podolská, K., Potužníková, K., Boška, J., Kozubek, M. (2020). Evidence of vertical coupling: Meteorological storm Fabienne on 23 September 2018 and its related effects observed up to the ionosphere. Ann. Geophys., Vol. 38, pp. 73–93, DOI: 10.5194/angeo-38-73-2020.

Koucká Knížová, P., Mošna, Z., Kouba, D., Potužníková, K., Boška, J. (2015). Influence of meteorological systems on the ionosphere over Europe. J. Atmos. Sol. Terr. Phys., Vol. 136, pp. 244–250, DOI: 10.1016/j.jastp.2015.07.017.

Koucká Knížová, P., Potužníková, K., Podolská, K., Hannawald, P., Mosna, Z., Kouba, D., Chum, J., Wuest, S., Bittner, M., Kerum, J. (2023). Multi-instrumental observation of mesoscale tropospheric systems in July 2021 with a potential impact on ionospheric variability in midlatitudes. Front. Astron. Space Sci., Vol. 10, No. 1197157. DOI: 10.3389/fspas.2023.1197157.

Kolendowicz, L, Taszarek, M., Czernecki, B. (2017). Atmospheric circulation and sounding-derived parameters associated with thunderstorm occurrence in Central Europe. Atmos. Res., Vol. 191, pp. 101-114, DOI: 10.1016/j.atmosres.2017.03.009.

Oyama, S., Watkins, B. J. (2012). Generation of atmospheric gravity waves in the polar thermosphere in response to auroral activity. Space Sci. Rev., Vol. 168, pp. 463–473, DOI: 10.1007/s11214-011-9847-z.

Rädler, A. T., Groenemeijer, P. H., Faust, E., Sausen, R., Púčik, T. (2019). Frequency of severe thunderstorms across Europe expected to increase in the 21st century due to rising instability. NPJ Clim. Atmos. Sci., Vol. 2, No. 30. DOI: 10.1038/s41612-019-0083-7.

Ren, D., Lei, J., Zhou, S., Li, W., Huang, F., Luan, X., et al. (2020). High-speed solar wind imprints on the ionosphere during the recovery phase of the August 2018 geomagnetic storm. Space Weather, 18, e2020SW002480, DOI: 10.1029/2020SW002480

Šauli, P., Boška, J. (2001). Tropospheric events and possible related gravity wave activity effects on the ionosphere. J. Atm. Sol. Terr. Phys. Vol. 63, pp. 945–950. DOI: 10.1016/S1364-6826(00)00205-4.

Taszarek, M., Allen, J., Púčik, T., Groenemeijer, P., Czernecki, B., Kolendowicz, L., Lagouvardos, K., Kotroni, V., Schulz, W. (2019). A climatology of thunderstorms across Europe from a synthesis of multiple data sources. J. Clim., Vol. 32, pp. 1813–1837. DOI: 10.1175/JCLI-D-18-0372.1.

Vadas, S. L., Azeem, I. (2021). Concentric secondary gravity waves in the thermosphere and ionosphere over the continental United States on March 25–26, 2015 from deep Convection. J. Geophys. Res. Space Phys., Vol. 126, No. e2020JA028275. DOI: 10.1029/2020JA028275.

Penetration of Energetic Electrons from Outer Radiation Belt to Lover L-Values and to Inner Radiation Belt

Dachev T.P.[1], Tomov B.T.[1], Matviichuk Y.N.[1], Dimitrov P.G.[1], Semkova J.V.[1], Koleva R.T.[1], Jordanova M.M.[1], Bankov N.G.[1], Mitev M.G.[1], Krastev K.N.[1], Malchev S.P.[1], Reitz G.[2], Header D.-P.[3]

[1]Space Research and Technology Institute, Bulgarian Academy of Sciences, Sofia, Bulgaria
tdachev59@gmail.com
[2]German Aerospace Center (DLR), Institute of Aerospace Medicine, Cologne, Germany
[3]Möhrendorf, Germany

Abstract

The radiation risk radiometer-dosimeter (R3D)-R2 instrument was situated outside the Russian segment of the International Space Station (ISS) and inside the ESA EXPOSE-R2 facility in the period November 2014 - January 2016. We detected a penetration of the relativistic electrons below L=2.5 in the recovery phase of the magnetic storm after 18 March 2015. In the period March 18-28 2015, the lower boundary of L=1.8 was reached. The relativistic electrons at low L disappeared on March 28, 2015. The magnetic storm on 25th of June 2015 again generated relativistic electrons' fluxes from the Outer Radiation Belt (ORB) at the L values below 2.5. The ORB enhancement on July 4 2015 emphasized them again. In this specific case, the minimal L values reached L=1.6. Almost all disturbances in the Disturbance Storm Time (Dst) index from July 11th, 2015 until January 1st, 2016 generated new portions of relativistic electrons in the L-values below 2.5. They existed for few days and disappeared until the next Dst disturbance.

Keywords: outer radiation belt; inner radiation belt; ISS.

Introduction

High-energy charged particles are trapped by the Earth's magnetic field and form two distinct belts of toroidal shapes surrounding the Earth: the Inner Radiation Belt (IRB) and the Outer Radiation Belt (ORB).

The IRB is situated at an altitude from 0.2 to 2.0 Earth radii at the geomagnetic equator and consists of electrons, with energies of up to 10 MeV, and protons with energies of up to 700 MeV. Outside of the ISS, the IRB energetic protons deliver a daily dose of 567-μGy d^{-1} [Dachev et. al., 2017].

The ORB is located in the altitudinal range from 3.4 to 10 Earth radii. The ORB energetic population is electrons with energies of a few MeV. The first observations of the ORB relativistic electron fluxes in the ISS, on the American laboratory module, were made in 2001 with a Liulin-E094 instrument [Dachev et al., 2002], [Reitz et al., 2005]. Later, the ORB relativistic electron fluxes were observed with more Liulin-type instruments flown on the ISS and LEO satellites [Dachev et al., 2009, 2015], [Dachev, et al., 2015a]. The average daily dose during the entire ESA EXPOSE-R2 mission from the ORB daily dose rate is 278-μGy d^{-1}. On quiet days, the ORB daily dose rates is practically zero but reached maximum dose rates up to 3,000-μGy d^{-1} in the disturbed periods after magnetic storms. The most extreme hourly dose rates values that we have registered were 28,840 μGy h^{-1}[Dachev et. al., 2017].

Materials and methods

R3DR2 instrument is a low mass (0.17 kg) and small-dimension (76×76×36 mm) Liulin type spectrometer (LTS) [Dachev et al., 2015a, 2017]. It measures solar UV and visible radiation in

four channels and cosmic ionizing radiation in 256 channels respectively. Figure 1 shows the mounting position of the R3DR2 instrument (in red rectangle) in the EXPOSE-R2 facility.

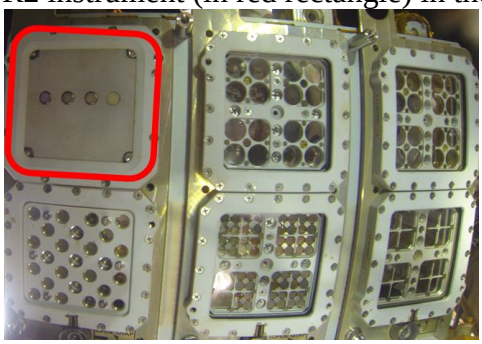

Figure 1. *External view of R3DER2 instrument (in the red rectangle) mounted on EXPOSE-R2 facility. (Picture taken by Russian cosmonaut Alexander Samokutyaev on October 22nd, 2014 during EVA-2 for mounting of EXPOSE-R2 facility outside Russian "Zvezda" module. (Picture credit of ESA/NASA/RKA)*

The doses (deposited energies) are determined in the R3DR2 instrument by Hamamatsu S2744–08 silicon PIN photodiode. The pulse amplitudes from ionized particles, gamma quanta and indirectly neutrons, first pass the charge-sensitive preamplifier then a 12-bit fast analogue-to-digital (A/D) converter, which digitizes them. The pulse amplitudes are proportional by a factor of 240 mV/MeV according to the AMPTEK A225F charge-sensitive preamplifier specifications. The energy loss in the detector and respectively the dose are transformed into digital signals and sorted into 256 channels by a multichannel analyzer. For every exposure interval of 10 s, a single 256 channels energy deposition spectrum is collected.

A system international (SI) determination of the dose is used to calculate the absorbed dose in the silicon detector. The dose in SI is the energy in Joules deposited in one kilogram of matter. The dose *D* (Gy) in the silicon detector is calculated from the spectrum as:

$$D = K * \Sigma_1^{256} (Ei * Ai)/MD, \quad (1)$$

Where *MD* is the mass of the detector (in kg), *Ei* is the energy loss (in Joules) in the channel *i*, *Ai* is the number of events in it, and *K* is a coefficient. Dachev et al. [2002, 2017] have published more details of the dose calculation procedures. According to the formula (1) the dose rate is a function of the count rate in the 256 channels or totally a function of the flux. That is why in the paper these two parameters are interchangeable.

The R3DR2 data selection procedures [Dachev 2009; Dachev et al., 2017] recognize in the near Earth space the following four primary radiation sources: (1) The globally distributed primary Galactic Cosmic Rays (GCR) particles and their secondary products; (2) The inner radiation belt (IRB) trapped protons in the region of the South Atlantic Anomaly (SAA); (3) The relativistic electrons and/or bremsstrahlung in the high latitudes of the station orbits, where the horns of the outer radiation belt (ORB) are situated; (4) The solar energetic particles (SEP). These four radiation sources were measured in the R3DR2 instrument ISS data [Dachev et al., 2016], too.

Results

Figure 2 presents the results. Panel (2a) shows the variations of the calculated daily average ORB dose rate from 24 October 2015 until 16 January 2016. Panel (2b) depicts the 3D L and time graphic of the inner and outer belt maximal flux variations. In the top part of panel 2b with black line are the Dst index variations, while the average altitude of ISS (in km) is presented on the bottom.

The simultaneously analysis of the red curve in Panel (2a) and the black curve in Panel (2b) shows that the average daily dose rate anticorrelate the daily Dst index. This is connected with the geomagnetic activity, represented with the Dst index (http://wdc.kugi.kyoto-u.ac.jp/index.html) or solar wind variations. During the quiet time, between October 24, 2014 and the middle of March 2015, the doses delivered by the relativistic electron flux in the ORB are at very low levels - up to 260 μGy d^{-1}. Relativistic electron flux typically decreases, by two or three orders of magnitude, during the main phase of geomagnetic storms and recovers to or increases beyond the pre-storm level during the recovery phase, within several days [Zheng et al., 2006].

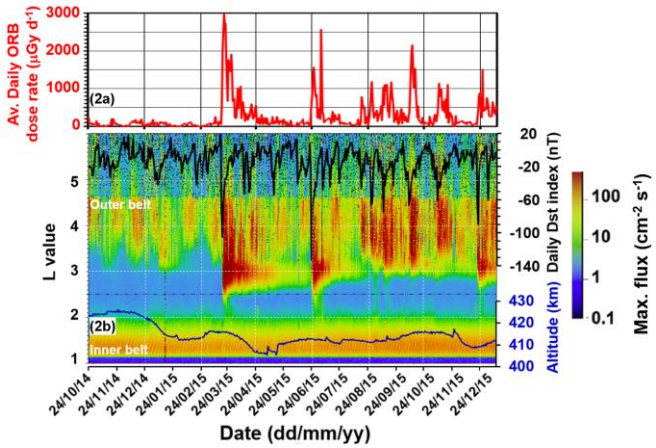

Figure 2. *Panel (2a) presents the Variations of the calculated daily average ORB dose rate from 24 October 2015 until 16 January 2016 as measured by the R3DR2 instrument. Panel (2b) shows 3D L and time graphic of the inner and outer belt maximal fluxes in same range for both belts between 0.1 and 4000 cm^{-2} s^{-1} as seen by the color code bar in the left hand side of the figure. The bins with size of 0.02 L value units are organized in a 442 daily vertical bars. They extend between L equal to two and six against the horizontal date axes. The ISS maximal flux bins cover the whole L values range from 2 to 6 in the Southern hemisphere, while in the Northern hemisphere the flux data bins are extended only up to L = 4.7, due to the asymmetries of the Earth magnetic field. This explains the borderline seen in Fig. 2 at L about 4.7 and the smaller population of the bins in the L range between 4.7 and 6.*

Panel 2b shows both belts. The IRB is distributed in the L range between L=1.2 and L=2.5. This feature is clearly seen in the four upper panels of Figure 3. The IRB maximal dose rate values reached 2500 μGy h^{-1}. The flux and dose rate were large during the interval from October to December of 2014; then, they fell until the end of June 2015 and increased again until the end of the measurements. These long-term variations correlated well with the variations in the average altitude of the station (blue line in the bottom of the Panel (2b). The altitudinal dependence in the bottom part of the IRB was studied by the R3DR data [Dachev et al., 2015].

Obvious depletions in the IRB flux, the daily and hourly maximal doses, were observed in the recovery phase of the magnetic storms presented with the Dst curve in Figure 2. We assume that the effect is similar to the one described by [Dachev et al., 2018].

The ORB in Panel (2b) of Figure 2 extends in the L range between 2.5 and 6. The ORB dynamics is much larger than the IRB belt dynamics in both categories maximal flux value and L-value extension.

Two periods are clearly seen in Figure 2 data. In the relatively "quiet" period, the ORB fluxes are relatively small and the equatorward boundary of the ORB varies in the interval of L between 3 and 4. The ORB relativistic electrons equatorward boundary never penetrates at L values below 2.5.

During the "disturbed" period, between 17 March 2015 and the end of the observations, strong variations in the ORB maximal flux and daily average dose rates were observed. The highest maxima was recorded on March 20th 2015, when the daily average dose rate was 2962 μGy d^{-1} and the averaged for the day flux was 361 cm^{-2} s^{-1}.

The penetration of the energetic electrons from outer radiation belt to lover L-values and to inner radiation belt in Figure 2 is seen as yellow-green veils, which extended from the equatorward boundary of ORB down to IRB. The equatorward boundaries of the penetrations are not clear seen. Figure 3 clarifies the penetration dynamics in time and L-value.

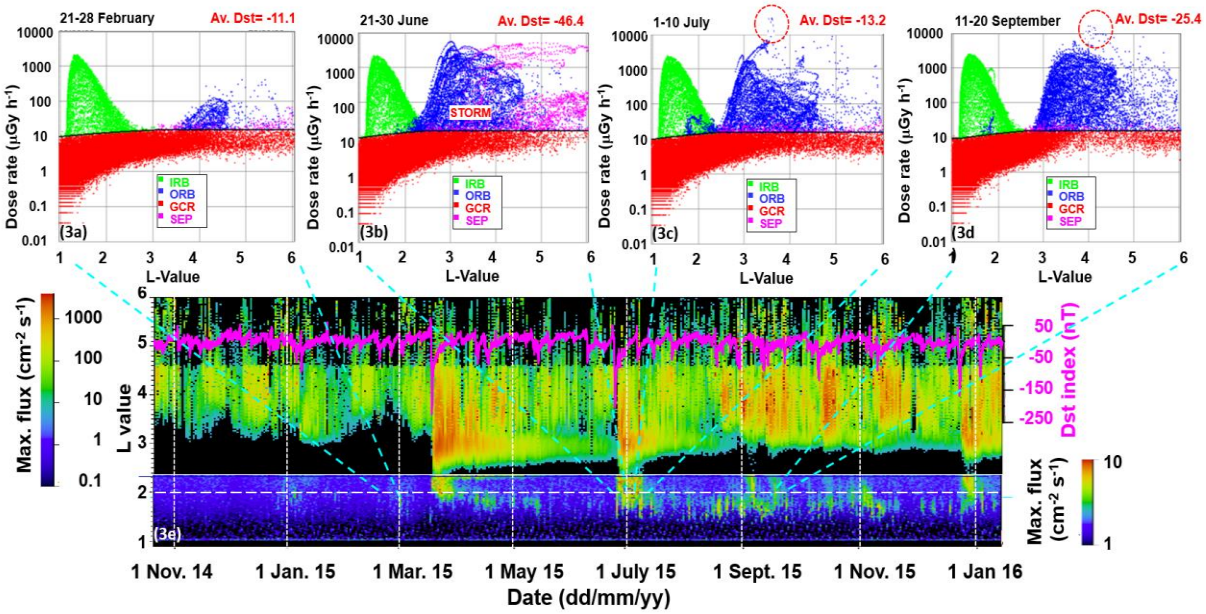

Figure 3. *The upper row with four Panels (3a) to (3d) illustrates the different cases of penetration of energetic electrons toward lower L-values and the inner radiation belt. The Panel (3c) contains two 3D L and time graphics with different maximal flux ranges. Panel (3e) aim is to show the penetration dynamics in time and L-value as seen by the two color code bars in the right and left side of the panels.*

Panel (3a) presents the latitudinal distribution of the dose rates against McIlwain's L values [McIlwain, 1961]. The L value is plotted on the x-axis. On the y-axis, the absorbed dose rate is plotted. Panel (3a) plots 69,312 points with 10-s resolution for 8 days from 21 to 28 February 2015.

Four different primary radiation sources separated by the heavy black line are seen in the data. These sources are plotted in Panel (3a) with four different colors: for the IRB-green, ORB-blue, GCR-red, and SEP-magenta. SEP data represent except the real solar energetic particles a small amount of secondary particles, which are characterized with similar than SEP requirements. From one 10 s independent measurement of the dose rate (D) and flux (F), we were able to calculate one dose to flux ratio (D/F). Using this, we were able to decide only what the predominant radiation sources is, but we are unable to extract the exact doses of each source [Dachev et al., 2017].

Panel (3a) illustrates the sources distribution during one of the quietest geomagnetic periods of the R3DR2 data. The average for 8 days Dst value is -11.1 nT. In these days the maximal ORB source value is at the level of about 220-μGy h^{-1}, which is the smallest in comparison with other three panels in the first row of Figure 3. In addition, the slot region is the largest and practically empty from any particles. No energetic electrons from the IRB source are observed.

Completely different sources distribution is shown on Panel (3b). The latter presents data for the period 21-30 June 2015 when a geomagnetic storm with a minimal Dst index of -204 nT on 23 June 2015 at 04 UT occurred (http://wdc.kugi.kyoto-u.ac.jp/index.html). GCR and IRB

sources do not show any drastic changes in comparison with the data in Panel (3a). The SEP source variations during this period are described in [Dachev et al., 2016], while the IRB source variations in [Dachev et al., 2018].

The ORB dose rate values variations are also well-studied [Dachev et al. 2017] that is why here we will concentrate on ORB spatial variations in L coordinates. The first difference from Panel (3a) seen in Panel (3b) is that the ORB electrons fulfil the whole slot region and extend down to L=1.7 inside the inner belt. Lucking in Panel (3e) we can see that similar process is observed after the main phase of the storm in March 2015. It happens at every Dst disturbance after 18th March 2015. The penetrated electrons patches in low L-value exist for a few days, disappear and appear again at next geomagnetic disturbance.

Second difference in Panel (3b) is the existence of two large profiles in L-value of SEP particles (magenta points), generated after the SEP event that started on 21 of June 2015 at 21:35 UT (https://umbra.nascom.nasa.gov/SEP/). The smaller SEP dose rate values profile reflects the values in the end of SEP event, while the larger the doses - the beginning [Dachev et al., 2016].

Panel (3c) presents the most dynamic 10 days ORB source distribution in L-values for the whole period of observations between November 2014 and January 2016. High dose rate patches are seen. The largest penetration of relativistic electrons below L=2 is observed. Also, in the dashed line oval in the top part of the panel are seen points with dose rate values larger than 10,000-μGy h^{-1}, which according to our classification in [Dachev et al., 2018] are indications of "Precipitation bands" [Blake et al., 1996]. The maximum ORB ever observed flux for 10-s of 11,813 cm^{-2} s^{-1} and dose rate of 28,840 μGy h^{-1} values were observed at about 22:30 local magnetic time on 4th of July 2015. The average daily dose rate maximum on the 4th of July is the second largest in Panel (3a) of Figure 3

Panel (3d) is remarkable that even that the slot region is empty of ORB energetic electrons in the L-value range 1.6-2 they energetic electrons still exists.

The Panel (3e) contains two 3D L and time graphics with different maximal flux ranges as seen by the two color code bars in the right and left side of the Panel. The lover part of the Panel (3e) in the L range from 1.2 to 2.4 presents the whole dynamics of the penetrations of relativistic electrons between 24 October 2014 and 16 January 2016.

Similarly to [Claudepierre et al. 2017], we recorded the first strong penetration of the relativistic electrons below L=2.5 on March 18, 2015. In the period March 18–28, 2015 the lowest boundary of L=1.7 was reached. Then the relativistic electrons at a low L disappeared on March 28, 2015. The storm on June 25, 2015 moved again the fluxes of ORB relativistic electrons at L-values below two and they are clearly seen in the lower part of Panel (3e). The ORB enhancement on July 4, 2015 emphasized them again but at this case the minimal L-values reached was L=1.6. Almost all disturbances in the Dst from July 11, 2015 until January 1, 2016 generated a new portion of relativistic electrons in the range of L-values between 1.6 and 2. They existed for few days and disappeared until the next Dst disturbance and magnetic substorm.

Conclusions

The most important achievement of the paper is the discovery and the proof of the existence of the relativistic electron fluxes (REF) in the R3DR2 data in the slot region and inner radiation belt in the time after the magnetic storms in March and June 2015;

All REF were observed in the period March-December 2015 during the EXPOSE-R2 mission. REF were not observed in the slot region and inner radiation belt during EXPOSE-E and EXPOSE-R missions. Never the less that, relativistic electrons fluxes do not pose a real health concerns for astronauts being on extravehicular activities it is important this phenomena to be further studied.

Acknowledgements

The authors would like to thank all Bulgarian and foreign specialists and organizations that participated in the development and funding of the projects with Liulin equipment. The authors would like to express their deepest gratitude to the astronauts and cosmonauts aboard the manned space stations "Mir" and ISS for conducting experiments with Liulin spectrometers.

Data availability

The data, used in this paper, are part of the "Unified web-based database with Liulin-type instruments" that are available online, free of charge at the following URL: http://esa-pro.space.bas.bg/database. The database contains data from nine Liulin type experiments around the Earth and Liulin-MO data in the path to Mars (2016-2017) and in Mars orbit (Since 2017) [Semkova et al., 2023]. Each data point contains up to 256 parameters, which except the measured values listed the time and space parameters of the carrier.

References

Blake, J.B., Looper, M.D., Baker, D.N., Nakamura, R., Klecker, B., Hovestadt, D., 1996. New high temporal and spatial resolution measurements by SAMPEX of the precipitation of relativistic electrons. Adv. Space Res. 18 (8), 171–186.

Claudepierre, S.G., et al. 2017. The hidden dynamics of relativistic electrons (0.7-1.5 MeV) in the inner zone and slot region. J. Geophys. Res. Space Physics 122. https://doi.org/10.1002/2016JA023719.

Dachev, T., Tomov, B., Matviichuk, Y., Dimitrov, P., Lemaire, J., Gregoire, G., Spurny, F., 2002. Calibration results obtained with Liulin-4 type dosimeters. Adv. Space Res. 30, 917–925. https://doi.org/10.1016/S0273-1177(02)00411-8.

Dachev, T.P., 2009. Characterization of near Earth radiation environment by Liulin type instruments. Adv. Space Res. 44, 1441–1449. https://doi.org/10.1016/j.asr.2009.08.007.

Dachev, T.P., Tomov, B.T., Matviichuk, Yu.N., Dimitrov, Pl.G., Bankov, N.G., Shurshakov, V.V., Ivanova, O.A., Hader, D.-.P., Schuster, M.T., Reitz, G., Horneck, G., 2015. "BION-M" №1 spacecraft radiation environment as observed by the RD3-B3 radiometer-dosimeter in April-May 2013. Journal of Atmospheric and Solar-Terrestrial Physics 123, 82–91. https://doi.org/10.1016/j.jastp.2014.12.011.

Dachev, T.P., Semkova, J.V., Tomov, B.T., Matviichuk, Y.N., Dimitrov, P.G., Koleva, R.T., Kubancak, I.N., 2015a. Overview of the Liulin type instruments for space radiation measurement and their scientific results. Life Sci. Space Res. 4, 92–114. https://doi.org/10.1016/j.lssr.2015.01.005.

Dachev, T.P., Tomov, B.T., Matviichuk, Y.N., Dimitrov, P.G., Bankov, N.G., 2016. High dose rates obtained outside ISS in June 2015 during SEP event. Life Sci. Space Res. 9, 84–92. https://doi.org/10.1016/j.lssr.2016.03.004.

Dachev, T.P., Bankov, N.G., Tomov, B.T., Matviichuk, Y.N., Dimitrov, P.G., Häder, D.-P, Horneck, G., 2017. Overview of the ISS radiation environment observed during the ESA EXPOSE-R2 mission in 2014–2016. Space Weather, Vol. 15, 1475–1489, https://doi.org/10.1002/2016SW001580.

Dachev, T.P., South-Atlantic Anomaly Magnetic Storms Effects as Observed outside the International Space Station in 2008-2016, 2018. JASTP, 179, 251-260. https://doi.org/10.1016/j.jastp.2018.08.009

McIlwain, C.E. (1961). Coordinates for mapping the distribution of magnetically trapped particles. Journal of Geophysical Research, 66, 3681–3691. https://doi.org/10.1029/JZ066i011p03681

Reitz, G., Beaujean, R., Benton, E., Burmeister, S., Dachev, T., Deme, S., Olko, P., 2005. Space radiation measurements on-board ISS-the DOSMAP experiment. Radiat Dosimetry 116, 374–379. https://doi.org/10.1093/rpd/nci262.

Semkova, J., Koleva, R., Benghin, V., Krastev, K., Matviichuk, Y., Tomov, B., Maltchev, S., Dachev, T., Bankov, N., Mitrofanov, I. and Malakhov, A., 2023. Observation of the radiation environment and solar energetic particle events in Mars orbit in May 2018-June 2022. Life Sciences in Space Research. https://doi.org/10.1016/j.lssr.2023.03.006.

Zheng, Y., Lui, A.T.Y., Li, X., Fok, M.-C., 2006. Characteristics of 2–6 MeV electrons in the slot region and inner radiation belt. J. Geophys. Res. 111, A10204. https://doi.org/10.1029/2006JA011748.

LOFAR-BG Current State

Dechev M.Ts.[1], *Kozarev K.*[1]

[1]Institute of Astronomy with NAO, Bulgarian Academy of Sciences; mdechev@astro.bas.bg

1. Abstract.

LOFAR (LOw Frequency ARray) is the largest radio telescope operating at the lowest frequencies that can be observed from Earth. LOFAR makes observations in the 10 MHz to 240 MHz frequency range with two types of antennas: Low Band Antenna (LBA) and High Band Antenna (HBA), optimized for 10-80 MHz and 120-240 MHz respectively. The electric signals from the LOFAR stations are digitised, transported to a central digital processor, and combined in software in order to map the sky. Now there are LOFAR stations in Netherlands (38 stations), Germany (six stations), Poland (three stations), France, Ireland, Latvia, Sweden, and the United Kingdom (one station each); stations in Italy and Bulgaria are funded to be built.

Keywords: LOFAR; radio; low frequency; astronomy; Rozhen observatory.

2. Introduction

The International LOFAR Telescope (ILT) is one of the foremost radio astronomy observatories in the world, established in 2010, and now undergoing a significant upgrade that will keep it at the cutting edge throughout the next decade and beyond. Highly innovative LOFAR electronic antenna stations are connected by wideband fiber connections to powerful computer clusters. The data are stored in archives encompassing many Petabytes, and processed with advanced algorithms and software involving the very same techniques used for the widely publicized recent M87 black hole image.

The ILT has the ability to transform science projects, probing deeply into the early Universe, allowing major progresses in the understanding of extremely energetic cosmic phenomena, and offering unique tools for studying the Sun, even of the Earth's Ionosphere and Space Weather phenomena. It is also possible to use its advanced technology platform to develop transformational science projects.

The ILT, as a major observatory in its own right, and also a science and technology pathfinder for the planned Square Kilometre Array (SKA), has not only sparked the interest of astronomer groups around the world, but is drawing international attention from commercial high-tech companies. LOFAR scopes out much of "modern" parameter space, with its advanced sensor technology, coupled to cutting-edge ultra-high volume data connectivity over fibre, and state-of-the-art information processing technology to handle the highly complex task of detecting millions upon millions of extremely faint celestial objects in the presence of a host of perturbing influences on the radio signals. To be sure, in the era of the SKA, the ILT will be an important complement, with higher image resolution and longer wavelength coverage, to which a Bulgarian LOFAR station will make important contributions.

3. LOFAR-BG – Part of The National Roadmap for Research Infrastructure 2020-2027

The initiative to establish a LOFAR-BG station of radio antennas is spearheaded by Dr. Kamen Kozarev of the Bulgarian Academy of Sciences.

In May 2020, the infrastructure project LOFAR-BG, coordinated by the Institute of Astronomy and National Astronomical Observatory (IANAO), was approved for inclusion in the updated National Roadmap for Scientific Infrastructure 2020-2027 (NRSI), created and supported by Bulgaria's Ministry of Education and Science. Currently, members of the national consortium for managing the project also include the Dept. of Astronomy of Sofia University, the Dept. of Astronomy of Shumen University, as well as the Dept. of Radio Communication and Video Technologies of the Technical University-Sofia. In the future, we will be adding new partners to the consortium.

The LOFAR-BG station (Figure 1.) will significantly enhance the observing capabilities of the ILT. First, it brings welcome extra sensitivity. A particular strength is the location in southeastern Europe: combining its sensor data with data from stations further north (in Poland) and west (in Italy) will give added "telephoto zoom" capability for more detailed imaging of the sky.

Bulgarian scientists will join in the ILT at the stage where considerable expertise with its novel technical concepts has already accrued. The LOFAR user community (among them more than a dozen ERC grantees already) is rapidly expanding, and an ever-increasing number of publications is emerging in the world's leading peer-reviewed scientific magazines. Joining will mean that the Bulgarian community can be tutored along very steep learning curves, and then can proceed to use the ILT for its research, as well as to contribute to the on-going development of ever more sophisticated electronics, data processing and analysis tools.

Further developments will surely take place in part in the context of existing and continuing national, multinational, and EC funding opportunities.

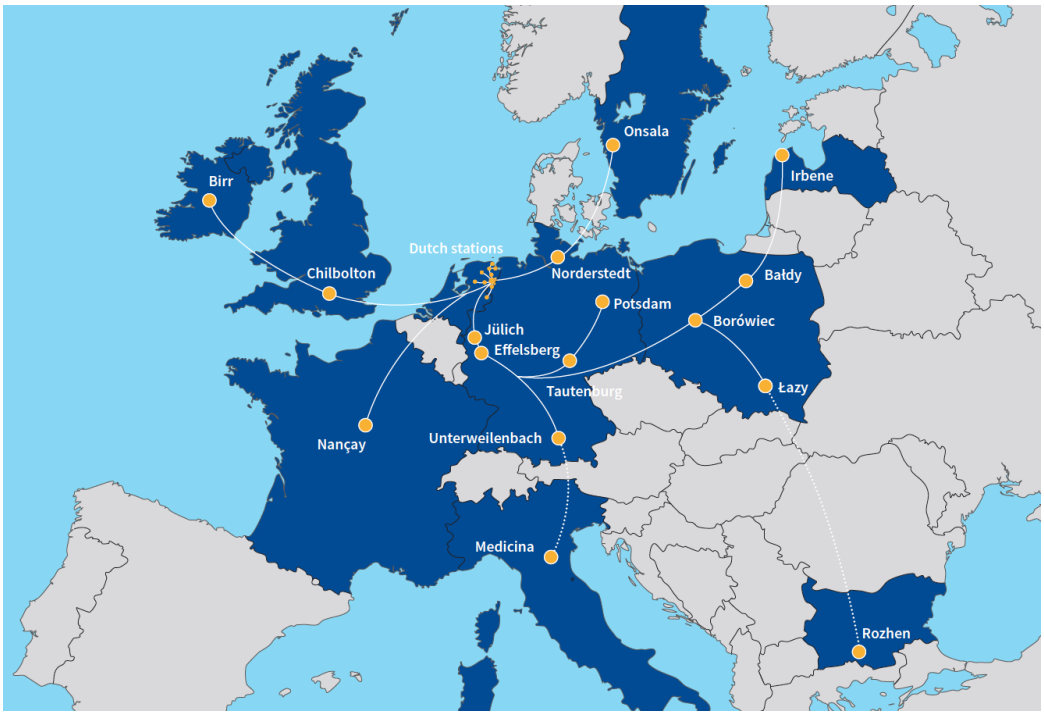

Figure 1. LOFAR Stations across Europe

4. LOFAR-BG – current state

We are currently working on preparing for the station (near NAO Rozhen, see Figures 2, 3):

- LOFAR-BG – part of The National Roadmap for Research Infrastructure 2020-2027
- Building power and communications infrastructure;
- Planning changes to the general municipal layout plan;
- Planning land works for flattening the terrain (2023 - 2024).

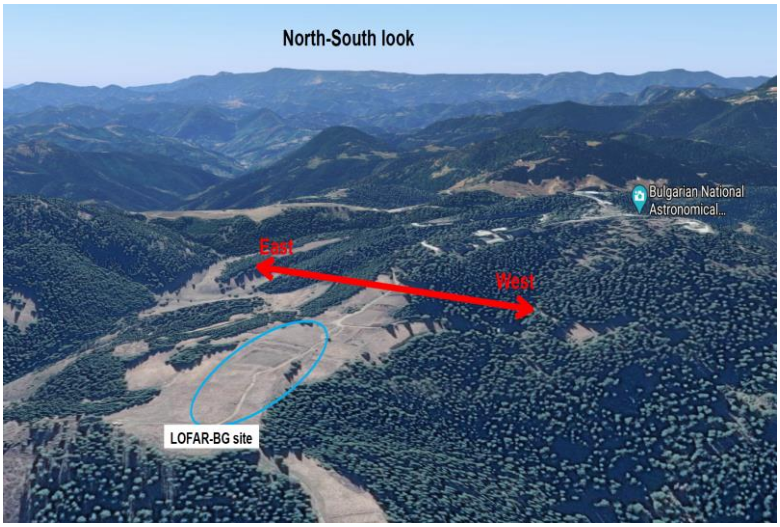

Figure 2. LOFAR -BG site near National Astronomical Observatory

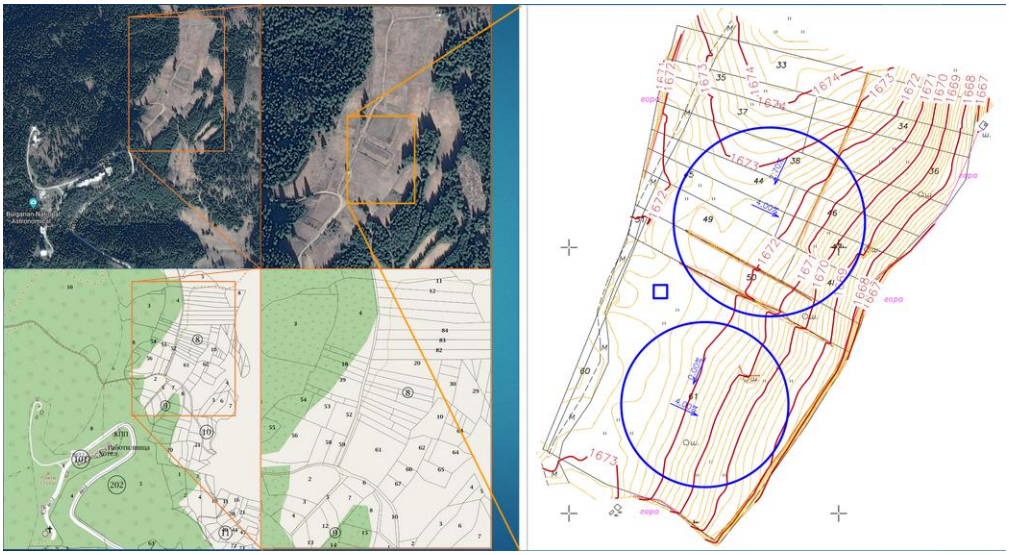

Figure 3. LOFAR-BG site and station plan

The Schedule for LOFAR-BG is shown here below:

Phase/Year	2021	2022	2023	2024	2025	2026	2027	2028	2029	2030	2031	2032	2033
Design / preparatory													
Building													
Operations													
ILT Participation													

IANAO has obtained the funding covering the purchase and construction of an International LOFAR2.0 station in Bulgaria

● The LOFAR-BG Consortium (through IANAO) contributes to the central operations of the ILT starting 1 January 2023.

● LOFAR-BG will participate in the development of upgrades of LOFAR within the LOFAR2.0 programme, by contributing to the development costs, hardware purchases and rollout.

● IANAO acts as the Representing Entity of Bulgaria in its role as a Founding Member of LOFAR ERIC.

● IANAO will participate in the DANTE development project, designing upgraded LOFAR high-band antenna tile electronics, which it intends to use in the LOFAR-BG station to be constructed.

● LOFAR-BG participates in the Incremental Development of LOFAR for Space weather (IDOLS) project

Closely related to the LOFAR-BG is the STELLAR (Scientific and Technological Excellence by Leveraging LOFAR Advancements in Radio astronomy) Horizon 2020 project. It started on September 1, 2020. with the following objectives:

- To transfer knowledge and capacity from ASTRON and DIAS to IANAO and TUS staff by means of versatile training activities;
- To expand the research potential of the local solar and space weather experts using LOFAR observations;
- To enable IANAO and TUS scientific and engineering personnel to develop expertise for building and operating a Bulgarian LOFAR station;
- To develop local educational curricula for sustainable development of radio astronomy in Bulgaria.

In 2023 we held 3 schools for Bulgarian students, PhD students, and scientists: LOFAR radio technology school; A radio astronomy and LOFAR school and a space weather and LOFAR school. All ectures from the seminars and trainings of schools can be found on the web site: https://www.stellar-h2020.eu.

The LOFAR-BG site is https://lofar.bg.

Acknowledgement

This work was supported by LOFAR-BG, part of the National Roadmap for Scientific Infrastructure (2020-2027), coordinated by the Ministry of Education and Science of Bulgaria (contracts D01-389/18.12.2020 and D01-177/29.07.2022).

Numerical Simulation of the LIULIN-MO Device

Krastev K.[1], Semkova S. [1], Koleva R. [1], Benghin V.[2], Drobyshev S.[2]

[1]Space Research and Technology Institute, Bulgarian Academy of Sciences
[2] Institute of Biomedical Problems of Russian Academy of Sciences

Abstract.

In this paper, we present the numerical simulation results of the Liulin-MO instrument on board the Trace Gas Orbiter (TGO) of the ExoMars-2016 mission to Mars [Semkova et al., 2018], focusing on the two solar proton events (SPE) of October 2021 and February 2022 [Semkova et al., 2023]. With the help of the simulation it is shown what is the energy of the protons of these events.

Introduction

One of the main problems in the registration and identification of ionizing radiation in space is the influence of the design of the instrument.

The spectrum of galactic cosmic rays is wide in both composition (from protons to the heaviest nuclei) and energies (from a few keV to $10^{21}eV$). The interaction of a specific component of the GCR spectrum, with the construction of the instrument and the detector system, is determined by the type and energy of the corresponding component of the spectrum. The secondary particles generated by this interaction in turn interact with the construction of the instrument and the detector system, thus the received signal from the detector system does not unambiguously determine the characteristics of the primary particle. The specifics of the main task consist in creating a model that reproduces as accurately as possible the environment and operation of the Liulin - MO instrument in interplanetary space.

The volume and complexity of the task require, as the only option, the use of numerical models for the transport of the radiation through the matter. There are many software packages for modeling the interaction of charged particles with matter. Some of them are designed for specific tasks and radiations. Geant4 is one of the most powerful packages, which includes a large set of possibilities and gives great freedom in the modeling of various tasks [Agostinelli et al., 2003]. It was developed by the Geant4 Collaboration (CERN and other institutes) in the object-oriented language C++. The application area of Geant4 includes particle physics and nuclear reaction research, medicine, particle accelerators and space exploration.

When studying the two solar proton events that happened on 28-31 October 2021 and 15-19 February 2022, the task is greatly facilitated because the type of particles (protons) is known. Why we consider the events to be primarily formed by protons is explained below.

Figure 1 shows all available data obtained from the Liulin-MO instrument from 2016 till now. The two SPE events subjects of our task are clearly visible. Figure 1 shows the dependence of the count rate on the energy channel of deposited energy. The two events differ in size but have approximately the same shape, which suggests that in both cases we have the same type of particles with the same energies.

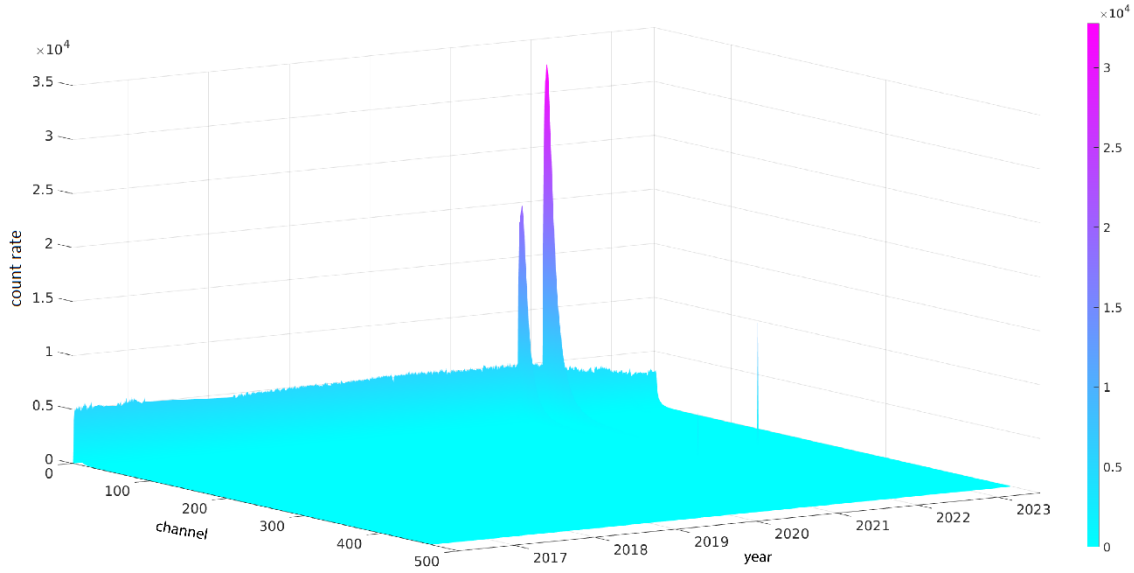

Figure 1: Dependence of count rate on date and channel for the single detector AB – Liulin-MO instrument.

Methods

The software we use is g4app application [Ivanov, S., 2021] using the Geant4 framework. In order to shorten the machining time we have made a simplified geometry of the Lliulin-MO instrument and TGO. The geometry we use is shown in Figure 2.

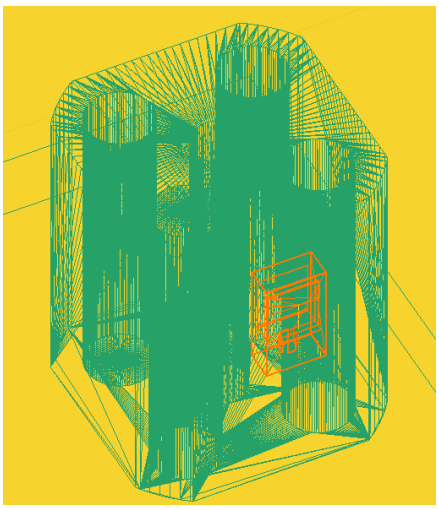

Figure 2: CAD model of the dosimeter Lyulin-MO, FRIEND and TGO. FREND and TGO in green, Liulin construction in orange lines.

The approach used in the modeling of the instrument is presented in [Zhao et al., 2013] and [Pak et al., 2018]. Figure 3 shows the schematic diagram of the simulation. The body of the Liulin-MO instrument is shown in yellow, the detector system is indicated in green. The points of the sphere serve as sources of generated particles, the distribution of generated particles is cosine.

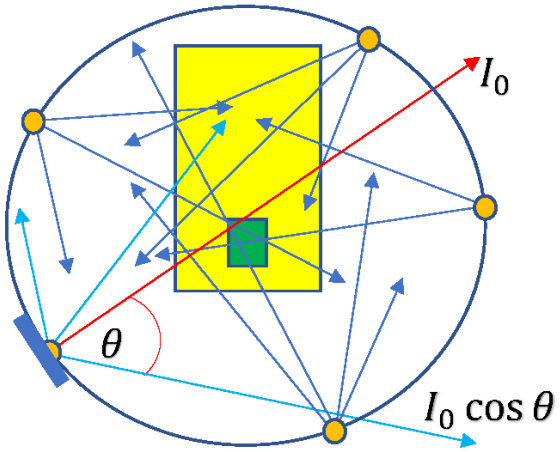

Figure 3: Schematic diagram of the simulation

The assumption we make about the flux of protons is that it is approximately isotropic. This assumption is based on the complex trajectories along which solar protons move in the interplanetary magnetic field. Reaching a distance of 1.5 AU from the sun, the flux can roughly be assumed to be isotropic. 10^8 protons are generated in the program for each of the energies 50, 100, 200, 300, and 400 MeV. In parallel we do a series of simulations for the same energies but the generated protons beam is not isotropic, it falls perpendicular to the surface of the two detectors composing the single detector AB (Figure 4).

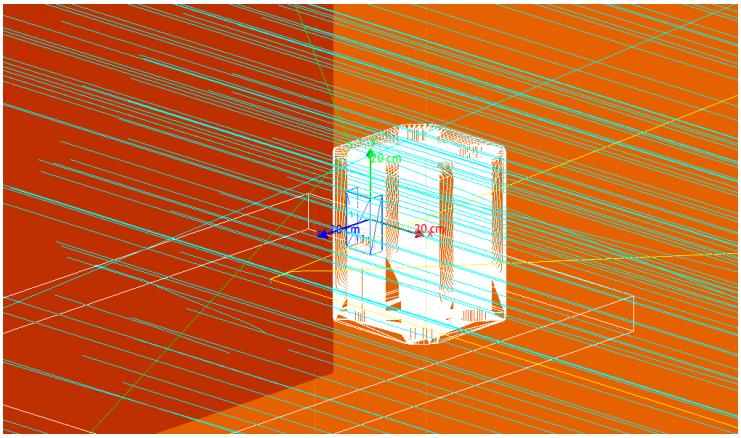

Figure 4: Simulation of a parallel beam of protons, the beam of protons is shown in cyan, in white - FREND+TGO, with blue Liulin-MO.

Results

Figure 5 shows the simulation results for isotropic proton flux. For each of the channels it is shown what percentage of the entire count rate is registered in it. It can be seen that we have the best match between the measured events and a simulated flux of protons with energies between 200 and 300 MeV. Of course, the real spectrum is a sum of protons with different energies, but from the obtained results we can claim that the main flux is protons with energies between 200 and 300 MeV. One might wonder why we only consider protons in modulation. The answer is that the minimum energy that can deposit helium or heavy nuclei in silicon detectors is about 450 keV. The maximum of both events is about 200 keV deposited energy.

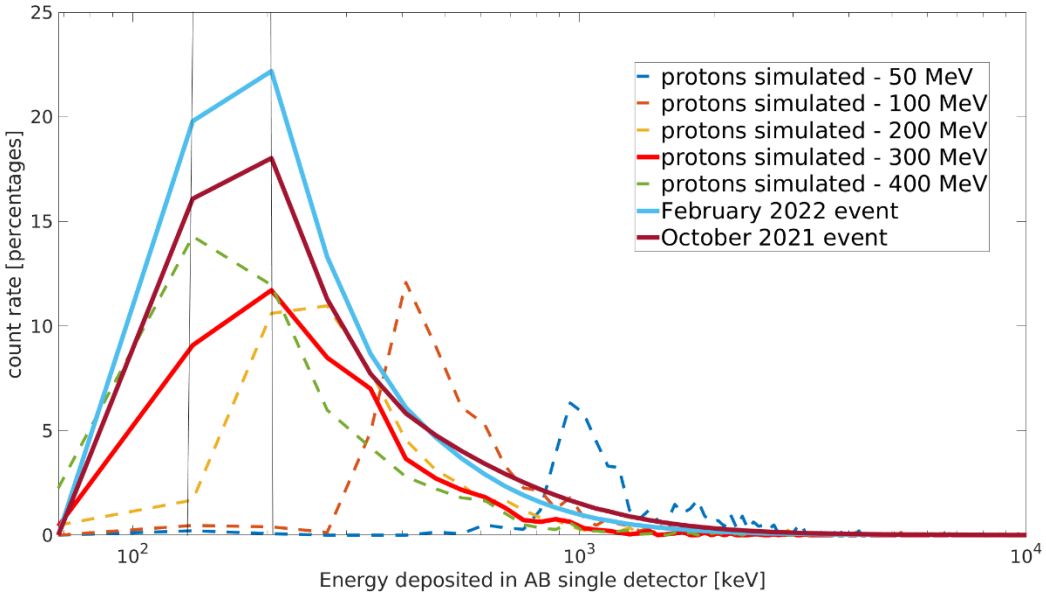

Figure 5: Simulation for isotropic radiation, proton count rate for different energies and both events (February and October). With solid lines are shown the February event in blue, the October event in wine and the 300 Mev protons simulation in red.

Figure 6 shows the simulation for a parallel beam of protons. It is again seen that the flux is composed of protons with energies between 200 and 300 MeV. Naturally, the accuracy of the obtained results is mainly formed by the assumptions stated above (about the isotropicity of the flux and the geometry of the task, which we have simplified). Comparing Figure 5 and Figure 6 we can conclude that the assumption of isotropic flux is very rough. If we abandon the isotropicity of the flux of solar proton events, then the task is reduced to finding the orientation of the instrument with respect to the direction of the flux. The task thus set becomes too complex and can be considered in the future.

For a flat detector the geometric factor is given by $2\pi S$ [Thomas & Willis., 1972], where S is the area of the detector. For the single Lulin-MO detector this formula gives a geometric factor $4\pi = 12{,}56\ cm^2 sr$. The resulting formula is true for isotropic radiation. Figure 7 shows the calculated geometry factors from the simulation for protons with the energies considered. The figure shows that for energies from 200 to 300 MeV, the geometric factors calculated from the simulation are 1.1 smaller than the analytically calculated geometric factor i.e. to get the actual flux of solar proton events we need to multiply Liulin-MO's data by coefficient 1.1.

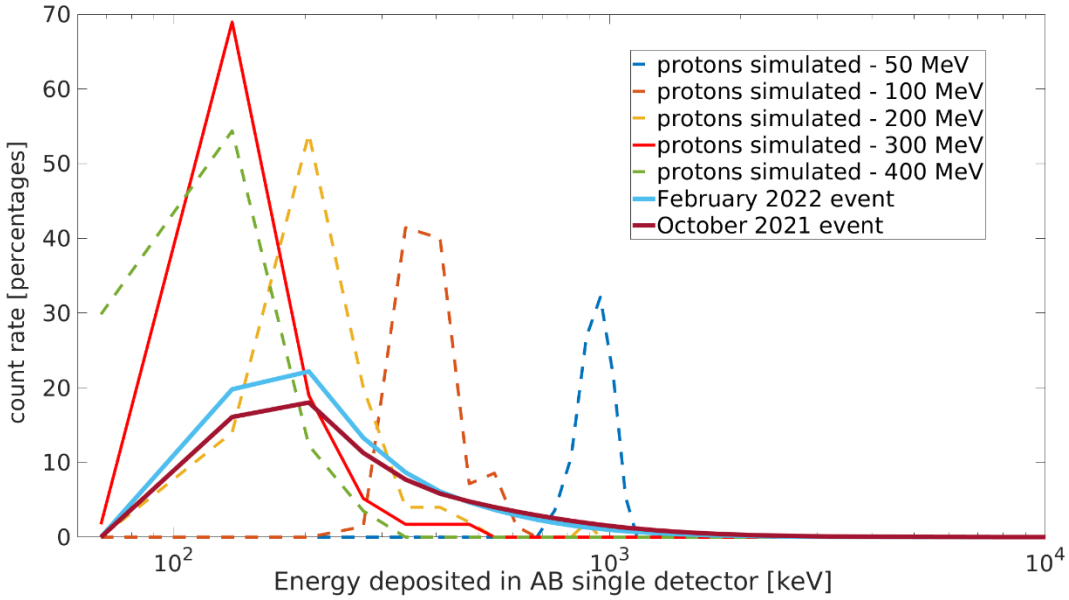

Figure 6: Simulation for a parallel beam of radiation, proton count rate for different energies and for both events (February and October). With solid lines are shown the February event in blue, the October event in wine and the 300 MeV protons simulation in red.

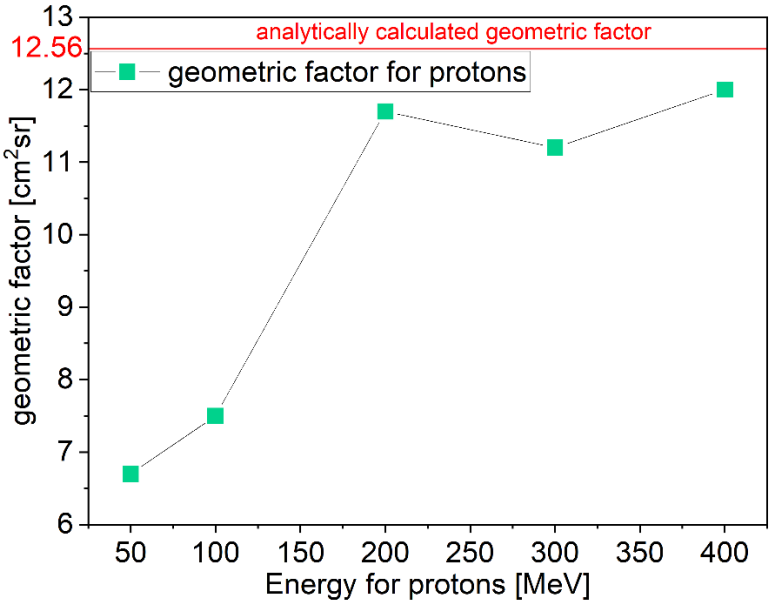

Figure 7: Simulation for isotropic radiation, the calculated geometry factor from the simulation for protons with different energies.

Conclusion

The numerical modeling is a powerful method for solving problems of radiation passage through matter. In many cases, this is the only possible approach for similar tasks. The results obtained in the present work are an initial stage of the development and application of more accurate models. Despite these simplified models, the obtained results show a good agreement with the experimental data. The main results obtained in the present work are:

1. It is shown that the flux of protons of the two solar proton events under consideration is with energies between 200 and 300 MeV.
2. To get the actual flux of solar proton events we need to multiply Liulin-MO's data by coefficient 1.1.

References

Agostinelli, S., et al., 2003. „Geant4 – a simulation toolkit", Nuclear Instruments and Methods in PhysicsResearch Section A: Accelerators, Spectrometers, Detectors and Associated Equipment, Vol. 506, Issue 3, Pages 250-303

Ivanov, S., Master's thesis, Sofia University, Faculty of Physics, 2021.

Pak S. et al., „A numerical method to analyze geometric factors of a space particle detector relative to omnidirectional proton and electron fluxes", Journal of the Korean Astronomical Society, August 2018

Thomas, G. R., & Willis, D. M., Analytical Derivation of the Geometric Factor of a Particle Detector Having Circular or Rectangular Geometry, JP, 5, 260, 1972

Semkova, J., et al, 2018. Charged particles radiation measurements with Liulin-MO dosimeter of FREND instrument aboard ExoMars Trace Gas Orbiter during the transit and in high elliptic Mars orbit, Icarus, Vol. 303, Pp 53-66, https://doi.org/10.1016/j.icarus.2017.12.034

Semkova J. et al, Observation of the radiation environment and solar energetic particle events in Mars orbit in May 2018- June 2022, Life Sciences in Space Research, 2023, https://authors.elsevier.com/sd/article/S2214-5524(23)00024-X

X. Zhao et al., „A Geometric Factor Calculation Method Based on the Isotropic Flux Assumption", CP,37, 126201, 2013.

Common Cycles of Solar Activity and Antarctic Oscillations

Chapanov Y.[1]

[1]Climate, Atmosphere and Water Research Institute, Bulgarian Academy of Sciences;
yavor.chapanov@gmail.com

Abstract

The Antarctic Oscillations play important role on various regional and global climatic event. These oscillations are used in study of recent climate change and to improve our knowledge about the climate dynamics. The main sources of these oscillations are the influence of solar activity on climatic variations and global warming. The solar activity affects climatic processes by the Total Solar Irradiance (TSI) variations, solar wind and solar magnetic field. The solar magnetic field and solar wind modulate the variations of heliosphere, geomagnetic field and cosmic rays, whose effect on atmosphere and climate is stronger on high-latitude polar regions. The cycles of solar magnetic field are connected with the North-South (N-S) solar asymmetry of sunspots. The solar influence on Antarctic Oscillations are analyzed by centennial time series of TSI and N-S solar asymmetry. The Antarctic Oscillations are represented by the time series of Southern Annular Mode (SAM) since 1850. The Common cycles of solar activity and Antarctic Oscillations are determined by the Method of Partial Fourier Approximation (PFA). Various common solar and atmosphere cycles in narrow frequency bands are detected, whose periodicity is between 3 and 80 years. This result may help to divide natural solar from anthropogenic effect in recent global warming and to improve scenario of future climate change.

Keywords: solar activity, Southern Annular Mode (SAM), TSI, N-S solar asymmetry, relative humidity.

Introduction

The Antarctic oscillation (AAO) or Southern Annular Mode (SAM) is a weather phenomenon at the Antarctic pole South of 40° latitudes. It is an important mode of climate variability for the Southern Hemisphere. The Antarctic Oscillation refers to a large scale alternation of atmospheric mass between the mid-latitudes and high latitudes surface pressure. It is defined as the difference of zonal mean sea level pressure between 40°S and 65°S. The AAO has the potential for clarifying climate regimes in the southern hemisphere.

The solar activity cycles affect all surface geosystems, including weather and climate indices, winds, rains, snow covers, mean sea level, river streamflows and other hydrological cycles. These processes are due mainly to the Total Solar Irradiance (TSI) variations, followed by weather and climate changes. Recently a new mechanism of climate modulation, based on cosmic ray variations, has been discovered. This mechanism explains chain processes arising from cosmic ray (CR) modulation by the heliosphere and geomagnetic field, followed by ozone production in near tropopause and water content change. The atmospheric water is the most powerful greenhouse gas and its changes produce significant variations of the temperature. The CR modulation by heliosphere depends on solar wind and solar magnetic field variations, represent by North-South (N-S) solar asymmetry. The solar activity affects terrestrial systems by means of direct radiation over Earth surface, influences charged particles of the solar wind, and the solar magnetic field. The solar wind directly affects Earth magnetic field, ionosphere and atmosphere. The variations of solar magnetic field modulate solar wind and cosmic rays in the frame of the solar system. The cosmic rays near Earth are modulated by Earth magnetic field variations, too. Recently, a new mechanism of climate variations, due to cosmic rays was proposed (Kilifarska, 2015; Kilifarska and Bojilova, 2019; Velichkova and Kilifarska, 2020, 2021). According to the new models, the cosmic rays produce an ionization of the atmosphere,

changes of atmospheric conductivity, and lightning, and an increase of ozone concentration. This mechanism is based on chain processes near tropopause by ozone production, temperature variations, followed by vertical winds and water content change. The last step of this chain affects strongly surface temperature, because the atmospheric water is one of the most powerful greenhouse gas. This model provides an explanation for the cascade processes in which cosmic rays, whose total energy is relatively small, cause climatic effects with much more energy. The solar activity cycles modulate the cosmic rays directly by the heliosphere and indirectly by the geomagnetic field changes, whose effect is visible mainly at high latitudes and regions with strong geomagnetic anomalies.

Data and Methods

The solar data are presented by the Total Solar Irradiance (TSI) and North-South solar asymmetry variations. The daily reconstruction of TSI data since 1850 is a composite of SATIRE-T reconstruction from (Krivova et al., 2014) for 1850 to 22 August 1974; and SATIRE-S reconstruction from (Yeo et al., 2014) for 23 August 1974 onwards (Fig.1). The 0.1-year values of TSI are calculated by means of robust Danish method (Juhl, 1984; Kegel, 1987; Kubik, 1982). This method allows to detect and isolate outliers and to obtain accurate and reliable solution for the mean values.

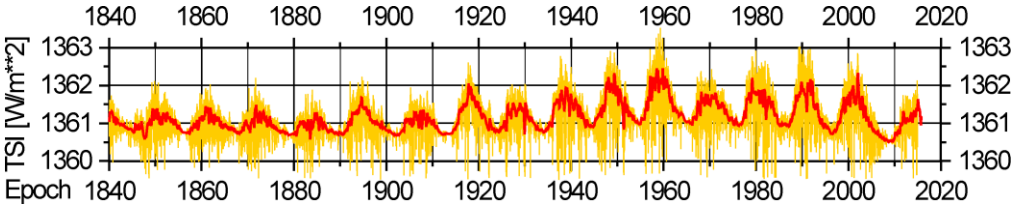

Figure 1. Time series of 0.1-year (in orange color) and daily values (in yellow color) of TSI.

The North-South solar asymmetry (Fig. 2) is determined from the relation $(S_n\text{-}S_s)/(S_n+S_s)$, where the S_n and S_s are monthly sunspot area on the Northern and Southern solar hemispheres, respectively (in units of millionths of a hemisphere). The data since 1874 are observed by the Royal Greenwich Observatory and merged after 1976 with the US Air Force (USAF) and the US National Oceanic and Atmospheric Administration (NOAA) data by D. Hathaway (https://solarscience.msfc.nasa.gov/greenwch.shtml).

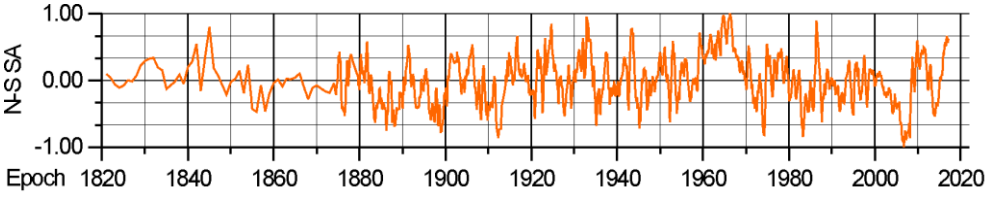

Figure 2. Time series of North-South solar asymmetry.

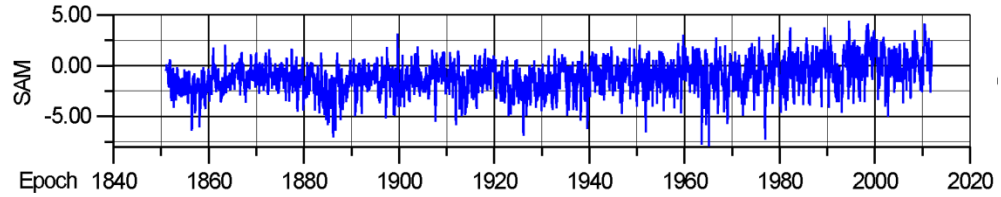

Figure 3. The time series of and Southern Annular Mode (SAM).

The Antarctic Oscillation time series since 1851 are prepared in Physical Science Laboratory of NOAA by the Method, described in (Gong and Wang, 1999) and available online at https://psl.noaa.gov/data/20thC_Rean/timeseries/monthly/SAM/sam.20crv2c.long.data (Fig. 3). The Antarctic Oscillation is defined as the difference of zonal mean sea level pressure

between 40°S and 65°S. Additional time series of mean relative humidity and temperature from the belts 40°S - 65°S and 65°S - 75°S are shown in Fig.4.

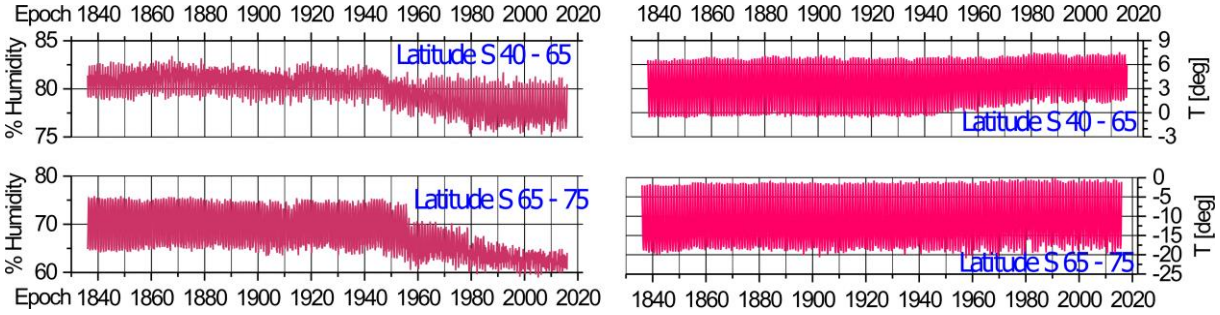

Figure 4. Relative humidity and temperature T from the belts 40°S - 65°S and 65°S - 75°S.

Results

The common cycles of SAM and solar activity are presented in Figs. 5 and 6.

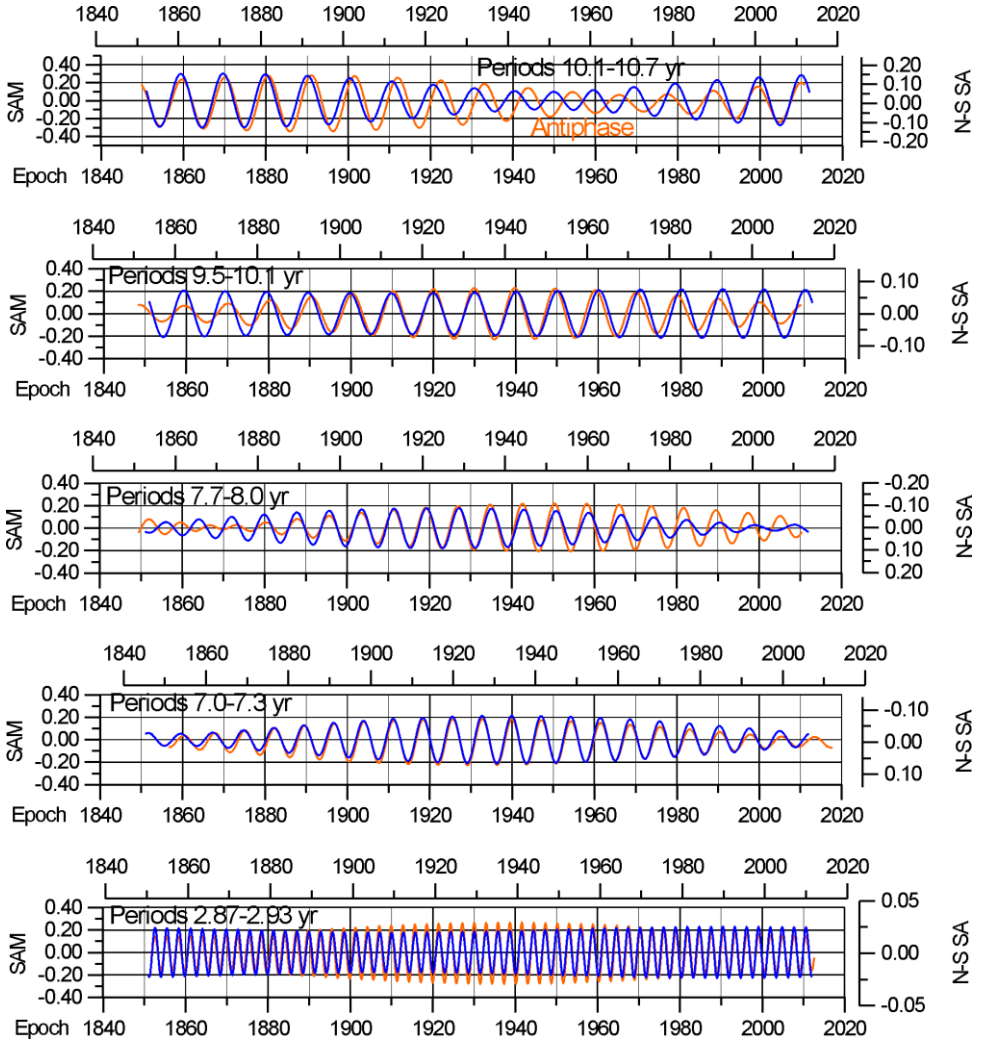

Figure 5. N-S solar asymmetry(orange color) influence on Antarctic Oscillation (blue color) with decadal and subdecadal periodicities

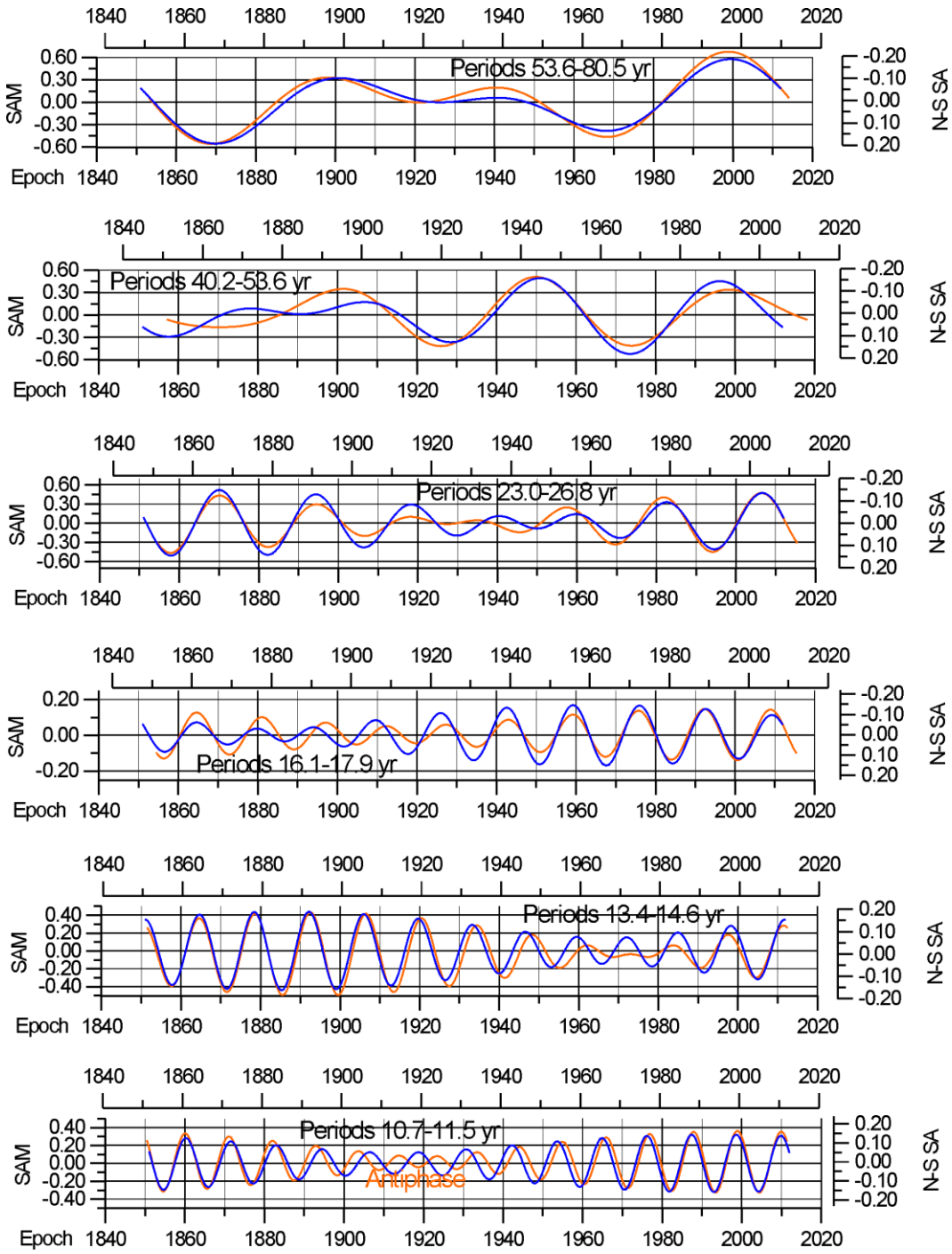

Figure 6. N-S solar asymmetry (orange color) influence on Antarctic Oscillation (blue color) with decadal periodicities.

The N-S solar asymmetry modulates solar magnetic field and corresponding variations of solar wind and heliosphere. These variations affect geomagnetic field, too. The high energy cosmic rays and charged particles penetrate heliosphere and they reach the Earth atmosphere after modulation by geomagnetic field. Maximal interaction between cosmic rays and atmosphere occur in high-latitude polar area, so the oscillations of the high latitude parts of the atmosphere are expected to be induced by cosmic rays, modulated by solar magnetic field variations. It is possible to detect tis interaction by common analyze of N-S solar asymmetry Index and Polar Indices. Common cycles of N-S solar asymmetry Index and Southern Annular

Mode are detected by the PFA Method (Chapanov et al., 2017) in 5 subdecadal (Fig. 5) and 6 decadal (Fig. 6) narrow frequency bands, whose periods are between 3 and 80 years. The determined common solar and atmospheric cycles have good agreement with short 30-year phase reverses around the 11-year solar cycle.

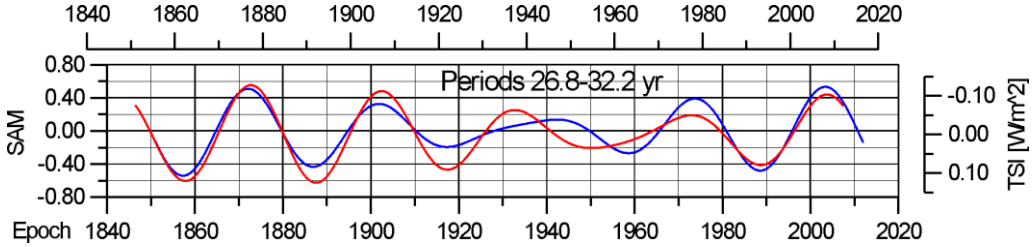

Figure 7. TSI (orange color) influence on Antarctic Oscillation (blue color) with decadal periodicities.

The decadal and subdecadal influence of N-S solar asymmetry on Antarctic oscillations is presented by common solar-ozone cycles are divided into 9 narrow frequency bands, whose periods are: 53.6-80.5 yr; 40.2-53.6 yr; 23.0-26.8 yr; 16.1-17.9 yr; 13.4-14.6 yr; 10.7-11.5 yr; 10.1-10.7 yr; 9.5-10.1 yr; 7.7- 8.0 yr; 7.0- 7.3 yr; and 2.87-2.93 yr

The mean variations of Antarctic Oscillation are determined in 2-year sliding window (Fig.8), where significant positive trends are visible after 1920 and 1965. The time series of relative humidity and temperature from latitudinal belt 40S – 65S demonstrate unusual behavior of strong jumps in 1945 and significant linear trends after 1945 and 1975/1980, more visible in the case of relative humidity. Possible explanation of these abrupt changes are jumps in solar magnetic field, expressed by the time series of N-S solar asymmetry (Fig. 9).

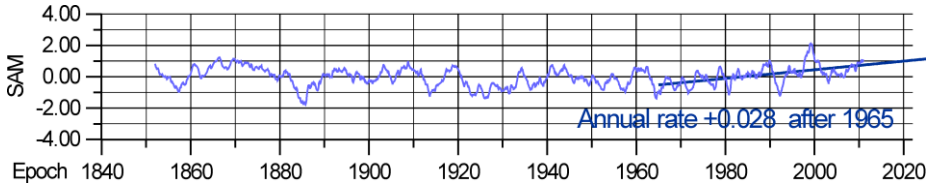

Figure 8. Mean variations of Antarctic Oscillation, determined in 2-year sliding window.

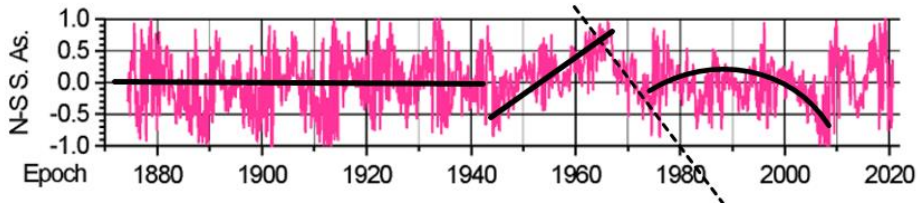

Figure 9. Some linear trends in variations of N-S solar asymmetry and strong jumps in 1945, 1975 and 2008.

Conclusions

The solar activity influence on Antarctic Oscillations is conducted by TSI variations and N-S solar asymmetry. Various narrow frequency bands are detected with common cycles of solar and atmospheric Indices, whose periods are between 3 and 80 years. The influence of N-S solar asymmetry dominates, because over the polar region the cosmic rays are concentrated by focus of geomagnetic field. Another zone of cosmic rays concentration is equatorial part of Pacific ocean, where the cosmic rays produce ozone in lower stratosphere and next strong influence on

ENSO event (Chapanov, 2019, 2021). An important aspect of recent climate change is visible global warming during the past decades. The mean variations of Antarctic Oscillations are calculated in 2-year sliding window. The averaged data have significant rising trends, with annual rate +0.028 after 1920 and 1965. A part of these trends are connected with the anthropogenic effects of global warming, but other significant part should be attached to the jumps of solar magnetic field, geomagnetic field, cosmic rays and stratospheric ozone. Other possible effects on rising trends are influences of solar activity, whose long-term oscillation is in the range of Gleissberg cycles of the solar activity with periodicity 80-120 years. So, in the case of significant long-term solar influence on global warming, connected with the Gleissberg cycles, it is possible to expect some decrease of the linear trends in climatic Indices in nearest future with probable initial epoch after 2030.

The separation of anthropogenic from natural effects of the global warming will be possible by new models of climate oscillations, based on the cycles of solar activity, lunar tides and solar magnetic jumps. Such kind of models of climate change may improve forecast accuracy and climatic scenario.

Acknowledgments

The study is supported by the National Science Fund of Bulgaria, Contract KP-06-N34/1 /30-09-2020 "Natural and anthropogenic factors of climate change – analyzes of global and local periodical components and long-term forecasts".

References

Chapanov Y., Ron C., Vondrák J., 2017, Decadal cycles of Earth rotation, mean sea level and climate, excited by solar activity. Acta Geodyn.Geomater., 14, No. 2 (186), 241–250, DOI: 10.13168/AGG.2017.0007

Chapanov Ya., 2019, ENSO Variations Driven by Solar Cycles, Expressed by N-S Solar Asymmetry, Proc. of Eleventh Workshop "Solar Influences on the Magnetosphere, Ionosphere and Atmosphere, Primorsko, Bulgaria, DOI:10.31401/WS.2019.proc, 152-157.

Chapanov Ya. 2021. Solar Harmonics and ENSO Variations. EAGE, Volume 2021, European Association of Geoscientists & Engineers, 2021, DOI:10.3997/2214-4609.202149BGS42, 1-5.

Juhl, J. 1984. The "Danish Method" of weight reduction for gross error detection. In: XV ISP Congress proc., Comm. III, Rio de Janeiro

Kegel, J. 1987. Zur Lokalizierung grober Datenfehler mit Hilfe ROBUSTER Ausgleichungsfervahren. Vermessungstechnik 35, Berlin, 348-350

Kilifarska, N.A. Bi-decadal solar influence on climate, mediated by near tropopause ozone. *J. of Atmosph. and Solar-Terrestrial Physics*, SI: Vertical Coupling 136, 2015, 216–230.

Kilifarska N., Bojilova R. Geomagnetic focusing of cosmic rays in the lower atmosphere –evidence and mechanism, *Compt. rend. Acad. Bulg. Sci*., 72(2), 2019, 365-374.

Velichkova Ts., Kilifarska N., Inter-Decadal Variations of the ENSO Climatic Mode and Lower Stratospheric Ozone, Comptes rendus de l'Acad´emie bulgare des Sciences, 73(4), 2020, 539-546.

Velichkova Ts., N. Kilifarska, Galactic Cosmic Rays Influence on the Earth's Climatic Modes, Bulgarian Journal of Physics, 47, 2021, 14–25.

Krivova N.A., Vieira L.E.A., Solanki S.K. 2010. Reconstruction of solar spectral irradiance since the Maunder minimum. J. Geophys. Res. 115 (A12112), 1-11.

Kubik, K. 1982. An error theory for the Danish method. In: ISP Symposium, Comm. III, Helsinki.

Yeo K.L., Krivova N.A., Solanki S.K., Glassmeier K.H. 2014. Reconstruction of total and spectral solar irradiance from 1974 to 2013 based on KPVT, SoHO/MDI and SDO/HMI observations. Astron. Astrophys. 570 (A85), 1-18

New Research Project: Ground-Based Monitoring of Cosmic Particles and Space Weather

Petrov N.[1], Tsvetkov Ts.[1], Tyutyundzhiev N.[2], Semkov E.[1], Mishev A.[4], Shirov G.[1], Zinkova Y.[1], Mutafov A.[1], Nichev H.[2], Petrov M.[2], Angelov H.[3], Arsov T.[3], Serafimov N.[3], Georgiev G.[3]

[1]Institute of Astronomy and National Astronomical Observatory, Bulgarian Academy of Sciences;
tstsvetkov@astro.bas.bg
[2]Institute of Electronics, Bulgarian Academy of Sciences
[3]Institute of Nuclear Research and Nuclear Energy, Bulgarian Academy of Sciences
[4]University of Oulu, Finland

1. Abstract.

During the various cosmic events, including supernova explosions, star formation processes, collisions or strong accretion processes in stars and black holes, etc., photons (light) covering the entire electromagnetic spectrum and high-energy particles (called cosmic rays) are released, with energies from tens of eV to thousands of GeV. Cosmic rays (CRs) consist of mainly protons (about 90%), atomic nuclei (primarily helium), as well as free electrons propagating in space with speed close to the speed of light. Of course, the diverse energy spectrum of CRs also includes high-energy particles that are product of solar activity processes. On the one hand, the answer to the nature and physics of these questions is directly related to the continuous monitoring of various manifestations of solar activity, such as sunspots, solar prominences, solar flares and coronal mass ejections. But on the other hand, the possibility of continuous observational series of data has opened up new fields of scientific debate with increasing attention being paid to small-scale structures and short-living manifestations of solar activity. They turn out to have a significant role in a global interconnection with all other members of the Solar system, including our planet Earth. Solar activity and the resulting solar radiation, together with the total cosmic radiation, appear to be the main cosmic factors influencing the Earth's global climate.

Keywords: space weather; energetic particles; neutrons.

2. Introduction

Throughout the long evolutionary change of our Solar system, in particular our planet Earth, climate changes have occurred and still occur under the complex combined influence of various factors, but among them the impact of cosmic factors is of primary importance, especially when we talk about time scales ranging from several decades to several centuries. Among the cosmic factors influencing the Earth's climate are the cosmic rays (CRs). Recently, an idea related to the climate change, called cosmoclimatology, was presented that suggests that variations in the intensity of CR flux influence [Svensmark, 2007], yet still under debate e.g. [Sloan and Wolfendale, 2008; Kulmala et al., 2010] and the recent CLOUD experiment results.
Solar radiation has a significant effect on the weather. "Weather" usually defines the short-term physical state of our atmosphere. However, it is determined by many complex and interacting phenomena that also affect local and global climates over long periods of time. The Sun and every other star have continuous radiation over a wide range of wavelengths with varying intensities. Electromagnetic solar radiation falling into the upper limit of the Earth's atmosphere is called extra-terrestrial radiation, which determines an average power of 1360.8 W/m^2 (solar constant). The radiation with the greatest importance and influence on Earth processes lies in the range 280-3000 nm (shortwave radiation) and 3 μm->40 μm (longwave radiation). The

maximum intensity of the solar spectrum at the Earth's surface is between 400 and 500 nm (depending on sky conditions).

Solar radiation reaching the Earth is key to managing the food and water resources that determine the population's viability. But of course, it is even more important to note that solar energy is the main reason for the existence of life on our planet at all. The Sun, as an energy source, is increasingly used to provide clean and renewable energy with no carbon footprint or greenhouse gas emissions. Solar energy can be used to generate electricity and provide heat, but of course this is also highly dependent on climate and weather.

The climate system, whether local or global, is a complex and highly interconnected environment consisting of the atmosphere, the hydrosphere, the solid Earth's surface, the cryosphere, and the biosphere. Under the influence of solar radiation and the rotation of the Earth, air masses move from one region to another on a large scale. Improved numerical methods and analysis of observed meteorological data in recent years have provided outstanding meteorological models for real-time forecasting of the weather system. These models are used both to study the dynamics of the weather and the climate system and to provide increasingly accurate short-term (a few days to a few weeks) weather forecasts. However, the spatial and temporal uncertainty of climate models is large, and global models cannot resolve horizontal scales finer than about 50 km, and regional projections are even less certain. Therefore, the probability of extreme weather events is still an open question.

Traditional approaches to the multiscale climate modeling problem are unlikely to lead to breakthroughs when used separately. Meteorological data for temperature and humidity near the Earth's surface are crucial inputs to atmospheric models for short-term forecasting. In-situ measurements of temperature and moisture profiles by radiosondes have limited temporal resolutions (e.g., twice daily) and spatial coverage, especially in remote regions. We offer not only the construction of a station of modern sensors for measuring meteorological parameters with high resolution in time (seconds or minutes of the day), but also the possibility of CR observations, which are a promising new source of meteorological data to narrow data gaps by providing indirectly measured continuous records of temperature and moisture.

Galactic and solar CR particles entering the Earth's atmosphere with energies above 0.5 GeV undergo nuclear interactions with molecules from the Earth's atmosphere and produce a secondary stream of particles that reaches sea level. The development of the neutron monitors by J. A. Simpson provided a method for detecting and recording low-energy secondary neutrons [Simpson, 2000]. These secondary CRs fall in the energy range from several hundred MeV to about 1 GeV. Neutron detectors are most sensitive to the low energy (1-20 GeV) part of the spectrum. With their reliability and basic simplicity, they are a means of studying long-term weather variations, but their sensitivity and high counting (measurement) rates make it possible to observe short-term weather changes as well.

In the 1960s, a new neutron monitoring method was developed with a statistical accuracy of 0.1% for hourly data. This monitor, called a "super" monitor or NM-64, uses more advanced data collection techniques. Data from this type of monitoring observations have proven to be extremely stable and are particularly valuable for long-term cosmic radiation studies. Today, there are about 59 neutron monitor stations in operation worldwide with a wide range of geomagnetic boundaries, altitudes, and viewing directions.

The energy of cosmic ray particles that can penetrate the Earth's upper atmosphere is a function of the geomagnetic field. The Earth's magnetic field can be used as a spectrometer that allows measurements of the cosmic ray spectrum down to low primary energies. The magnetic width of a particular neutron monitoring station determines the lowest magnetic rigidity of the primary flux that can reach the detectors, the so-called “cut off rigidity”. Accordingly, the altitude of the station also determines the amount of absorbing atmosphere above it. As a result,

the amount of secondary CRs absorbed decreases with height because of the lower absorption number. By using a combination of lead (to create local interactions), paraffin or polyethylene (to soften or slow down the neutron component), and multiple slow neutron detectors, the particle counting rate can be greatly increased.

Nowadays, the measurement of solar radiation is extremely important in many different fields of application, such as climatology, meteorology, hydrology, pollution forecasting, solar energy, agriculture, and material testing [Dhasmana et al., 2023; Waldman et al., 2020]. Measuring solar radiation for climatology and weather forecasting is an important part of many of our daily activities that we can no longer do without. For example, the data obtained is essential for shipping and aviation. To understand and predict climate changes, high-precision and reliable measurements over long periods of time are needed to quantify small and slow, but significant trends. Weather observation and prediction are absolutely vital to our modern civilization and its technical progress. Transport and trade by land, sea and air cannot be sustained without continuous measurement and collection of weather data. Protecting human lives by predicting avalanches, torrential rains, hurricane-force winds and other hazards would not be possible without continuous monitoring of solar radiation.

In recent years, the measurement of solar radiation has also become increasingly important in the field of material testing, where, for example, the resistance to UV radiation of products and coatings comes to the fore. Accurate solar radiation data is critical to the solar energy industry. In research and development, selection of optimal locations and types of systems, performance monitoring and maintenance planning.

3. Project Implementation

3.1. Methodology

The new research project will investigate climate changes both in our country and on a global scale, using CR flux measurement combined with modern standardized sensors for various meteorological parameters. A ground-based continuous monitoring of CRs will allow our country to be included in a common global network, covering different parts of the globe.

To implement part of the tasks and objectives of the project, we envisage using data on solar activity from observations of already existing infrastructures – the new 30-cm chromospheric telescope at the NAO Rozhen [Tsvetkov and Petrov, 2021], as well as observations from ground-based observatories outside the country. For a better continuous observational sample data from space-based solar observatories (e.g., SDO, STEREO, SOHO, etc.) will also be used.

The work on observational databases of solar activity is the connecting element to the achievement and implementation of the main work packages of our project (Table 1). Suggested work packages will lead to the construction of a modern monitoring system for measurement and analysis of CR flux parameters and Earth's low atmosphere parameters.

Table 1. *Work organization on work packages (WP) and the tasks included in each of them.*

	Tasks
WP1	Creating a small network of mini-NMs at different altitudes in Bulgaria and becoming part of global neutron detectors network.
WP2	Building meteorological stations next to NMs in order to collect accurate and continuous data of basic meteorological parameters.
WP3	Creating a secure database open for teams with purely scientific and scientific-applied activities.

3.2. Goals and issues

One of the main reasons for the rapid rise of average global temperature (Fig. 1) is the increase of atmospheric carbon dioxide from the burning of fossil fuels. Scientific research shows that extreme weather events such as floods (due to sea level rise), strong storms and heat waves are likely to become more frequent and more intense. Such extreme weather conditions and unusual climate patterns are already evident today. Such events have a diverse impact on the living conditions of our planet, which obliges a transition to a low-carbon economy worldwide in order to be prepared and resist catastrophic climate changes.

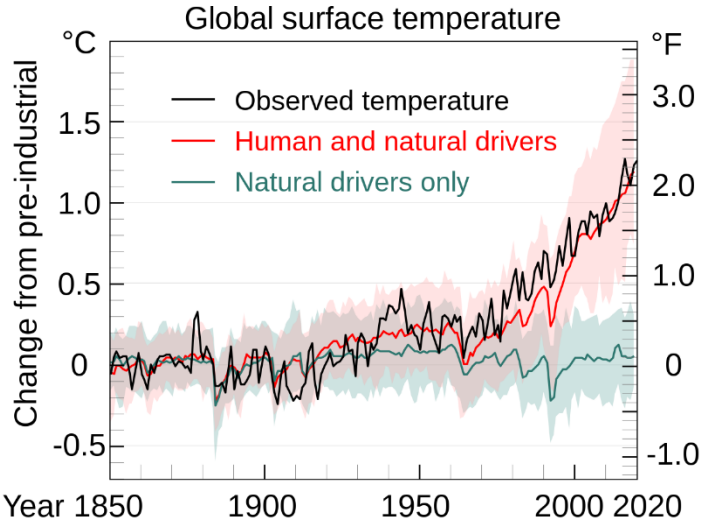

Figure 1. *Changes in mean surface air temperature since the industrial revolution according to data from the Intergovernmental Panel on Climate Change (IPCC).*

It is impossible to study the Earth's climate without studying the activity of the Sun since it modulates the Earth's climate over tens and hundreds of years. The relationship between solar activity and the Earth's environment (also known as "space weather") is not trivial and involve many interacting processes.

Satellite data show that the strength of solar radiation may correlate with the 11-year cycle of solar activity. That is why scientists continue to look for the connection between solar activity and climate changes on Earth. It has not yet been established exactly how closely the climate cycles coincide with the 11-year cycle of solar activity. Despite individual cases of coincidence are found, there are still no reliable statistical data to define a certain regularity. Solar events such as coronal mass ejections (CMEs) and solar energetic particle events (SEPs) can also influence changes in Earth's climate. This shows that there is disagreement among scientists about the direct effect of solar luminosity on climate. Therefore, understanding, analyzing and predicting space weather becomes important for the proposed approach to climate research.

The main goal of our research project is to build a modern monitoring system of CR fluxes and meteorological data. Accomplishing this primary goal aims to enable new models to more accurately predict short- and long-term climate changes on Earth related to cosmic factors that determine the space weather. The tasks and goals set in the project are of fundamental

importance for the study of climate change in our country, but it is also an important step towards the opportunity for us to join the world networks for monitoring and analysis of global climate change on Earth.

3.3. Expected results and conclusions

- Continuous monitoring of CRs.
- Continuous monitoring of basic meteorological parameters.
- Exploring the relationship between solar activity, CRs and local meteorological parameters.
- Obtaining a new knowledge about the physics of interaction between CRs and local meteorological phenomena.
- Creating catalogs describing the manifestations of solar activity and unobserved anomalies of meteorological data.
- Acquiring deeper knowledge of the processes and phenomena considered as precursors of meteorological anomalies and/or extreme meteorological events.
- Obtaining more complete picture of the close relationship between solar flares, eruptive prominences and CMEs with measurements of the density of CRs that reach the ground.
- Determining statistical dependences in the cyclic behavior of the number and spatial distribution of eruptive prominences, solar flares and CMEs with the observed fluxes of CRs and meteorological parameters.

Acknowledgment

This work is supported by the National Science Fund of Bulgaria with contract No. KP-06-N64/3.

References

Dhasmana, M. K., Mondal, A., Zachariah, M. (2023). On the role of climate change in the 2018 flooding event in Kerala, Environ. Res. Lett., Vol. 18, Issue 8, id. 084016, 11 pp.

Kulmala, M., Riipinen, I., Nieminen, T. et al. (2010). Atmospheric data over a solar cycle: no connection between galactic cosmic rays and new particle formation, Atmos. Chem. Phys., Vol. 10, Issue 4, pp. 1885-1898.

Simpson, J. A. (2000). The Cosmic Ray Nucleonic Component: The Invention and Scientific Uses of the Neutron Monitor, Space Sci. Rev., Vol. 93, Issue 1/2, p. 11-32.

Sloan, T., Wolfendale, A.W. (2008). Testing the proposed causal link between cosmic rays and cloud cover, Environ. Res. Lett., Vol. 3, id. 024001.

Svensmark, H. (2007). Cosmoclimatology: a new theory emerges, Astron. Geophys., Vol. 48, Issue 1, pp. 1.18-1.24.

Tsvetkov, Ts., Petrov, N. (2021). Development of Solar Observations in Bulgaria: New 30-cm Chromospheric Telescope. Bulg. J. Phys., Vol. 48, Issue 1, pp. 55-61.

Waldman, K. B., Todd, P. M., Omar, S., Blekking, J. P., Giroux, S. A., Attari, S. Z., Baylis, K., Evans, T. P. (2020). Agricultural decision making and climate uncertainty in developing countries, Environ. Res. Lett., Vol. 15, Issue 11, id.113004, 18 pp.

Hypothetic Atmospheric Response to SEP Explaining Peculiar Electric Fields and Currents at High Latitudes

Tonev P., Asenovski S.

Space Research and Technology Institute BAS, Sofia, Bulgaria, e-mail: ptonev@bas.bg

Abstract.

Experimental measurements of atmospheric electric characteristics conducted at high geomagnetic latitudes during several strong solar proton events with ground-level enhancements demonstrate well-expressed peculiarities in variations of the vertical electric field E_z and the related electric current J_z in stratosphere, as well as at surface. Considered here is a specific peculiarity which is observed in each experiment: J_z becomes unusually large for time period which well exceeds the time of relaxation of electric charges in the global atmospheric electrical circuit. An interpretation of this peculiarity is represented based on hypothetical processes in polar mesopause and around during SEP.

Introduction.

Experimental investigations of the atmospheric electric fields and currents in the stratosphere and at surface at high geomagnetic latitudes during major solar energetic particles events (SEP) (Mironova et al., 2015) accompanied by ground level enhancement (GLE) demonstrate well-expressed typical peculiarities (Holzworth et al., 1987, Kokorowski et al., 2006, Shumilov et al., 2015). Essentially, these are strong (usually more than 100%) and long-continuing (from tens of minutes to many hours) deviations of the vertical electric current J_z from the fair-weather current J_{FW} by fair-weather conditions (Tonev, 2022). These deviations include increases of J_z on the first phase of SPE, as well as decreases or even reversals of J_z on a later phase, which cannot be explained by the theory of the global atmospheric electric circuit (GEC) (Rycroft et al., 2008). Hypothetic processes are considered here as response of the polar upper atmosphere to SEP which can lead to such peculiarities. The basic hypothetic process is dynamic creation of aerosol particles in the polar mesopause and around. Indirect experimental confirmations of this process are considered. The enhanced ionization during SEP leads initially to increase of conductivity σ in polar mesosphere and around, and later the process of aerosol formation can cause dramatic decrease of σ. Such process can cause redistribution of atmospheric electric currents leading to the observed peculiar J_z variations.

The peculiarity observed by experimental measurements.

During solar cycles 21-23 several experimental studies of atmospheric electrical characteristics and their behavior during SEP have been conducted at high geomagnetic latitudes which coincide by a chance with major SPE/GLEs. These experimental studies represent measurements of electric field **E** and, in some cases, conductivity σ (so that current **J** can be obtained from Ohm's law $\mathbf{J} = \sigma\mathbf{E}$) of two types: *i*) balloon-borne measurements in stratosphere; *ii*) at surface. There are only several such experiments because of the rareness of major SEP events, and of their unpredictability. First, obtained are variations of the vertical electric field E_z in stratosphere (at 30 km altitude) on two balloon stations, at (55.75°N, 97.85°W), and (64.9°N, 147.8°W), respectively, during SPE/GLE 4 August 1974 (Holzworth

and Mozer, 1979). In spite of incompleteness of measurement data, already this earlier experiment of such type indicates for typical peculiarities (their Fig.1). These peculiarities are demonstrated clearer in two similar, and more complete stratospheric experiments during SPE/GLEs on: *S1*) 16 February 1984 (Holzworth et al., 1987), and *S2*) 20 January 2005 (GLE69) (Kokorowski et al., 2006). Measurements in case *S1* are on two balloon stations located at altitude 26 km: EMA7 (38.7°S, 65.7°E) at invariant latitude Λ=–48.8° (cutoff rigidity 2.8 GV), and EMA8 (44.6°S, 142.7°E) at Λ= –56.3° (cutoff rigidity 1.4 GV), respectively. At EMA8 (at the upper latitude) a peculiar response is observed of atmospheric conductivity σ, as well as of vertical electric field E_z and corresponding electric current J_z. Particularly, J_z increases more than twice, and this variation is not transient since it lasts about 1/2 hour, longer than the relaxation time τ_{RGEC} of GEC (~7 minutes). None effect is detected on EMA7 at lower latitude. Thus, strong and peculiar response of electrical characteristics in stratosphere occurs at high (sub-high) geomagnetic latitudes, but not at lower latitudes.

In experimental case *S2* balloon-borne measurements of conductivity σ, as well as of components of the electric field **E** and of electric current density **J** are conducted during the whole day of occurrence of SPE/GLE69 (20.01.2005) (Kokorowski et al., 2006). During the day the balloon station moved from (70.9°S, 10.9°W) at 30.9 km altitude to (71.4°S, 21.5°W) at 33.2 km altitude. Similar peculiarities appear in variations of vertical electric field E_z and current $J_z=\sigma E_z$: too big (>100%) enhancement of J_z for too long (>> τ_{RGEC}) time. Experiment *S2* is used in this paper as a sample case which is best illustration of the peculiarities studied.

Similar experimental measurements are conducted at ground level, as well, at high geomagnetic latitudes (Apatity, geomagnetic latitude 63.3°) during three major SPE/GLEs in 2001 (Shumilov et al., 2015). Measured are the atmospheric electric field (AEF) E_z at surface during SPE/GLEs, respectively, on: *G1*) 15 April; *G2*) 18 April; and *G3*) 4 November. The results of these experiments demonstrate similar, as in stratosphere, peculiarities in variations of vertical electric field E_z and the related current J_z, as summarized below.

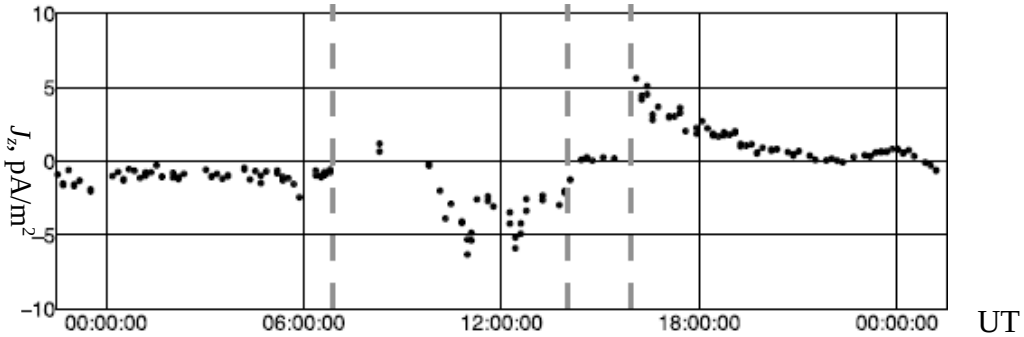

Fig.1. Density of vertical electric current J_z at balloon station MINIS Flight 2 South on January 20, 2005 with coordinates changing from (70.9°S, 10.9°W), 30.9 km altitude, to (71.4°S, 21.5°W), 33.2 km altitude) (Kokorowski et al., 2006). The SPE/GLE 69 onset (06:51 UT) is marked by the left vertical dashed line. From ~09:30 until 14:00 UT (for 4.5 hours) J_z is much bigger (up to ~300+%) than its value by quiet conditions before SPE.

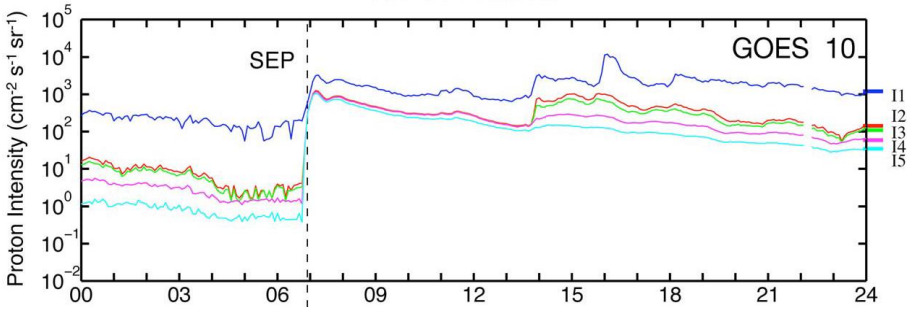

Fig.2. Integrated energetic proton flux on 20.01.2005 from GOES-10 data for channels: >1 MeV, >5 MeV, >10 MeV, >30 MeV, >50 MeV (*I1-I5*) (Kokorowski et al., 2006).

Each case *S1, S2, G1-G3* demonstrates several succeeding typical peculiarities in variations of the electric current J_z. The first peculiarity in each case is an unusually big enhancement of electric current J_z so that it becomes much larger than the fair-weather electric current J_{FW} within time period well exceeding the time τ_{GEC} of electric charge relaxation in GEC, τ_{GEC} ~7 minutes. The goal of this work is to give a hypothetic explanation of this initially occurring peculiarity in each case. Fig.1 illustrates this type of peculiarity for case *S2*: it shows variations of J_z in Antarctic stratosphere (~32 km altitude) during the day of GLE 69. Fig.2 shows simultaneous data of integrated energetic proton flux from GOES-10 data of energetic proton intensity for channels: >1 MeV, >5 MeV, >10 MeV, >30 MeV, >50 MeV (*I1-I5*). The peculiarity considered is represented by an unusually strong (up to about 300+%) positive deviation of J_z from J_{FW} for time t_{P1}~4.5 hours: from ~09:30 until 14:00 UT. Here both J_{FW} and J_z are downward. One can see that the time period of deviation begins well after the onset of SPE at 06:51 UT. We just note occurrence of peculiarities of other types after 14:00 UT: *a*) from 14:00 UT until 15:56 UT J_z almost vanishes (J_z~0); *b*) from 15:56 UT until the end of the day J_z reverses to upward (J_z>0), yet $|J_z|>|J_{FW}|$ for the most of time. Peculiarities *a*) and *b*) will be studied in another publication.

The same type of extremely big positive deviations of J_z from J_{FW} within time period $t_{P1} >> \tau_{GEC}$ occurs in each of considered cases of SPE/GLE under fair-weather conditions. Such peculiarity cannot be explained by the theory of GEC considered as isolated from outer electric sources (Farrell and Desch, 2002). (Dejnakarintra et al., 1985) also show that the detected large variations of electric field and current cannot be result of conductivity changes in polar middle atmosphere caused by enhanced ionization. Our conclusion is that the electric current J_z is a result of superposition of the fair-weather current J_{FW} with an additional current J_A produced by unknown electric source which is external with respect to GEC:

$$J_z = J_{FW} + J_{Az} \quad (1)$$

Here J_{Az} is the vertical component of the electric current J_A superimposed to the fair-weather current J_{FW}. The peculiarity in case *S2* (Fig.1) is characterized by downward current J_{Az} (J_{Az}<0) which is comparable to, or bigger than J_{FW}. We show below that in other cases, *S1*, *G1-G3*, the peculiarity considered has similar characteristics. In this paper we propose a hypothetic mechanism of generation of J_{Az} during strong SPEs.

Experimentally determined relative deviations of current J_z from fair-weather current

We characterize peculiarity considered in each experimental case *S1*, *S2* (in stratosphere), and *G1-G3* (at surface) by the ratio between the additional current J_{Az} and the fair-weather current, $R_A = J_{Az} / J_{FW}$. Used are the parameters: *i*) maximum positive value of R_A (R_{Amax}); *ii*) time period t_{JA} of the peculiar variation. These are presented below for cases *S1*, *S2*, *G1* - *G3*:

Case SPE/GLE	λ	z, km	~R_{Amax}, %	t_{JA}, hours	Reference
S1: 16.02.1984	–56.3°	26	120	0.3	Holzworth et al. (1987)
S2: 20.01.2005	–70°	32	300	3.6	Kokoropwski et al. (2006)
G1: 15.04.2001	+63.3°	surface	>400	~3.0	Shumilov et al. (2015)
G2: 18.04.2001	+63.3°	surface	400	5.5	Shumilov et al. (2015)
G3: 04.11.2001	+63.3°	surface	200	~2.0	Shumilov et al. (2015)

For each case parameters R_{Amax} and t_{JA} demonstrate presence of large additional electric current J_{Az} compared to the fair-weather current J_{FW} for time $t_{JA} >> \tau_{rGEC}$. This means that J_{Az} is dominant current in Eq.(1) for this time, thus, it is generated by an external electric source. There is difficulty with determination of such source due to the fast (quasi-exponential) increase of conductivity with altitude z. Here we present a hypothetic source of electric current J_{Az} activated during SEP.

Aerosol dynamics in stratosphere during SEP

A series of experimental studies shows that few days after major SPEs significant increase of aerosol particle density occurs in stratosphere at high latitudes (Shumilov et al., 1985, Mironova et al., 2012). Here this fact is illustrated for SPE/GLE on 16 February 1984 (case *S1*) in Fig.3 (Shumilov et al., 1985). In this case demonstrated is gradual increase of aerosol density in stratosphere at latitudes z = 15-30 km from the second day until the fourth day of SPE. Also, the disturbance in the profile descends with time. Mironova et. al. (2012) present similar but more thorough and detailed conclusions for SPE/GLE 69 (case *S2*). It is reasonable to conclude from these results that the aerosol enhancement during SEP has a relationship with enhanced ionization at polar and high geomagnetic latitudes which is strongest above the stratosphere, at altitudes up to ~95 km. The lower latitudinal boundary of this enhancement depends on the geomagnetic cutoff rigidity for the specific geomagnetic activity conditions. The delayed aerosol increase in stratosphere at high latitudes is hypothetically manifestation of two processes: 1) Increase of the aerosol density in atmospheric regions above stratosphere in relationship with highly enhanced ionization during SEP in these regions. 2) Transport of newly created aerosol particles (AP) to lower atmospheric regions as result of sedimentation or electrostatic force together with simultaneous growth of descending APs. The descending of APs to regions of bigger atmospheric density is slowed down: accumulation of grown-up APs would occur in a stratospheric layer situated well below the creation of APs.

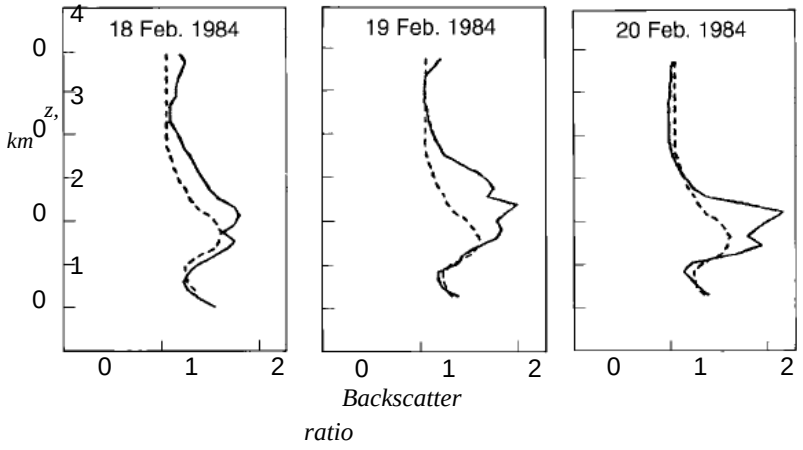

Fig.3. Scattering ratio profiles (solid lines) on 18, 19, and 20 February 1984 (Shumilov et al., 1985). Dashed curves are for quiet conditions before SPE.

Hypothetic dynamic processes in polar mesopause during SEP

We consider hypothetical processes 1 - 5 in polar mesopause and close to it during major SPEs. These processes imply presence of aerosol particles in the undisturbed mesopause before the onset of SPE which is experimentally demonstrated by structures in summer mesopause, such as noctilucent clouds (NLC), and polar mesopause summer echoes (PMSE). Short description of hypothetic processes 1 - 5 follows:

1. The enhanced ionization during SPE leads to gradual growth of APs in the mesopause due to faster attachment of ions to APs. An AP (in general, multi-charged) is assumed to be spherical, and is characterized by its radius r and by the number q_e of elementary charges carried. According to theoretical investigations (Hoppel, 1985), the attachment coefficients $v_\pm$ of an ion or electron of respective polarity to an oppositely charged AP with radius r and charge number q_e ($q_e>0$ for positively charged AP, and $q_e<0$ in the opposite case) increases quasi-exponentially with q_e. Also, the average number of elementary charges $q_{ea}(r)$ carried by an AP with radius r increases quasi-linearly with r. As result, the effective coefficients of attachment of ions to APs with radius r $v_{\pm eff}(r)$ can be represented as follows: $v_{\pm eff}(r) = v_\pm(r,q_{ea}(r))$. From these properties we find that during the enhanced production of ions in polar mesopause related to SPE the attachment rate increases at least quasi-exponentially with time t. r also will increase quasi-exponentially with time. The process of aerosol growth occurs in a region R_A with significant initial AP density S_0 (initially, the polar mesopause).

2. Additional quasi-exponential growth of APs with time can occur by attachment of neutral particles to APs.

3. The size of APs in the mesopause remains limited: r < 50 - 70 nm. By fast growth of APs this implies an effective lost mechanism of large APs. The gravitational sedimentation is too slow to compete with the quasi-exponential growth of APs. A more effective process of effective limitation of the aerosol maximum size is segmentation of large enough APs into two or more new APs. This process leads to multiplication of APs and thus to an increase of their density S. We estimate approximately how the density S of APs varies with time under simplest assumptions for the time period of SPE of energetic proton flux peak:

a) Once the radius r of an AP reaches its critical value r_{max}, it splits into two equal APs with radius $r_{min}=2^{-1/3}r_{max}$;

b) APs grow exponentially with time t as result of attachments of ions and neutral particles:

$$r_{AP}(t) \sim \exp(t/t_G),$$

where t_G is time of increase of AP radius r_{AP} from minimum (r_{min}) to maximum (r_{max});

c) Growth of APs is unlimited;

d) $S(r)$ has uniform distribution by r for $r_{max} \le r \le r_{min}$.

Then, S [cm^{-3}] satisfies the equation:

$$dS/dt = f_s = S/t_G \qquad (1)$$

where f_s is splitting frequency per cm^3: $f_s = S/t_G$ [$cm^{-3}s^{-1}$]. Eq.(1) is solved with initial condition at start time t_s of the process of splitting, $S(t_s) = S_0$. The solution is:

$$S = S_0 \exp(t/t_G). \qquad (2)$$

Eq.(2) shows that the AP density increases exponentially with time t by idealistic conditions. Hence, processes 1-3 demonstrate initial quasi-exponential growth of 'seed' APs up to their maximum size. Then, multiplication of APs leads to exponential increase of S with time.

4. Both, the quasi-exponential growth of APs size due to ion-to-AP attachment, as well as the quasi-exponential increase of their density S after time t_s, determine transfer of electric charges from small carriers (ions) to large carriers (APs) and decrease of ion and electron densities with time. This transfer of charges leads to diminishing of conductivity σ because of the decrease of electron and ion densities leading also to decrease of the charge carrier mobility in average. Actually, the conductivity variations follow changes in the balance between ions and multi-charged APs. It is described by the following balance equations for positive and negative ions (including electrons) with densities $n_\pm$ and positively/negatively charged APs with densities $S_\pm(r)$:

$$dn_\pm/dt = q - \alpha n_+ n_- - B_\mp n_\pm \qquad \text{where} \qquad B_\mp = \int_r \nu_{\mp eff}(r) S_\mp(r) dr \qquad (3)$$

Here q is the ionization rate; α is the effective coefficient of recombination, $\nu_{\pm eff}(r)$ is the effective coefficients of attachment of ions to AP with radius r. As we show, coefficients $B_\pm$ increase quasi-exponentially with time, and thus exponential decrease of n_+ and n_- is follows from Eq.(3). This last leads to quasi-exponential decrease of the electron and ion conductivities $\sigma_{i,e} = e\mu_{i,e}n_{i,e}$ with time. At the initial stage of SPE conductivity $\sigma = \sigma_i + \sigma_e$ enhances mainly due to the increase of the electron density, and later σ decreases dramatically with the intensified transfer of electric charges to APs and diminishing of $n_\pm$.

5. Formation of dynamic structure of spatial charges in region R_A. During SEP uncompensated positive elementary charges are being injected into polar and high-latitudinal middle atmosphere and are being accumulated in region R_σ where conductivity $\sigma <$. As result, a sub-region R_+ of positive spatial electric charge with density $\rho>0$ is formed in an upper portion of R_σ at polar geomagnetic latitudes. In the rest sub-region R_- negative electric charge is being accumulated including a layer below R_+. The electric current J_{Az} is interpreted here as an upward electric current of negative ions which is feeding the negative screening charge in this layer.

Conclusion.

The problem is formulated about the nature of the significant additional electric fields $\mathbf{E}_A$ and currents $\mathbf{J}_A$ superimposed to the fair-weather current J_{FW} in GEC at high latitudes during major SPE/GLEs according to measurements in stratosphere and at surface at high latitudes. Hypothetic processes initialized in polar mesopause are presented as responsible for generation of $\mathbf{E}_A$ and $\mathbf{J}_A$. It is shown that electric source can be created as result of accumulation of incoming charges which can cause variations of the vertical electric current J_z detected by experimental measurements. Hypothetically, this can be achieved by creation and growth of aerosol particles in middle atmosphere at polar and high latitudes during SEP. More detailed description of the hypothetic mechanism of the electric current J_A generation will be subject of further publications. Creation of aerosol, thus hypothesized, can have effect on formation of weather and climate. Significant changes in electric currents in GEC can affect also processes in troposphere responsible for weather formation.

Acknowledgements: This research is supported by the Bulgarian National Science Fund, grant No KP-06-N44/2

References

Dejnakarintra, M., U. S. Inan, Carpenter, D. L. (1985). Transient Tropospheric Electric Fields Resulting from Sudden Changes in Ionospheric Conductivity, J. Geophys. Res., 90(A12), 901271-90281.

Farrell, W. M., M. D. Desch (2002). Solar proton events and the fair weather electric field at ground, Geophys. Res. Lett, 29 (9), 1323, 10.1029/2001GL013908, 2002.

Holzworth, R.H., Mozer (1979). Direct Evidence of Solar Flare Modification of Stratospheric Electric Fields, J. Geoiphys. Res., 84 (C1), 1979.

Holzworth, R.H., K. W. Norville, P. R. Williamson (1987). Solar flare perturbations in stratospheric current systems, Geophys. Res. Lett., 14 (8), 852-855.

Hoppel, W. A. (1985), Ion-aerosol attachment coefficients, ion depletion, and the charge distribution on aerosols, J. Geophys. Res., 90(D4), 5917–5923.

Kokorowski, M., Sample, J.G., et al. (2006). Rapid fluctuations of stratospheric electric field following a solar energetic particle event, Geophys. Res. Lett., 33, L20105.

Mironova, I.A., I. G. Usoskin, G. A. Kovaltsov, S. V. Petelina (2012). Possible effect of extreme solar energetic particle event of 20 January 2005 on polar stratospheric aerosols: direct observational evidence, Atmos. Chem. Phys., 12, 769–778, 2012, doi:10.5194/acp-12-769-2012

Mironova, I. A., K. L. Aplin, et al. (2015). Energetic Particle Influence on the Earth's Atmosphere, Space Sci. Rev. (2015) 194:1–96, doi: 10.1007/s11214-015-0185-4.

Rycroft, M., Harrison, R.G., Nicoll, K.A., Mareev, E.A. (2008). An Overview of Earth's Global Electric Circuit and Atmospheric Conductivity, Space Sci. Rev. (2008) 137: 83–105, doi: 10.1007/s11214-008-9368-6

Shumilov, O. I., E. A. Kasatkina, K. Henriksen, E. V. Vashenyuk (1996). Enhancement of stratospheric aerosols after solar proton event, Ann. Geophys. 14, 1119-1123 (1996).

Shumilov O.I., Kasatkina E.A., A. V. Frank-Kamenetsky (2015). Effects of Extraordinary Solar Cosmic Ray Events on Variations in the Atmospheric Electric Field at High Latitudes, Geomag. Aeron., 2015, Vol. 55, No. 5, pp. 666–674 doi: 10.1134/S0016793215050151.

Tonev, P.T. (2022). Peculiar atmospheric electric field response at high latitude to three major SEP events in 2001 and possible interpretation, Proc. 14-th Workshop "Solar Influences on the Magnetosphere, Ionosphere and Atmosphere" Primorsko, Bulgaria, 6-10 June, 2021.

Solar Activity Influences on Extratropical Cyclone Trajectories in the North Atlantic

Veretenenko S.V., Dmitriev P.B.

Ioffe Institute, Russian Academy of Sciences, St. Petersburg, Russia; s.veretenenko@mail.ioffe.ru

Abstract

In this work we continue studying long-term variability of the main trajectories of extratropical cyclones (storm tracks) in the North Atlantic, basing on the data of MSLP (Mean Sea Level Pressure) archives from the Climatic Research Unit, UK (1873-2000) and NCEP/DOE AMIP-II Reanalysis (1979-2021). It was revealed that the average latitudes of storm tracks in the cold months (October-March) at longitudes from 60ºW to 10ºW undergo oscillations with the periods of ~80-100, ~40-45 and ~22 years, which indicates their possible connection with solar activity. Cyclone trajectories were found to be shifted southward at the maximum of the Gleissberg cycle and northward at its minimum, with the peak-to-peak amplitude of the secular variations reaching ~5º in the western North Atlantic. Since 1960s, at the descending branch of the secular cycle, cyclone trajectories have been shifted northward again. On the bidecadal time scale, a northward shift of storm tracks was revealed in even solar cycles, the effect being the most pronounced (~1-2º) in the eastern part of the North Atlantic. The detected oscillations of cyclone trajectories indicate long-term changes in the position of the polar jet stream, which is influenced by the intensity of the stratospheric polar vortex. A possible mechanism of solar influences on the polar vortex state involves ionization changes due to energetic charged particles (galactic cosmic rays and auroral electrons), which affect the chemical composition and temperature regime of the polar atmosphere.

Keywords: cyclone trajectories; solar activity; galactic cosmic rays.

Introduction

Extratropical cyclonic activity (formation, development and movement of cyclones and anticyclones) is an important part of the general circulation of the atmosphere providing the mass and heat exchange between high and low latitudes. Mobile extratropical cyclones, usually forming and developing over oceans, influence significantly weather and climate at middle latitudes in both hemispheres. In the Northern hemisphere, cyclones coming from the North Atlantic are responsible for many hazardous events over Europe. Recently, heavy rainfall caused by cyclone Bernd (July 2021) resulted in a severe flood in Central Europe with more than 2 hundred victims. Thus, a study of possible influence of solar activity and related phenomena on cyclonic activity at extratropical latitudes is of great importance to improve the quality of weather and climate forecasts.

According to the data [Brown and John, 1979], cyclone trajectories in the eastern North Atlantic revealed a solar cycle dependence, with their mean latitude of storm tracks in winter being 2.5º further south at solar maximum than at solar minimum. Tinsley [Tinsley, 1988] showed that this effect is the most pronounced, reaching ~6º, under the west phase of quasi-biennial oscillations of the atmosphere. On a longer time scale, model studies of circulation in the North Atlantic region during the Maunder minimum of solar activity were carried out in [Luterbacher et al., 2001]. The results of this study showed the southward shift of cyclone tracks under reduced solar activity, which seems to be in disagreement with the results by Brown and John [1979] and Tinsley [1988], who revealed a northward shift of North Atlantic cyclones with decreasing sunspot activity on a decadal time scale. So, further studies are needed to clarify possible influence of solar activity on extratropical cyclone movement on longer time scales.

For this reason, the aim of this work is to consider long-term variations in trajectories of extratropical cyclones in the North Atlantic and their possible association with solar activity.

Experimental data and their analysis

It is known that North Atlantic cyclones usually arise near the eastern coasts of North America and move, as a rule, in the north-eastern direction towards Iceland and, then, towards the Barents Sea. The cyclone movement and evolution results in the formation of an extended region of lowered pressure (a baric trough) on monthly maps of sea level pressure (SLP). The examples of a baric trough in cold months, when extratropical cyclogenesis is most intensive, are presented in Figure 1. The white line indicates the axis of a baric trough (the central line connecting minimal pressure values at different longitudes), which corresponds to a region of predominant passages of cyclones (storm track). One can see that the position of storm tracks may noticeably vary depending on a time period.

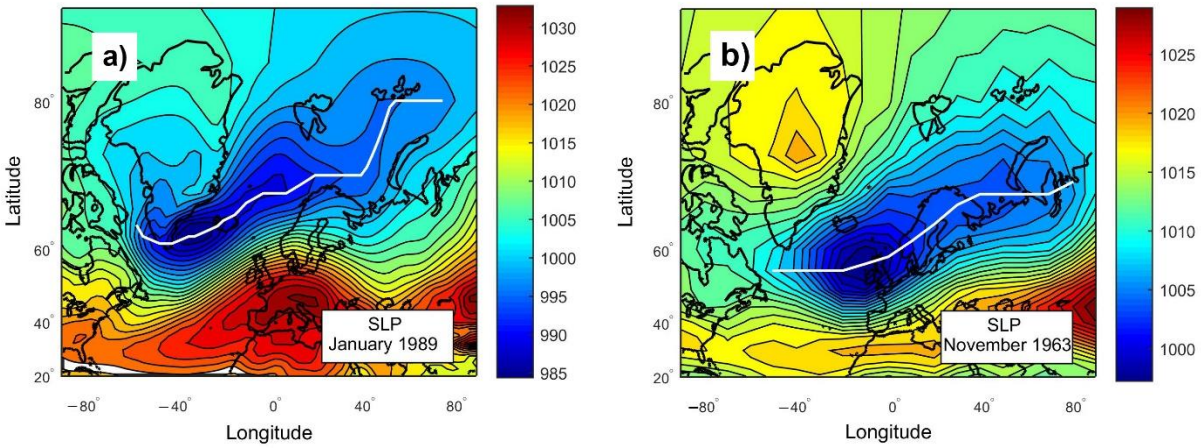

Figure 1. *Distribution of mean monthly values of SLP (in hPa) in the North Atlantic area for January 1989 (a) and November 1963 (b). The baric trough axes indicating the main directions of cyclone movement (storm tracks) are shown by white lines.*

As experimental base for this study, we used gridded monthly data from MSLP (Mean Sea Level Pressure) archives of the Climatic Research Unit (https://crudata.uea.ac.uk/) for 1873-1978 and NCEP/DOE AMIP-II Reanalysis (https://psl.noaa.gov/) for 1979-2021. To determine the position of a storm track, pressure minima and their latitudes were found for the longitudes from 60ºW to 10ºW. Then the latitudes of pressure minima were averaged over cold months (October-March), which is the period of intensive cyclogenesis at middle latitudes.

Temporal variations of the obtained storm track latitudes are presented in Figure 2. One can see noticeable variability of North Atlantic storm tracks both on interannual and longer time scales, including multidecadal and secular. Secular variations (periods ~80-100 years) seem to be more pronounced in the western North Atlantic (longitudes 60-40ºW), where cyclones usually form and deepen most intensively. This is confirmed by the results of spectral analysis (Figure 3, left panel) performed using the method of a sampling estimate of the normalized spectral density [Jenkins and Watts, 1968]. In the eastern North Atlantic, where processes of cyclone filling become more frequent, secular variations in storm track latitudes weaken, but bidecadal (~22 years) and multidecadal (~40-45 years) ones intensify.

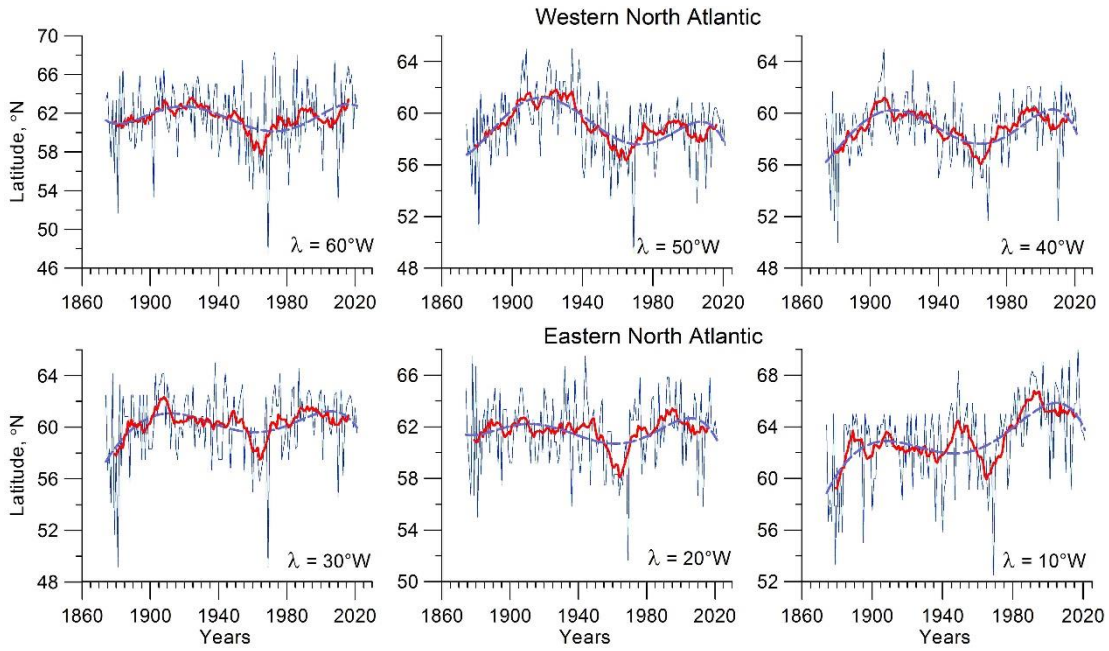

Figure 2. *Temporal variations of average storm track latitudes in cold months (October-March) at different longitudes of the North Atlantic. Thick red lines and dashed blue lines show 11-year running averages and 5th order polynomial approximation, respectively,*

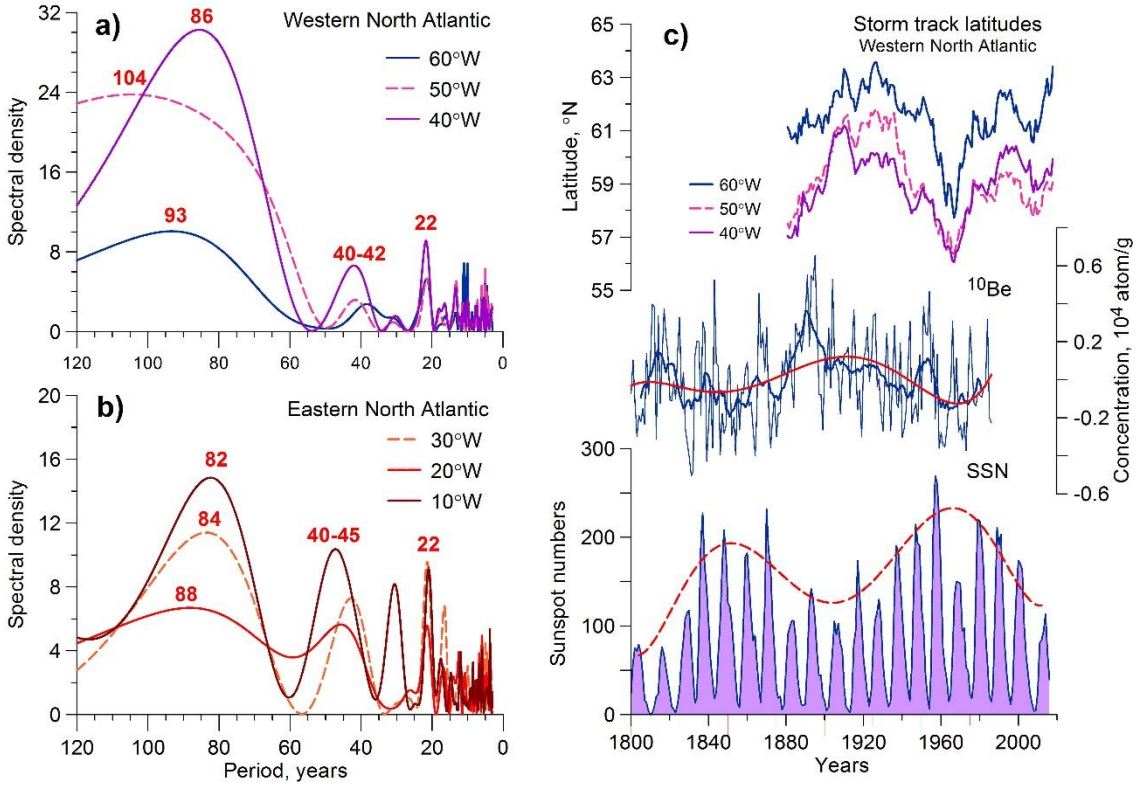

Figure 3. *Left: Sampling estimates of the normalized spectral density of storm track latitudes in the western (a) and eastern (b) North Atlantic. Right (c): long-term variations of storm track latitudes in the western North Atlantic (11-year running averages), the ^{10}Be concentration in polar ice (after the linear trend removal) and yearly sunspot numbers SSN (http://www.sidc.be/silso/datafiles). Thick blue and red lines show 11-year running averages and the 5th order polynomial approximation of the ^{10}Be concentration, respectively. The dashed red line shows the 5th order polynomial approximation of SSN at maxima of the 11-year cycle.*

Figure 3c presents a comparison of long-term variations in storm track latitudes (11-year running averages) in the western North Atlantic with sunspot numbers SSN and concentration of the cosmogenic isotope ^{10}Be in polar ice [Beer et al., 1990]. ^{10}Be concentration is used to characterize the intensity of galactic cosmic rays (GCRs), which are currently believed to be one of most plausible agents transferring solar signals to the lower atmosphere. One can see that during the period of the minimum of the secular Gleissberg cycle (~1900-1930), when GCR intensity was enhanced, storm tracks in the western North Atlantic were noticeably shifted to the north. At the maximum of the secular cycle (~1940-1960), which was accompanied by a decrease in GCR intensity, storm tracks were shifted southward. The peak-to-peak amplitude of the secular variations in cyclone trajectories amounts to ~5º. Since the ~1960s, at the descending phase of the secular solar cycle, storm track latitudes in the western North Atlantic have been increasing again. Thus, the above results suggest a possible influence of solar activity on extratropical cyclone trajectories in the North Atlantic.

To confirm a reliability of bidecadal periodicities in cyclone trajectories, an additional analysis of the high-frequency components (HFCs) of the studied time series was carried out. The HFCs were calculated using the Blackman–Tukey high-frequency filter with different "cut-off" frequencies (periods) $T_{cut\text{-}off}$. The results of spectral analysis of the HFCs are presented in Figure 4. One can see stable maxima of spectral density at the periods ~22-23 years at all the studied longitudes of the North Atlantic, which indicates the reliability of bidecadal oscillations in storm track latitudes.

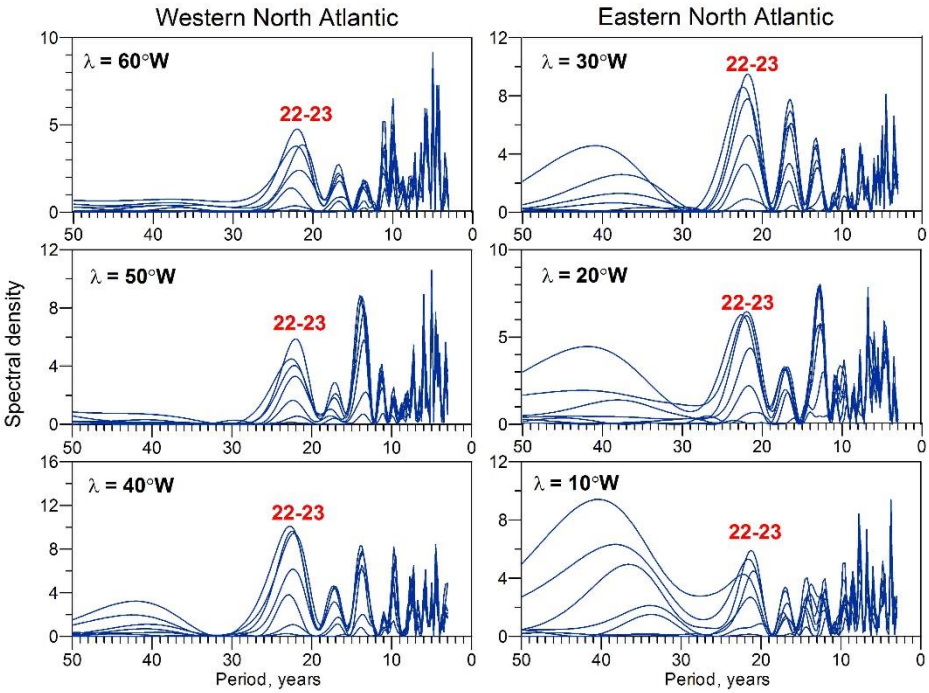

Figure 4. *Sampling estimates of the normalized spectral density of storm track latitudes (HFCs with different cut-off parameters $T_{cut\text{-}off}$ = 7, 11, 17, 23, 29, 37 and 43 years) at different longitudes.*

To clarify the nature of the detected bidecadal oscillations, a superposed epoch analysis (SPEA) of variations in storm track latitudes for even (12th to 24th) and odd (13th to 23rd) solar cycles was performed. The variations were obtained by subtracting a secular variation (presented as the 5th order polynomial) and averaged over the western (40-60ºW) and eastern (10-30ºW) North Atlantic. The results of SPEA are shown in Figure 5, the year of the solar maximum being taken as a zero year.

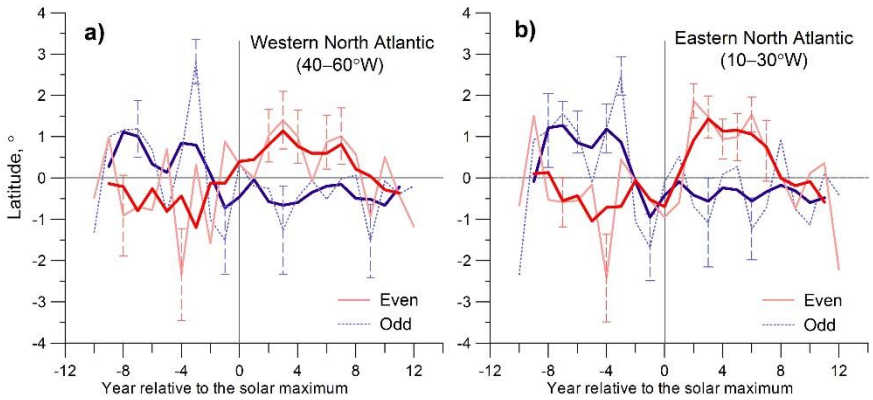

Figure 5. *Mean (SPEA) changes of storm track latitudes (after the subtraction of a secular variation) in the western (a) and eastern (b) North Atlantic for 7 even (12th to 24th) and 6 odd (13th to 23rd) solar cycles. The year of solar maximum is taken as a zero year. Thick lines show 3-year running averages. Vertical dotted lines show 2 standard errors of the mean.*

The results of the SPEA showed that variations of cyclone trajectories differ noticeably in even and odd solar cycles. In even cycles they are shifted to the north relative to a secular variation, the effect being the most pronounced (up to ~1-2º, with the confidence level above 0.95) in the eastern North Atlantic, whereas in odd cycles they are slightly shifted to the south. The largest northward shift in even cycles is observed from the 2nd to 6th year, i.e., at the descending phase and the minimum of the solar cycle.

The obtained results suggest a link between latitudinal oscillations of cyclone trajectories and solar cycles, first of all, the secular Gleissberg cycle and the ~22-year magnetic (Hale) cycle. Multidecadal (~40-45 years) variations, similar to those in storm track latitudes (Figures 3 and 4), are observed in north-south asymmetry of sunspot activity [Obridko and Nagovitsyn, 2017]. Let us consider possible mechanisms of solar influences on cyclone trajectories. The movement of extratropical cyclones is known to be closely related to the position of the polar jet stream, which is influenced by the intensity of the stratospheric polar vortex. Under a strong vortex, the polar jet strengthens and shifts poleward, resulting in a poleward shift of cyclone trajectories, whereas under a weak vortex, it slows down and shifts towards the equator. Thus, the variations of storm track latitudes on secular, multidecadal and bidecadal time scales provide evidence for corresponding oscillations in the position of the polar jet stream and the intensity of the polar vortex. The polar vortex seems to strengthen at the minimum of the Gleissberg cycle and in even solar cycles, resulting in the northward shift of cyclone trajectories, and to weaken at the secular maximum and odd cycles.

As the stratospheric polar vortex is formed in the area accessible for different kinds of energetic charged particles [Veretenenko, 2022], a possible factor of the vortex intensification may be galactic cosmic rays, whose fluxes are strongly influenced by solar activity. Secular variations of GCRs are clearly seen in the ^{10}Be concentration (Figure 3c) and may reach ±15-20%, according to the reconstruction [Stozhkov et al., 2004]. The 22-year cycle is manifested in GCR intensity as an alternation of dome-shaped and peaked maxima depending on the polarity of the Sun's overall magnetic field. Figure 6a shows the results of the SPEA of yearly cosmic ray fluxes measured in the mid-latitude stratosphere [Stozhkov et al., 2009] in even and odd solar cycles. One can see that in even cycles (when the polarity becomes positive near the sunspot maximum) GCR influx in the atmosphere noticeably exceeds that in odd cycles (when the polarity becomes negative). This difference is most pronounced at the descending phase of solar cycles, i.e., when the northward shift of cyclone tracks is the largest (Figure 5). Another agent influencing the vortex state may be geomagnetic activity, which also reveals ~22-year oscillations (Figure 6b), and related auroral electron precipitations.

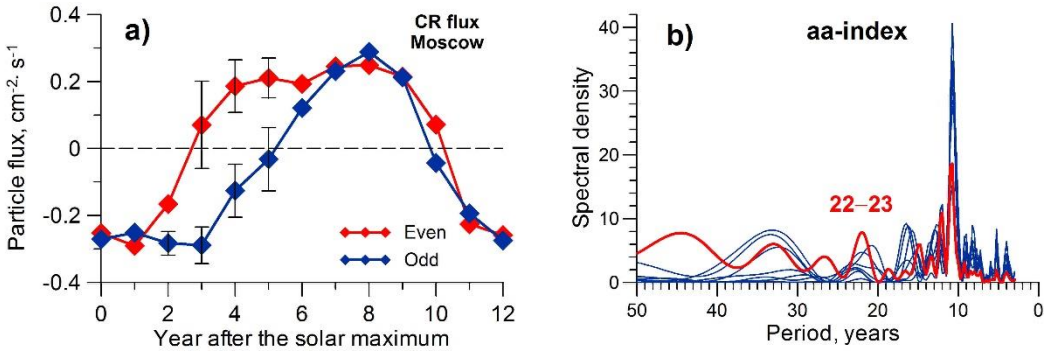

Figure 6. *a) Mean (SPEA) variations of cosmic ray fluxes (detrended) in the stratosphere in even and odd solar cycles. The year of solar maximum is taken as a zero year. b) Sampling estimates of the normalized spectral density of geomagnetic aa-index for the initial series (red line) and HFCs with different cut-off parameters $T_{cut\text{-}off}$ = 7, 11, 17, 23, 29, 37 and 43 years (blue lines).*

An intensification of the vortex may be caused by ionization increases in the polar atmosphere due to variations of energetic charged particles. Ionization increases contribute to enhanced production of nitrogen and hydrogen oxides destroying ozone, which under polar night conditions acts as a greenhouse gas absorbing outgoing longwave radiation of the Earth and the atmosphere. So, ozone depletion may result in a cooling of the polar middle atmosphere contributing to an increase of temperature gradients between middle and polar latitudes and, then, the vortex intensification. Another way of the vortex strengthening may involve radiative forcing of cloudiness changes associated with enhancement of vertical electric currents due to ionization increases [Tinsley, 2008].

Conclusions

Latitudes of the predominant cyclone trajectories (storm tracks) in the North Atlantic undergo oscillations with periods of ~80-100, ~40-45 and 22 years, which may be associated with solar activity. Cyclone trajectories were found to be shifted noticeably to the north at the minimum of the secular Gleissberg cycle, as well as at the descending phase and the minimum of even-numbered solar cycles. A possible mechanism of the detected effects seems to involve the intensification of the polar vortex due to ionization increases associated with galactic cosmic rays and auroral electron precipitations.

References

Beer, J., Blinov, A.; Bonani, G. et al. (1990). Use of 10Be in polar ice to trace the 11-year cycle of solar activity, Nature, Vol. 347, pp. 164-166.

Brown, G.M., John, J.I. (1979). Solar cycle influences on tropospheric circulation, J. Atmos. Terr. Phys., Vol. 41, pp. 43-52.

Jenkins, G., Watts, D. (1968). Spectral Analysis and Its Application; Holden-Day: San Francisco, CA, USA.

Luterbacher, J., Rickli, R., Xoplaki, E. et al. (2001). The late Maunder Minimum (1675–1715) – A key period for studying decadal scale climatic change in Europe, Clim. Chang., Vol. 49, pp. 441-462.

Obridko, V.N., Nagovitsyn, Yu.A. (2017). Solar activity, cyclicity and prediction methods. VVM, St. Petersburg

Stozhkov, Y.I., Okhlopkov, V.P., Svirzhevsky, N.S. (2004). Cosmic ray fluxes in present and past times, Sol. Phys., Vol. 224, pp. 323-333. https://doi.org/10.1007/s11207-005-5193-1

Stozhkov, Y.I., Svirzhevsky, N.S., Bazilevskaya, G.A., et al. (2009). Long-term (50 years) measurements of cosmic ray fluxes in the atmosphere, Adv. Space Res. Vol.44, pp. 1124-1137. DOI:10.1016/j.asr.2008.10.038

Tinsley, B.A. (1988). The solar cycle and the QBO influences on the latitude of storm tracks in the North Atlantic, Geophys. Res. Lett., Vol. 15, No 5, pp. 409-412.

Tinsley, B.A. (2008). The global atmospheric electric circuit and its effects on cloud microphysics, Rep. Progr. Phys., Vol. 71, pp. 66801-66900. **DOI** 10.1088/0034-4885/71/6/066801

Veretenenko, S. (2022). Stratospheric polar vortex as an important link between the lower atmosphere circulation and solar activity, Atmosphere, Vol. 13, No 7, 1132. https://doi.org/10.3390/atmos13071132

Problems Arising in Studying the Mechanism of a Solar Flare by the Way of Comparing the Results of MHD Simulations Above the Real Active Region with Observations

Podgorny A.I.[1], *Podgorny I.M.*[2]

[1]Lebedev Physical Institute RAS, Moscow, Russia; podgorny@lebedev.ru
[2]Institute of Astronomy RAS, Moscow, Russia

1. Abstract.
The primordial release of solar flare energy in the solar corona above the active region can be explained by the mechanism according to which flare energy is accumulated in magnetic field of the current sheet. MHD simulation above the real active region is continued to study the mechanism of a solar flare. For this purpose, the calculation should start a few days before the flare, when the flare energy has not yet accumulated in the corona. A general agreement between the flare positions found from the results of MHD simulations and observations is shown. However, a detailed comparison raises problems. Comparison of the MHD simulation results with observations showed the need to modernize the MHD simulation methodoы and ways of its implementation.

Keywords: Solar flare; current sheet; magnetohydrodynamic simulation.

2. Introduction

Numerous observations ([Lin et al., 2003] and others) indicate that the primordial release of solar flare energy occurs in the solar corona at an altitude of 15,000–70,000 km. It becomes necessary to explain the slow accumulation of magnetic energy, so that it can be able to release fast. These processes are explained by the solar flare model, according to which the flare energy is accumulated in the magnetic field of the current sheet formed in the vicinity of the singular line [Syrovatskii 1966]. Further, in the process of quasi-stationary evolution the current sheet transfers into an unstable state [Podgorny and Podgorny 2012]. The instability in the current sheet causes a flare release of energy with all the observed manifestations, which are explained by the electrodynamic model of the flare proposed by I.M. Podgorny in [Podgorny et al., 2010]. The model was developed based on the results of observations and numerical magnetohydrodynamics (MHD) simulations and uses analogies with the substorm electrodynamic model proposed earlier by its author [Podgorny et al., 1988].
Since the configuration of the magnetic field of the corona cannot be found from observations, to study the mechanism of a solar flare, it is necessary to carry out MHD simulations above a real active region, in which the conditions for the magnetic field on the solar surface are taken from observations.

3. Setting of problem and MHD simulation methods

The system of MHD equations in a dimensionless form was numerically solved for the region of the solar corona above active region 10365, which has the shape of a rectangular parallelepiped ($0<x<1$, $0<y<0.3$, $0<z<1$), the lower side of which XZ ($y=0$) is located on the solar surface contains the active region. The y-axis is directed from the Sun perpendicular to the photosphere. The x-axis is directed from East to West, and the z-axis from North to South. The units of length, magnetic field, plasma density and temperature are chosen to be their typical values $L_0=4 \times 10^{10}$ cm, $B_0 = 300$ G, $n_0 = \rho_0/m_i=10^8$ cm^{-3} and $T_0 =1$MK$=10^{6o}$K. The unit of plasma velocity is the Alfvén velocity $V_0 = V_A = B_0 / \sqrt{4\pi\rho_0} = 0.65\times10^{10}$ cm/s.

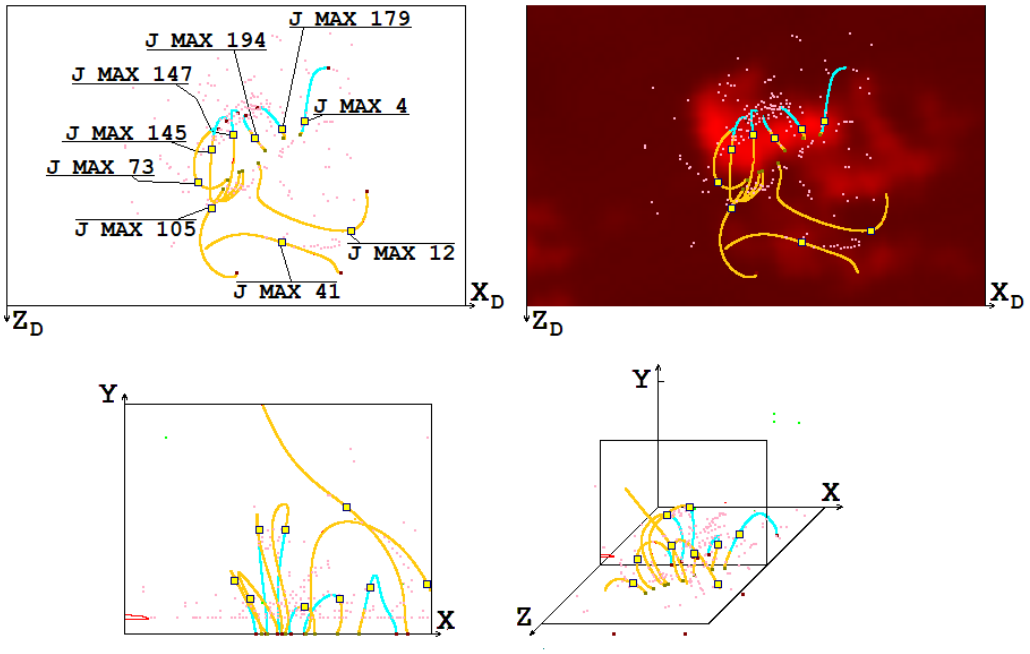

Figure 1. Comparison of the magnetic field configuration and the positions of the current density maxima with the distribution of radio emission intensity at a frequency of 17 GHz on 26 May 2003 at 02:32:05, three hours before the M1.9 flare for simulation with high viscosities ($Re_m = 3\times10^4$, $Re = 10^4$). The positions of the current density maxima are shown as green points. The magnetic field configuration is presented by magnetic lines which pass through selected current density maxima (J MAX) with the numbers 4, 12, 41, 73, 105, 145, 147, 179 and 194. Three-dimensional magnetic lines in the computation domain and their projections on the picture plain and on the central plane of the computation domain (z = 0.5) The magnetic lines in front of the central plane are shown as bold light brown lines and behind the central plane of the computational domain as light blue lines.

To select dimensionless parameters the principle of limited simulation [*I.M. Podgorny 1978*] was used, according to which much larger or much smaller unit, dimensionless parameters remain much larger or smaller than unit when simulated without their exact preservation. The main parameters characterizing the influence of ordinary and magnetic viscosity are the Reynolds numbers Re and Re_m, which are the inverse values of dimensionless viscosities ($Re_m = V_0 L_0/\nu_{m0}$, $\nu_{m0} = c^2/4\pi\sigma_0$; $Re = \rho_0 L_0 V_0/\eta$,). Large viscosities ($Re_m = 3\times10^4$, $Re = 10^4$) stabilize numerical instabilities well, and at low viscosities ($Re_m = 10^9$, $Re = 10^7$) disturbances propagating from the solar corona are practically not suppressed, which makes it possible to accumulate sufficient magnetic energy for a solar flare in the corona.

For the numerical solution, an upwind, absolutely implicit finite-difference scheme was developed which is conservative with respect to the magnetic flux [*Podgorny and Podgorny 2004*]. The methods were applied with the aim of constructing a scheme that remains stable for the maximum possible time step. The scheme was realized in the computer program PERESVET. The simulations were carried out by means of parallel computing threads on graphics cards using CUDA technology. For low magnetic viscosities numerical instabilities arise near the boundary of the computational domain, for the stabilization of which methods have been developed.

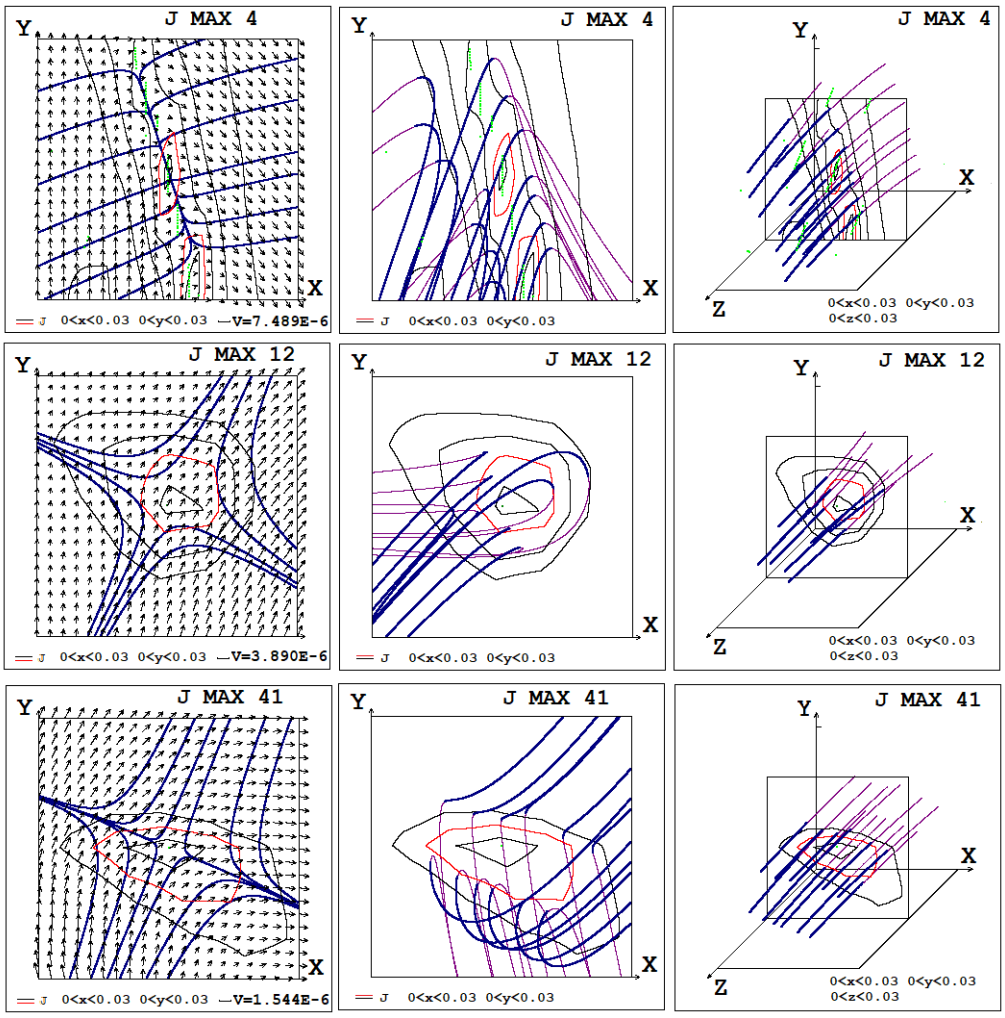

Figure 2. The configurations of the magnetic field and plasma flow near the selected 4th, 12th and 41th current density maxima on 26 May 2003 at 02:32:05 for simulation with high viscosities ($Re_m = 3\times10^4$, $Re = 10^4$). The configurations are shown by plane magnetic lines which are tangential to projections of magnetic vectors on the plane of the current sheet configuration (this plane is perpendicular to the singular line on which the current density maximum is situated; in this plane, the configuration of the current sheet is most distinctly pronounced), by projections of magnetic lines on the plane of configuration and by 3-dimensional magnetic lines.

The configuration of the magnetic field obtained by MHD simulation is so complex that it is impossible to determine the positions of singular lines and the current sheets appearing near them from it. For this purpose, a graphical search system of flare positions has been developed [*Podgorny and Podgorny 2013*]. The system is based on the search for current density maxima, which are reached in the middle of the current sheets. The current density maxima are located on the singular lines of the magnetic field.

4. Results: comparing of flare positions obtained from results of MHD simulation for different viscosities with observations

The Figures (1-3) present the results of MHD simulations for high magnetic and ordinary viscosities ($Re_m = 3\times10^4$, $Re = 10^4$) and for low viscosities ($Re_m = 10^9$, $Re = 10^7$), as well as a comparison of these results with observations of radio emission at frequency of 17 GHz obtained with the Nobeyama Radioheliograph (https://solar.nro.nao.ac.jp/norh/index.html). The results are presented for 02:32:05 on May 26, 2003, three hours before the M1.9 flare, when the magnetic field energy for the flare was accumulating in the corona. The currents, which that stores magnetic energy for the flare, heat up the corona, which cause radiation.

There are differences in the location of the current density maxima for calculations with high and low viscosities (Figures 1, 3). At the same time, for both variants, a sufficiently large number of maxima are located in the bright region of strong preflare radiation, which confirms the flare mechanism based on the accumulation of energy in the magnetic field of the current sheet. For low viscosities, a smaller part of the maxima is located in the bright region, and the total number of maxima is several times greater than in the calculation for high viscosities. This behavior of the current density maxima in calculations for two sets of parameters is apparently largely due to the appearance of a numerical instability, the stabilization of which is a significant problem if the viscosity is low. The current density in the created maxima under low viscosity conditions is 100 to 1000 times less than the current density under high viscosity conditions. The velocity of the plasma flow near current sheet for low viscosities is ~ 100 times higher than the velocity for high viscosities (Fig. 2,3). These results are a consequence of the low suppression of perturbations under conditions of low viscosity and confirm the need for MHD simulations under such conditions, despite the difficulties that arise due to the appearance of numerical instability.

Figures 1, 2 show the positions of nine selected current density maxima numbered 4, 12, 41, 73, 105, 145, 147, 179 and 194 (the maxima are numbered in order of decreasing current density in them) and the magnetic field configurations near these maxima for calculation with high viscosities. The remaining maxima are depicted by purple dots. The magnetic field configuration is represented by magnetic lines passing through the selected maxima. In the picture plane, the positions of the current density maxima and magnetic lines are superimposed on the intensity distribution of radio emission at a frequency of 17 GHz, obtained with the Nobeyama radioheliograph. To compare the positions of the six current density maxima numbered 8, 16, 19, 20, 47 and 234, the magnetic lines passing through them, and the magnetic field configurations in the calculation for low magnetic viscosities are briefly shown in Figure 3. The remaining current density maxima are shown as green dots. These results are presented in detail in the figures in [*Podgorny and Podgorny 2023*]. The flare release of energy is most likely in the current sheet formed at the current density maximum, which has the following properties. The diverging magnetic field should not strongly dominate over the X-type field [*Podgorny et al., 2021*]. The longitudinal magnetic field should not significantly exceed the field in the plane of the current sheet configuration (i.e., the plane perpendicular to the magnetic field vector at the point of maximum current density); this is expressed in the fact that the magnetic lines in space (3rd column of figures in Figure 2), located near a singular line passing through the point of maximum current density, should diverge, significantly different from straight lines. The point of maximum current density should be located near the top of the magnetic loop. As can be seen from Figures 1, 2 and 3, the current density maxima with such

properties are located both in the bright region of flare radiation or near it, and far from the bright region of flare radiation for both calculation options. At the same time, a greater number of maxima with such properties are located in the region of bright flare radiation for calculations with high viscosities (Re_m= 3×10^4, Re= 10^4), which, apparently, is also associated with the conditions for the appearance of numerical instabilities.

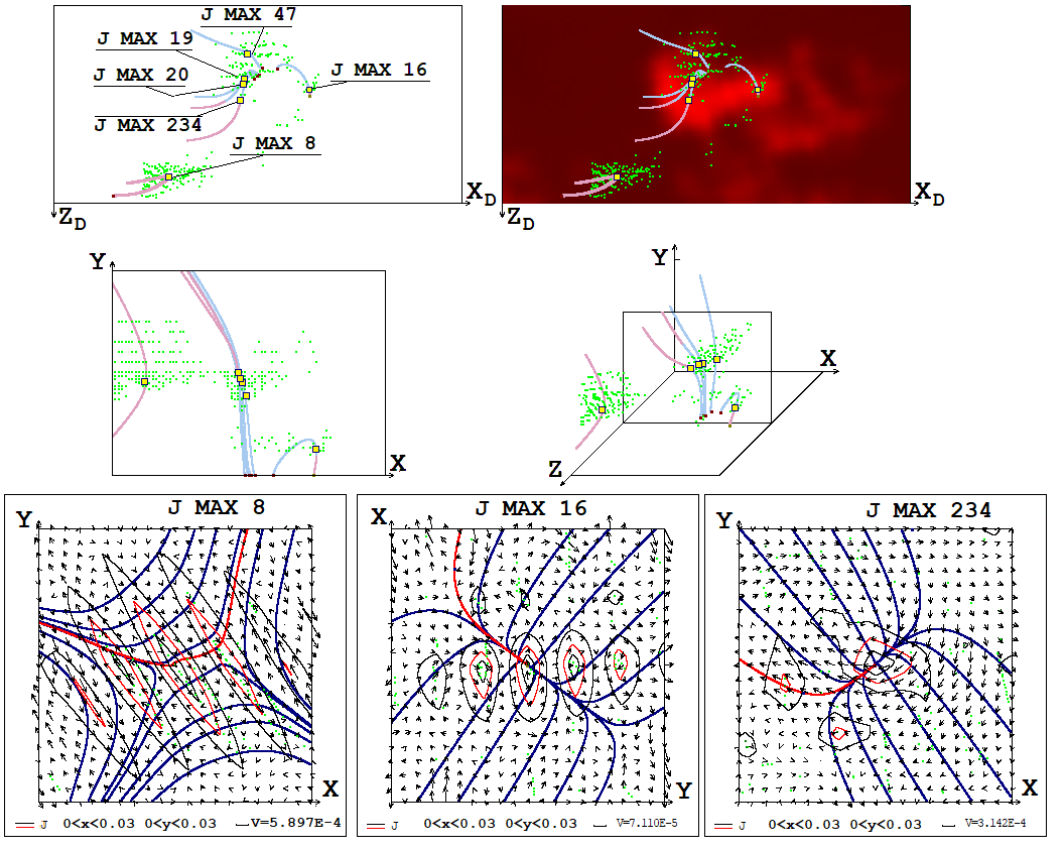

Figure 3. Comparison of the magnetic field configuration and the positions of the current density maxima with the distribution of radio emission intensity at a frequency of 17 GHz on 26 May 2003 at 02:32:05, three hours before the M1.9 flare for simulation with low viscosities (Re_m= 10^9, Re= 10^7). The positions of the current density maxima are shown as green points. The magnetic field configuration is presented by magnetic lines which pass through selected current density maxima (J MAX) with the numbers 8, 16, 19, 20, 47 and 234. The configurations of the magnetic field and plasma flow near the selected current density maxima.

5. Conclusions

1. A numerical simulation technique has been developed and modernized, including the development of a finite-difference scheme, methods for stabilizing the numerical instability that occurs near the boundary of the computational domain, and methods for solving a number of auxiliary problems.

2. It is shown that a large number (about a hundred) of current density maxima, which are located in the places of formation of current sheets on singular lines, are in the region of bright flare radiation, which confirms the mechanism of a solar flare based on the accumulation of energy in the magnetic field of the current sheet.

3. However, a sufficiently large number of current density maxima are located far from the bright region of the flare radiation (at a distance of more than 10 Mm). Moreover, many current

density maxima located far from the bright region of the flare radiation have properties that contribute to the appearance of a flare (the relatively small effect of a divergent magnetic field superimposed on the X-type configuration; a relatively small component of the longitudinal magnetic field; the location of the current density maximum near the top of the magnetic loops). This problem could arise due to an inaccurate numerical solution, and further improvement of numerical methods is necessary to solve it.

4. MHD simulations for relatively high viscosities (conventional and magnetic) showed suppression of the perturbation propagating into the corona from the solar surface, this inhibit the accumulation of large energy for a solar flare. At the same time, at high viscosities, the solution is much more stable and the position of a relatively larger number of current density maxima is in the region of bright flare radiation or near it (in this case, for calculations with high viscosities, the total number of current density maxima is less than for calculations with lower viscosities). Carrying out MHD simulations above the active region for low viscosities and for high viscosities and comparing the results of these variants of calculation makes it possible to better study the flare situation. The results obtained for sufficiently low viscosities ($Re_m = 3\times10^4$, $Re = 10^4$), at which a numerical instability arose, which significantly complicated the calculations, and for sufficiently high viscosities ($Re_m = 10^9$, $Re = 10^7$), at which weak current sheets only began to formed indicate the need for simulations for intermediate values between the indicated viscosities. It may be necessary to perform several calculations for a number of sets of intermediate viscosities in order to select the optimal MHD simulation parameters.

References

Lin R.P., Krucker S., Hurford G.J. et al. (2003) RHESSI observations of particles acceleration and energy release in an intense gamma-ray line flare. Astrophys. J., 595, L69-L76. https://doi.org/10.1086/378932

Podgorny I.M. (1978) Simulation Studies of Space. Fundamentals of Cosmic Physics. 1. №1. 1 - 72.

Podgorny, I.M.; Dubinin, E.M.; Israilevich, P.L.; Nicolaeva, N.S. (1988) Large-scale structure of the electric field and field-aligned currents in the auroral oval from the Intercosmos-Bulgaria satellite data. Geophys. Res. Lett. 15, 1538–1540. https://agupubs.onlinelibrary.wiley.com/doi/abs/10.1029/GL015i013p01538

Podgorny, A.I.; Podgorny, I.M. (2004) MHD simulation of phenomena in the solar corona by using an absolutely implicit scheme. Comput. Math. Math. Phys. 44, 1784–1806

Podgorny, I.M.; Balabin, Y.V.; Vashenyuk, E.V.; Podgorny, A.I. (2010) The generation of hard X-rays and relativistic protons observed during solar flares. Astron. Rep., 54, 645–656. https://doi.org/10.1134/S1063772910070085

Podgorny, A.I., Podgorny, I.M. (2012) Magnetohydrodynamic simulation of a solar flare: 1. Current sheet in the corona. Geomagn. Aeron. 52, 150–161. https://doi.org/10.1134/S0016793212020107

Podgorny, A.I.; Podgorny, I.M. (2013) MHD simulation of solar flare current sheet position and comparison with X-ray observations in active region NOAA 10365. Sun Geosph. 8, 71–76.

A. I. Podgorny, I. M. Podgorny, A. V. Borisenko, N. S. Meshalkina. (2021) MHD Simulation of a Flare Situation in Real Scale of Time Above AR 10365: Development of a Technique, Choice of Parameters, The Appearance of Field Singularities at Flare Sites. Proc. 13th Workshop "Solar Influences on the Magnetosphere, Ionosphere and Atmosphere" Primorsko, Bulgaria, September, 2021, 80 - 85. https://doi.org/10.31401/WS.2021.proc

Podgorny, A.I.; Podgorny, I.M.; Borisenko, A.V. (2023) MHD Simulations of the Solar Corona to Determine the Conditions for Large Solar Flares and the Acceleration of Cosmic Rays during Them. Physics 2023, 5(3), 895-910. https://doi.org/10.3390/physics5030058

Syrovatskii, S.I. ()1966 Dynamic dissipation of energy in the vicinity of the magnetic field neutral line. Sov. Phys. JETP, 23, 754–762. Available online: http://jetp.ras.ru/cgi-bin/e/index/e/23/4/p754?a=list

Possible Method for Determining Direction of Motion of Coronal Mass Ejections

Roša D.[1], Skokić I.[1,2], Hržina D.[1], Maričić D.[1], Šterc F.[1], Romštajn I.[1]

[1]Zagreb Astronomical Observatory, Zagreb, Croatia; drosa@zvjezdarnica.hr
[2]Hvar Observatory, Faculty of Geodesy, University of Zagreb, Croatia

1. Abstract

This article presents a possible method of determining the direction of motion of a coronal mass ejection (CME) by measuring the secular (perspective) acceleration and radial velocity. The method is already used in stellar astronomy for measuring the proper motions of stars. In solar physics the direction and propagation of CMEs is one of the most discussed topics in space weather phenomena. Using the appropriate methodology is crucial for finding different approaches to estimate the direction and position of Earth directed CMEs.

Keywords: Coronal mass ejections (CMEs), kinematics, secular (perspective) acceleration.

2. Introduction

In many astronomical fields, there is the underlying problem of determination of the real velocity and direction of movement of a heavenly body. The problem is difficult to solve, especially in case of CMEs. The ejected material is not a point-like so the morphology cannot be clearly identified from a series of photographs which is the case for other celestial bodies. Additional problems are generally a non-uniform motion, changes in morphology and internal motions. Several methods have been developed to determine CME kinematics to an extent, such as: the Point-P [Howard et al., 2006], Fixed-Φ [Kahler and Webb, 2007], harmonic mean-HM [Lugaz et al., 2009] and visual fitting method [Wood et al., 2009; Maloney et. al., 2009]. Satellites, for example Solar and Heliospheric Observatory (SOHO) [Brueckner et. al. 1995], Solar Terrestrial Relations Observatory (STEREO) [Kaiser et al., 2008] and Parker Solar Probe [Fox et al., 2016], are a source of observational data. Two STEREO spacecrafts provide stereoscopic imaging of the solar phenomena, which enables more accurate forecasting of CMEs interaction with Earth.

3. The method based on secular acceleration

This method does not require stereoscopic observations. Observations by one satellite are sufficient, based on the assumption that by observing a certain feature of a CME, it is possible to determine its position on the celestial sphere and its radial velocity very accurately. Assuming that a recognizable feature at a given time interval of the observations moves uniformly, the problem is uniquely solvable. The method is related to a study of the proper motion of stars and the effect of perspective (secular) acceleration [Green, 1988; Perryman, 2009].
Figure 1 shows the observing body (or any of its recognizable features) uniformly moving along a straight line with velocity V from position X' to position X. The coordinate system was chosen in such manner that its origin O (in which is the observer) and the velocity vector V are in the same plane. Coordinate x-axis is perpendicular to the velocity vector of the body. The distance of body in its position X' is r. That distance and the angle θ indicated in Figure 1, define the position of the body in the selected coordinate system.

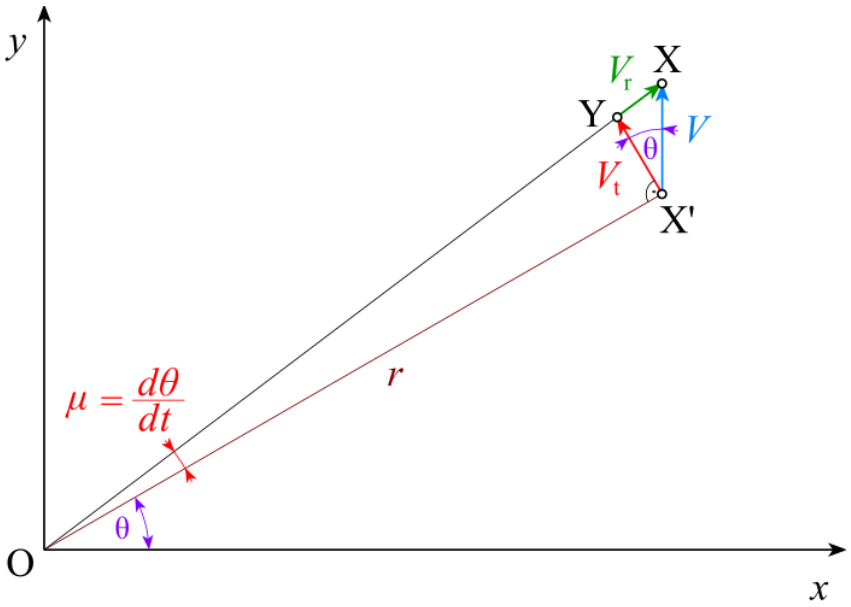

Figure 1. *Radial (V_r) and transversal (V_t) velocity component of the body.*

Distance X'X which body traverses over a selected time interval of observations is very small in comparison to the distance r. Therefore, in the first approximation, the velocity of angular displacement of the body on the celestial sphere (μ) can be considered constant:

$$\mu = \frac{d\theta}{dt} = \text{const.}$$

We can decompose the velocity of the body into the radial component V_r that is given as:

$$V_r = \frac{dr}{dt} \tag{1}$$

and transversal component given with expression:

$$V_t = r\frac{d\theta}{dt} \tag{2}$$

From the Figure 1 we see that these components relate to the velocity V of the body with following expressions:

$$\begin{aligned} V_r &= V\sin\theta \\ V_t &= V\cos\theta \quad . \end{aligned} \tag{3a, b}$$

Assuming that the angle μ is small, the transversal component is:

$$\text{tg}\mu \approx \mu(\text{rad}) = \frac{\overline{\text{YX'}}}{r}$$

Distance YX' can be expressed as the product of the transversal velocity component (V_t) and the associated time Δt. Than we have:

$$\mu(\text{rad}) = \frac{V_t \Delta t}{r} \tag{4}$$

Let us find now the expression for change of angular displacement. Taking into account the expression (2), we can rewrite the equation (3b) in the form:

$$V\cos\theta = r\frac{d\theta}{dt}$$

By differentiating, we get:

$$-V\sin\theta\frac{d\theta}{dt} = \frac{dr}{dt}\frac{d\theta}{dt} + r\frac{d^2\theta}{dt^2}$$

As $\mu = d\theta/dt$ and $V\sin\theta = dr/dt = V_r$, we easily derive an expression:

$$\frac{d\mu}{dt} = -\frac{2\mu}{r}V_r \tag{5}$$

The expression (5) represents a change of angular displacement that is called secular or perspective acceleration. If we are able to perform sufficiently accurate measurements of the displacement of the body and to determine the amount of the secular acceleration ($\Delta\mu/\Delta t$), then it is possible to exactly determine the velocity and direction of motion of the body. Let us suppose that μ is the measured average displacement of the body in the observed time interval Δt. Using the expression (5) we find the distance to the body is:

$$r = |r| = \frac{2\overline{\mu}V_r}{\frac{\Delta\mu}{\Delta t}}$$

where the radial velocity is determined from the spectral measurements. Knowing the distance, we can find (using the expression (4)) the tangential velocity component (V_t). Direction of the motion is determined by the angle θ, which can be found using the formula:

$$\theta = \arctan\left(\frac{V_r}{V_t}\right) \tag{6}$$

which follows from the expression (3a, b). The velocity V is given by expression:

$$V = \sqrt{V_t^2 + V_r^2} \tag{7}$$

which follows directly from Figure 1, or from the expressions (3a, b).

4. Conclusions

The method based on secular acceleration makes it possible to determine the real velocity of the observed feature, its distance and direction of motion, which is important for space weather forecasting. The difficulty is that the method requires accurate astrometric and spectroscopic measurements. In the following research, we will try to apply the method to specific observational data.

References

Brueckner, G.E., Howard, R.A., Koomen, M.J. et al. (1995). The Large Angle Spectroscopic Coronagraph (LASCO), Solar Phys. 162, 357, DOI: 10.1007/978-94-009-0191-9_10.

Fox, N.J., Velli, M.C., Bale, S.D. et al. (2016). The Solar Probe Plus Mission: Humanity's First Visit to Our Star, Space Sci Rev 204, 7, DOI: 10.1007/s11214-015-0211-6.

Green, R.M. (1988). Spherical astronomy, Cambridge University Press, Cambridge, Great Britain.

Howard, T.A., Webb, D.F., Tappin, S.J., Mizuno, D.R., Johnston, J.C. (2006). Tracking halo coronal mass ejections from 0 – 1 AU and space weather forecasting using the Solar Mass Ejection Imager (SMEI), J. Geophys. Res., 111, A04105, DOI: 10.1029/2005JA011349.

Kahler, S.W., Webb, D.F. (2007). V arc interplanetary coronal mass ejections observed with the Solar Mass Ejection Imager, J. Geophys. Res. 112, 11. DOI: 10.1029/2007JA012358.

Kaiser, M.L., Kucera, T.A., Davila, J.M., St. Cyr, O.C., Guhathakurta, M., Christian, E. (2008). The STEREO Mission: An Introduction, Space Sci. Rev. 136, 5-16, DOI: 10.1007/s11214-007-9277-0.

Lugaz, N., Vourlidas, A., Roussev, I.I., Morgan, H. (2009). Solar-Terrestrial Simulation in the STEREO Era: The January 24-25, 2007 Eruptions, Solar Phys. 256, 269, DOI: 10.1007/s11207-009-9339-4.

Maloney, S.A., Gallagher, P.T., McAteer, R.T.J. (2009). Reconstructing the 3-D Trajectories of CMEs in the Inner Heliosphere, Solar Phys. 256, 149, DOI: 10.1007/s11207-009-9364-3.

Perryman, M. (2009). Astronomical Applications of Astrometry: Ten Years of Exploitation of the Hipparcos Satellite Data, Cambridge University Press, Great Britain

Wood, B.E., Howard, R.A. (2009). An Empirical Reconstruction of the 2008 April 26 Coronal Mass Ejection, Astrophys. J. 702, 901, DOI: 10.1088/0004-637X/702/2/901.